

 DTU Compute

Department of Applied Mathematics and Computer Science

Two-dimensional magnetic crystals from first-principle

Daniele Torelli

Kongens Lyngby 2020



DTU Physics
Department of Physics
Technical University of Denmark

Fysikvej
Building 309
2800 Kongens Lyngby, Denmark
Phone +45 4525 3344
info@fysik.dtu.dk
www.fysik.dtu.dk

Abstract

The main and most productive project I have undertaken during my Phd involves the study and characterization of magnetic monolayers from first-principle calculations. In the following pages are presented methods developed during this time and the results that followed.

The motivation for this kind of research lies in the undeniable increasing interest that scientific community is showing towards materials design for novel technological applications. Two-dimensional (2D) materials, characterized by a thickness of just few atoms, have always been deemed an optimal compromise between extension and lightness. The isolation of the first 2D material, graphene, hit the ground running in 2004, exhibiting as well strength and electric proprieties out of the ordinary. Since then, thanks to advancement in both theoretical and experimental expertise, many others have been successfully synthesised.

But until very recently, magnetism has eluded researchers in Flatland. Only in 2017 it was demonstrated that a single monolayer of CrI_3 exhibits intrinsic out-of-plane ferromagnetic order up to a temperature of 45 K, and just few others examples are nowadays known to do the same. This may sounds quite surprising looking at the fair variety of available bulk systems which display a robust magnetism even at high temperatures. Furthermore, many of these crystals are in a multilayered form, meaning they could be mechanically exfoliated into free standing nano-sheets. But magnetic proprieties result to changes dramatically when the dimensionality of the system is reduced and better insights are required to predict new promising candidates.

The interactions between magnetic moments inside a crystal contribute in outlining its magnetic proprieties, such as the critical temperature. This is defined as the temperature above which thermal fluctuations prevent any magnetic order in a sample and sets the conditions for its usability in real devices. Magnetic anisotropy, originating from to the geometry of the system, also plays a crucial role, in particular for 2D materials. In a microscopic model, these interactions are typically reproduced by the Heisenberg model and in this work we investigate the role of some of its most relevant terms.

We also suggest the spin-wave gap as a main descriptor for the critical temperature of ferromagnetic order in 2D systems, which can be easily obtained from first-principle methods, such as Density Functional Theory calculations.

Combining the results of classical Monte Carlo simulations, we further simplified and generalized our method in order to perform high-throughput computational search of 2D materials with high critical temperature. Our results are in good agreement with available data in literature and provide a list of new promising candidates for further experimental investigations.

The screening has been run over the Computational 2D Materials Database, the Crystal Structure Database and the Crystallographic Open Database, and can be used as a future reference for benchmarking.

The thesis consists of a brief introduction to the established theory in the field followed by the list of publications produced by the submitter, each introduced by a short commentary and a summary of the original contents presented.

Resumé

Det vigtigste og mest produktive projekt jeg har arbejdet på, på min PhD, involverer studiet og karakteriseringen af magnetisk enkeltlag fra ab-initio beregninger. På de følgende sider præsenteres metoder udviklet på min PhD og de resultater der fulgte deraf.

Motivationen for denne form for forskning ligger i den unægteligt øgede interesse, som det videnskabelige samfund viser omkring materiale-design for nye teknologiske applikationer. To-dimensionale (2D) materialer, karakteriseret ved en tykkelse på få atomer, har altid været anset for et optimalt kompromis mellem udvidelse og lethed. Isoleringen af det første 2D materiale, graphen i 2004, viste sig at have ekstraordinære egenskaber omkring styrke og elektriske egenskaber. Siden dengang, takke være fremskridt i både teoretisk og eksperimentel ekspertise, er mange andre blevet syntetiseret sidenhen.

Men indtil for nyligt, magnetisme har undgået forskerne i fladland. Kun i 2017 blev det demonstreret at et enkelt enkeltlag af CrI_3 har en intrinsisk ferromagnetisk orden ud-af-planen for temperature op til 45 K, og kun få andre eksempler er i dag kendt for at have det samme. Deyte lyder måske overraskende, når man kigger på brede vifte af tilgængelige bulk systemer, som udviser en magnetisme selv ved høje temperature. Ud over dette, er mange af disse systemer i multilagsform, hvilket betyder den kan blive mekanisk eksfolieret til fritstående nano lag. Men magnetiske egenskaber reagerer på ændringer drastisk når dimensionaliteten af systemet bliver reduceret og bedre indsigt er nødvendig for at forudsige nye lovende kandidater.

Interaktionerne mellem magnetiske momenter inden i en krystal bidrager med at vise dets magnetiske egenskaber, såsom den kritiske temperatur. Denne er defineret som den temperatur over hvilken, termiske fluktuationer forhindrer nogen magnetisk orden i en prøve og sætter betingelserne for dets brugbarhed i virkelige apparater. Magnetisk anisotropi stammer fra geometrien af systemet, spiller også en afgørende rolle, specielt for 2D materialer. I en mikroskopisk model, vil sådanne interaktioner typisk være reproduceret af Heisenberg modellen og i dette studie undersøger vi rollen af nogle det vigtigste led.

Vi foreslår også at spin-bølge gappet som en hoveddeskriptor for den kritiske temperatur af ferromagnetisk orden i 2D systemer, som nemt kan fås fra ab-initio metoder, som Densitets Funktional Teoretiske beregninger.

Ved at kombinere resultaterne med klassiske Monte Carlo simuleringer, simplificerer og generaliserer vi vores metode så vi kan udføre high-throughput udregninger af 2D materialer med høje kritisk temperatur. Vores resultater er i god overensstemmelse med tilgængelig data i litteraturen og giver en liste af nye lovende kandidater for fremtidig eksperimentel undersøgelse.

Screeningen er blevet kørt i databaserne: "The Computational 2D Materials Database", "The Crystal Structure Database" og "The Crystallographic Open Database", og kan blive benyttet som en fremtidig reference for sammenligning.

Denne afhandling består af en kort introduktion til at etablere teorien for dette felt, efterfulgt af en liste af publikationer lavet af forfatteren, hver især introduceret af en kort kommentar og et resumé af det originale indhold af publikationerne.

Preface

This thesis is submitted in candidacy for the Ph. D. degree in physics from the Technical University of Denmark. The work was carried out at the Center for Atomic-scale Materials design (CAMd) at the Department of Physics in the period January 2017 to December 2019, under supervision of Associate Professor Thomas Olsen and Senior Scientist Niels Bech Christensen. The Ph. D. project was funded by an internal scholarship from DTU.

Kongens Lyngby, January 1, 2020



Daniele Torelli

Contents

| | |
|---|------------|
| Abstract | i |
| Resumè | iii |
| Preface | v |
| Contents | vii |
| 1 Introduction | 1 |
| 1.1 Quest for new materials | 1 |
| 1.2 High-throughput methods | 2 |
| 1.3 Outline | 3 |
| 2 Magnetic systems and How to Model Them | 5 |
| 2.1 Magnetic materials | 5 |
| 2.2 Quantum magnetism: the Heisenberg model | 8 |
| 2.3 Holstein-Primakoff representation | 11 |
| 2.4 Spin-wave theory | 12 |
| 2.5 Anisotropic terms | 15 |
| 2.6 Other interactions | 17 |
| 3 Density Functional Theory and Energy Mapping Analysis | 21 |
| 3.1 Electronic structure | 21 |
| 3.2 Density Functional theory | 22 |
| 3.3 Spin-dependent DFT | 25 |
| 3.4 Energy mapping analysis | 27 |
| 4 Monte Carlo methods | 31 |
| 4.1 Principles of Monte Carlo simulations | 31 |
| 4.2 Metropolis algorithm | 32 |
| 4.3 Implementation | 33 |
| 5 Summary of the results | 39 |
| 5.1 Paper I: Calculating critical temperatures for ferromagnetic order in two-dimensional materials | 39 |
| 5.2 Paper II: The Computational 2D Materials Database: high-throughput modeling and discovery of atomically thin crystals | 43 |
| 5.3 Paper III: Discovering two-dimensional topological insulators from high-throughput computations | 46 |
| 5.4 Paper IV: High throughput computational screening for 2D ferromagnetic materials: the critical role of anisotropy and local correlations | 47 |
| 5.5 Paper V: First Principles Heisenberg Models of 2D magnetic materials: The Importance of Quantum Corrections to the Exchange Coupling | 49 |
| 5.6 Paper VI: High throughput computational screening for two-dimensional magnetic materials based on experimental databases of three-dimensional compounds | 50 |

| | | |
|----------|---|------------|
| 6 | Conclusions and Outlook | 55 |
| 7 | Papers | 57 |
| 7.1 | Paper I: Calculating critical temperatures for ferromagnetic order in two-dimensional materials | 57 |
| 7.2 | Paper II: The Computational 2D Materials Database: high-throughput modeling and discovery of atomically thin crystals | 67 |
| 7.3 | Paper III: Discovering two-dimensional topological insulators from high-throughput computations | 104 |
| 7.4 | Paper IV: High throughput computational screening for 2D ferromagnetic materials: the critical role of anisotropy and local correlations | 116 |
| 7.5 | Paper V: First Principles Heisenberg Models of 2D magnetic materials: The Importance of Quantum Corrections to the Exchange Coupling | 128 |
| 7.6 | Paper VI: High throughput computational screening for two-dimensional magnetic materials based on experimental databases of three-dimensional compounds | 136 |
| | Bibliography | 143 |

1.1 Quest for new materials

Technological progress has always been driven by big leaps in materials capabilities. Any device's performance hinges on the suitability, efficiency and quality of the materials chosen to fabricate it and, conceivably, Leonardo Da Vinci's intuitions about flying machines would have been realised centuries ago if only lighter and stronger materials were available all along. In the same way, discovery of new materials is deemed to play a central role for any major challenge we will have to face over the next decades, from efficient data storage to clean energy production. For this reason a big deal of theoretical and experimental research has been directed toward it.

In particular, ultra-thin or two-dimensional (2D) materials exhibit many promising features for advancement in almost any technological issue. Moreover, the development of new synthesis methods allows for a control and accuracy never obtained before.

An ideal class of candidates for 2D materials is represented by multi-layered Van der Waals crystals: the weak couplings between the atomic planes facilitate the mechanical exfoliation into atomically-thin monolayers. In 2004, the discovery and isolation of graphene[1], a densely packed single layer of carbon atoms, has been extremely encouraging and demonstrated that physical proprieties of materials can change quite drastically when a reduced dimensionality is considered. Before that, it was theoretically predicted that 2D materials could not even exist because of the structural instability that thermal fluctuations would have triggered[2]. On the contrary, lightness and mechanical strength[3], tunable optical proprieties[4] and high charge conductivity are only some of the greatest features that make graphene one of the most remarkable material available today.

However, magnetism is not among these proprieties, and many strategies have been pursued in order to induce magnetism in intrinsically non-magnetic materials. Most commonly, the introduction of point defects like vacancies[5, 6] or adatoms[7, 8, 9], or extended defects as zig-zag termination[10] provide the polarization inequality needed for a non-vanishing net magnetization. Nevertheless, passivation effects may spoil the effort and reduce control in realistic environment. A different route is represented by the exploitation of the proximity effect. In this case, an atomically flat magnetic substrate, as YIG[11] or EuS[12] is coupled to the nano-sheet of graphene and, enhancing a strong interfacial exchange field, it induces a magnetic response onto the non-magnetic layer, in the form of Quantum Anomalous Hall effect (QAHE). However, while interfacial couplings proved to be a versatile and promising approach to enrich magnetic phases[13], these results cannot be conclusive, since QAHE may arise from spurious magnetic defects or spin-dependent scattering at the interface[14, 15].

On the other hand, intrinsically magnetic monolayers turned out to be a great challenge as well. The Mermin-Wagner theorem[16] is known to prevent any long-range magnetic order arising from short-range interactions at any finite temperature in 1D and 2D systems with a continuous symmetry. In realistic samples, however, the symmetry can be spontaneously broken by magnetic anisotropies which introduce a finite energy gap between the ordered ground state and the first thermally excited states. Nevertheless, only in 2017 the first 2D magnetic monolayers were successfully synthesized and experimentally confirmed, namely CrI₃[17] and Cr₃GeTe₂[18]. Since then, 2D magnetic materials especially in the ferromagnetic phases gained a lot of interest. In the last couple of years, an increasing number of papers reported theoretical predictions for new candidates, in few cases confirmed by experimental observations. In particular, evidence for room temperature magnetism has been reported for MnSe₂[19] and VSe₂[20, 21]. However, the number of Van der Waals magnetic structures is very large and many of the 2D counterparts still unexplored.

A new and fascinating approach to enhance and control magnetic phases is by means of interfacial engineering. Layered 2D materials have the ability to form heterostructure by stacking different monolayers one on top of the other[22]. The possibility of an -at least in theory- seamlessly integration of one or more (non-)magnetic monolayers offers a vast opportunity for the realization and control of novel functionalities. Some examples are shown in Fig. 1.1. In addition, twisting of one layer with respect to the other is an extra degree of freedom that proved to be very powerful in bilayer graphene. At certain magic angles, Moire patterns emerge inducing magnetism[23] and most notably superconductivity[24].

2D magnetic materials are a unique platform for investigating fundamentals models of magnetism and their phase transitions, but most importantly they may provide the ideal functionalities for future application. The study and the assembly of new devices are still at an early stage but in rapid progress. Most of them hinge on the control and manipulation of magnetic states when coupled to external perturbations like light, electrical bias or mechanical strain. Among the most promising application for magnetic 2D materials is in spintronics devices. Spintronics utilizes the extra spin degree freedom of electrons for novel transport electronics. In particular, if we stack a ferromagnetic material on top of a non-magnetic material, the heterostructure exhibits different electronic states for the different spin channels[25]. This may lead to a novel version of electronic, based on the spin rather than on the charge. Among the most important consequence are spin-transfer torque[26, 27] and tunneling magneto-resistance effects[28], utilized for magnetic sensors and next generation magnetic random access memory devices[29].

1.2 High-throughput methods

A rough count estimates in 80,000 the number of different materials in the world[30]. This number includes a broad variety of traditional materials, from the ones that can be found in nature, like minerals and woods, to artificially synthesized ceramics and plastics. But for a more and more demanding society, new classes of materials need to be realized and new methods to be developed. Even limiting ourselves to elements in the periodic table that are non-toxic and abundant, the number of hypothetical new materials we can imagine is massive. Despite the increasing interest in materials science,

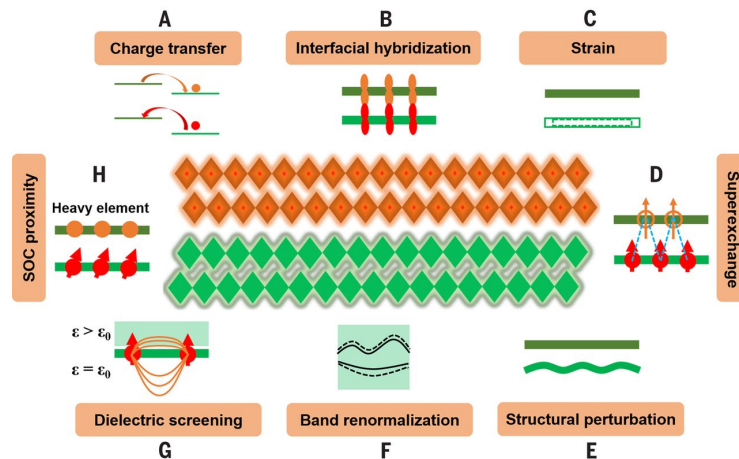


Figure 1.1: **Interfacial engineering of 2D magnets.** The presence of a long range magnetic order in a material can affect adjacent dissimilar layers when these are interacting in heterostructure system. Some of the possible interactions are (a) a hole/electron transfer between the two layers, (b) interfacial hybridization between the orbitals of two different layers, (c) strain effects, (d) superexchange interactions between magnetic ions (red arrows), mediated by non-magnetic ions (orange circles), (e) structural perturbation, (f) electronic, magnonic or phononic dispersion engineering, (g) dielectric screening of exchange fields generated by coupled electrons (red arrows), (h) spin-orbit coupling enhancement due to proximity effects with heavy elements atoms. From [15]

these possibilities has to remain for the most part experimentally unexplored. The immense progress in computer power over the last decades and the development of more and more accurate theoretical models, generated a new research field. Computational materials design hinges on the possibility to simulate proprieties of materials with great accuracy starting from just their molecular structure. Indeed, materials can be defined by their chemical compositions and their location in a phase diagram. It must have been very hard for chemists before the development of molecular theory to find suitable and unique definitions for even simple medium. For example, one could try to describe water as being wet, transparent, odorless and tasteless but many other liquids may have the same sensible proprieties. It took several centuries and brilliant scientists to link the physical proprieties of water to a specific arrangement of atoms, and today we know it as a molecule of H_2O with a well defined geometry and in a certain range of temperature and pressure. Materials scientists, following Francis Crick's adage "if you want to study *function*, study *structure*[31]", nowadays are adopting an approach which is in same sense inverse and much faster. Starting from the disposition of atoms, they are able to track back the more tangible physical proprieties of extended samples. These can be analyzed in depth and under stress conditions, and new materials with sought-after characteristics can be suggested for experimental investigations. Efficient methods must be deployed to computationally analyse the properties of atomic structure in voluminous database and high-throughput-based screening approaches are in great expansion.

Moreover, the development and refinement of methods and big data management, can be beneficial for others approaches in the quest for new materials. Most notably machine learning is becoming very popular and successful in materials science problems[32, 33]. One of the purpose of this approach is to facilitate machine learning and to enable artificial intelligence to aid the search for new materials, by looking at correlation trends in the vaster and vaster ocean of available data.

1.3 Outline

This first chapter served as review of the status of the research in magnetic condensed matter physics and in particular on the potential future applications based on 2D magnetic materials. The rest of thesis is organized as follows:

- In Chapter 2 we introduce the background information and terminology needed to understand the rest of the thesis. Magnetism and magnetic materials will be presented in the microscopic quantum framework and the most relevant spin-lattice models used in literature to describe them will be shortly derived.
- Chapter 3 is focused on the fundamentals behind Density Functional Theory (DFT), a powerful tool widely used in computational chemistry and physics to investigate proprieties of many-body quantum systems without the full resolution of Schrodinger's equations. Energy Mapping analysis, which connects the models introduced in Chapter 2 with the output results of DFT calculations is shortly presented.
- In Chapter 4 we introduce classical Monte Carlo simulations, an auxiliary method used throughout the project in synergy with *ab-initio* calculations. The model, the implementation and tests results performed during the project are also showed.
- In Chapter 5, a summary of the motivations, methods and main results for each scientific publication is given.
- Finally, in Chapter 6 we recap the key points of the project and possible outlook for future research, comparing the results with similar works in the field.

Chapters 2,3,4 are short introductions to the theoretical frameworks and tools used in the project, and are not intended to be encyclopedic nor in-depth expositions. To avoid overlaps, additional informations and main results can be found in Chapter 5 and particularly in Chapter 7 at the end of the thesis. Here are shown the papers published in scientific journals during the Ph. D[34, 35, 36, 37] and a draft of those submitted or still in preparation.

CHAPTER 2

Magnetic systems and How to Model Them

Proprieties of magnetic materials, like attracting or repelling each others, or freely align relative to Earth's axis, have fascinated humankind since the very ancient times. Magnetism, with its invisible forces, is one of the first natural phenomenon human minds really had to struggle with and, over more than two millennia, many explanations spanning from the magic realm to quantum mechanics have been proposed. In the mean time, tangible applications like compasses for navigation and permanent magnets in synchrotrons, always played a central role in advancement of knowledge and technological progress.

Early scientific experiments and speculations about it date back to Middle Ages, but it is only since the 19th century that some light had been shed on the fundamental mechanisms, thanks to the contribution of, among many others, Oersted, Ampere, Faraday, Weiss and Curie. Few decades later, quantum mechanics and research inspired by Maxwell, Langevin, Dirac, Pauli and Heisenberg provided most of the missing pieces.

Today we can try to summarize almost two centuries of science in this field stating that magnetisation is an emergent quantum many-body phenomenon originating from electromagnetic interactions taking place in a material. In particular, unpaired electrons in atomic sub-shells are key players and *spin* is a fundamental part of their wave functions.

An exhaustive introduction to magnetism goes beyond the intention and definitely the extent of this chapter¹. Here we briefly introduce relevant terminology and the theoretical background present in the rest of the thesis. Heisenberg model and spin-wave theory in particular, can be used to evaluate low-energy magnetic excited states. They are outlined along with the prominent applications and limitations.

2.1 Magnetic materials

The various theories of magnetism available nowadays are validated on the basis of the length or energy scale of the phenomenon they want to describe, but they all hinge on the concept of a vector magnetic moment \mathbf{m} sensitive to magnetic fields. In a material, when the direction of the magnetic moments vary slowly or on a distance scale larger than the atomic structure of the material (1-1000 nm), the *magnetization* is defined in terms of a continuous field $\mathbf{m}(\mathbf{r})$. This *micromagnetic model*, which integrates quantum mechanical effects with a mainly semi-classical approach, is vastly used to derive responsive proprieties in large systems, or the inner structure of domain walls and their dynamics [41, 42, 43].

The *atomistic spin-lattice model* has a discrete perspective (on a length scale < 1 nm) and assigns to the elementary building blocks of matter, like electrons and nucleons, a distinct magnetic moment \mathbf{m} . In classical physics, \mathbf{m} is directly linked to the motion of the particle, like its angular momentum. For example, an electron orbiting around a nucleus generates a magnetic moment (called *orbital* magnetic moment) proportional to the electric current and the area of the closed loop. Quantum particles posses also an intrinsic magnetic moment, called *spin*, since in a classical picture (wrong but powerful) they

¹Excellent examples can be find at [38, 39, 40], which inspired some of the derivations showed in the following sections.

act as tiny spheres spinning on themselves. Then, the "eastward" or "westward" motion differentiates the only two possible states (also called *spin up* or *down*, with opposite sign).

The proprieties of a permanent magnet can be typically explained as a cooperative effect of orbital and spin moments of unpaired electrons sitting at atomic sites in a crystal and interacting with each others. Unless specified, local *magnetic moments* and *spins* will be used as synonyms from now on and indicate the resulting vector at each atomic site. In most of the systems considered here, the orbital magnetic moments is anyway quenched because of geometrical arguments, thus the magnetization is a consequence of the imbalance of electrons with opposite spin. The arrangement of localized spins in a crystal outlines a *magnetic spin lattice*.

The validity of localized-spin models with short-range interactions is often a topic of scientific debate since some of its assumptions are not always fully satisfied. For example, magnetic interactions are typically long-range and co-participate in many phenomena across the entire lattice. Moreover, in particular for metals, because of non-localized itinerant electrons, it's not always possible to assign an integer value to the size of magnetic moments, or a well defined geometry to the lattice. In general, the range of its validity depends crucially on the electronic proprieties of the system under investigation. However, microscopic models form the basis of very reliable tools to qualitatively predict the proprieties of extended materials.

At larger scale (> 0.1 mm) magnetic materials are classified in terms of their phases, the dominant response to the application of an external magnetic field, called *susceptibility*. In materials with a *diamagnetic* response, a weak internal magnetic field is generated in the opposing direction, while *paramagnetic* effects are explained in terms of local magnetic moments aligning with it and enhancing it at some degrees. At some extent, all condensed matter exhibits a magnetic response which promotes the development of more magnetic order, along the direction of the external magnetic field. In a related classifications, some materials under certain conditions, exhibit spontaneous magnetic order even when the external magnetic field is removed. When this is not the case, paramagnetic response dominates, and thus the system is said to have a *paramagnetic* (PM) phase. *Ferromagnetism* (FM) is one example of magnetic order, where local spins point all in the same direction and with the same magnitude. Other *collinear* magnetic phases (where spins are parallel to each other but not necessarily pointing in the same direction) are the *antiferromagnetic* (AFM) and *ferrimagnetic* (where neighbouring parallel spins -or groups of- point in opposite direction with the same or different magnitude respectively). Among the *non-collinear magnetic phase*, some examples are the conical and helicoidal spin-density

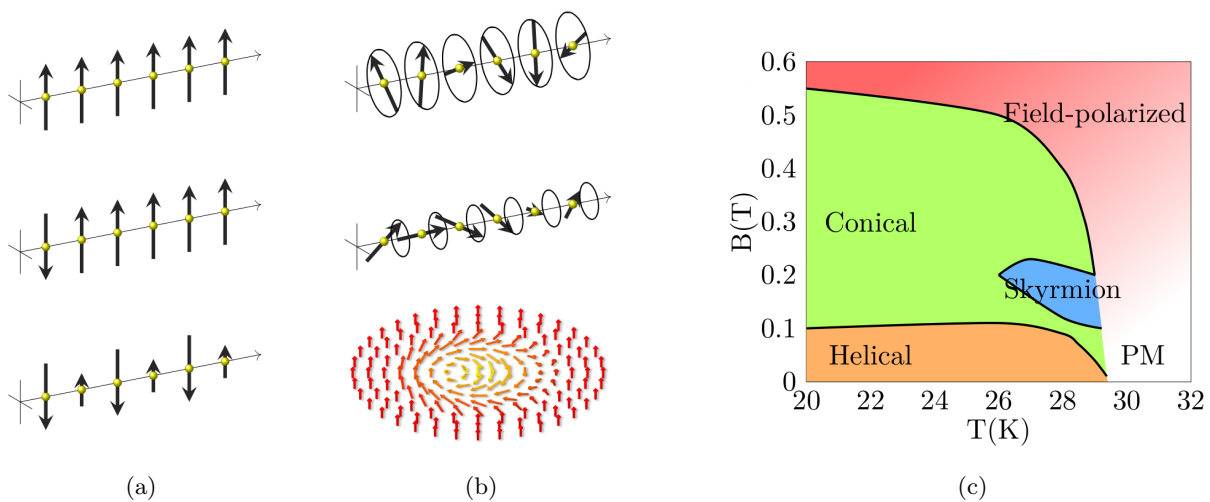


Figure 2.1: **Magnetic phases.** (a) Examples of 1D collinear magnetic phases (from top to bottom): ferromagnetism, antiferromagnetism and ferrimagnetism, which is a superposition of nonequivalent anti-ferromagnetic sublattices. (b) Examples of non-collinear magnetic phases (from top to bottom): helical, conical and skyrmion (figure from [44]). (c) Magnetic phase diagram of cubic MnSi (graphical re-elaborations of data points taken from [45], where the skyrmion-phase is called A-phase).

wave phases, where spins are characterized by an out-of-phase precession around the same axis and a fixed wave vector. Examples of these magnetic phases for a one-dimensional spin chains are shown in Fig. 2.1(a) and (b). The last example of non-collinear phase is a skyrmion, a topologically protected pseudo-vortexes with a trivial FM phase away from the center. Experimentally observed for the first time in MnSi[45] and later on in other systems with a strong spin-orbit coupling and a symmetry group without inversion symmetry, are envisioned to be used as binary bits in next generation magnetic memory devices.

The magnetization $\mathbf{M} = (M_x, M_y, M_z)$ is defined as the sum of all the magnetic moments \mathbf{m}_i of the lattice normalized by the number of spins N (or the volume V of the sample in the micromagnetic model)

$$\mathbf{M} = \frac{\sum_i \mathbf{m}_i}{N} \quad (2.1)$$

and quantitatively evaluated along an arbitrary direction, generally the z-axis. For each system, the maximal value M_s of its modulus is reached in the FM configuration (saturation). For AFM phases, the contributions from the two opposite sub-lattices cancel out and $\mathbf{M} = 0$. This would be the same output for a measurement in PM phase but for a very different reason. In the latter, the randomized spin orientations average out to a vanishing net magnetic moment. Experimentally, these cases are discriminated applying an external magnetic field and measuring the susceptibility. Generally more than one magnetic configurations is allowed in the magnetic phase diagram of a material, depending on externally tunable parameters such as temperature, pressure and magnitude of the applied magnetic field \mathbf{B} . The magnetic ground state of a system stems out of a complex interplay between its geometrical and chemical properties. In real samples, grain boundaries and defects affects the magnetic response as well. The phase diagram of MnSi is showed in Fig. 2.1(c) as example.

Temperature in particular causes random fluctuations in the alignment of magnetic moments and effectively lowers the net magnetization of the sample in a non trivial way. An example is showed in Fig. 2.2: starting from a FM ground state (along z-axis) at $T=0$, the saturated magnetization slowly decreases when higher temperatures are reached, since some spins are thermally excited and allowed to diverge from their ground state direction. At a critical temperature called *Curie temperature* T_C , the systems swiftly becomes PM and the \mathbf{M} continuously drops to zero in a phase transition of second order. Simultaneously, the heat capacity of the system $C_V = \frac{\partial U}{\partial T}$ reaches a peak. While the local magnetic moments still exist, they all point in random directions and without an external magnetic field, no magnetic order is possible above T_C . A second-order magnetic phase transition around T_C is characterized by a set of critical exponents for the order parameter, in this case M_z . For example, the shape of the magnetization curves as a function of T and of a vanishing external field B can be written as

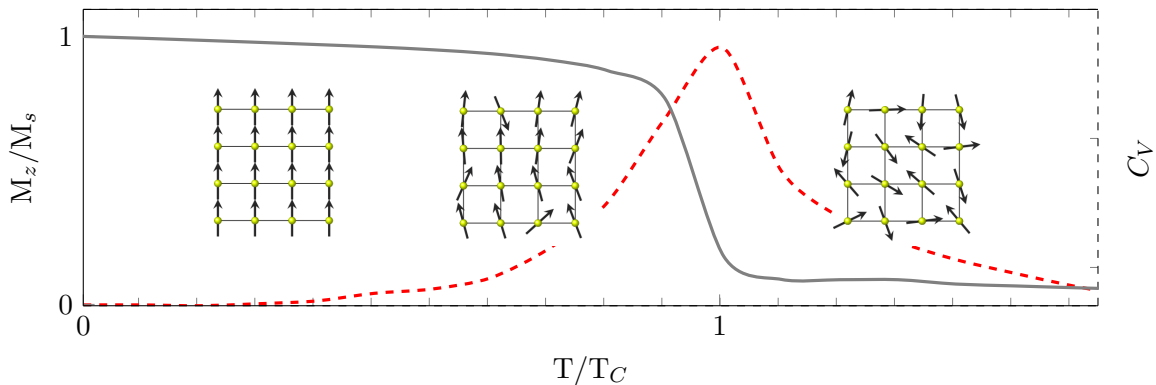


Figure 2.2: **Magnetic transition.** A phase transition from ferromagnetic and paramagnetic order occurs at critical temperature T_C when the order parameter of the system, as i.e. M_z in a magnetization curve, drops to zero or equivalently when the heat capacity C_V exhibits a peak.

$$M_z(T, B = 0) = \begin{cases} M_s |\epsilon|^\beta, & \text{if } T < T_C \\ 0, & \text{if } T > T_C \end{cases} \quad (2.2)$$

where $\epsilon = \frac{T-T_C}{T_C}$ is the reduced temperature and β the critical exponent. These behaviours do not depend on the particular material, and not even on the nature of the transition. For this reason are said to fall into the same *universality class*, which is characterized by underlying symmetries. However, theoretical models and numerical methods not always succeed in capturing most of the features present in experimental results. This is mainly due to the oversimplification of models, that don't take into account i.e. coexistence of different phases in real samples and most fundamentally, convoluted behaviour in the low-temperature regime and near the critical temperature. While a more accurate description of the shape of 2.2 is still an active field of research[46, 47] and beyond the scope of this work, numerical methods proved to be a correct approach for the evaluation of T_C . Anyway, for fully reliable methods, a quantum-mechanical framework is necessary and more insights about fundamentals origin of magnetism in materials are required, especially in systems with a reduced dimensionality.

2.2 Quantum magnetism: the Heisenberg model

According to classical physics, magnetism should be possible only at temperature near absolute zero. While this may naively explain why we stick magnets mainly on refrigerators, a deeper understanding of magnetism requires a quantum treatment. To show that, we consider the magnetic field produced by a dipole \mathbf{m}_1 in spherical coordinate

$$\mathbf{B}_1(\mathbf{r} = r\hat{r}) = \frac{\mu_0}{4\pi r^3} [3(\mathbf{m}_1 \cdot \hat{r})\hat{r} - \mathbf{m}_1] \quad (2.3)$$

where μ_0 is permeability of free space. In such a field, a second magnetic moment \mathbf{m}_2 at a distance \mathbf{r}_{12} has a magnetic potential energy $U = -\mathbf{m}_2 \cdot \mathbf{B}_1(\mathbf{r}_{12})$, which reaches its maximum when $\mathbf{m}_1 \parallel \mathbf{m}_2 \parallel \mathbf{r}_{12}$. Assuming the magnitude of the atomic magnetic moments m_1 and m_2 to be a Bohr magneton μ_B and the distance between them twice the Bohr radius a_0 , we obtain $U \approx 0.1meV \approx 1K$.

This analysis is valid for any material and shows that the energy of the classical dipole-dipole interactions between atoms, which should justify the alignment of magnetic moments, is very low. In comparison, thermal energy per molecule scales with temperature as $3T/2$. Randomness introduced by thermal fluctuations dominates already at low energy destroying any magnetic order.

A stronger interaction is required to explain the experimentally observed high-temperature magnetic order, i.e. up to 1043 K for iron. In 1926, Heisenberg[48] and Dirac[49] independently realized that this interaction is a consequence of Coulomb repulsion between electrons in concert with the antisymmetric nature of the many-body wave functions of electrons. The spin selectivity is thus a consequence of the Pauli principle, namely the requirement that no two same-spin electrons can occupy the same state.

Magnetism in solid state physics is mainly due to electrons, who carry spin $S = 1/2$. In the quantum-mechanical framework, the physical observables of a quantum spin $s = 1/2$ are given by the the spin operators S^x , S^y and S^z , which satisfy the commutation rules

$$[S_i^\alpha, S_i^\beta] = i\epsilon_{\alpha\beta\gamma} S_i^\gamma \quad (2.4)$$

with $(\alpha, \beta, \gamma) = (x, y, z)$ and ϵ the Levi-Civita tensor. Rules 2.4 are known to define the special unitary group $SU(2)$ of rotation and S^α are the $(2s + 1) \times (2s + 1)$ generators of the group. We explicitly comment that in this context x, y, z are "internal coordinates" of a point-like particle and not directions in real space. A suitable representation is given by $S^\alpha = \hbar/2\sigma^\alpha$, where

$$\sigma^x = \begin{pmatrix} 0 & 1 \\ 1 & 0 \end{pmatrix}, \quad \sigma^y = \begin{pmatrix} 0 & -i \\ i & 0 \end{pmatrix}, \quad \sigma^z = \begin{pmatrix} 1 & 0 \\ 0 & -1 \end{pmatrix} \quad (2.5)$$

are the Pauli matrices. The eigenvectors of S^z read

$$\chi_{\uparrow} = \begin{pmatrix} 1 \\ 0 \end{pmatrix}, \quad \chi_{\downarrow} = \begin{pmatrix} 0 \\ 1 \end{pmatrix} \quad (2.6)$$

and are also called spinors "up" and "down" ($|\uparrow\rangle$ and $|\downarrow\rangle$ in bra-ket notation) with eigenvalues $\pm\frac{1}{2}$ respectively. These are the projections S_z along the z-direction but commonly referred as just "spin". This formalism comes in handy when spins states need to be made explicit. For example the Coulomb interaction is written as

$$H_C = \frac{1}{2} \int \frac{\rho(\mathbf{r}_1)\rho(\mathbf{r}_2)}{|\mathbf{r}_1 - \mathbf{r}_2|} d\mathbf{r}_1^3 d\mathbf{r}_2^3 \quad (2.7)$$

where $\rho(\mathbf{r})$ is the operator for the charge density and in second-quantized notation reads

$$\rho(\mathbf{r}) = -e \sum_{\sigma} \Psi_{\sigma}^{\dagger}(\mathbf{r}) \Psi_{\sigma}(\mathbf{r}) \quad (2.8)$$

In Eq. 2.8, $\sigma = \uparrow, \downarrow$ is the possible spin orientation and $\Psi_{\sigma}(\mathbf{r})$ is the fermionic field operator.

It is convenient to expand the operator $\Psi_{\sigma}(\mathbf{r})$ into orthonormal Wannier functions $\phi_{\mathbf{R}m}$ marked by ionic position \mathbf{R} and a collection m of quantum numbers. We explicitly introduce spins and the expansion then reads

$$\Psi_{\sigma}(\mathbf{r}) = \sum_{\mathbf{R}m} c_{\mathbf{R}m} \phi_{\mathbf{R}m}(\mathbf{r}) \chi_{\sigma} \quad (2.9)$$

where $c_{\mathbf{R}m}$ are fermionic annihilation operators, obeying anti-commutation relations $\{c_{\mathbf{R}m\sigma}, c_{\mathbf{R}'m'\sigma'}^{\dagger}\} = \delta_{\mathbf{R}\mathbf{R}'} \delta_{mm'} \delta_{\sigma\sigma'}$ and $\{c_{\mathbf{R}m\sigma}, c_{\mathbf{R}'m'\sigma'}\} = \{c_{\mathbf{R}m\sigma}^{\dagger}, c_{\mathbf{R}'m'\sigma'}^{\dagger}\} = 0$.

Eq. 2.7 becomes

$$\begin{aligned} H_C = & \frac{1}{2} \sum_{\mathbf{R}_1 m_1} \dots \sum_{\mathbf{R}_4 m_4} \int d\mathbf{r}_1^3 d\mathbf{r}_2^3 \phi_{\mathbf{R}_1 m_1}^*(\mathbf{r}_1) \phi_{\mathbf{R}_2 m_2}^*(\mathbf{r}_2) \frac{e^2}{4\pi\epsilon_0 |\mathbf{r}_1 - \mathbf{r}_2|} \phi_{\mathbf{R}_3 m_3}(\mathbf{r}_2) \phi_{\mathbf{R}_4 m_4}(\mathbf{r}_1) \\ & \times \sum_{\sigma_1 \sigma_2} \chi_{\sigma_1}^{\dagger} \chi_{\sigma_2}^{\dagger} \chi_{\sigma_2} \chi_{\sigma_1} c_{\mathbf{R}_1 m_1 \sigma_1}^{\dagger} c_{\mathbf{R}_2 m_2 \sigma_2}^{\dagger} c_{\mathbf{R}_3 m_3 \sigma_2} c_{\mathbf{R}_4 m_4 \sigma_1} \end{aligned} \quad (2.10)$$

Exploiting orthogonality in spinors and using bra-ket notation for the integral expressions, we obtain

$$\begin{aligned} H_C = & \frac{1}{2} \sum_{\mathbf{R}_1 m_1} \dots \sum_{\mathbf{R}_4 m_4} \langle \mathbf{R}_1 m_1, \mathbf{R}_2 m_2 | \frac{e^2}{4\pi\epsilon_0 |\mathbf{r}_1 - \mathbf{r}_2|} | \mathbf{R}_3 m_3, \mathbf{R}_4 m_4 \rangle \\ & \times \sum_{\sigma_1 \sigma_2} c_{\mathbf{R}_1 m_1 \sigma_1}^{\dagger} c_{\mathbf{R}_2 m_2 \sigma_2}^{\dagger} c_{\mathbf{R}_3 m_3 \sigma_2} c_{\mathbf{R}_4 m_4 \sigma_1} \end{aligned} \quad (2.11)$$

Let's first consider the on-site interaction, meaning $\mathbf{R}_1 = \mathbf{R}_2 = \mathbf{R}_3 = \mathbf{R}_4 := \mathbf{R}$. If we assume that the spatial states are localised enough, then the contributions from integrals in m are non-zero only when the bra and the ket states have some overlap, namely when (i) $m_1 = m_4$ and $m_2 = m_3$ or (ii) $m_1 = m_3$ and $m_2 = m_4$. In the first case, we define the *direct integrals*

$$\begin{aligned} K_{m_1 m_2} & := \langle m_1, m_2 | \frac{e^2}{4\pi\epsilon_0 |\mathbf{r}_1 - \mathbf{r}_2|} | m_2, m_1 \rangle \\ & = \int d^3 r_1 d^3 r_2 |\phi_{m_1}(\mathbf{r}_1)|^2 \frac{e^2}{4\pi\epsilon_0 |\mathbf{r}_1 - \mathbf{r}_2|} |\phi_{m_2}(\mathbf{r}_2)|^2 \end{aligned} \quad (2.12)$$

while in the second case, the *exchange integrals*

$$\begin{aligned}
J_{m_1 m_2} &:= \langle m_1, m_2 | \frac{e^2}{4\pi\epsilon_0 |\mathbf{r}_1 - \mathbf{r}_2|} | m_1, m_2 \rangle \\
&= \int d^3 r_1 d^3 r_2 \phi_{m_1}^*(\mathbf{r}_1) \phi_{m_2}^*(\mathbf{r}_2) \frac{e^2}{4\pi\epsilon_0 |\mathbf{r}_1 - \mathbf{r}_2|} \phi_{m_1}(\mathbf{r}_2) \phi_{m_2}(\mathbf{r}_1)
\end{aligned} \tag{2.13}$$

The Coulomb interaction becomes

$$\begin{aligned}
H_C &= \frac{1}{2} \sum_{\mathbf{R}} \sum_{m_1 m_2} \sum_{\sigma_1 \sigma_2} \left\{ K_{m_1 m_2} c_{\mathbf{R} m_1 \sigma_1}^\dagger c_{\mathbf{R} m_2 \sigma_2}^\dagger c_{\mathbf{R} m_2 \sigma_2} c_{\mathbf{R} m_1 \sigma_1} + J_{m_1 m_2} c_{\mathbf{R} m_1 \sigma_1}^\dagger c_{\mathbf{R} m_2 \sigma_2}^\dagger c_{\mathbf{R} m_1 \sigma_2} c_{\mathbf{R} m_2 \sigma_1} \right\} \\
&= \frac{1}{2} \sum_{\mathbf{R}} \sum_{m_1 m_2} \sum_{\sigma_1 \sigma_2} \left\{ K_{m_1 m_2} c_{\mathbf{R} m_1 \sigma_1}^\dagger c_{\mathbf{R} m_1 \sigma_1} c_{\mathbf{R} m_2 \sigma_2}^\dagger c_{\mathbf{R} m_2 \sigma_2} - J_{m_1 m_2} c_{\mathbf{R} m_1 \sigma_1}^\dagger c_{\mathbf{R} m_1 \sigma_2} c_{\mathbf{R} m_2 \sigma_2}^\dagger c_{\mathbf{R} m_2 \sigma_1} \right\}
\end{aligned} \tag{2.14}$$

where we have used anti-commutation properties of fermionic operators. We can now define the number and spin operators at site \mathbf{R} as

$$\begin{aligned}
n_{\mathbf{R} m} &:= \sum_{\sigma} c_{\mathbf{R} m \sigma}^\dagger c_{\mathbf{R} m \sigma} \\
S_{\mathbf{R} m}^\alpha &:= \sum_{\sigma \sigma'} c_{\mathbf{R} m \sigma}^\dagger (\sigma_{\sigma \sigma'}^\alpha / 2) c_{\mathbf{R} m \sigma'}
\end{aligned} \tag{2.15}$$

where σ^α (with $\alpha = x, y, z$) is the Pauli vector, defined by matrices 2.5.

By setting $\mathbf{S}_{\mathbf{R} m} = (S_{\mathbf{R} m}^x, S_{\mathbf{R} m}^y, S_{\mathbf{R} m}^z)$, we have can evaluate

$$\sum_{\sigma_1 \sigma_2} c_{\mathbf{R} m_1 \sigma_1}^\dagger c_{\mathbf{R} m_1 \sigma_2} c_{\mathbf{R} m_2 \sigma_2}^\dagger c_{\mathbf{R} m_2 \sigma_1} = \frac{n_{\mathbf{R} m_1} n_{\mathbf{R} m_2}}{2} + 2 \mathbf{S}_{\mathbf{R} m_1} \cdot \mathbf{S}_{\mathbf{R} m_2} \tag{2.16}$$

which finally leads to

$$H_{C(\text{on-site})} = \sum_{\mathbf{R}} \frac{1}{2} \sum_{m_1 m_2} \left\{ \left(K_{m_1 m_2} - \frac{1}{2} J_{m_1 m_2} \right) n_{\mathbf{R} m_1} n_{\mathbf{R} m_2} - 2 J_{m_1 m_2} \mathbf{S}_{\mathbf{R} m_1} \cdot \mathbf{S}_{\mathbf{R} m_2} \right\} \tag{2.17}$$

The first term inside parenthesis is the on-site Coulomb interaction. It can be shown that $K_{m_1 m_2} \geq J_{m_1 m_2} \geq 0$ and that in particular $K_{m_1 m_2} - 1/2 J_{m_1 m_2} > 0$. The "classical" contribution $K_{m_1 m_2}$ is thus effectively lowered in the quantum treatment by $J_{m_1 m_2}$, but it still is repulsive. The second term instead has a full quantum-mechanical origin and favours a ferromagnetic alignment (qualitatively expressed by the Hund's first rule). In particular, for a single relevant orbital with $\sigma = \uparrow, \downarrow$ from Eq. 2.14 we obtain

$$\begin{aligned}
H_{C(\text{on-site})} &= \frac{1}{2} \sum_{\mathbf{R}} \int d^3 r_1 d^3 r_2 \phi^*(\mathbf{r}_1) \phi^*(\mathbf{r}_2) \frac{e^2}{4\pi\epsilon_0 |\mathbf{r}_1 - \mathbf{r}_2|} \phi(\mathbf{r}_2) \phi(\mathbf{r}_1) \sum_{\sigma_1 \sigma_2} c_{\mathbf{R} \sigma_1}^\dagger c_{\mathbf{R} \sigma_2}^\dagger c_{\mathbf{R} \sigma_2} c_{\mathbf{R} \sigma_1} \\
&= \frac{1}{2} \sum_{\mathbf{R}} \int d^3 r_1 d^3 r_2 \phi^*(\mathbf{r}_1) \phi^*(\mathbf{r}_2) \frac{e^2}{4\pi\epsilon_0 |\mathbf{r}_1 - \mathbf{r}_2|} \phi(\mathbf{r}_2) \phi(\mathbf{r}_1) \left(c_{\mathbf{R} \uparrow}^\dagger c_{\mathbf{R} \downarrow}^\dagger c_{\mathbf{R} \downarrow} c_{\mathbf{R} \uparrow} + c_{\mathbf{R} \downarrow}^\dagger c_{\mathbf{R} \uparrow}^\dagger c_{\mathbf{R} \uparrow} c_{\mathbf{R} \downarrow} \right) \\
&= \sum_{\mathbf{R}} \int d^3 r_1 d^3 r_2 \phi^*(\mathbf{r}_1) \phi^*(\mathbf{r}_2) \frac{e^2}{4\pi\epsilon_0 |\mathbf{r}_1 - \mathbf{r}_2|} \phi(\mathbf{r}_2) \phi(\mathbf{r}_1) c_{\mathbf{R} \uparrow}^\dagger c_{\mathbf{R} \downarrow}^\dagger c_{\mathbf{R} \downarrow} c_{\mathbf{R} \uparrow} \\
&= \sum_{\mathbf{R}} U' c_{\mathbf{R} \uparrow}^\dagger c_{\mathbf{R} \downarrow}^\dagger c_{\mathbf{R} \downarrow} c_{\mathbf{R} \uparrow} = \sum_{\mathbf{R}} U' c_{\mathbf{R} \uparrow}^\dagger c_{\mathbf{R} \uparrow} c_{\mathbf{R} \downarrow}^\dagger c_{\mathbf{R} \downarrow} = \sum_{\mathbf{R}} U' n_{\mathbf{R} \uparrow} n_{\mathbf{R} \downarrow}
\end{aligned} \tag{2.18}$$

where $U' > 0$ is called Hubbard term and will be discussed further in section 3.3.1.

For inter-ion interactions, we can consider \mathbf{R}_i as an extra quantum number. From Eq. 2.11 we have non-zero first order perturbation if $\mathbf{R}_1 = \mathbf{R}_4$ and $\mathbf{R}_2 = \mathbf{R}_3$ or if $\mathbf{R}_1 = \mathbf{R}_3$ and $\mathbf{R}_2 = \mathbf{R}_4$. This leads, adopting the notation $\mathbf{R}_i = i$ in subscripts, to the analogous of Eq. 2.17

$$H_{C_{\text{inter}}} = \frac{1}{2} \sum_{\mathbf{R}_1 \mathbf{R}_2} \left\{ \left(K_{12} - \frac{1}{2} J_{12} \right) n_1 n_2 - 2J_{12} \mathbf{S}_1 \cdot \mathbf{S}_2 \right\} \quad (2.19)$$

In the case of half-filling, meaning that only one electron is present at each orbital ($n_i = 1$), the interaction is simply

$$H_H = - \sum_{\mathbf{R}_1 \mathbf{R}_2} J_{12} \mathbf{S}_1 \cdot \mathbf{S}_2 \quad (2.20)$$

As before, $J_{12} > 0$, meaning that the Coulomb repulsion between electrons in different orbitals favours spin-parallel configurations.

The model 2.20 with only the dominant two-particles interaction is called *Heisenberg model* and typically written as

$$H_H = -\frac{1}{2} \sum_{ij} J_{ij} \mathbf{S}_i \cdot \mathbf{S}_j = - \sum_{\langle ij \rangle} J_{ij} \mathbf{S}_i \cdot \mathbf{S}_j \quad (2.21)$$

where in the first expression the sum runs over all lattice sites i and j while the sum in the second, equivalent, expression runs over all the couples of neighbouring lattice sites.

The model 2.21 is defined by quantum spin operators $\mathbf{S}_i = (S_i^x, S_i^y, S_i^z)$. From Eq. 2.5, sums and products of spin operators reduce to sum and products of the corresponding matrices:

$$H_H = - \sum_{\langle ij \rangle} J_{ij} \left[S_i^x S_j^x + S_i^y S_j^y + S_i^z S_j^z \right] \quad (2.22)$$

However, interactions may also contain only one or two components, as in the case of Ising model

$$H_I = - \sum_{\langle ij \rangle} J_{ij} S_i^z S_j^z \quad (2.23)$$

and *XY* models

$$H_{XY} = - \sum_{\langle ij \rangle} J_{ij} \left[S_i^x S_j^x + S_i^y S_j^y \right] \quad (2.24)$$

respectively.

2.3 Holstein-Primakoff representation

Eq. 2.4 shows that the commutator of two spin operators is a spin operator itself. When analytical approaches are involved, as in this case, it might make derivations cumbersome to carry on and more convenient representation are used instead. The Holstein-Primakoff (HP) representation expresses spin operators in terms of canonical bosonic creation and annihilation operators a_i^\dagger and a_i at each site as

$$\begin{aligned} S_i^+ &= \sqrt{2S - a_i^\dagger a_i} a_i = \sqrt{2S - n_i} a_i \\ S_i^- &= a_i^\dagger \sqrt{2S - a_i^\dagger a_i} = a_i^\dagger \sqrt{2S - n_i} \\ S_i^z &= S - a_i^\dagger a_i = S - n_i \end{aligned} \quad (2.25)$$

In HP notation we can write

$$H_H = -J \sum_{\langle ij \rangle} \mathbf{S}_i \cdot \mathbf{S}_j = -J \sum_{\langle ij \rangle} \left[S_i^z S_j^z + \frac{1}{2} (S_i^+ S_j^- + S_i^- S_j^+) \right] \quad (2.26)$$

The new spin operators are called raising and lowering operators $S_i^\pm = S_i^x \pm iS_i^y$ and we also introduce the number operator $n_i = a_i^\dagger a_i$ which simply counts the number of bosons $\langle n_i \rangle$ at each site. The reason why HP representation is more advantageous lies in the fact that relevant commutators now are just complex numbers but also because the vacuum of a_i corresponds to fully polarized state (the eigenvalue of S_i^z reaches its maximum S). This becomes useful when studying the ferromagnetic ground state and its excitations as we will see in the next sections.

2.4 Spin-wave theory

If all the exchange interactions $J_{ij} = J$ are non-negative, the fully polarized states are ground states and we are in the ferromagnetic configuration. It is easy to convince that the ground state corresponds to a state where all spins are aligned and point to the same ordering direction. This is conventionally chosen to be the positive z-direction. If we consider for simplicity a 1D spin-1/2 chain it can be written as

$$\Psi_0 = |\uparrow, \dots, \uparrow, \uparrow, \dots, \uparrow\rangle = |S, \dots, S, S, S, \dots S\rangle \quad (2.27)$$

where $|\uparrow, \dots, \uparrow\rangle = |\uparrow\rangle \otimes \dots \otimes |\uparrow\rangle$.

The first excited state is less trivial. A naive candidate is the state where only one spin is flipped $S \rightarrow -S$ (in general, for non spin-half system it is reduced by 1: $S \rightarrow S - 1$), namely

$$\Psi_1 = |\uparrow, \dots, \uparrow, \downarrow, \uparrow, \dots, \uparrow\rangle = |S, \dots, S, -S, S, \dots S\rangle \quad (2.28)$$

Eq. 2.28 doesn't define an eigenstate of H_H , since the terms with $S_j^+ S_j^-$ would shift the flipped spin to neighbouring site and change the state. Moreover, if we evaluate its expectation energy we obtain a fairly large energy gap relative to the ground state

$$\begin{aligned} \Delta_1 &= E_1 - E_{GS_{FM}} \\ &= \langle \Psi_1 | H_H | \Psi_1 \rangle - \langle \Psi_{GS_{FM}} | H_H | \Psi_{GS_{FM}} \rangle \\ &= -J \sum_{j \neq 0} \langle \Psi_1 | \frac{S_0^+ S_j^- + S_0^- S_j^+}{2} + S_0^z S_j^z | \Psi_1 \rangle + J \sum_{j \neq 0} \langle \Psi_{GS_{FM}} | \frac{S_0^+ S_j^- + S_0^- S_j^+}{2} + S_0^z S_j^z | \Psi_{GS_{FM}} \rangle \\ &= -J \sum_{j \neq 0} \langle \Psi_1 | S_0^z S_j^z | \Psi_1 \rangle + J \sum_{j \neq 0} \langle \Psi_{GS_{FM}} | S_0^z S_j^z | \Psi_{GS_{FM}} \rangle \\ &= -J \sum_{j \neq 0} S(S-1) + J \sum_{j \neq 0} S^2 = SJ \end{aligned} \quad (2.29)$$

A better guess for low-energy excited states is guided by exploiting all the possible orientation of a vector free to rotate in a 3D space. Heisenberg model can be interpreted as

$$H_H = -J \sum_{\langle ij \rangle} \mathbf{S}_i \cdot \mathbf{S}_j \rightarrow H_H^i = -\mathbf{S}_i \cdot \left[J \sum_j \mathbf{S}_j \right] \quad (2.30)$$

The last equation is the interaction between a spin \mathbf{S}_i and an effective exchange magnetic field arising from the interaction with the surrounding spins \mathbf{S}_j .

In Heisenberg picture, the equation of motion for a spin \mathbf{S}_i reads

$$\frac{d\mathbf{S}_i}{dt} = \frac{i}{\hbar} [H_H^i, \mathbf{S}_i] = -\frac{1}{\hbar} \left[J \sum_j \mathbf{S}_j \right] \times \mathbf{S}_i \quad (2.31)$$

Since we are in the low-energy regime, we can assume the first excited state to be close to the fully polarized ground state, and thus writing the spins in the form $\mathbf{S}_i = (S_i^x, S_i^y, S_i^z) \approx (S_i^x, S_i^y, S)$ and $S_i^{x(y)} S_i^{x(y)} \approx 0$. This brings, for the different components, to

$$\begin{aligned} \hbar \frac{dS_i^x}{dt} &= -\sum_j J [S_j^y S_i^z - S_j^z S_i^y] \approx -\sum_j JS [S_j^y - S_i^y] \\ \hbar \frac{dS_i^y}{dt} &= -\sum_j J [S_j^z S_i^x - S_j^x S_i^z] \approx \sum_j JS [S_j^x - S_i^x] \\ \hbar \frac{dS_i^z}{dt} &= \sum_j J [S_j^x S_i^y - S_j^y S_i^x] \approx 0 \end{aligned} \quad (2.32)$$

These equations have been derived in a pure classic picture and describe a precession of spins around z-axis with a constant phase shift between neighbouring spins. Collectively, they are slightly perturbed states by means of small oscillations of spins around the z-direction (see Fig. 2.3).

For a more formal description, being N the number of spins and z the coordination number of a system (i.e. $z = 4$ for a square 2D lattice), we write the Hamiltonian 2.21 using HP operators

$$\begin{aligned} H_H &= -J \sum_{\langle ij \rangle} \mathbf{S}_i \cdot \mathbf{S}_j \\ &= -J \sum_{\langle ij \rangle} \left[S_i^z S_j^z + \frac{1}{2} (S_i^+ S_j^- + S_i^- S_j^+) \right] \\ &= -\frac{JNS^2z}{2} - JS \sum_{\langle ij \rangle} [a_i^\dagger a_j + a_j^\dagger a_i - a_i^\dagger a_i - a_j^\dagger a_j] + O(S^0) \end{aligned} \quad (2.33)$$

In the last passage we truncated the square root expansion in $1/S$ at the first order, meaning that terms containing four or more bosonic operators are neglected. This can be regarded as a semi-classical approximation, since the limit $S \rightarrow \infty$ corresponds to a classical picture where the eigenvalue of \mathbf{S}_i^2 converge to the squared length of a classical spin vector S^2 and we will come back to this.

The quadratic terms left in 2.33 can be diagonalized introducing Fourier transformed operators

$$\begin{aligned} a_{\mathbf{k}} &= \frac{1}{\sqrt{N}} \sum_i \exp^{-i\mathbf{k}\cdot\mathbf{r}_i} a_i \\ a_{\mathbf{k}}^\dagger &= \frac{1}{\sqrt{N}} \sum_i \exp^{-i\mathbf{k}\cdot\mathbf{r}_i} a_i^\dagger \end{aligned} \quad (2.34)$$

which preserves the bosonic commutations relations. Inserting them into 2.33 and using $\sum_i \exp i(\mathbf{k} - \mathbf{k}') \cdot \mathbf{r}_i = N\delta_{\mathbf{k}\mathbf{k}'}$ we obtain

$$H_H = -\frac{JNS^2z}{2} + \sum_{\mathbf{k}} \omega_{\mathbf{k}} a_{\mathbf{k}}^\dagger a_{\mathbf{k}} \quad (2.35)$$

with

$$\omega_{\mathbf{k}} = 2JS \sum_{\delta} (1 - \cos \mathbf{k} \cdot \delta) = JSz(1 - \gamma_{\mathbf{k}}) \quad (2.36)$$

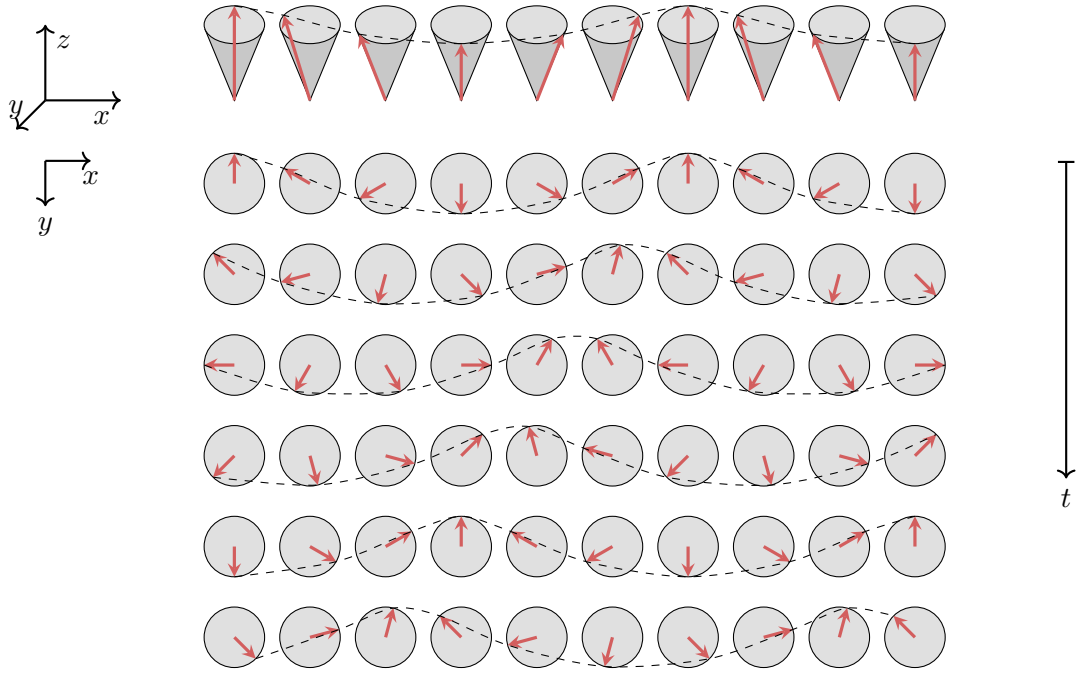


Figure 2.3: **Spin waves.** (top) Representation of out-of-phase spin wave on a 1D chain viewed in perspective at a frozen time t_0 . (bottom) Evolution in time of a spin wave on a 2D square lattice seen from above. Red arrows indicate the spin orientation, while the grey cones are a visual guide for the spin precession. Dashed line outlines the spin wave, drawn through the ends of the vectors.

and

$$\gamma_{\mathbf{k}} = 2/z \sum_{\delta} \cos \mathbf{k} \cdot \delta = 2/z \sum_{\nu=1}^d \cos k_{\nu} \delta_{\nu} \quad (2.37)$$

Here δ is defined as the vector connecting interacting sites, as in $j = i + \delta$.

Eq. 2.35 describes a system of independent harmonic oscillators labelled by wavevector \mathbf{k} with energy $\omega_{\mathbf{k}}$. One quantum of spin wave is a pseudo-particle called *magnon* and is created by the operator $a_{\mathbf{k}}^{\dagger}$. Truncation in Eq.2.33 is thus equivalent to neglect magnon-magnon interactions terms, as $a_i^{\dagger} a_i a_j^{\dagger} a_j$.

Thermal fluctuations, instead of acting on individual spins, are shared by the entire lattice in the shape of a spin wave. In the limit $\mathbf{k} \rightarrow 0$ the dispersion is quadratic,

$$\omega_{\mathbf{k}} \approx JS|\mathbf{k}|^2 \quad (2.38)$$

as shown in Fig. 2.4.

We note that the $\mathbf{k} = 0$ magnon, called *Goldstone* mode, corresponds to a uniform spin rotation and does not cost any energy. This results from the fact that the Hamiltonian 2.33 is invariant under rotation. Magnons are introduced and removed from the system by the operators 2.34 and one can show that $a_{\mathbf{k}}^{\dagger} |\Psi_{GS_{FM}}\rangle$ is indeed an eigenstate of H_H . Conversely, this is not true for $a_{\mathbf{k}}^{\dagger} a_{\mathbf{k}'}^{\dagger} |\Psi_{GS_{FM}}\rangle$ since in our approximation we neglected interactions.

Being non-interacting bosons, their behaviour is controlled by Bose-Einstein statistic, according to which the mean number of magnons with momentum \mathbf{k} depends on the temperature $T = \beta/k_B$ as in

$$\langle n_{\mathbf{k}} \rangle = \langle a_{\mathbf{k}}^{\dagger} a_{\mathbf{k}} \rangle = \frac{1}{e^{\beta\omega_{\mathbf{k}}} - 1} \quad (2.39)$$

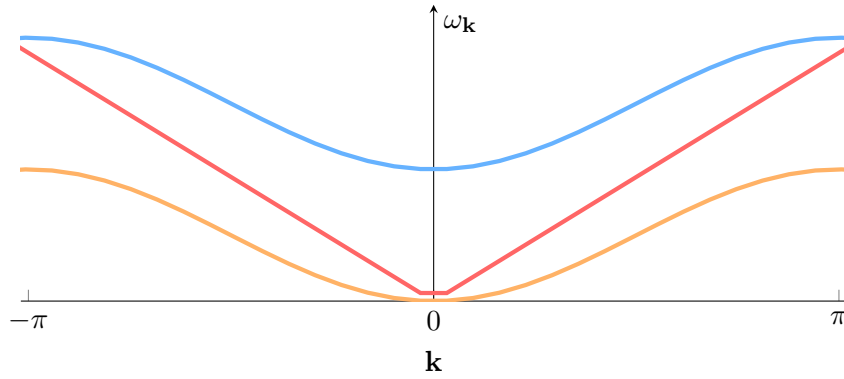


Figure 2.4: **Spin-wave dispersion relation.** Magnon dispersion for a system with FM isotropic (in blue), FM anisotropic (in orange) and AFM isotropic (in red) interactions.

2.4.1 Hohenberg-Mermin-Wagner theorem

At $T = 0$, it is easy to see that the ground state has no magnons and the magnetization M reaches its maximal value. As we increase the temperature, we introduce more energy in the system and thermally excite new magnons, each of which undermines the global magnetic order. Eventually, it reaches a critical mass and is so large that it is not possible to talk of magnetic order anymore. The system undergoes a phase transition into paramagnetism and the order parameter M drops to 0. We can look at how M depends on T evaluating

$$M = S - \Delta M(T) \quad (2.40)$$

where $\Delta M(T) = \sum_{\mathbf{k}} \langle n_{\mathbf{k}} \rangle$ counts the total number of magnons present in the system at temperature T . Since the Heisenberg model allows for continuous rotation of spins, the very low-frequency oscillations are the first to appear and we can pass to the integral version. The bosonic density of states depends on the dimensionality d of the system and expanding Eq. 2.39 to first order we obtain

$$\Delta M \propto \int dk k^{d-1} \frac{k_B T}{S k^2} \propto \frac{k_B T}{JS} \begin{cases} 1/k + \dots, & d = 1 \\ -\log k + \dots, & d = 2 \end{cases} \quad (2.41)$$

While it can be shown that for $d = 3$ the value of ΔM is always finite and obeys the Bloch law $\Delta M \approx T^{3/2}$ at low energy, for $d = 1$ and $d = 2$ it diverges at any non-zero T . The result $M \rightarrow -\infty$ means that infinitely many magnons can be excited with minimal energies and thus no long range magnetic order is possible. This is generalized by the *Hohenberg-Mermin-Wagner* (MW) theorem[16] which states that no magnetic order is possible at any finite temperature in 1D or 2D systems with a continuous symmetry and short-range interactions, as is the case for the isotropic Heisenberg model.

2.5 Anisotropic terms

In section 2.4.1 we derived the MW theorem, according to which in 1D and 2D Heisenberg systems, no long-range magnetic order is possible at any finite temperature. This is in striking contrast with experimental observations[17]. The reason lies in the fact that Eq. 2.21 has a full $SU(2)$ spin rotation symmetry. The model is isotropic and all full-polarized configurations are degenerate in energy. An elementary cell in a realistic ionic environment generally lacks this rotational symmetry. The Heisenberg model is thus generalized

$$H = - \sum_{\alpha, \beta=1}^3 \sum_{\langle ij \rangle} J_{ij}^{\alpha\beta} S_i^\alpha S_j^\beta \quad (2.42)$$

where the tensor $J_{ij}^{\alpha\beta}$ couples the α, β -components of the spin operators at site i, j . Crystal symmetry reduces number of non-zero elements and typically for 2D system the out-of-plane component has a peculiar nature compared to the in-plane directions. This commonly yields to a uni-axial anisotropic exchange

$$\begin{aligned} H &= - \sum_{\langle ij \rangle} \left[J_{ij}^x S_i^x S_j^x + J_{ij}^y S_i^y S_j^y + J_{ij}^z S_i^z S_j^z \right] \\ &= - \sum_{\langle ij \rangle} J_{ij} \left[S_i^x S_j^x + S_i^y S_j^y + (1 + \epsilon) S_i^z S_j^z \right] = - \sum_{\langle ij \rangle} \left[J_{ij} \mathbf{S}_i \cdot \mathbf{S}_j + B S_i^z S_j^z \right] \end{aligned} \quad (2.43)$$

where additional term ϵ (absorbed by A in the last equation) favoured out-of-plane ($B > 0$) or in-plane ($B < 0$) magnetization, introducing *magnetic anisotropy* (MA). As it is clear from Eq. 2.43, MA means that the energy depends on the orientation of the magnetization as measured with respect to the crystallographic axes, and at same extent or in same form, it is always present in real samples. Moreover, without it, magnetism would be fairly useless, since almost all applications hinge on the fact that same directions (easy axis) are easier to magnetize than others (hard axis) with an external magnetic field. *Super-exchange interactions* [50] between spins mediated by non-magnetic ions in non-planar geometries, are typically modelled in simulations as an effective anisotropic term as in Eq. 2.43.

Another source of anisotropy arises from *spin-orbit coupling* (SOC). This term is a consequence of relativistic corrections in the electronic Hamiltonian. From a classical picture (again, wrong but powerful), it arises from the interaction between the vector spin \mathbf{S} of a charged particle with its own orbital motion, thus the orbital angular momentum $\mathbf{L} = \mathbf{r} \times \mathbf{p}$ (see Fig. 2.5). A proper derivation starts from the time independent Dirac equation[51], which accounts for the relativistic effect neglected in the Pauli equation for fermionic particles[52]. After algebraic manipulation and a semi-classical expansion in power of the $1/mc^2$, one obtain a series of terms in the Hamiltonian of the Dirac equation:

$$H = H_{NR} + H_{SI} + \frac{\hbar^2}{2m_e^2 c^2} \frac{\partial V}{r \partial r} \mathbf{S} \cdot \mathbf{L} \quad (2.44)$$

Here H_{NR} is the non-relativistic part, H_{SI} do not depend on spin and is the *Darwin term* and a corrections to the kinetic energy, while

$$H_{SOC} = \frac{\hbar^2}{2m_e^2 c^2} \frac{\partial V}{r \partial r} \mathbf{S} \cdot \mathbf{L} = \lambda \mathbf{S} \cdot \mathbf{L} \quad (2.45)$$

is the SOC coupling. For an electron in a crystal lattice, the orbital motion that defines \mathbf{L} is strongly affected by the atomic potential landscape. Consequently, some direction will be privileged the magnetization. The anisotropy that arises from SOC is generally called *magneto-crystalline anisotropy* since is a measure of how strong the spin is locked to a specific crystal direction. Assuming a quenching of angular momentum, only the spin degree of freedom remains. For transition metal elements, where the SOC is much smaller than exchange couplings, it is common to treat it in perturbative theory. Eq. 2.45 has non-zero corrections only at second (or higher) order, namely

$$H_{SOC} = |\lambda|^2 \sum_n \frac{\langle 0 | L_\mu | n \rangle \langle n | L_\nu | 0 \rangle}{E_0 - E_n} S_\mu S_\nu = -S_\mu \Lambda_{\mu\nu} S_\nu \quad (2.46)$$

where the indices μ, ν run over the crystallographic axes. Rotating the tensor $\Lambda_{\mu\nu}$ in the same basis and writing $A \propto |\lambda|^2$, we obtain the uniaxial anisotropy for the system

$$H_{SOC} = \sum_i A_x (S_i^x)^2 + A_y (S_i^y)^2 + A_z (S_i^z)^2 \quad (2.47)$$

As before, the strongest contributions arises from the last term, generally of the order of 1 meV.

The general anisotropic Heisenberg model can thus be written as

$$H = -\frac{1}{2} \sum_{ij} J_{ij} \mathbf{S}_i \cdot \mathbf{S}_j - \sum_i A_i (S_i^z)^2 - \frac{1}{2} \sum_{ij} B_{ij} S_i^z S_j^z \quad (2.48)$$

where generally the couplings are kept only for nearest neighbours' sites and the Heisenberg parameters $J_{ij} \equiv J$, $A_i \equiv A$, $B_{ij} \equiv B$ are symmetric and constant.

The dispersion relation for a FM system described by 2.48 can be obtained in way similar to the isotropic case, though additional approximations are needed in case of magnonic interactions. More information can be found in sections 5.1, 5.4, 5.6 and the referred publications. The magnon dispersion relation is in general shifted upwards by a constant proportional to MA (see Fig. 2.4). This yields to a finite energy gap that protects the ordered ground state and defines a privileged axis that breaks the spherical symmetry. The Mermin-Wagner theorem is thus evaded, but not when i.e. $A < 0$ and $B < 0$. In this case, an easy-plane is defined instead and rotational symmetry preserved on the xy -plane. It is easy to see that for $A \rightarrow \infty$ the Heisenberg model becomes a binary state system equivalent to an Ising model. The opposite limit is the already mentioned XY model.

2.6 Other interactions

One can derive other exchange interactions beyond the Heisenberg model expanding localized models as the Hubbard model (see sec.(3.3.1)) in a perturbative approach. Some examples are the four-spin exchange interaction

$$H_{4-spin} = \sum_{ijkl} K_{ijkl} [(\mathbf{S}_i \mathbf{S}_j)(\mathbf{S}_k \mathbf{S}_l) + (\mathbf{S}_j \mathbf{S}_k)(\mathbf{S}_l \mathbf{S}_i) - (\mathbf{S}_i \mathbf{S}_k)(\mathbf{S}_j \mathbf{S}_l)] \quad (2.49)$$

which describe four consecutive hops of electrons, and a biquadratic exchange

$$H_{biq} = \sum_{ij} Q_{ij} (\mathbf{S}_i \mathbf{S}_j)^2 \quad (2.50)$$

Since these terms scale with the magnetic moments to 4th order, they are usually neglected and we show them here only for completeness. However, they may play an important role in lifting degeneracies of the Heisenberg model and in frustrated magnets.

Anti-symmetric exchange, like the *Dzyaloshinskii – Moriyainteraction*, results from second-order perturbative theory of the spin-orbit coupling interaction. They are generally written as

$$H_{DMI} = \sum_{ij} \mathbf{D}_{ij} (\mathbf{S}_i \times \mathbf{S}_j) \quad (2.51)$$

where

2.6.1 AFM quantum corrections

In previous sections we analyzed the ground-state of a system with dominant ferromagnetic interactions. When $J < 0$ the interactions are anti-ferromagnetic and spins privilege anti-parallel alignment. The ground state is generally more complex even in the classical picture (see sec. 3.4) and we will shortly outline the most important features of the AFM ground state and first excited states.

One might naively guess that the so-called Néel state

$$\Psi_{\text{Néel}} = |\dots, \uparrow, \downarrow, \uparrow, \downarrow, \dots\rangle = |\dots, S, -S, S, -S, \dots\rangle \quad (2.52)$$

having spins on neighbouring sites pointing in opposite directions, represents the quintessential expression of anti-ferromagnetism and thus being the ground state. Conversely, it is easy to show that it is not even an eigenstate of the Heisenberg model 2.33 since the ladder operators would flip pairs of adjacent spins. While in the ferromagnetic case the raising and lowering operators always destroy the

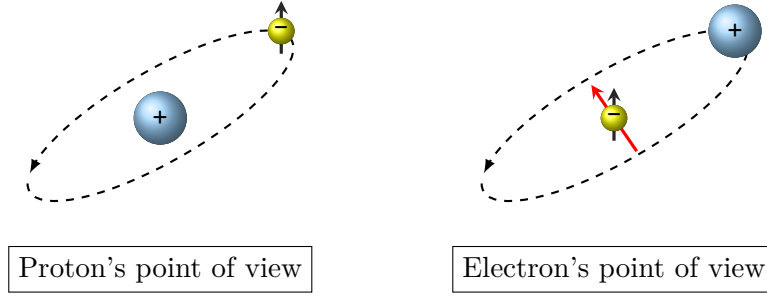


Figure 2.5: **Spin-orbit coupling.** SOC is the interaction of the spin \mathbf{S} (black arrow) of an electron (negatively charged yellow sphere) with its own orbital angular momentum \mathbf{L} , mainly affected by the geometry of the system. In a classical picture, this can be seen as an effective magnetic field (red arrow) generated by the positively charged nucleus orbiting around the electron in the electron's rest frame.

ferromagnetic ground state, leaving only the contribution from the $S_i^z S_j^z$ terms of the Hamiltonian, here their action changes the state so that $H_H \Psi_{\text{Néel}}$ is not proportional to solely $\Psi_{\text{Néel}}$ anymore.

The Néel state is still a good starting point though. We can split the entire lattices with N spin into two sublattices with $N/2$ spins each. For bipartite lattices the nearest neighbours of a spin on the lattice A are all of the sublattice B , as i.e. in a chessboard configuration. The true ground state would probably have spins pointing predominantly in i.e. $+S$ direction for sublattice A and spins pointing predominantly in the opposite direction for sublattice B . At first, we define convenient bosonic HP operators. Equations in 2.25 are still valid for the sublattice A with spin projection $+S$, while for B , the opposite direction for the spin projection is reflected as

$$\begin{aligned} S_j^+ &= b_j^\dagger \sqrt{2S - b_j^\dagger b_j} \\ S_j^- &= \sqrt{2S - b_j^\dagger b_j} b_j \\ S_j^z &= -S + b_j^\dagger b_j \end{aligned} \quad (2.53)$$

where $i \in A$ and $j \in B$ for Eqs. 2.25 and 2.53. If we insert these expressions in the Hamiltonian, we can expand the square roots and keeping only the quadratic terms to order S (thus neglecting the interaction terms) leads to

$$H = \frac{NzJS^2}{2} - JS \sum_{\langle ij \rangle} [a_i^\dagger a_i + b_j^\dagger b_j + a_i b_j + b_j^\dagger a_i^\dagger] \quad (2.54)$$

where z is the coordination number, i.e., 4 for square lattice. As we did for the FM case, we then introduce the Fourier-transformed operators, of the type

$$\begin{aligned} a_i &= \frac{1}{\sqrt{N/2}} \sum_{\mathbf{k}} e^{i\mathbf{k} \cdot \mathbf{R}_i} a_{\mathbf{k}} \\ b_j &= \frac{1}{\sqrt{N/2}} \sum_{\mathbf{k}} e^{-i\mathbf{k} \cdot \mathbf{R}_i} b_{\mathbf{k}} \end{aligned} \quad (2.55)$$

Using the standard bosonic commutation relations, the substitution leads to:

$$H = \frac{NzJS^2}{2} - JSz \sum_{\mathbf{k}} [a_{\mathbf{k}}^\dagger a_{\mathbf{k}} + b_{\mathbf{k}}^\dagger b_{\mathbf{k}} + \gamma_{\mathbf{k}} (a_{\mathbf{k}} b_{\mathbf{k}} + a_{\mathbf{k}}^\dagger b_{\mathbf{k}}^\dagger)] \quad (2.56)$$

where $\gamma_{\mathbf{k}}$ is defined as in 2.37. The first two terms in Eq. 2.56 are in diagonal form, but unlike the FM case, the last two terms required an additional canonical Bogliubov-Valatin transformation that maps

$$\begin{aligned} a_{\mathbf{k}} &= \cosh(\phi_{\mathbf{k}})\alpha_{\mathbf{k}} - \sinh(\phi_{\mathbf{k}})\beta_{\mathbf{k}}^{\dagger} \\ b_{\mathbf{k}} &= -\sinh(\phi_{\mathbf{k}})\alpha_{\mathbf{k}}^{\dagger} + \cosh(\phi_{\mathbf{k}})\beta_{\mathbf{k}} \end{aligned} \quad (2.57)$$

The new operators $\alpha_{\mathbf{k}}$ and $\beta_{\mathbf{k}}$ are still bosonic operators and inserting them into 2.56 reads, after algebraic manipulation,

$$H = \frac{NzJS(S+1)}{2} + \sum_{\mathbf{k}} \hbar\omega_{\mathbf{k}} \left[\alpha_{\mathbf{k}}^{\dagger}\alpha_{\mathbf{k}} + \beta_{\mathbf{k}}^{\dagger}\beta_{\mathbf{k}} + 1 \right] \quad (2.58)$$

where $\hbar\omega_{\mathbf{k}} = -JSz\sqrt{1-\gamma_{\mathbf{k}}^2}$. This Hamiltonian is now in a diagonal form: operators $\alpha_{\mathbf{k}}^{\dagger}$ and $\beta_{\mathbf{k}}^{\dagger}$ create non-interacting magnons with energy $\omega_{\mathbf{k}}$. Without losing generality we assume a spin chain ($d=1$ and $z=2$) and it is easy to see that at small \mathbf{k} we have a linear dispersion relation (see Fig. 2.4):

$$\hbar\omega_{\mathbf{k}} = -2JS\sqrt{1-\gamma_{\mathbf{k}}^2} \simeq -2JS\sqrt{1-(\cos k\delta)^2} \sim -2JS\delta k \quad (2.59)$$

The ground state in the approximation of no magnon-magnon interactions $|\Psi_{NIM}\rangle$ is defined as the vacuum of the annihilation operators, namely

$$\begin{aligned} \alpha_{\mathbf{k}}|\Psi_{NIM}\rangle &= 0 \\ \beta_{\mathbf{k}}|\Psi_{NIM}\rangle &= 0 \end{aligned} \quad (2.60)$$

For any \mathbf{k} , and the energy is obtained as

$$E_{NIM} = \frac{NzJS(S+1)}{2} - zJS \sum_{\mathbf{k}} \sqrt{1-\gamma_{\mathbf{k}}^2} \quad (2.61)$$

The last term is evaluated numerically[38] on a grid in the reciprocal space and depends on its dimensionality d :

$$E_{NIM} = dNJS^2 \begin{cases} (1 + 0.363/S) & \text{for } d = 1, \\ (1 + 0.158/S) & \text{for } d = 2, \\ (1 + 0.097/S) & \text{for } d = 3 \end{cases} \quad (2.62)$$

E_{NIM} is always lower than the energy of Néel state $E_{\text{Néel}} = \frac{zNJS^2}{2}$. The corrections is thus more significant for systems with low spin S (as we expect for quantum fluctuations corrections) and low d . Moreover, the expectation value of the magnetization in one sublattice is also affected:

$$M_{NIM|A} = \langle \Psi_{NIM} | S - a_i^{\dagger} a_i | \Psi_{NIM} \rangle = S - \frac{2}{N} \sum_{\mathbf{k}} \langle \Psi_{NIM} | S - a_{\mathbf{k}}^{\dagger} a_{\mathbf{k}} | \Psi_{NIM} \rangle \quad (2.63)$$

Adopting the Bogoliubov-Valatin operators one gets

$$\Delta M|_A = S - M_{NIM|A} = -\frac{1}{2} + \frac{2}{N} \sum_{\mathbf{k}} \left(n_{\mathbf{k}} + \frac{1}{2} \right) \frac{1}{\sqrt{1-\gamma_{\mathbf{k}}^2}} \quad (2.64)$$

Passing to the continuum limit, at $T = 0$ ($n_{\mathbf{k}} = 0$) and $d = 1$, the last sum becomes

$$\frac{1}{N} \sum_{\mathbf{k}} \frac{1}{\sqrt{1-\gamma_{\mathbf{k}}^2}} \propto \lim_{k_0 \rightarrow \pi} \int_{k_0}^{\pi} (1 - \cos^2 k)^{-1/2} dk \quad (2.65)$$

which diverges when $k_0 \rightarrow -\infty$. The sub-lattice magnetization has zero expectation value, meaning that the ground state is not stable due to quantum fluctuations for any value of S and T (also the ground state is unstable). For 2D and 3D systems the average spin is evaluated numerically[38] and reduced by

$$M_{NIM}|_A = \frac{NS}{2} \begin{cases} (1 - 0.197/S) & \text{for } d = 2 \\ (1 - 0.078/S) & \text{for } d = 3 \end{cases} \quad (2.66)$$

CHAPTER 3

Density Functional Theory and Energy Mapping Analysis

Quantum mechanics is certainly one of the most successful theories ever produced. Being concerned with the nature of the most elementary building blocks of the universe, it is considered to be a fundamental description of nature. Many phenomena and laws of physics, not only expressions of the microscopic world, can be derived from quantum mechanics.

Louis de Broglie first proposed the wave nature of matter in 1924. This idea was later combined with work done on quantisation by, among others, Planck and Einstein about two decades earlier. This revolution in thinking eventually led to a new theory of matter, replacing the idea of particles with definite positions in space, with waves and positional uncertainty. The theory, which became known as quantum mechanics, quickly established itself within physics by describing nature with unprecedented accuracy, but ceaselessly poses new challenges.

While in the previous chapter we already introduced some concepts and formulation of quantum mechanics, in this one we first describe the founding principles of many-body quantum mechanics and discuss the unavoidable approximations made to describe complex systems. We thus introduce Density Functional Theory (DFT), one of the most powerful and widely used tool for calculating ground state observables of many-body systems. All DFT results have been obtained with the electronic structure software package GPAW[53, 54] based on the Projector Augmented Wave method (PAW) formalism[55] using plane wave (PW) basis sets and combined with the Atomic Simulation Environment (ASE)[56]. The specific settings for DFT calculations are not discussed here but can be found in the *Method* sections in each publication listed in chapter 7. Relaxation of geometrical structures and convergence tests with respect to PW cut-off energy and k -point grids density are implied for the rest of the thesis.

In the last part of the chapter, we present the Energy Mapping analysis, a method that maps results from DFT calculations to spin-lattice models, in order to extract relevant parameters.

3.1 Electronic structure

In a simplified picture and at a convenient scale, matter is made of atoms with a central nucleus and electrons (de-)localised all around. The primary concern with nowadays solid state physics and quantum chemistry is the calculation of the ground state properties of such a collection of atoms. This challenging task is entrusted to the Schrödinger equation (SE). For a system with M nuclei and N electrons, in the time-independent version it reads

$$\hat{H}\Psi(\{\mathbf{r}_i\}_N, \{\mathbf{R}_k\}_M) = E\Psi(\{\mathbf{r}_i\}_N, \{\mathbf{R}_k\}_M) \quad (3.1)$$

where E is the energy eigenvalue of Hamiltonian operator \hat{H} corresponding to the many-body wave function $\Psi(\{\mathbf{r}_i\}_N, \{\mathbf{R}_k\}_M)$, with \mathbf{R}_k and \mathbf{r}_i being the space coordinates of the k -th nucleus and of the i -th electron respectively. The general Hamiltonian comprises kinetic energies of electrons (nuclei) $\hat{T}_{e(n)}$ and all the possible combinative interactions \hat{V} between each other and with the external environment

$$\hat{H} = \hat{T}_e + \hat{T}_n + \hat{V}_{nn} + \hat{V}_{ee} + \hat{V}_{ne} + \hat{V}_{ext} \quad (3.2)$$

An early approximation to Eqs. 3.1 and 3.2 is the Born-Oppenheimer approximation, which states that the motion of nuclei and their mutual interactions are negligible when compared to the ones of the electrons, because of the much larger mass. The Hamiltonian for a system with N interacting electrons with mass m and electric charge $-e$, moving in an external potential $v(\mathbf{r})$, is thus written as

$$\hat{H} = \sum_i^N \left(-\frac{\hbar^2 \nabla_i^2}{2m} - \sum_k^M \frac{Z_k e^2}{|\mathbf{R}_k - \mathbf{r}_i|} + v(\mathbf{r}_i) \right) + \sum_i^N \sum_{j \neq i}^N \frac{1}{2} \frac{e^2}{|\mathbf{r}_j - \mathbf{r}_i|} \quad (3.3)$$

The first term is the sum of all the single particle kinetic energies, of the Coulomb attractions between negatively charge electrons and M positively charged (with atomic number Z_k) nuclei and the coupling with an external potential. The second sum describes the electron-electron interaction. It makes solving Eq.3.3 a computational problem that intimidatingly scales exponentially with the number of electrons. In order for quantum mechanics to be a practical theory and provide an accurate description of the electronic proprieties of a system, an approach different than the exact solution of Eq.3.3 is required. Once the external potential is set, solving the SE defines the wave functions from which we obtain the value of the observables as expectation values of corresponding operators.

For example, the total electron density is defined as the integral over all but one of the spatial coordinates:

$$n(\mathbf{r}) = N \int \dots \int \Psi^*(\mathbf{r}_1, \mathbf{r}_2, \dots, \mathbf{r}_N) \Psi(\mathbf{r}_1, \mathbf{r}_2, \dots, \mathbf{r}_N) d\mathbf{r}_2 \dots d\mathbf{r}_N \quad (3.4)$$

This formulation derives from the fact that the wave function is written as Slater determinant (Hartree-Fock approximation[57, 58]). It is thus anti-symmetrized (in order to satisfy the Pauli exclusion principle) and reflects the indiscernibility of particles. The function $n(\mathbf{r})$ determines the probability of finding any of the N electrons within the volume element $d\mathbf{r}$ but necessitates the knowledge of Ψ and thus the resolution of Eq.3.3, which in turn depends on electronic density. While , the standard approach to describe electronic proprieties is then self-consistent.

3.2 Density Functional theory

Density Functional Theory (DFT) is based on a different approach. It is a formally exact reformulation of the many-body quantum mechanics but its fundamental concept is that any propriety of a system with many interacting electrons can be mapped to a functional¹ of the ground state electronic density $n_0(\mathbf{r})$. This in principle determines all the information stored in the many-body wave function for the ground state.

The first work on the field dates back to 1927, when Thomas[59] and Fermi[60] derived the kinetic energy of an electronic system as an explicit functional of the density $E_{TF}[n_0]$. They consider homogeneous gas of non-interacting electrons with density equal to the local density at any given point obtaining for an external potential $v(\mathbf{r})$, usually the one originating from static nuclei plus any other that can be controlled from outside the system i.e. electric field. The Hamiltonian in Eq. 3.2 is thus generally reduced to the sum of electron kinetic energies, electron-electron interactions and external potential

$$\hat{H} = \hat{T} + \hat{V}_{ee} + \hat{V}_{ext} \quad (3.5)$$

Notwithstanding the simplicity of the approximation and the lack of relevant physical features, the functional-based method makes its point in a numerical context, since it drastically reduce the dimensionality of the problem.

¹A functional $F[\phi]$ assigns to a function ϕ a real or complex number.

3.2.1 Hohenberg-Kohn theorems

DFT as it is meant nowadays has been theoretically developed by Hohenberg and Kohn in 1964 [61], who formulated it as an exact theory of the static electronic many-body problem. The method lies on the following theorems:

Theorem 3.2.1 *For a non-degenerate system subject only to a time-independent scalar potential, all physical quantities, including the many-body wave function Ψ and the external potential $v(\mathbf{r})$ are uniquely determined by the charge density $n(\mathbf{r})$.*

Theorem 3.2.2 *For a given external potential, the ground state density $n_0(\mathbf{r})$ is that which minimises the energy of the system.*

The first theorem means that we can establish a unique mapping between the electronic density $n(\mathbf{r})$ of a particular system and the external potential $v(\mathbf{r})$ acting on it. Any effective potential is then written as a functional of the density

$$V(\mathbf{r}) = V[n](\mathbf{r}) \quad (3.6)$$

and since the ground state wave function Ψ_0 is determined by the external potential, we can also establish the one-to-one relationship

$$\Psi_0 = \Psi[n_0] \quad (3.7)$$

All other physical observables can thus be derived, at least in principle, from the charge density. Most notably, the total energy reads

$$E[n] = F[n] + V_{ext}[n] \quad (3.8)$$

where $F[n] = \hat{T}[n] + \hat{V}_{ee}[n]$ is an universal functional of the density defined as the sum of the kinetic and interaction energies and independent of the external potential.

With these considerations in mind, the second theorem is then a variational procedure to find the ground-state charge density $n_0(\mathbf{r})$ of a given external potential $v(\mathbf{r})$. It follows from the fact that any arbitrary exchange-antisymmetric N-electron state $|\Psi\rangle$ (which leads to any other different density $n(\mathbf{r})$) must obey

$$E[n_0] = F[n_0] + V[n_0] = \min \langle \Psi | \hat{T} + \hat{V}_{ee} | \Psi \rangle + \int n_0(\mathbf{r})v(\mathbf{r})d\mathbf{r} \quad (3.9)$$

where $E_0 = E[n_0] = \langle \Psi_0 | \hat{H} | \Psi_0 \rangle$ is the total ground state energy.

A schematic representation of HK theorems is the following:

$$\begin{array}{ccc} v(\mathbf{r}) & \xleftarrow{HK} & n_0(\mathbf{r}) \\ \downarrow & & \uparrow \\ \Psi_i(\{\mathbf{r}\}) & \longrightarrow & \Psi_0(\{\mathbf{r}\}) \end{array}$$

A normal arrow stands for the usual resolution of the Schrödinger equation: from $V_{ext}(\mathbf{r})$ we obtain all the states of the system $\Psi_i(\{\mathbf{r}\})$ (including the ground-state $\Psi_0(\{\mathbf{r}\})$) and the ground-state density $n_0(\mathbf{r})$. The arrow labelled with *HK* indicate the direction of HK theorems and completes the circle.

To sum up, the ground state wave function is the one which minimises an universal functional $F[n]$ of the density, whilst reproducing the ground state density. In the non-degenerate case, this definition uniquely determines the ground state wave function in terms of n_0 , without explicitly specifying any external potential. Hence, it is the density, rather than the many-body wave function, that can be used to obtain the ground state energy of the system, i.e. from $\frac{\delta E[n]}{\delta n} = 0$. Anyway, this task still requires the troublesome computation of the many-body wave function (see Eq. 3.9) since no expressions of $F[n]$ depending explicitly on the density (and not via wave functions) is known at date.

3.2.2 Kohn-Sham equations

DFT would remain a minor technical curiosity if it were not for the ansatz made by Kohn and Sham[62], which provided the first practicable procedure to exploit the abstract framework advanced by the HK theorems. The key of Kohn-Sham (KS) scheme is to treat electrons as non-interacting particles, so to bypass the exponential scaling factor due to the interacting terms in Eq. 3.3. Then, HK theorems guarantee that any charge density can be reproduced by a unique effective, external potential. The SE equations for a system of N interacting electrons is thus replaced by a set of N SE equations (called KS equations) for non-interacting electrons:

$$\begin{aligned} \left[-\frac{\hbar^2}{2m}\nabla^2 + v_{KS}(\mathbf{r}) \right] \phi_i(\mathbf{r}) &= \\ \left[-\frac{\hbar^2}{2m}\nabla^2 + v_{ext}(\mathbf{r}) + v_H(\mathbf{r}) + v_{xc}(\mathbf{r}) \right] \phi_i(\mathbf{r}) &= \\ \left[-\frac{\hbar^2}{2m}\nabla^2 + v_{ext}(\mathbf{r}) + \int \frac{n(\mathbf{r}')}{|\mathbf{r} - \mathbf{r}'|} d\mathbf{r}' + \frac{\delta E_{xc}}{\delta n(\mathbf{r})} \right] \phi_i(\mathbf{r}) &= \epsilon_i \phi_i(\mathbf{r}) \end{aligned} \quad (3.10)$$

The interactions are replaced by a single-particle potential, called KS potential V_{KS} , which retains the electron density of the original system with interacting particles (see Fig. 3.1). It includes the "harmless" single-particle interactions with the external perturbations, the Hartree Coulomb repulsion v_H and the *exchange-correlation* (XC) potential v_{xc} . The latter is an umbrella term that accounts for the effects of dealing with anti-symmetric wave functions (exchange) and for balancing the overestimation of repulsive Hartree energy between any electron pair (correlation)². Essentially it stands for whatever has been missed out when moving into the KS scheme. It is also the only unknown term and despite being a widely explored research area, no exact general expression, explicitly in terms of the electron density, is available. Luckily, v_{xc} is small compared to the whole v_{KS} and approximations made to it yields to reasonably accurate results, but often only work for specific problems.

3.2.3 Exchange-correlation functionals

Since the advent of modern computers and the opportunity to perform high-demanding calculations, there has been a growing interest in DFT methods[63] and for its time-dependent version[64]. Nowadays it is one of the most active field in physics and the number of XC functionals available is huge and

²The correlation effects generally also account for the difference between the non-interacting and interacting kinetic energies.

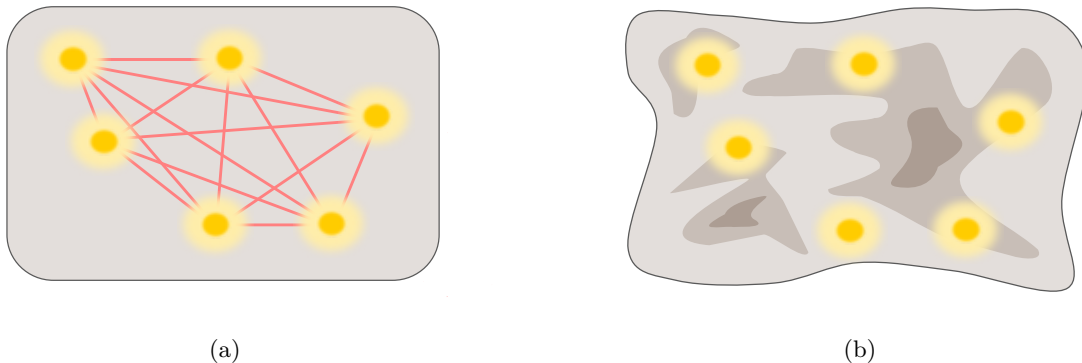


Figure 3.1: **KS ansatz.** A way to visualize the idea behind KS method and how it substitutes (a) a system of interacting electrons introducing an (b) auxiliary system of non-interacting electrons but with an effective potential V_{KS} so that the electronic density (cartoonized in yellow) is the same.

for every taste[65, 66]. Here we will give just a brief overview of the most used classes of functionals in material science and throughout this project. The first and simplest approximation is the Local Density Approximation LDA which acquires the local XC energy at a position \mathbf{r} assuming the entire system to be an infinite, homogeneous electron gas with density equal to $n(\mathbf{r})$. While being still vastly used for systems having relatively homogeneous electronic densities (like metals), it is well-known to fail in predicting optical proprieties of materials (as an underestimation of the optical band gaps in insulators and semiconductors[67]), among others drawbacks. More advanced functionals are the semi-local Generalized Gradient Approximation GGAs, which expand from LDA making the XC energy a functional of the spatial variation of the density as well. The functional employed in this project is the GGA functional PBE[68] (by Perdew, Burke and Ernzerhof) and it is one of the most used in the field.

3.3 Spin-dependent DFT

In principle, it should be possible to extract from the electronic density also all the magnetic proprieties of the system, such as magnitude and alignment of magnetic moments. In practice, it is easier to redefine DFT so to explicitly include the spin-density matrix, replacing the scalar density $n(\mathbf{r})$ by an Hermitian 2x2 spin-density matrix $\tilde{n}(\mathbf{r})$, composed of a scalar (charge) $n(\mathbf{r})$ and vectorial (spin density) $\mathbf{s}(\mathbf{r})$ part. As we did in 2.2, we define the spin density in terms of the two-component spinorial wavefunction $\phi(\mathbf{r})$ as

$$\mathbf{s}(\mathbf{r}) = \langle \phi(\mathbf{r}) | \boldsymbol{\sigma} | \phi(\mathbf{r}) \rangle, \quad \Phi(\mathbf{r}) = \begin{pmatrix} \phi^\uparrow(\mathbf{r}) \\ \phi^\downarrow(\mathbf{r}) \end{pmatrix} \quad (3.11)$$

with $\boldsymbol{\sigma}$ being the Pauli vector in Eq. 2.5.

With the 2x2 unit matrix as \mathbf{I} , the density matrix can be expanded into the scalar and vectorial part,

$$\tilde{n}(\mathbf{r}) = \frac{1}{2} [n(\mathbf{r})\mathbf{I} + \boldsymbol{\sigma} \cdot \mathbf{s}(\mathbf{r})] = \frac{1}{2} \begin{pmatrix} n(\mathbf{r}) + s_z(\mathbf{r}) & s_x(\mathbf{r}) - is_y(\mathbf{r}) \\ s_x(\mathbf{r}) + is_y(\mathbf{r}) & n(\mathbf{r}) - s_z(\mathbf{r}) \end{pmatrix} \quad (3.12)$$

Here the charge density $n(\mathbf{r}) = \text{Tr}[\tilde{n}(\mathbf{r})]$ and magnetization density $\mathbf{s}(\mathbf{r}) = \sum_{\alpha\beta} \tilde{n}_{\alpha\beta}(\mathbf{r}) \boldsymbol{\sigma}_{\alpha\beta}$ (with $\alpha, \beta = \uparrow, \downarrow$). The matrix components are given by $\tilde{n}_{\alpha\beta}(\mathbf{r}) = \phi_i^{\alpha*}(\mathbf{r}) \phi_i^\beta(\mathbf{r})$

Likewise, potential matrices are decomposed into a scalar and a magnetic field

$$\begin{aligned} \tilde{v}(\mathbf{r}) &= v(\mathbf{r})\mathbf{I} + \mu_B \boldsymbol{\sigma} \cdot \mathbf{B}(\mathbf{r}) \\ \tilde{v}_{xc}(\mathbf{r}) &= v_{xc}(\mathbf{r})\mathbf{I} + \mu_B \boldsymbol{\sigma} \cdot \mathbf{B}_{xc}(\mathbf{r}) \end{aligned} \quad (3.13)$$

with Bohr magneton $\mu_B = \frac{e\hbar}{2m}$.

Then Eqs. 3.10 are written in the form

$$\left[\left(-\frac{\hbar^2 \nabla^2}{2m} \int \frac{n(\mathbf{r}')}{|\mathbf{r} - \mathbf{r}'|} d\mathbf{r}' \right) \mathbf{I} + \tilde{v}(\mathbf{r}) + \int \frac{n(\mathbf{r}')}{|\mathbf{r} - \mathbf{r}'|} d\mathbf{r}' + \frac{\delta E_{xc}}{\delta \tilde{n}(\mathbf{r})} \right] \begin{pmatrix} \phi_i^\uparrow(\mathbf{r}) \\ \phi_i^\downarrow(\mathbf{r}) \end{pmatrix} = \epsilon_i \begin{pmatrix} \phi_i^\uparrow(\mathbf{r}) \\ \phi_i^\downarrow(\mathbf{r}) \end{pmatrix} \quad (3.14)$$

As in Eq. 3.10, one generally expands ϕ_i into a linear combinations of a suitable basis, then Eq. 3.14 becomes an eigenvalue problem and the eigenvectors give the coefficients of the expansion. The computational effort scales in the most general case with the third power of the dimension of the chosen basis. Compared to the non-magnetic case, now this number is doubled. Therefore the computational effort increases by a factor eight. Additional factors may come from the fact that non-collinear magnetism reduces symmetry and larger irreducible part of the Brillouin zone is needed to be sampled. Moreover, computations of quantities relative to magnetic structures are often more demanding since higher accuracy is needed.

If we can write the potential matrices in diagonal form, we can also decouple Eq. 3.14 into two equations, one for each spin component, equivalent to Eq. 3.10

$$\begin{aligned} \left[-\frac{\hbar^2}{2m} \nabla^2 + v_C(\mathbf{r}) + v(\mathbf{r}) + B_z(\mathbf{r}) + v_{xc}^\uparrow(\mathbf{r}) \right] \phi_i^\uparrow(\mathbf{r}) &= \epsilon_i^\uparrow \phi_i^\uparrow(\mathbf{r}) \\ \left[-\frac{\hbar^2}{2m} \nabla^2 + v_C(\mathbf{r}) + v(\mathbf{r}) + B_z(\mathbf{r}) + v_{xc}^\downarrow(\mathbf{r}) \right] \phi_i^\downarrow(\mathbf{r}) &= \epsilon_i^\downarrow \phi_i^\downarrow(\mathbf{r}) \end{aligned} \quad (3.15)$$

As for traditional DFT, the accuracy of results depends crucially on the approximation for v_{xc} , which are generally the spin-selective versions of LDA or GGA functionals.

Eqs. 3.13 however, have no spin-dependent terms. This means that while magnetization can emerge as a net inequality between the two spin-channels, the magnetic moment has no privileged direction in the space. The Magnetic Anisotropy (MA) is introduced evaluating the Spin-Orbit Coupling (SOC) expectation value (see sec. 2.45) in a basis of scalar-relativistic Kohn-Sham eigenstates[69].

3.3.1 DFT+U

Local and semi-local XC functionals tend to underestimate the strong on-site Coulomb repulsion between strongly correlated electrons. An example is a system with not fully occupied shells of localized electrons such as d and f orbitals. These are often the responsible for magnetism in transition metal elements and one of the most despicable consequence is the incorrect description of experimentally characterized AFM Mott insulators as FM metals. In the previous chapter we have seen the on-site Coulomb repulsion can be easily written in terms of the product of the occupation numbers (Eq. 2.18). Being $U' > 0$, the interaction is AFM and justifies the second Hund's rule. The Hubbard model is based on the following Hamiltonian for particles interacting on a lattice

$$H_U = -t \sum_{\mathbf{R}\mathbf{R}'\sigma} \left[c_{\mathbf{R}\sigma}^\dagger c_{\mathbf{R}'\sigma} + c_{\mathbf{R}'\sigma}^\dagger c_{\mathbf{R}\sigma} \right] + U' \sum_{\mathbf{R}} n_{\mathbf{R}\uparrow} n_{\mathbf{R}\downarrow} \quad (3.16)$$

where $c_{\mathbf{R},\sigma}$, $c_{\mathbf{R},\sigma}^\dagger$ are fermionic creation and annihilation operators at site \mathbf{R} and for a particle with spin $\sigma = \uparrow, \downarrow$. The relative amplitude of the "hopping" parameter t between (mainly nearest neighbouring) sites and of the on-site \mathbf{R} repulsion between opposite sign spins, determines the proprieties of the system. In the case of half-filling, (when the number of electrons is the same of sites), standard DFT is a reliable method when $t \gg U'$: single-particles terms dominate and the system is characterized by many itinerant particles (as the case of metals). Conversely, for large value of U , particles can't overcome the repulsive potential of other electrons. These correlation effects are not taken into account in DFT, which is based on non-interacting KS particles. DFT+U method is developed to improve the description of highly correlated system, by treating the on-site Coulomb interaction with an additional Hubbard-like term for the correlated states alone.

In the Dudarev[70] derivation, the correction for the total energy is in terms of an effective Hubbard value U and it reads

$$E_{DFT+U} = E_{DFT} + \frac{U}{2} \sum_{\sigma} \left[\sum_a \text{Tr}(n_{a,\sigma} - n_{a,\sigma} n_{a,\sigma}) \right] \quad (3.17)$$

for a relevant atomic orbital a , with occupation matrix $n_{a,\sigma}$.

In theory the value of U corresponds to a well-defined physical propriety, namely the strength of a screened Coulomb interactions between spins, thus should be determined from first principles arguments. Several solutions have been proposed in this sense[71, 72]. However, these derivations typically cannot be generalize (i.e. they strongly depends on the implementation of the basis set embedded in the code) and require very demanding calculations. Furthermore, they are not guaranteed to provide more accurate results[73]. In general, a straightforward method for obtaining accurate value from *ab-initio* is still under investigation.

On the other hand, an often accepted procedure is to tune the Hubbard value to the one that fits well-defined properties of the system, i.e. the one yielding to good agreement with experimental unit cell or measured optical band gap. It should be emphasized that there is no reason to believe that a semi-empirical fit would work for the same element in a different material. However, in most cases (including this project) an "exact" value of U is not required. As long as it prevents, at some extent, unwanted de-localization and does not over-localized the states (when U is too high), reasonable values (i.e. the one commonly used in literature) can still be used to suggest qualitative assessment of electronic correlations and outline trends in specific systems.

3.4 Energy mapping analysis

The evaluation of Heisenberg parameters such as J , A and B is based on a mapping of the ground state energies provided by spin-dependent DFT calculations over the atomistic spin-lattice model[74]. A trivial example is the extraction of exchange coupling J for an isolated spin dimer $|\cdot\rangle = |S_i, S_{zi}\rangle \otimes |S_j, S_{zj}\rangle$ where for a single state $|S, S_z\rangle = |\frac{1}{2}, \pm\frac{1}{2}\rangle$ for spin up and down respectively. We rewrite the spin Hamiltonian for the dimer as

$$H = JS_i^z S_j^z + (J/2) [S_i^+ S_j^- + S_i^- S_j^+] \quad (3.18)$$

and with

$$\begin{aligned} \hat{S}^z |S, S_z\rangle &= S^z |S, S_z\rangle \\ \hat{S}^+ |S, S_z\rangle &= \sqrt{S(S+1) - S_z(S_z+1)} S_z |S, S_z+1\rangle \\ \hat{S}^- |S, S_z\rangle &= \sqrt{S(S+1) - S_z(S_z-1)} S_z |S, S_z-1\rangle \end{aligned} \quad (3.19)$$

we can evaluate the energy of the possible configurations. The tensor product of two spin-1/2 particles can be decomposed into the triplet representation and singlet state representation respectively

$$\begin{aligned} |T\rangle &= |\uparrow\uparrow\rangle, \frac{1}{\sqrt{2}} (|\uparrow\downarrow\rangle + |\downarrow\uparrow\rangle), |\downarrow\downarrow\rangle \\ |S\rangle &= \frac{1}{\sqrt{2}} (|\uparrow\downarrow\rangle - |\downarrow\uparrow\rangle) \end{aligned} \quad (3.20)$$

It easily follows that the energy difference, or splitting, between the triplet and singlet is exactly the exchange coupling J :

$$E(|T\rangle) - E(|S\rangle) = J \quad (3.21)$$

The ground state configuration depends on the sign of the interaction J (ferromagnetic with $J > 0$ and anti-ferromagnetic with $J < 0$). The same technique can be apply to more complex systems and with more convoluted Hamiltonian. In particular, if energies are obtained from DFT calculations, quantum mechanical effects are at same extent embedded in the Kohn-Sham method and the classical Heisenberg model should be avoided (see Paper V). However, the Energy Mapping analysis scheme is vastly used also on top of a classical Heisenberg model[75, 76]. In this case, spin operators \mathbf{S} are treated as vector with spin component along the x, y and z directions. Moreover, often only configurations with a collinear magnetism are considered and thus the mapping is effectively on a re-scaled Ising model.

As example, we can compare the energies of the FM and AFM-chessboard configuration of a square lattice (Fig.3.2(a)-(b)). For a single atom inside the unit cell

$$\begin{aligned} E_{FM} &= -4\frac{1}{2}JS^2 = -2JS^2 \\ E_{AFMc} &= 4\frac{1}{2}JS^2 = 2JS^2 \end{aligned} \quad (3.22)$$

from which $J = \frac{E_{AFMc} - E_{FM}}{4JS^2}$ is easily derived. For triangular lattices in Fig. 3.3(c)-(d)

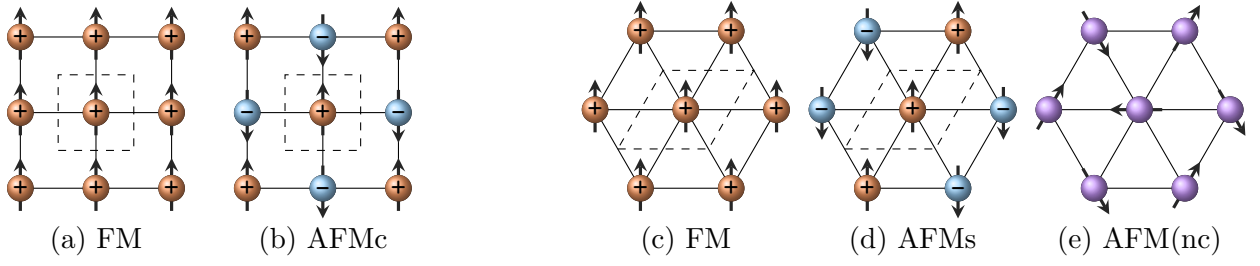


Figure 3.2: **Magnetic configurations for energy mapping analysis.** Spin states are at equivalent lattice sites and are distinguished by a sign (+ or -), arrow (\uparrow or \downarrow) and color (red or blue) for better clarity. Examples for square lattice ((a) ferromagnetism FM and (b) chessboard anti-ferromagnetism AFMc) and triangular lattice ((c) ferromagnetism FM, (d) striped anti-ferromagnetism AFMs and (e) non-collinear AFM, assuming easy-plane anisotropy) are shown. Dashed lines delimit the geometrical unit cell, for a better understanding of Eq. 3.22-3.23 in the text. The magnetic unit cell (the one used in calculations) is in repeated for AFM configurations.

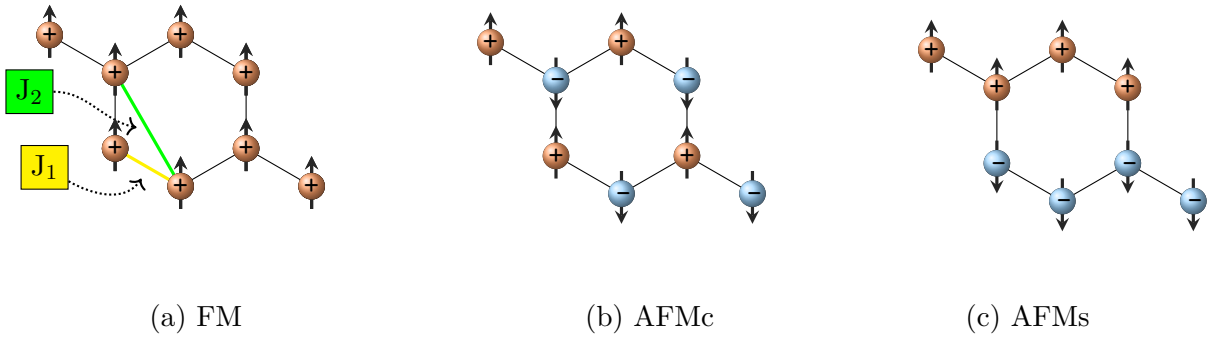


Figure 3.3: **Magnetic configurations for energy mapping analysis 2.** Spin states are at equivalent lattice sites and are distinguished by a sign (+ or -), arrow (\uparrow or \downarrow) and color (red or blue) for better clarity. Examples for honeycomb lattice in the (a) ferromagnetic FM (b) complete anti-ferromagnetic AFMc and (c) striped anti-ferromagnetic AFMs configuration.

$$\begin{aligned}
 E_{FM} &= -6\frac{1}{2}JS^2 = -6JS^2 \\
 E_{AFMs} &= -2\frac{1}{2}JS^2 + 4\frac{1}{2}JS^2 = 2JS^2
 \end{aligned}
 \tag{3.23}$$

from which $J = \frac{E_{AFMs} - E_{FM}}{8JS^2}$.

The square AFMc configurations is an example of a *total* anti-ferromagnetic configuration, which occurs when each spin state has only anti-ferromagnetic interactions with neighbouring sites. For geometrical reasons it's not always possible to have a total anti-ferromagnetic configuration. The most notable example is the triangular lattice. While for the square lattice (including only first nearest neighbours) the sign of J_1 is always well defined, this is not true for a triangular anti-ferromagnetic lattice. The atom in the unit cell in Fig.3.2(d) is surrounded by equivalent site atoms but with a different interaction signs. These interplays generally leads to magnetic frustration or geometrical Jahn-Teller distortion. The real anti-ferromagnetic ground state becomes a non-collinear configuration where all spins are rotated of 120° with respect to each others (Fig.3.2(d)).

In general, to extract N parameters, $N + 1$ independent configurations are required. An example is given in Fig. 3.3 for an honeycomb lattice with two exchange paths J_1 and J_2 . Energy mapping analysis is in fact equivalent to the resolution of a system of equations

$$\begin{bmatrix} a_{11} & \dots & a_{M1} \\ a_{12} & \dots & a_{M2} \\ \vdots & \vdots & \vdots \\ a_{1N} & \dots & a_{MN} \end{bmatrix} \begin{bmatrix} J_1 \\ J_2 \\ \vdots \\ J_N \end{bmatrix} = \begin{bmatrix} E_1 \\ E_2 \\ \vdots \\ E_N \end{bmatrix}$$

for the set $\{J_n\}_N$ of unknown parameters. Each row n represents a different magnetic configuration with magnetic contribution to the total energy equal to E_n . The matrix is quadratic and ideally invertible. Anyway from DFT calculations we compute the total energy $E'_n = E_0 + E_n$ and not just E_n . The part that does not depend on the spin, namely E_0 , is thus an extra unknown variable.

The anisotropy parameters A and B and exchange coupling J can be extracted by comparing the energy differences of magnetic configurations with in-plane/out-of-plane and FM/AFM configurations. The contribution from anisotropic terms can be attained in GPAW computing the spin-orbit coupling (SOC) correction on top of a converged calculations. In practice, only the SOC contribution to the total energy are calculated, as expectation value of the SOC Hamiltonian (Eq. 2.45), via non self-consistent diagonalization in the Kohn-Sham eigenstate basis[69]. Still, at least four configurations are required since the magnetic configurations are not all independent (all in-plane configurations are linear combination of each others) and the contributions from the isotropic part of the Hamiltonian are still unknown. In Fig. 3.4 are shown some examples of collinear magnetic configurations used for computational screening in Paper IV. If N_{AFM} is the number of nearest neighbour with AFM coupling and N_{FM} is the number of of nearest neighbour with FM coupling in the anti-ferromagnetic configuration (i.e. 4 and 2 respectively for system in Fig.3.2(d)), it is easy to see that Heisenberg parameters can be extracted as (see Paper IV):

$$\begin{aligned} A &= \frac{\Delta E_{FM} \left(1 - \frac{N_{FM}}{N_{AFM}}\right) + \Delta E_{AFM} \left(1 + \frac{N_{FM}}{N_{AFM}}\right)}{2S^2} \\ B &= \frac{\Delta E_{FM} - \Delta E_{AFM}}{N_{AFM}S^2} \\ J &= \frac{E_{AFM}^{\parallel} - E_{FM}^{\parallel}}{N_{AFM}S^2} \end{aligned} \quad (3.24)$$

with $\Delta E_{FM(AFM)} = E_{FM(AFM)}^{\parallel} - E_{FM(AFM)}^{\perp}$ being the energy differences between in-plane and out-of-plane spin configurations.

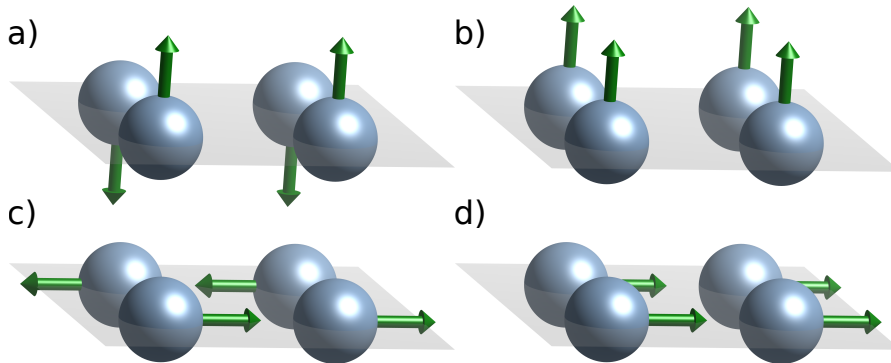


Figure 3.4: **Collinear magnetic configurations.** Examples of spin configurations for the calculation of Heisenberg parameters A , B and J : (a) out-of-plane anti-ferromagnetism, (b) out-of-plane ferromagnetism, (c) in-plane anti-ferromagnetism, (d) in-plane ferromagnetism. Figure from Paper IV.

CHAPTER 4

Monte Carlo methods

Monte Carlo methods are a class of powerful and widely used tools in computational analysis. Originally developed in the beginning of last century for estimating integrals over poorly-behaving functions and high-dimensional domains, they rapidly spread and been successfully applied to a broad variety of problems, including simulation of physical phenomena and the proprieties of ensembles[77, 78]. The name is inspired by a famous Casino in Monaco, but the older name of "*statistical sampling*" coined by Nicolas Metropolis in the early 50s is more revelatory: the method consists in repeated random sampling in order to solve numerical estimations of unkonwn parameters. A famous example is the approximation of π by tossing N number of times a needle of lenght d to the floor, ruled with parallel lines at a distance d apart. If M is the number of times the needle lands on one of those line, from geometrical argument it follows that $\pi = \lim_{N \rightarrow \infty} \frac{2NI}{Md}$. With the advent of modern computers, numerical methods took a big leap forward and they are still effectively used, sometimes being the only tractable approach. For example, while the Ising model is exactly solvable in 1D and 2D, no exact solution is available in 3D and numerical simulations are required.

In this chapter we introduce the theory behind the Monte Carlo methods generally used to solve statistical physics problems. We then describe the implementation of the Metropolis algorithm for systems based on the Ising/Heisenberg model and some test results we run to optimize our calculations time and accuracy-wise. The code has been written in language Python[79].

4.1 Principles of Monte Carlo simulations

In statistical physics, the goal is typically to calculate the expectation value $\langle Q \rangle$ of some observable Q of a system. This is done by averaging the values Q_μ over all the possible states μ with energy E_μ , weighted by the Boltzmann distribution:

$$\langle Q \rangle = \frac{\sum_{\mu} Q_{\mu} e^{-\beta E_{\mu}}}{\sum_{\mu} e^{-\beta E_{\mu}}} \quad (4.1)$$

where $\beta = \frac{1}{k_B T}$ is the thermodynamic beta (k_B being the Boltzmann constant) at temperature T . The denominator is the partition function Z of the system. When dealing with very big systems or when statistical proprieties are relevant, the number of states increases rapidly and a complete analytical solution is often unreasonable to obtain. A 3D Ising model system with just $10 \times 10 \times 10$ binary states counts $2^{1000} \sim 10^{301}$ states to evaluate. Monte Carlo methods operate by randomly sampling only a subset of states M from some probability distribution p_{μ} . The expectation value is then rather called *estimator* Q_M and, even if it inherently introduces inaccuracy, it becomes more and more accurate as the chosen subset is extended or qualitatively improved. Eq. 4.1 then becomes

$$Q_M = \frac{\sum_{i=1}^M Q_{\mu_i} p_{\mu_i}^{-1} e^{-\beta E_{\mu_i}}}{\sum_{j=1}^M p_{\mu_j}^{-1} e^{-\beta E_{\mu_j}}} \quad (4.2)$$

and $Q_M \rightarrow \langle Q \rangle$ for $M \rightarrow \infty$. In Eq. 4.2, p_{μ_i} are the probability distribution from which we randomly choose the subset $\{\mu_1, \dots, \mu_M\}$ of states. The Monte Carlo method proves to be particular efficient when the system is spending the majority of its time in a small number of states since it provides a technique for picking those dominating states which contribute the most to the averages and ignoring the others (*importance sampling*). A natural choice for p is the Boltzmann distribution

$$p_{\mu} = Z^{-1} e^{-\beta E_{\mu}} \quad (4.3)$$

for all states, so that

$$Q_M = \frac{1}{M} \sum_{i=1}^M Q_{\mu_i} \quad (4.4)$$

This solution simplifies the expression for the estimator since the knowledge of the partition function Z (and thus an overview of all the possible states) is not necessary anymore, but it doesn't provide any suggestions on how to efficiently generate the trial states. A common strategy is to consider small energy fluctuations, meaning that trial states should differ from the present state only by a small random perturbation.

Indeed, the application of Monte Carlo simulations on a system hinges on the idea of repeatedly choose new random trial states, which differ from the initial one by small random changes, and then accepting or rejecting them according to some criteria. The sequence of accepted states forms a *Markov chain* in the phase space of the system since the *transition probability* $P(\mu \rightarrow \nu)$ of moving from one state μ to following state ν is invariant in time and depends only on the proprieties of the current state and not on any prior events.

The choice of P should fulfill the condition of *ergodicity*, which is the requirement that any state ν is accessible starting from any other state μ in a finite number of steps, as long as their Boltzmann weights are non-zero. This allows the system to fully explore all the possible states, at least in theory. In most cases, another requirement is also the condition of *detailed balance*, that assures that the system, once it reaches the equilibrium, is indeed represented by the chosen distribution (in this case Boltzmann distribution). It is mathematically expressed as the condition:

$$p_\mu P(\mu \rightarrow \nu) = p_\nu P(\nu \rightarrow \mu) \quad (4.5)$$

Left-hand side is the probability of being in a state μ multiplied by the transition probability of moving from initial state μ to final state ν , thus Eq. 4.5 also shows how the rate at which the system makes transition into and out any state is equal. This generally prohibits the generation of limit cycles, that occurs when the probability of a subset of states changes in a cyclic pattern.

If we require that the final distribution must be a Boltzmann distribution, we obtain from Eqs.4.5 and 4.3 that P should fulfill

$$\frac{P(\mu \rightarrow \nu)}{P(\nu \rightarrow \mu)} = \frac{p_\nu}{p_\mu} = e^{-\beta(E_\nu - E_\mu)} \quad (4.6)$$

Another constrain on P is the sum rule

$$\sum_{\nu} P(\mu \rightarrow \nu) = 1 \quad (4.7)$$

which simply assures the process to actually generate some state ν (which in theory can still be the initial state μ).

In any Monte Carlo method is possible to split the transition probability $P(\mu \rightarrow \nu)$ into two functions:

- *selection probability* $g(\mu \rightarrow \nu)$, which gives the probability of generating the new state ν to evaluate
- *acceptance ratio* $A(\mu \rightarrow \nu)$, the probability of accepting the new state ν once it has been generated.

In the next section we show one of the most popular solution, with a very simple but powerful algorithm.

4.2 Metropolis algorithm

The constraints outlined in Eqs. 4.6, 4.7 and the requirements of ergodicity, guarantee that the equilibrium distribution of states is the Boltzmann distribution but leave enough room in choosing the

transition probabilities. The most famous and widely applied Monte Carlo algorithm is the **Metropolis algorithm**, introduced in 1953 by Nicolas Metropolis on simulation of rigid-sphere gases[80]. In a Metropolis algorithm the selection probabilities are set to be all equal. For an Ising system with N spins then

$$g(\mu \rightarrow \nu) = \frac{1}{N} \quad (4.8)$$

meaning that, assuming a single-spin-flip dynamics, starting from an initial state μ there are N possible trial states ν we can reach (where a single spin is flipped). To fulfill the condition of detailed balance, we write

$$\frac{P(\mu \rightarrow \nu)}{P(\nu \rightarrow \mu)} = \frac{A(\mu \rightarrow \nu)}{A(\nu \rightarrow \mu)} = e^{-\beta(E_\nu - E_\mu)} \quad (4.9)$$

If A is too low, we will hardly move to any new states. To make the model as efficient as possible, we need to maximise the acceptance ratio. This can be done by setting to 1 the largest of the two acceptance ratios in the mid part of Eq. 4.9 (i.e. the denominator if $E_\mu \leq E_\nu$) and adjust the other so that the last equality holds. This finally leads to the Metropolis algorithm

$$A(\mu \rightarrow \nu) = \begin{cases} e^{-\beta\Delta E}, & \text{if } \Delta E \geq 0 \\ 1, & \text{otherwise} \end{cases} \quad (4.10)$$

where $\Delta E = E_\nu - E_\mu$. Once the temperature T is set, the sequence of instructions implemented is summarize in the following box

Metropolis algorithm

1. Initialize the system with a random spin configuration.
2. Flip a spin at random site i into a new random spin orientation.
3. Calculate the energy difference ΔE between the old and the new configuration.
4. Generate a random number $0 < k < 1$.
5. Accept the new configuration only if $\exp -\frac{\Delta E}{k_B T} > r$.
6. Go back to 2.

Despite the spread use of the word "random", results are very meaningful. However, the choice of parameters in actual simulations is crucial in order to optimize the efficiency, speed and accuracy of the algorithm.

4.3 Implementation

To actually perform simulation of spin models, we first define a lattice of spins. In this work we focus on 2D spin lattice with a triangular (also called hexagonal), honeycomb and square geometry (see Fig. 4.1), which mimic the most common 2D magnetic lattice in of real samples. The exact positions of the magnetic ions are not important since the number of nearest neighbours is enough to define the geometry of the systems. The nominal value of the spin S is usually calculated from first principles calculations of the ground state. In the same way Heisenberg parameters such as exchange coupling J and anisotropic terms can be extracted from Energy Mapping analysis, as explained in previous chapters. The setting for a Monte Carlo simulations requires

- initial spin configuration: typically a random spin orientation (with vectors free to rotate around the unit sphere) or ferromagnetic orientation.

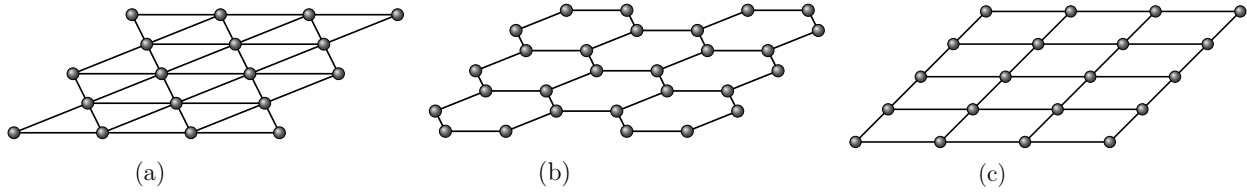


Figure 4.1: **2D lattices.** Two-dimensional lattices used in this work for Monte Carlo calculations: (a) triangular (also called hexagonal), (b) honeycomb and (c) square lattice.

- size of the system: defined as the number of spins in the lattice ($N \times N$). Periodic boundary conditions are implemented, meaning that spins at the edge of the lattice are neighbours and thus interact with the corresponding spins on the opposite edge of the system. This also means that the system is completely translationally invariant, but may trigger spurious finite size effect for systems smaller than spins' correlation lengths. Finite size effects are inevitable in any simulations. However, they become negligible in most cases when N is chosen to be big enough.
- number of steps: the algorithm should run for a period long enough for the system to reach equilibrium: it critically depends on size of the system and complexity of the model.
- final averaging: at the end of the simulation, a certain number of final steps in the Markov chain are averaged to yield smoother results.

The choice of the starting state shouldn't be of particular importance since, thanks to the ergodicity condition and assumed a sufficient number of steps, all initial states would eventually lead to the same ground state. However, a not uncommon problem when the system is initialized with a random spin configuration is the formation of nonphysical spins clusters, each pointing in opposite directions. In Fig. 4.2 is shown an example for ferromagnetic Ising model with square geometry. Spin up and down are represent by white and black boxes. At finite temperatures $T < T_C$, only spin flips at the edge of clusters are generally accepted (i.e the spin inside the red box labeled with 2) since the energy fluctuation is lower: $\Delta E = -2J - (2J)$. Conversely, flipping a spin inside the cluster (as the spin labeled with 1) leads to a bigger energy fluctuation $\Delta E = -8J - (8J)$. With temperature $T > 0$ at which N anti-ferromagnetic couplings are "tolerated", a phase separation may occur and splits the system in half. The simulation is stuck around a local minimum and the order parameter, typically the average magnetization $\sum_i s_i / N^2$ drops to zero at $T \neq T_C$. A remedy designed for Ising model is the

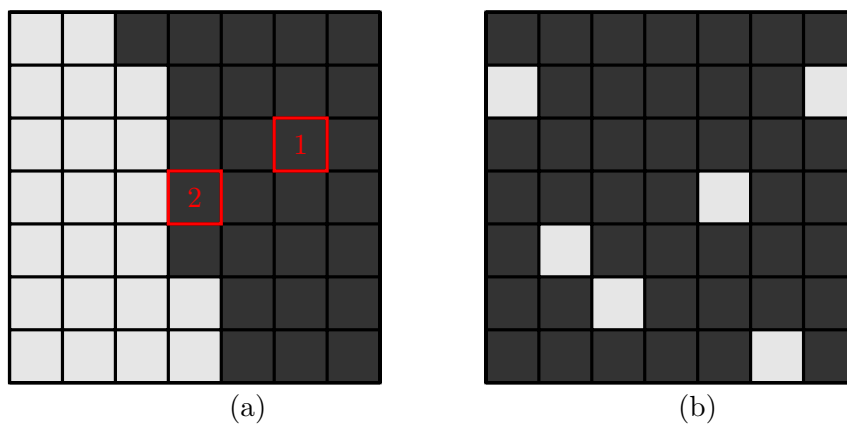


Figure 4.2: **Ising model.** Example of phase splitting in Ising model: the two systems have a similar energy since the number of AFM interactions is roughly the same and connected to the temperature T . However the magnetization M is close to zero for the first one and has a finite value for the second. For $T < T_C$, a MC simulations may be stuck with a phase splitting configuration, since only spins at the edge boundaries are likely to be flipped.

Wolff algorithm[81], in which a cluster of neighbouring spins pointing in the same directions is flipped as a whole instead. An analogous version for Heisenberg and other continuous models is given, but a simpler and effective solution is starting with an ferromagnetic configuration at $T = 0$. Alternatively, a small anisotropy in one direction (simulating a Zeeman interaction with an external magnetic field) breaks the out-of-plane symmetry, defining a privileged direction and shrinking clusters pointing in the opposite one. For temperature scans simulations, *temperature annealing* has also been implemented, where the final equilibrium configuration for a certain temperature is used as starting configuration for the successive temperature, simulating real experiments.

4.3.1 Code testing

In practical, along the real system X under investigation, another twin system X' with the same size is initialized. In the algorithm 4.2, steps (2)-(6) loop over all spins $X'(i')$ of the auxiliary system. At each loop, it picks a random site i of the primary system and applies the spin flip $X(i) \rightarrow X'(i')$. This is often called a MC *move*. It then evaluates the energy difference, keep the new configuration according to step (5) and repeat for site $i' + 1$ of the auxiliary system. To guarantee that each spin has a chance to be flipped, a complete MC step is to be considered as a complete swept of all sites in auxiliary system (meaning a number of MC moves equal to the size $N \times N$).

In Fig. 4.3 some equilibrium configurations are shown from a test on a 12x12 Heisenberg square systems. Color code is for the out-of-plane component of each spin while the in-plane arrows are the projected x and y components. As expected, systems with higher anisotropy A/J have higher critical temperatures and support magnetic order for longer.

We tested the code against a simple case where analytical evaluation is easily obtainable, namely when the exchange coupling is the only non zero parameter in the model. For a system with only two spins \mathbf{S}_1 and \mathbf{S}_2 , then the energy depends only on their relative orientation. The partition function is written as

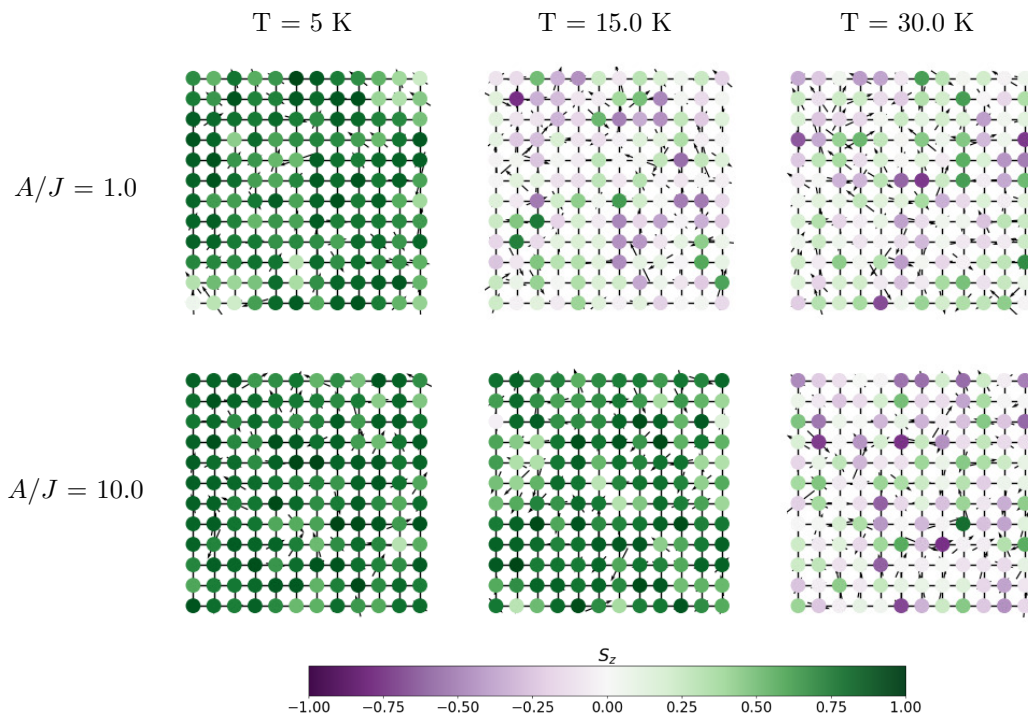


Figure 4.3: **MC on Heisenberg Model.** MC equilibrium configurations for square Heisenberg systems with different degree of anisotropy A/J at different temperature. At each site, the color indicates the z-component of the spin while the arrows are the normalized in-plane components.

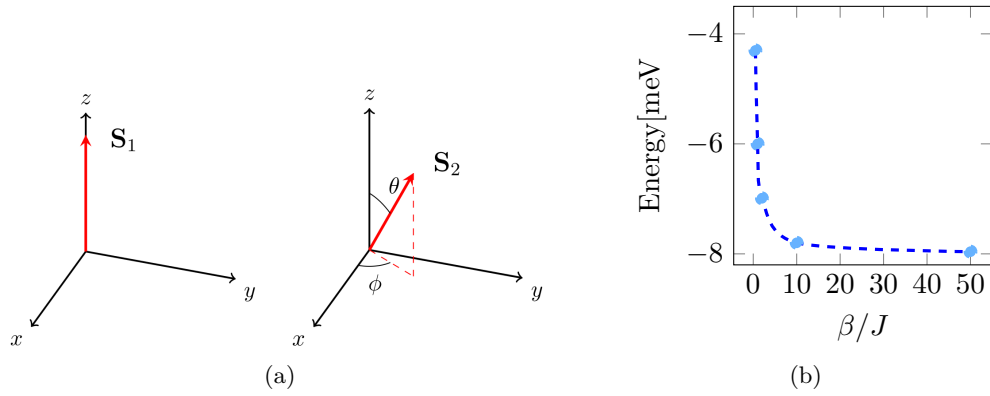


Figure 4.4: **Testing MC against analytical results.**(a) The energy of isotropic Heisenberg model depends only on the coordinated of one spin \mathbf{S}_2 respect to another \mathbf{S}_1 . (b) Results from MC calculation (scatter plot) over the predicted behavior of energy as a function of temperature (dashed line).

$$Z = 4\pi \int_0^\pi d\theta \sin \theta \int_0^{2\pi} d\phi \exp^{-J\beta \cos \theta} \quad (4.11)$$

where (θ, ϕ) are angles of \mathbf{S}_2 in spherical coordinate system (as in Fig. 4.4(a)) and $\beta = \frac{1}{k_B T}$ is the thermodynamic beta. The integral over ϕ brings another factor 2π while for the integral over θ we can substitute the variable $x = \cos \theta$:

$$Z = 16\pi^2 \frac{\sinh J\beta}{J\beta} \quad (4.12)$$

The energy is then found as

$$E = -\frac{\partial}{\partial \beta} \ln Z = J \left(\frac{1}{J\beta} - \coth J\beta \right) \quad (4.13)$$

For a square lattice with periodic boundary conditions, each coupling has an extra factor 4 which leads to

$$E = zJ \left[\frac{1}{4J\beta} - \coth zJ\beta \right] \quad (4.14)$$

where z is the coordination number of the system. Renormalized energies at different temperatures from MC simulation are shown in Fig. 4.4 and show good agreement with the analytical results.

Finally in Fig. 4.5 are shown additional tests that asses what already commented in previous pages.

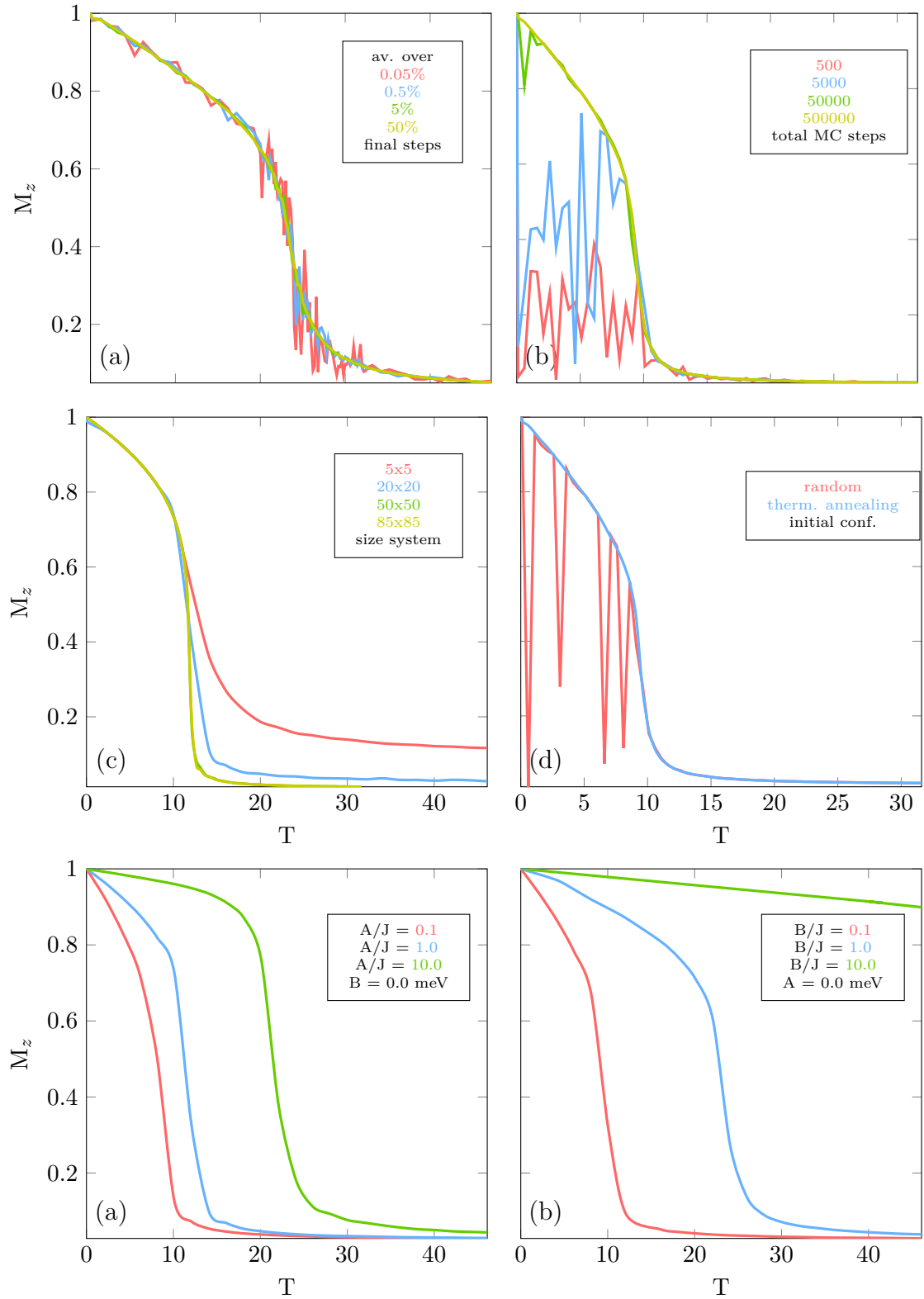


Figure 4.5: **Monte Carlo testing.** Magnetization curves obtained for MC simulations on square systems, varying (a) the number of last steps to average over, (b) the total number of MC steps, (c) the size of the system and (d) initial configuration for each value of T . The value of critical temperature is generally not affected, but smoother and best results are obtained increasing the number of MC steps, overaging over a large number of final steps, larger systems and a thermal annealing approach. The Heisenberg parameters are $J = 1$ meV, $S = 1$, $B = 0.0$ meV and $A = 1.0$ meV (for (a) and (c)) or $A = 0.1$ meV (for (b) and (d)). Magnetization curves obtained for MC simulations on 25x25 square systems, varying (e) A/J and (f) B/J . The stronger influence of anisotropic exchange B on the robustness of the magnetic order is due to the coordinate number z that prevent flip-back when the order is reached. Furthermore, over a certain value it behaves as a effective Ising model which is known to pose an upper bound for the persistence of magnetic order in spin lattices.

CHAPTER 5

Summary of the results

5.1 Paper I: Calculating critical temperatures for ferromagnetic order in two-dimensional materials

In this paper we test our methods, using tools of chapter 3 and 4. The main idea is to evaluate the predictive power for critical temperature in magnetic systems, based on the descriptor spin-wave gap Δ and classical Monte Carlo calculations. We then benchmark it with the available experimental data, in particular critical temperature for monolayer CrI_3 . In particular, the Curie temperature of the bulk crystal decreases from 61 K to 45 K when the monolayer limit is reached[17, 82].

The spin-wave gap Δ of a system is the energy gap between the ferromagnetically ordered ground state and the first excited state. As we have seen in the second chapter, this is a collective out-of-phase precession of spins around the ground state privileged direction. The emergent phenomenon is a spin-wave and the associate bosonic pseudo-particle is called magnon. The starting point is the anisotropic Heisenberg Hamiltonian

$$H = -J \sum_{\langle ij \rangle} J \mathbf{S}_i \cdot \mathbf{S}_j - A \sum_i (S_i^z)^2 - B \sum_{\langle ij \rangle} S_i^z S_j^z \quad (5.1)$$

The isotropic part can be written in terms of HP operators as

$$H = -2J \sum_{\langle ij \rangle} \left[(S - b_i^\dagger b_i)(S - b_j^\dagger b_j) + S b_i^\dagger \left(1 - \frac{b_i^\dagger b_i}{2S}\right)^{1/2} \left(1 - \frac{b_j^\dagger b_j}{2S}\right)^{1/2} b_j + \right. \\ \left. + S b_i^\dagger \left(1 - \frac{b_i^\dagger b_i}{2S}\right)^{1/2} b_i b_j^\dagger \left(1 - \frac{b_j^\dagger b_j}{2S}\right)^{1/2} \right] \quad (5.2)$$

If we expand the square roots in terms of $1/S$ it reads

$$H = -NzJS^2 + 2JS \sum_{\langle ij \rangle} (a_i^\dagger a_i + a_j^\dagger a_j - b_i^\dagger a_j - a_i a_j^\dagger) \\ - 2J \sum_{\langle ij \rangle} \left[a_i^\dagger a_i a_j^\dagger a_j - \frac{1}{4}(a_i^\dagger a_i^\dagger a_i a_j + a_i^\dagger a_j^\dagger a_j a_j) \right. \\ \left. + a_i^\dagger a_i a_i a_j^\dagger + a_i a_j^\dagger a_j^\dagger a_j \right] + \dots \quad (5.3)$$

which in Paper 1 is rewritten as

$$H = E_0 + S\tilde{H}_0 + \tilde{H}_1 + \frac{1}{S}\tilde{H}_2 + \dots \quad (5.4)$$

The contributions of anisotropic terms are only in E_0 , \tilde{H}_0 , and \tilde{H}_1 :

$$\begin{aligned}
-A \sum_i (S_i^z)^2 &= -A \sum_i (S - a_i^\dagger a_i) (S - a_i^\dagger a_i) = -ANS^2 - A \sum_i (n_i^2 - 2Sa_i^\dagger a_i) \\
-\frac{1}{2}B \sum_{ij} S_i^z S_j^z &= -\frac{1}{2}B \sum_{ij} (S - a_i^\dagger a_i) (S - a_j^\dagger a_j) = -\frac{BNS^2 z}{2} - \frac{1}{2}B \sum_{ij} (a_i^\dagger a_i a_j^\dagger a_j - Sa_i^\dagger a_i - Sa_j^\dagger a_j)
\end{aligned} \tag{5.5}$$

with z being the number of nearest neighbours for each lattice site.

After Fourier transformation, and assuming non-interacting magnons (neglecting \tilde{H}_1 and any higher order terms), the spin-wave gap Δ can be obtained as the energy difference between the fully-polarized FM ground state ($n_{\mathbf{k}} = 0$ for any $\mathbf{k} > 0$) and the energy of the system with one magnon shared by the entire lattice ($n_{\mathbf{k}} = 1$). The Mermin-Wagner theorem states that no energy-gap is open by isotropic part, while terms 5.5 contribute with

$$\Delta = A(2S - 1) + SBz \tag{5.6}$$

Eq. 5.6 can be seen as a generalization of the measure of out-of-plane MA in the system, when both single-ion anisotropy A and anisotropic exchange coupling B parameters are non-vanishing. For the Marmin-Wagner theorem, we thus expect long range ferromagnetic order at finite temperature only when $\Delta > 0$. Having set $J_{ij}^x = J_{ij}^y = 0$ in Eq. 2.43, we are assuming zero in-plane anisotropy (or negligible). For 2D systems this is often a good approximation but for some geometries, i.e. when magnetic ions do not form a flat lattice, this is not always true (see section 5.4 and section 3.8 in Paper IV).

The term $(2S - 1)$ reduces to $2S$ if a full quantum renormalization of the anisotropic interactions is derived in spin-wave theory[18, 83]. In the limit $S \rightarrow \infty$ they both converge to the result. However, we decided to be consistent with the classical treatment of Heisenberg model in Energy mapping analysis (sec.3.4), where S are considered as simple vectors. It follows that for $S = \frac{1}{2}$ systems, the spin-wave gap can be opened only by anisotropic exchange interactions. For a specific system, Energy Mapping analysis allows to calculate all the Heisenberg parameters in Eq. 5.1 by a comparison of the energies of different magnetic configurations obtained with DFT calculations, as described in sec. 3.4. We stress the importance of comparing energies between magnetic configurations with the same relaxed structures, so to address any energy difference to magnetic interactions only. The value of S can be obtained from DFT calculations, integrating the spin-polarized charge density over the entire unit cell of the ferromagnetic ground state

$$2S = \int_{FM} |m_\uparrow(d\mathbf{r}) - m_\downarrow(d\mathbf{r})| d\mathbf{r} \tag{5.7}$$

where k is the number of magnetic ions. The integral gives the number of unpaired electrons in the unit cell, each of whom carrying $s=1/2$ intrinsic angular momentum. Thus dividing by 2 we obtain the total spin sitting at each magnetic ions. As already mentioned, this is true for insulating systems, where electrons are bound to the atomic site and S has an integer or semi-integer value. In case the density of states is not zero at the Fermi surface, i.e. in metals, electrons are free to move around the lattice and the number of localized interacting particles is not well defined.

With these parameters we run classical MC simulations at different temperatures and identified the critical one (see Fig. 5.1(a)). In Fig. 5.1(b), critical temperatures for three different lattices (square, honeycomb and hexagonal) are plotted and fitted in function of the A/J in systems with $B = 0$ meV. It is easy to see that the limit for high degree of anisotropy is the Ising limit (dashed lines at T_C^{Ising} for any specific geometry), which provides a tabulated[84] upper bound for T_C .

On the other hand, the limit for $B \rightarrow \infty$ (assuming $A = 0$ meV) is an Ising model with increasing effective exchange $\frac{B+J}{2}$ (not shown here). This is straightforward for $S = 1/2$ systems, where S^z can only assume one of the two values $S^z = 1/2, S^z = -1/2$. In case of $S > 1/2$, the effective values of S is re-scaled to take into account the presence of in-between states, i.e. neutral states $S^z = 0$. Fittings of critical temperatures leads to the semi-empirical equation for T_C

$$T_C = T_C^{Ising} f\left(\frac{\Delta}{J(2S-1)}\right) \quad (5.8)$$

As long as Heisenberg parameters are known, Eq. 5.8 allows to calculate the critical temperature of any 2D systems with simple magnetic lattice. However, when $S = 1/2$, function f is not well defined and custom-built MC simulations are required. Another drawback is that for metallic systems, the Heisenberg model is not a suited theoretical framework and we expected less reliable predictions. However, Eq. 5.8 is a major improvement than mean-field theory derivations [38](typically used for bulk systems and neglecting MA). Moreover, it is based on MC simulations of Heisenberg model, which seems to soundly embed magnon-magnon interactions effects, neglected in the derivation of Δ .

Indeed, while being a good guess at low energies, they should be taken into account when we the system is in the nearby of a finite T_C . To benchmark MC results, we tested it against a well-known approach. The *Random Phase Approximation*[38] provides an approximation of the magnon-magnon interactions present in \tilde{H}_1 . When anisotropy is included in the system, a mean-field treatment of the 4-operators terms leads to a temperature-dependent reduction of the dispersion relation at small \mathbf{k} , that needs to be calculated self-consistently. This is reflected in the derivation of the effective magnetization as well, from which we can extract the critical temperature. However, due to the mean-field approximation effects, it fails to reproduce Ising-like models with high degree of out-of-plane anisotropy. We thus expect the MC-based method to be accurate and reliable when the system is a ferromagnetic insulator, and with the right awareness, to yield reasonably sensitive predictions for metals. We test our model investigating monolayer CrI_3 . Since the recent synthesis and the observation of out-of-plane Ising-like intralayer ferromagnetism and interlayer anti-ferromagnetism, it attracted a lot interest. Many theoretical works contributed in elucidating the origin of its magnetism, commonly attributed to an interplay between SOC-enhanced single-ion anisotropy and super-exchange interactions mediated by iodine atoms [83, 85, 86, 87, 88]. Magnetic moment of $3\mu_B$ are localized at Cr atoms, arranged on a honeycomb lattice, are the only ones contributing to the total magnetic moment. In addition, it is also an insulator, having an optical band gap of ≈ 1 meV both in the FM and AFM ground state.

In the second part of the paper we calculated its critical temperature and investigated the effects of Hubbard corrections which we briefly summarize.

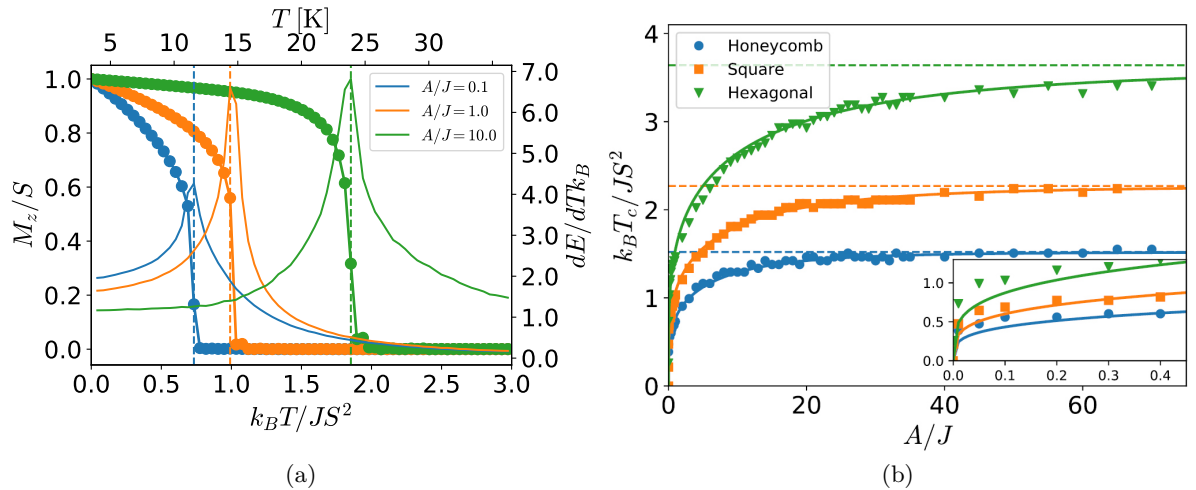


Figure 5.1: **Critical temperature from MC calculations on anisotropic systems.** (a) Magnetization and heat capacity as a function of temperature for the square lattice with three different values of A/J . The critical temperatures are indicated by dashed vertical lines. (b) Critical temperature as a function of scaled anisotropy A/J calculated with classical Monte Carlo simulations for the honeycomb, square, and hexagonal lattices with ferromagnetic exchange. The solid lines are obtained from the empirical fitting. The Ising limit is indicated by dashed lines for the three lattices. Figures from Paper I.

If we extend Eq. 5.1 to higher neighbouring orders, we get

$$\begin{aligned}
 H = & -J_1 \sum_{\langle ij \rangle} \mathbf{S}_i \cdot \mathbf{S}_j - J_2 \sum_{\langle\langle ij \rangle\rangle} \mathbf{S}_i \cdot \mathbf{S}_j - J_3 \sum_{\langle\langle\langle ij \rangle\rangle\rangle} \mathbf{S}_i \cdot \mathbf{S}_j \\
 & - A \sum_i (S_i^z)^2 - B \sum_{\langle ij \rangle} S_i^z S_j^z
 \end{aligned} \tag{5.9}$$

where J_n is the exchange coupling between lattice coupled of n -nearest neighbouring sites, for honeycomb lattice showed in Fig. 5.5(a). In order to calculate N parameters, $N+1$ independent magnetic configurations are needed, and typically bigger unit cells. Here we evaluated 6 magnetic configurations (1 FM and 5 AFM) on a 2×2 unit cell. The evaluation critically depends on the choice of magnetic configurations, as showed in Fig. 5.2. A sensible choice for converged results is to include the FM and fully AFM configurations when possible. Results can be found in section 3.3 of Paper I. Energy mapping analysis on Eq. 5.9 leads to $J_1 = 2.3$ eV, $J_2 = 0.4$ eV, $J_3 = -0.1$ eV, while for a Eq. 5.1 we obtain $J_1 = 2.2$ eV. Anisotropic terms are of the order of 0.1 meV, which bring to a fairly robust $\Delta \approx 1$ meV and a critical temperature of 32 K. An Hubbard correction increases the value of Δ and for $U = 2$ eV we obtain $T_C = 42$ K, in good agreement with experimental value of 45 K[17]. In general we expect that the inclusion of higher order exchange coupling may yield to more realistic MC simulations, but in this case J_2 and J_3 are much smaller than J_1 and, although they influence the shape of the simulated magnetization curve, they provide comparable T_C (Fig.5.5).

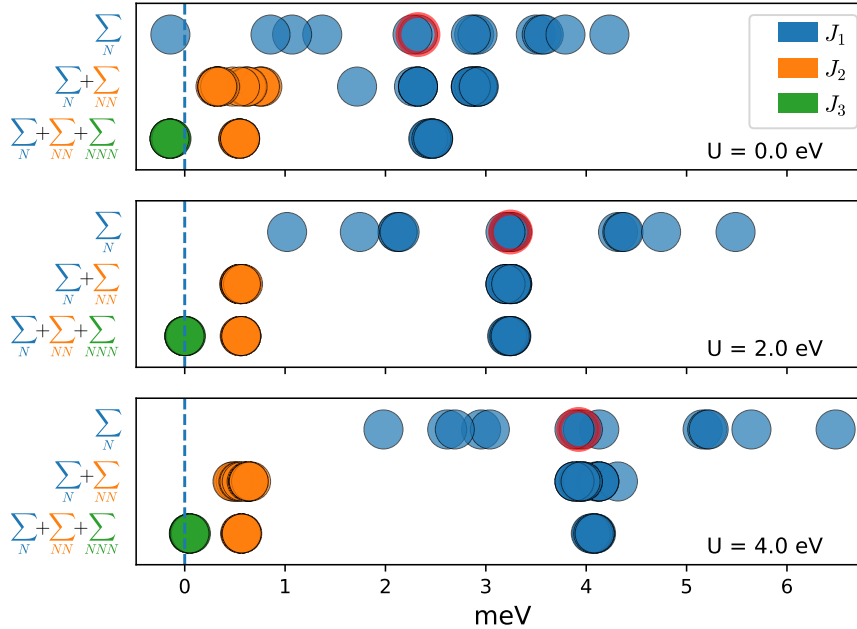


Figure 5.2: **Exchange couplings dependence on Hubbard terms.** Each graph represents evaluation of exchange parameters from DFT+U ($U = 0, 2, 4$ eV). In a graph, each circle stands for the calculation of an exchange coupling parameter (blue for nearest neighbours coupling J_1 , orange and green for second and third order couplings J_2 and J_3) for an Heisenberg model including only nearest neighbour J_1 (top row), next-nearest neighbour J_2 and next-to-the-next-nearest neighbour J_3 coupling. Red circles indicate J_1 couplings from FM and fully AFM configurations.

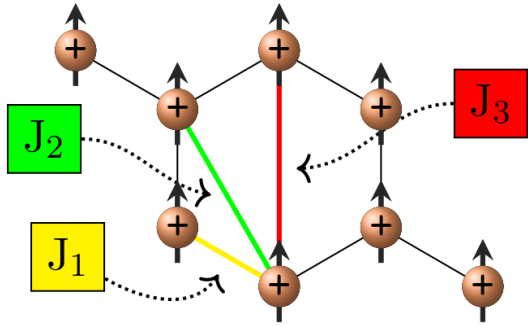


Figure 5.3: (a)

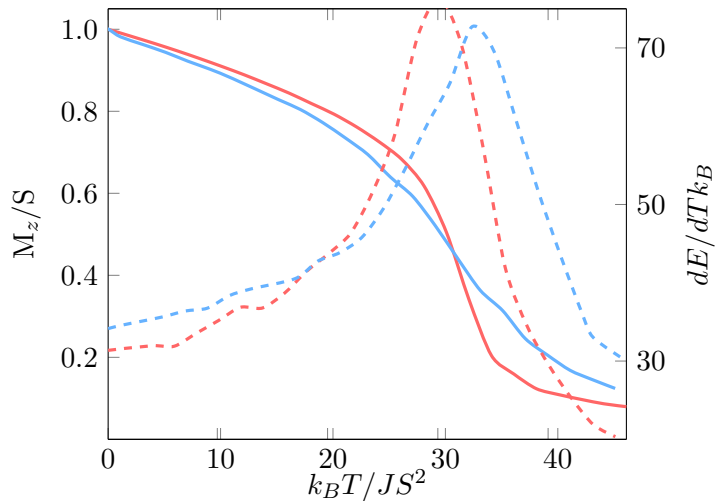


Figure 5.4: (b)

Figure 5.5: **Effect of J_2 and J_3 .** (a) Nearest J_1 , next-nearest J_2 and next-to-the-next nearest neighbours path in honeycomb magnetic lattice. Each site has 3 J_1 paths, 6 J_2 paths and 3 J_3 paths. (b) Magnetization curves and heat capacity obtained from MC simulations with (red) only nearest neighbour interactions and (blue) including next and next-to-the-next nearest neighbours with parameter for monolayer CrI_3 obtained from Energy Mapping analysis.

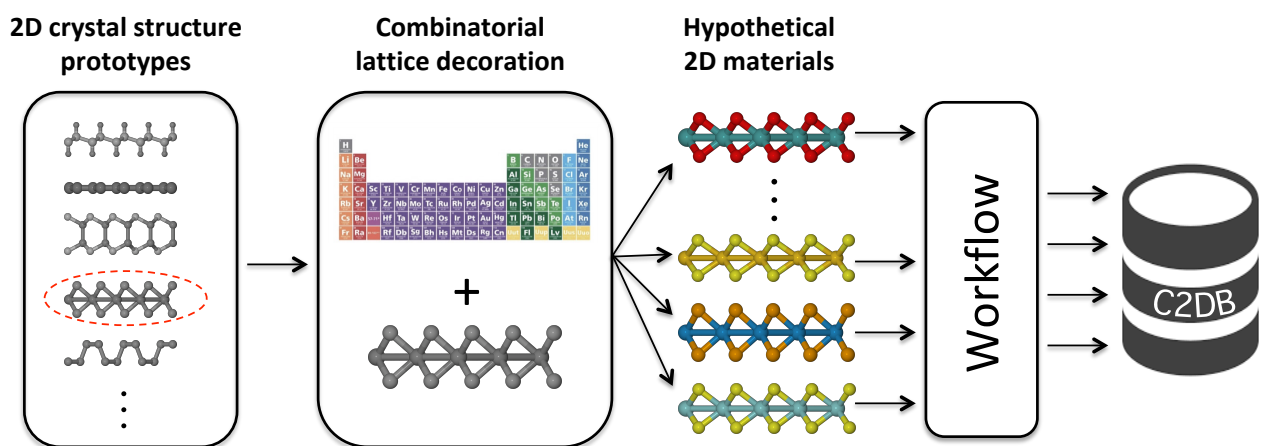
5.2 Paper II: The Computational 2D Materials Database: high-throughput modeling and discovery of atomically thin crystals

This paper is the result of the collective effort of many researchers at CAMD and an on-going project which aims to extend the tools developed, also at one and three-dimensional systems. In this section I will only shortly comment the key concepts behind it and some results relative to magnetic proprieties. Additional information can be found in Paper II and [89, 90].

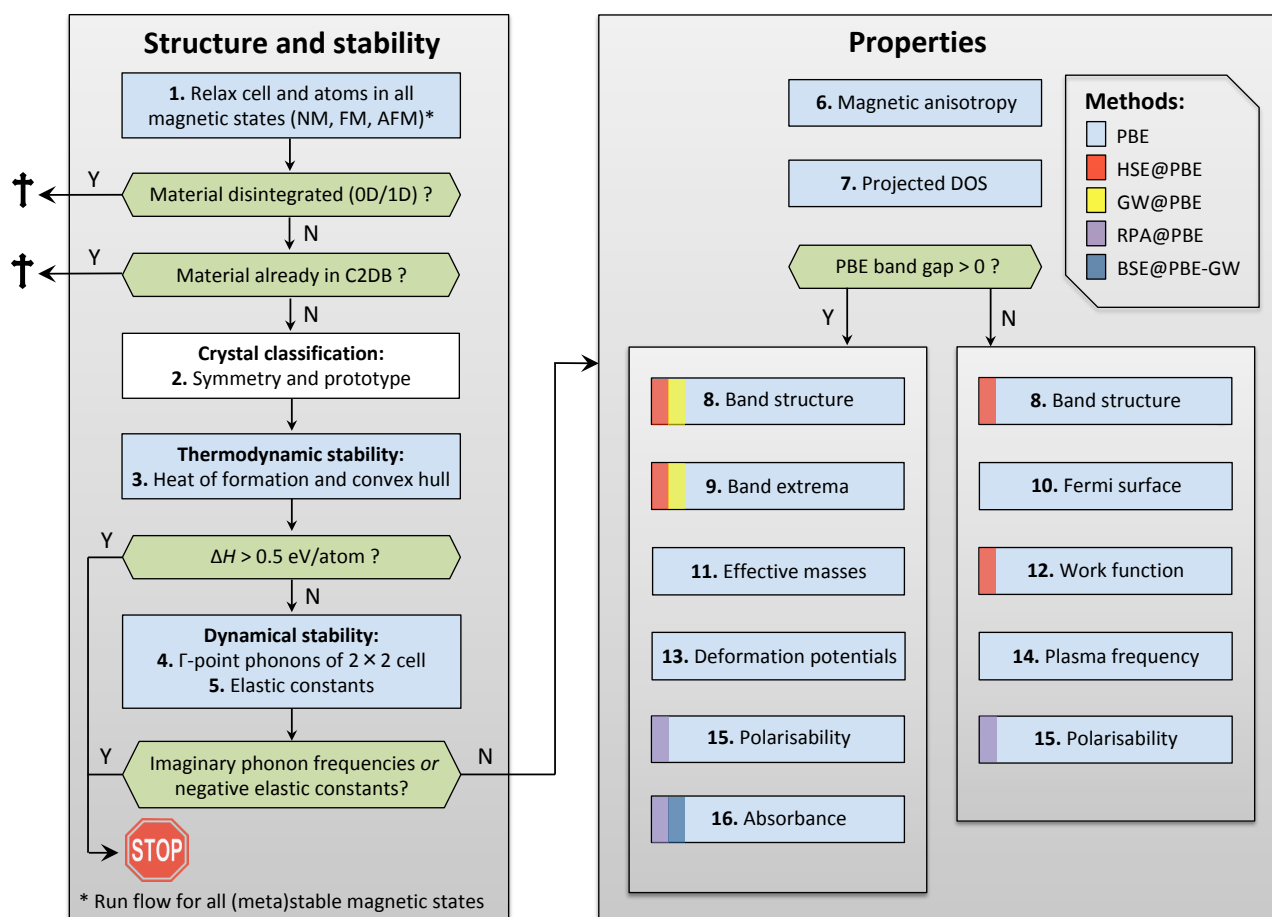
The main purpose of the Computational 2D Materials Database (C2DB) is to gather in a single and freely accessible online depository[90], data as accurate as possible about 2D materials calculated from first-principle methods. Thus, C2DB is an encyclopedia of 2D systems[89] which lists geometrical, thermodynamic, elastic, electronic, magnetic and optical proprieties, aiming mostly at accuracy and consistency of results rather than volume. Over time it evolved into the creation of an efficient and stable computational workflow which runs in a mostly automated routine, also thanks to the creation and integration of *myqueue*[91], a Linux command-line interface for the handling of computational tasks and collection of data.

This permitted a relative fast gathering of data for almost 2000 materials primarily classified by their prototype, namely in terms of the Wickoff sites of the atoms within the unit cell, and the magnetic phase. Prototypes are inspired by experimentally known and stable monolayers, such as graphene, or layered Van der Waals materials which has not been exfoliated yet. In Paper II they are generally referred and named after the most iconic or academically relevant representative.

Nowadays, roughly 50 2D materials are experimentally available but many more are expected to be stable once deposited or mechanically exfoliated from their bulk version. The process which generates novel hypothetical 2D structures and thus may the next ones to be synthesized is showed in Fig. 5.6(a). The bare prototypical atomic arrangements are decorated with a new set of elements, chosen among similar ones to maximise the change of having similar proprieties, i.e. a dynamical and thermodynamical stable ground state. In Fig. 5.6(a) is showed the example of MoS_2 , a vastly studied 2D material that can be obtained by Chemical Vapor Deposition (CVD)[92, 93] or mechanical exfoliation[94]. Among others, it gained a lot of interest for application due to its semiconducting optical



(a)



(b)

Figure 5.6: **C2DB apparatus**. (a) The main process providing data into C2DB: it starts with the identification of bare prototypical 2D structures (from experimentally known examples or designed by intuition), which are subsequently decorated by combinatorial methods. Finally the (c) computational workflow calculates, analyses and gathers relevant data into a (local or online) depository. Pictures from Paper 2.

direct-gap[95] and strong spin-orbit coupling[96]. The "combinatorial lattice decoration" generates a number of novel 2D structures based on the geometry and stoichiometry of MoS_2 . In particular, we can assume that substituting Mo with another transition metal M and S with another chalcogen X, we have good chances of finding a novel stable 2D crystal. This class of materials is called Transition Metal Dichalcogenides (TMD) MX_2 and indeed it counts many experimentally known compounds[97]. An improved approach for the decoration step is based on chemical similarity between elements [98, 99].

Once a crystal structure is defined, the workflow showed in Fig. 5.6(b) calculates with almost no input from the user the structure and stability proprieties. The workflow is inspired mainly by the need of robustness (it should work across very different classes of materials without failing) and simplicity, with a tunable accuracy. The first step is the geometrical relaxation of the unit cell and internal coordinates of the non-magnetic and for the ferromagnetic configuration (initializing the magnetic moments of each atoms with a magnetic moment equal to $1 \mu_B$). If two metallic atoms are present in the unit cell, an anti-ferromagnetic relaxation is run as well. The thermodynamic (calculation of heat of formation) and dynamical stability tests (phonon analysis at Γ of the 2×2 repeated unit cell) are crucial, since they assess whether or not the monolayer under investigation is likely to be synthesised as free-standing nano-sheets. However, in real 2D system stability is often attained after coupling to a suitable substrate. The calculations of optical, electronic and magnetic proprieties is thus extended to any candidates that do not disintegrate during the relaxation process.

Since the publication of Paper II, the number of entries in C2DB increased from roughly 1900 to over 3700, with more than 680 highly stable materials. Among these, nearly 150 (50) are expected to be stable in a FM (AFM) configuration, with a MA (note that in C2DB, a negative value of MA corresponds to out-of-plane anisotropy) that ranges from -26 meV (ReCl_3) to 41 meV (ReBr_3) per magnetic ion.

The proprieties of 2D materials obtained from high-throughput screening can serve as be a useful guide for experimental research and for inspiring data-driven approaches to study and exploit trends and correlations. For example, in Fig. 5.7 are shown the magnitude of magnetic anisotropy (in red) and magnetic moments (in blue) per magnetic atom in the unit cell, averaged over all materials in C2DB with the same composition (at the time of the publication, around 350 magnetic materials). One can notice that high value of MA are mainly determined by the non-magnetic atom (like the halides I, Br, Cl) rather than by the magnetic atom. This confirms the crucial role of the super-exchange interactions (mediated by non-magnetic ion) at the origin of magnetism in 2D and ultra-thin materials[50, 100, 83]. Finally, in Fig. 5.8 we shows that metals tend to exhibit a wider range of value for magnetic anisotropy, both in-plane and out-of-plane (though we note once again that the assumptions at the basis of Energy Mapping analysis and Heisenberg model are not well defined for itinerant ferromagnets). However, the recent discovery of atomically-thick Ising-like FM CrI_3 [17], with an out-of-plane MA of just 0.85 meV per Cr atom, proved that robust intrinsic ferromagnetism is a prospect within reach for many insulators in the database, which display comparable or stronger MA.

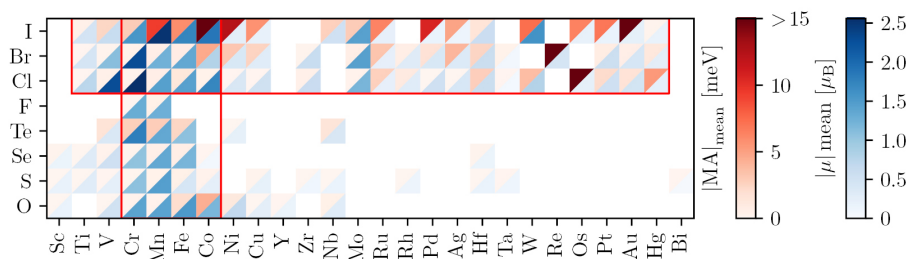


Figure 5.7: **Magnetic proprieties of materials in C2DB.** Absolute MA (red triangles) and magnetic moments (blue triangles) of magnetic materials in C2DB. The two red boxes highlight halides and 3d metal. From Paper II.

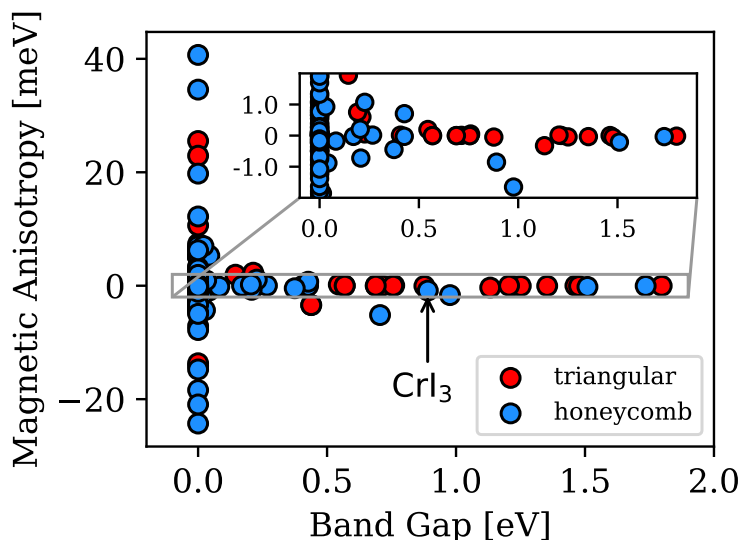


Figure 5.8: **Magnetic anisotropy and optical band-gap of materials in C2DB.** Overview of MA and optical band gap values for 2D materials in C2DB with a triangular and honeycomb magnetic lattice.

5.3 Paper III: Discovering two-dimensional topological insulators from high-throughput computations

This paper is included for completeness but the contribution of the submitter is minor.

The project involved the screening of C2DB in search of two-dimensional topological insulators. In particular, an high-throughput screening of C2DB (see Paper II and [90]) has been performed for a systematic search of insulators with a non-trivial topology. In a nutshell, a 2D topological insulator exhibits conducting edge states with a spin selectivity locked to the direction of propagation[101, 102]. This can be a consequence of the intrinsic magnetization of the system and spin-orbit coupling (SOC) in Quantum Anomalous Hall Insulators (QAHI) or just a strong SOC in Quantum Spin Hall Insulators (QSHI). The conducting states are explained in terms of the non-trivial topology of their bandstructure, which is protected by Time Reversal (TR) symmetry and labeled by the \mathbb{Z}_2 invariant ν . This is strictly linked to the Berry phase in the momentum space and can be investigated by *ab-initio* methods. QSH effects have been predicted and observed in many systems, both 3D[103, 104] and 2D[105, 106, 69], but no intrinsically ferromagnetic QAHI has been experimentally reported at present. Although ferromagnetism can be induced into topological materials through substitutional doping[107], only few candidates in their pristine form have been proposed based on Density Functional Theory (DFT) calculations. Among them, the 2D materials graphene[108], OsCl₃[109] and CoBr₂[110].

Here a list of new promising materials is showed, including six dynamically stable QAHI. Among them, FeBr₃ and CoBr₃ are predicted to have low heat of formation, which is a strong evidence for thermodynamical stability (see sections 2.3 and 2.4 in Paper II) and an exciting likeability to be synthesised in future. Respectively, critical temperatures of 2 K and 274 K have been obtained from a method based on classical Monte Carlo simulations and Energy Mapping analysis (see sec. 5.1). However, this procedure maps ground state energies obtained from DFT calculations to spin-lattice Heisenberg model configurations with highly localized electrons and may be unfitting for the very weak insulating nature of the materials here considered. In addition, DFT calculations turned out to be highly sensitive to the choice of exchange-correlation functional and U value for Hubbard corrections. Still, the paper lists 48 QSHI and 21 crystalline topological insulators[111, 112], only a third of which previously known, proving once again the potentiality of a screening-based approach in materials design for future applications.

5.4 Paper IV: High throughput computational screening for 2D ferromagnetic materials: the critical role of anisotropy and local correlations

In this paper, the computational workflow for the calculation of Heisenberg parameters in magnetic 2D materials exposed in sec. 5.1 has been applied to C2DB database. In particular, the search focused on robust intrinsic ferromagnets with an out-of-plane magnetic anisotropy (MA). The Curie temperature above which a long-range ordered system loses its net magnetization is a crucial feature for the design of future ultra-thin devices, based i.e. on spintronic technology.

In Paper I we showed that a reliable method to calculate it, is based on classical Monte Carlo simulations of spin-lattice systems with material-specific parameters obtained from first principles calculations. However, for trustworthy results, simulations on very large systems and numerous MC steps are required. With the algorithm presented in section 4.2, assuming a system with 50x50 spins and roughly half a million of MC steps, a full MC simulation requires at least one day of computational effort for the evaluation of the residual magnetization for just one temperature T . This is not very practical for high-throughput screening of a database with several hundreds of entries. We thus employed the workflow designed in Paper I based on semi-empirical fitting of MC simulations for the calculation of Curie temperatures in square, honeycomb and triangular 2D magnetic lattices. Relevant Heisenberg parameters J , A and B are obtained as in Sec. 3.4.

At the time of the screening, C2DB comprises 3712 materials with structural, optical, electronic and magnetic properties obtained from first principle calculations. However, many of these entries are actually the same material with a different magnetic (meta-)stable ground state. The number of unique structures with either a square, honeycomb or triangular magnetic lattice is 570 and forms the initial group of candidates. In a preliminary and rough screening, the class of Transition Metal Halogen Chalcogen (TMHC) materials can be included among the triangular prototypes although metals are arranged in a distorted triangular lattice organized over two distinct layers (see Fig. 3 in Paper IV). In 276 cases we obtained a ferromagnetic ground state ($J > 0$), comparing energies with the non-magnetic and anti-ferromagnetic configurations. We emphasize that only one of the few possible anti-ferromagnetic configuration has been considered for each prototype. The total number of structures with one of the mentioned geometry is 357, and 270 have a finite optical band gap in the ground state configuration.

In 2D materials, MA is crucial to escape Mermin-Wagner (MW) theorem, which prevents any long-range magnetic order at any finite temperature in systems with continuous spin rotational symmetry. As mentioned in sec. 5.1, the main descriptor for MA and thus for a finite critical temperature is given by the sign of the spin wave gap $\Delta = A(2S - 1) + BSz$ where z is the coordination number of the lattice. The final number of materials with positive J and Δ is 79, but only 48 of them are predicted to be thermodynamically and dynamically stable.

The workflow is summarized in Fig. 5.9. The final step is the calculation of T_C based on Eq. 5.8. As mentioned in sec. 5.1, the fitting is not well defined for $S = 1/2$ systems, for which dedicated MC simulations are needed. The list of insulating materials and discussion of each of them can be found in sec. 3 of Paper IV.

However, recent calculations highlighted an error in the paper, which will be shortly communicated to the editor after a more extensive investigation. Exchange couplings and spin-wave gaps, and thus critical temperatures have been obtained comparing results from different versions of the code GPAW. In particular, FM ground state energies have been obtained using GPAW 1.4.0, while the AFM configurations run with GPAW 1.4.0[113]. Even keeping all settings unaltered, it is not a good idea to compare energies from different versions of the code. Corrected values of Tab. 2 in Paper IV are showed in Tab. 5.1 in this section. The corrections are minimal and in general yield to higher value of critical temperatures. The only exceptions are MnO_2 (with a T_C that is reduced from 63 K to 19 K) and CoCl_2 (from 55 to 31 K, in ever better agreement with the experimental results of 24 K on bulk systems[114]). Discussions in section 3 of Paper IV are thus qualitatively still valid. Any other calculations in the paper have been obtained running the same version of GPAW and thus do not

required any errata corrige.

For TMHC materials we found non-negligible in-plane anisotropies and thus we performed a deeper analysis. Eq. 2.48 can be generalized including anisotropic terms $A^{x(y)}$ and $B^{x(y)}$ along the in-plane axis and next-nearest neighbours coupling J_2 . MC calculations revealed that the in-plane magnetic order is possible. In particular, we predict 5 materials with in-plane anisotropy and $T_C > 100$. Easy-plane order in 2D is a relatively unexplored field since according to the MW theorem, the rotational symmetry of spins inhibits any long-range order. The resulting XY Heisenberg model is rather characterized by *Kosterlitz-Thouless* (KT) transition at critical temperature T_{KT} [115]. The system moves from an high-temperature disordered phase to a quasi long-range ordered phase, defined by a slower algebraic decay in spins' correlation (instead of exponential decay). Inevitable finite size effects, both in real samples and simulated systems, induce however a spurious net magnetization[116]. In our case the magnetization arises from in-plane anisotropy and thus from a physically sound propriety of the system, which breaks the the continuous symmetry and circumvent MW theorem .

All results showed so far have been obtained adopting the GGA-PBE approximation to the exchange-correlation functional[68]. In this work we also vastly investigated the role of an Hubbard correction PBE+U. The entire workflow, including geometrical relaxation, has been re-run for every materials with at least one element with a partially filled d -shell (roughly half of them). As we discussed in section 3.3.1, the correct value of U is very system-specific. An *ab-initio* derivation would require high-demanding re-calculations for each type of material, magnetic configuration, and even GPAW setting. It should be clear that for a screening study this is an unpractical path. Here, a set of typically accepted U values for transition metals have been chosen and kept for the entire study. In particular we choose the same U values adopted by the Open Quantum Materials Database [117, 118]. The inclusion of Hubbard correction has a rather dramatic effect on the ground state proprieties of magnetic materials: no general trend is observed and only few examples can be compared. Most notably we note that for CrI_3 the critical temperatures increases linearly and match the experimental value[17] for $U \approx 2.5$ eV.

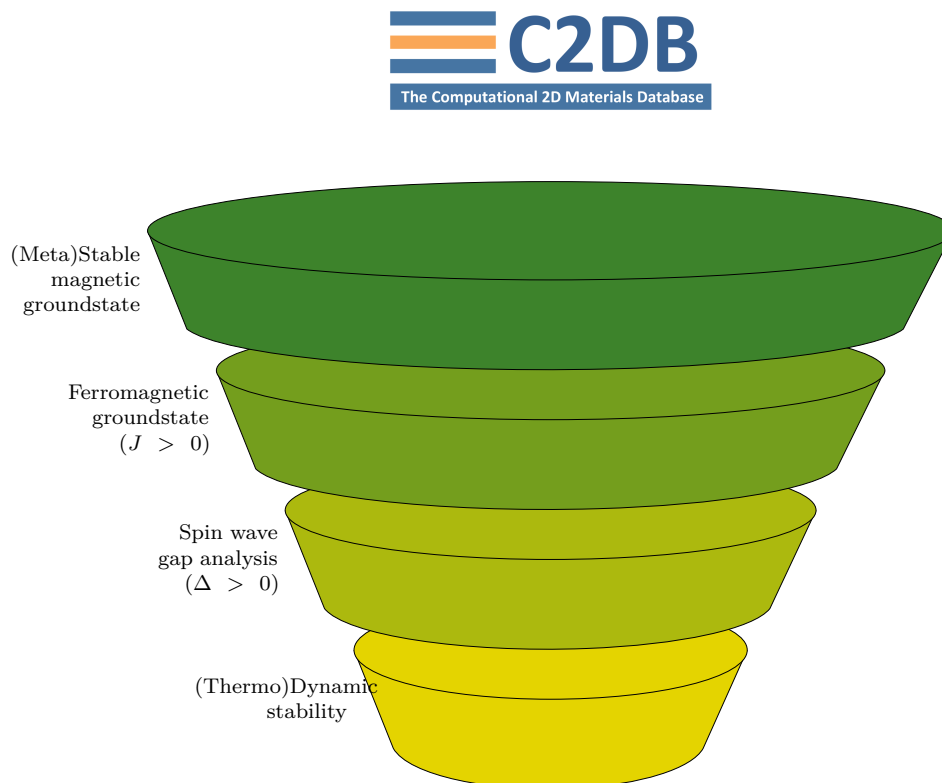


Figure 5.9: **Screening funnel.** Workflow used for screening of C2DB database

| Formula | Prototype | J [meV] | Δ [meV] | S [μ_B] | T_C [K] |
|-------------------|------------------|-----------|----------------|-----------------|-----------|
| FeCl ₂ | MoS ₂ | 15.15 | 0.056 | 2.0 | 208 |
| CuCl ₃ | BiI ₃ | 15.26 | 0.058 | 1.0 | 37 |
| CrI ₃ | BiI ₃ | 2.31 | 0.961 | 1.5 | 35 |
| CoCl ₂ | CdI ₂ | 1.99 | 0.058 | 1.5 | 31 |
| CrBr ₃ | BiI ₃ | 1.98 | 0.232 | 1.5 | 23 |
| MnO ₂ | CdI ₂ | 0.54 | 0.305 | 1.5 | 19 |
| NiCl ₂ | CdI ₂ | 7.17 | 0.001 | 1.0 | 14 |
| CrCl ₃ | BiI ₃ | 1.4 | 0.033 | 1.5 | 13 |
| RuCl ₂ | MoS ₂ | 18.70 | 2.263 | 2.0 | 606 |
| RuBr ₂ | MoS ₂ | 16.11 | 1.766 | 2.0 | 509 |

Table 5.1: Correction to Tab.2 in Paper IV.

5.5 Paper V: First Principles Heisenberg Models of 2D magnetic materials: The Importance of Quantum Corrections to the Exchange Coupling

Insulating magnetic materials are described by the Heisenberg model, in which the interactions between localized spin are quantified by the exchange coupling J as in 2.21. This parameter is crucial for defining magnetic properties of the system and can be extracted by Energy Mapping analysis. The procedure is simply to compare the ground state energy of a fully polarized ferromagnetic (FM) configuration and an anti-ferromagnetic (AFM) configuration, typically the AFM Néel state

$$J = \frac{\Delta E}{z2S^2} \quad (5.10)$$

where ΔE is the difference between the FM and AFM ground state energy.

These are attainable from DFT calculations.

In a quantum-mechanical framework however, the resolution of the AFM bipartite lattice, even neglecting magnon-magnon interactions, yields to a different ground state with a lower energy than the Néel state. In 1D system the latter is even unstable at any T . The fork is particularly significant for lower dimensions and low value of spin S . The correction can be evaluated numerically and inserted in the Energy Mapping analysis scheme. This is expected to provide a better description of the energies at play and thus their modeling.

In this short letter we show that at some extent, these corrections β are embedded in DFT methods, which in theory are an exact resolution of many-body Schrodinger equations. In sec. 2.6.1 we provided all the theoretical background. In particular, assuming Eqs. 2.62 to describe the true AFM ground state (in the approximation of no magnon-magnon interactions) E_{NIM} , the exchange coupling is readily written as

$$J = \frac{\Delta E}{zS^2(1 + \beta/2S)} \quad (5.11)$$

with $\Delta E = E_{NIM} - E_{FM}$. If DFT is indeed returning E_{NIM} as the AFM energy even in collinear DFT calculations, the correct equation for J is 5.11 and not 5.10.

An evaluation as accurate as possible of J is very important since it is naturally linked to the robustness of magnetic order in the system. In particular the Curie temperature can be computed by a fitting of MC simulations, as showed in sec. 5.4. Since the new AFM ground state is lower in energy, the "corrected" FM J are revised downwards, as well as T_C by a factor $\sim 5 - 10\%$. Additionally, Eqs. 2.66 indicate that the magnetization of the AFM ground state is reduced as well. In Fig. 5.10 are shown the ratio m_{AFM}/m_{FM} for 51 insulating materials from C2DB, with different geometry. A trend is clear, with quantum corrections decreasing for higher value of S . A significant deviation from the predicted behaviour (dashed lines) is also clear, in particular for the square lattice. However, it is

a solid evidence that DFT, and specifically GGA functional PBE, is able to catch, at some extent, the re-normalization of magnetic moments predicted in quantum mechanical derivation of AFM ground state in lower dimensional systems.

5.6 Paper VI: High throughput computational screening for two-dimensional magnetic materials based on experimental databases of three-dimensional compounds

This section refers to Paper VI, which is still in preparation. I will briefly comment on the preliminary work and early results.

Low dimensional materials are characterized by weak Van der Waals (vdW) interactions holding the material together. For example, multi-layered bulk systems have a natural tendency to organize into a layered structure where strong covalent bonds guarantee the in-plane cohesion and the vdW forces weakly stabilize the material along the out-of-plane direction. This kind of materials, called vdW structures, can be easily exfoliated into free-standing nano-sheets. Ideally, they may also be combined into heterostructures by stacking one on top of the other like tower of LEGO to create novel systems with unprecedented functionalities. A famous example is the cleavage of graphene from graphite[1] and its recombination in new heterostructures[119, 120]. Being able to identify natural vdW structures is the fastest route to the discovery of novel stable monolayers.

Here we employed a computational technique to identify low-dimensional materials, based on a geometrical analysis of the atomic distances in the unit cell[121]. In short, we can assign a scoring parameters s_d (with $d = 1, 2, 3$) to each material quantifying the degree of relevance of a particular dimensionality. Value of s_d ranges from 0 to 1 according to the likeability of finding dimension d substructures in the system and fulfills $\sum_d s_d = 1$. The method has been implemented, tested and run over the Inorganic Structure Database (ICSD)[122] and Crystallographic Open Database (COD)[123] by a previous Ph. D. student[121]. Results can be freely browsed online at [124]. The technique allows to classify bulk experimentally analyzed systems in terms of the dominant dimensionality:

- point-like clusters 0D,
- rod-like isolated 1D chains,

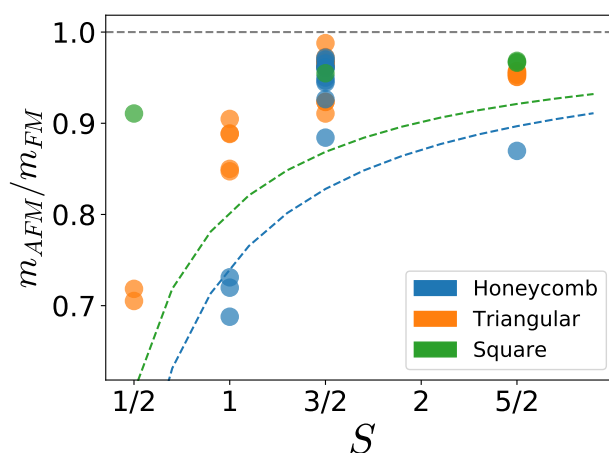


Figure 5.10: **AFM correction in DFT-derived parameter m .** Ratio of average magnetic moments in ferromagnetic configurations insulating materials. The dashed lines show the results obtained from a spin-wave analysis of the Heisenberg model with square and honeycomb lattices. From Paper V.

- multi-layered 2D structure,
- 3D bulk material with isotropic atomic expansion,
- mixed-dimensionality (i.e. $s_d < 0.5$ for every $d=0,1,2,3$).

Some examples of low-dimensional materials from COD are given in Fig. 5.11 and an overview of the distribution in COD and ICSD are shown in Fig.5.12 where 0D and 3D materials dominate, respectively. ICSD and COD databases combined count more than 500.000 materials, but roughly two-third are corrupted, incomplete entries or duplicates. We thus obtained a starting set of 167767 bulk materials[121]. We then selected the 4264 entries with a dominant 2D nature ($s_2 > 0.5$), isolated and exfoliated the 2D component with a computational function integrated in ASE[56]. Finally, we restricted to unit cell with less than 20 atoms, less than 5 different elements and at least one transition metal to increase the chance of having a magnetic ground state. The number of final structures on which we run the same method presented in sec. 5.4 is in total 651. Results are showed in Tab. 5.2 and 5.3 for FM and AFM ground states respectively. Note that "corrected" values J_{corr} and $T_{C,corr}$ are defined in sec. 5.5.

In general, we obtain a good agreement with previously reported results. Small fluctuations may arise from numerical noises when almost zero Heisenberg parameters are found (i.e. Δ for NiCl_2). CrI_3 monolayer has been reported to be an Ising-like ferromagnet with robust out-of-plane magnetization. The experimental critical temperature is 45 K, in good agreement with our prediction. SQUID (Superconducting Quantum Interference Device) measurements on MnSe_2 films in the MoS_2 prototype, grown by molecular beam epitaxy (MBE), has been found to host out-of-plane magnetism up to room temperature[19]. Although we expect it to be a metal, we predict $T_C = 62\text{K}$. One of the experimentally known material that we failed to predict is $\text{Cr}_2\text{Ge}_2\text{Te}_6$ [18]. A recent experimental investigations showed that low-dimensional systems exhibit a small out-of-plane magnetization. The bulk system is known to exhibit ferromagnetism up to a critical temperature of 61 K[125, 126], that decreases continuously down to nearly 20 K when the bilayer limit is reached, since monolayer samples were found to degrade rapidly and became invisible under the optical microscope[18]. According to our calculations, the ferromagnetic ground state is metallic and has a negative spin-wave $\Delta \approx -0.02\text{meV}$. A more extensive analysis, including the influence of Hubbard correction or strain test may lead to better agreement and unveil the origin of magnetism in $\text{Cr}_2\text{Ge}_2\text{Te}_6$.

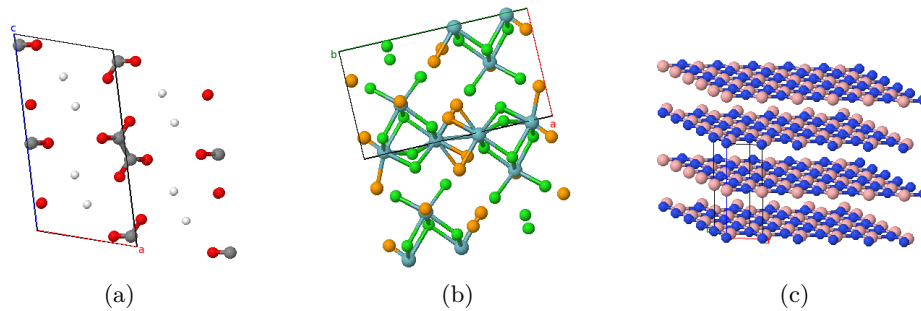


Figure 5.11: **Low-dimensional materials.** Examples of (a) 0D material ($\text{C}_4\text{H}_4\text{O}_8$, #5900034_{COD}, $s_0=0.994$), (b) rod-like 1D material ($\text{Nb}_6\text{Cl}_{14}\text{Se}_{10}$, #1525157_{COD}, $s_1=0.900$) and (c) 2D layered material (B_2N_2 , #1010602_{COD}, $s_2=0.983$).

Finally, combinatorial lattice decoration (see sec. 5.2) of prototypes NiRe_2O_8 , MgMnGe and CrGa_2Se_2 (not yet present in C2DB) is a promising path to take in order to find novel 2D materials. However, further investigations regarding thermodynamic and dynamic stability is required, as well as the influence of Hubbard corrections and the possible presence of in-plane magnetic anisotropy.

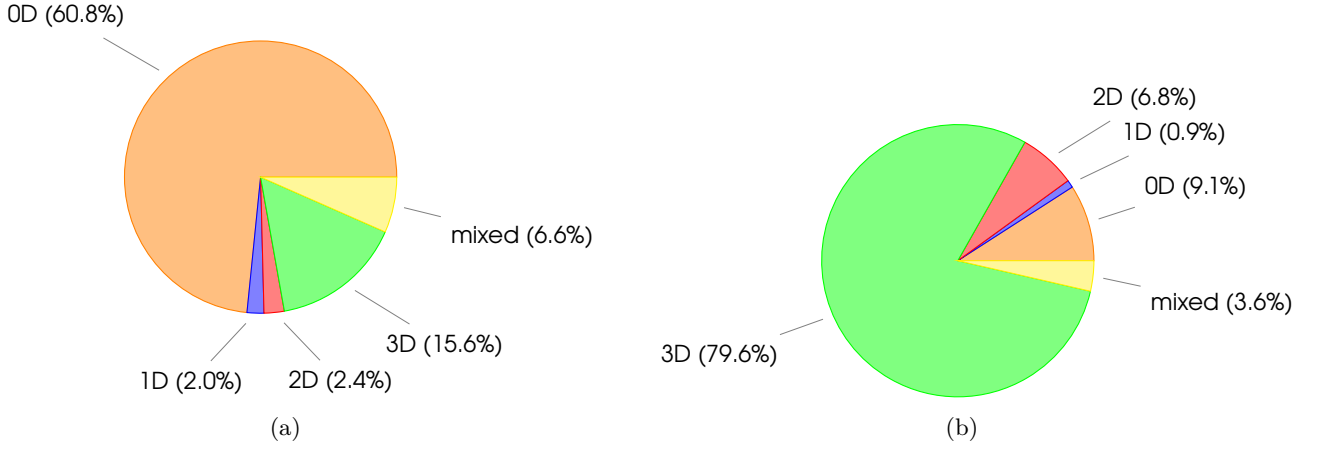


Figure 5.12: **Distribution of structures in COD and ICSD.** Distribution of 0D,1D,2D,3D and mixed structures in (a) COD (139052 total entries) (b) and ICSD (28715 total entries),

Table 5.2: **Screening FM materials.** List of 2D ferromagnetic materials obtained from screening ICSD+COD. Critical temperatures with * are calculated from MC simulations for square, honeycomb and triangular lattice (for other geometries the result is not listed). The *id* number indicates the unique identification number in the online database[124, 121] and the structure respects the stoichiometry of the bulk system to avoid confusion. The spin S is expressed in term of Bohr magneton μ_B , J and Δ in meV, E_{GAP} in eV and temperature in K. Highlighted entries are robust insulating system (optical band gap $E_{GAP,FM(AFM)} > 0.1$ eV)

| id | Struct | S | J_{corr} | Δ | $E_{GAP,FM}$ | $E_{GAP,AFM}$ | $T_{C,corr}$ |
|---------|-----------|-----|------------|----------|--------------|---------------|--------------|
| 39427 | Ti6Cl18 | 1/2 | 0.784 | -0.144 | 0.0 | 0.15 | - |
| 1535681 | Fe6Cl18 | 1/2 | 0.947 | 2.773 | 0.01 | 0.27 | 10.0* |
| 9009099 | CoBr2 | 3/2 | 1.221 | -0.37 | 0.27 | 0.23 | - |
| 20566 | CoO2 | 1/2 | 17.103 | 0.446 | <0.001 | 0.0 | 5.0* |
| 2310380 | Ni3Cl6 | 1 | 6.629 | 0.0 | 1.22 | 1.11 | 11.0 |
| 1010575 | Cr6Cl18 | 3/2 | 1.309 | 0.032 | 1.74 | 1.9 | 13.0 |
| 76421 | Fe6Br18 | 1/2 | 28.439 | 2.553 | 0.0 | 0.25 | 5* |
| 251655 | Cr6I18 | 3/2 | 2.199 | 0.936 | 0.9 | 1.01 | 34.0 |
| 151400 | Fe2Cl6 | 1/2 | 85.511 | -0.588 | 0.01 | 0.0 | - |
| 4344519 | Y6Cl6 | 1/2 | 5.851 | -0.032 | 0.0 | 0.39 | - |
| 20717 | Ru6Cl18 | 1/2 | 0.07 | -0.009 | 0.0 | 0.0 | - |
| 29035 | Ti2Cl6 | 1/2 | 8.28 | -0.015 | 0.0 | 0.18 | - |
| 9008030 | CoCl2 | 3/2 | 1.755 | 0.046 | 0.37 | 0.41 | 28.0 |
| 246907 | VI2 | 3/2 | 0.366 | -0.095 | 1.21 | 1.15 | - |
| 9009128 | Fe3Cl6 | 2 | 4.828 | -0.108 | 0.0 | 0.0 | - |
| 1010151 | Cr6Br18 | 3/2 | 1.909 | 0.23 | 1.51 | 1.65 | 23.0 |
| 9011538 | Ni3I6 | 1 | 7.592 | 0.356 | 0.0 | 0.33 | 68.0 |
| 8101148 | FeBr2 | 2 | 3.239 | -0.198 | 0.0 | 0.0 | - |
| 44753 | Fe2Te2 | 1 | 37.36 | 2.426 | 0.0 | 0.0 | 238.0 |
| 1538289 | VSe2 | 1/2 | 18.261 | -0.419 | 0.0 | 0.0 | - |
| 4343683 | Sc6Cl6 | 1/2 | 35.851 | -0.002 | 0.0 | 0.07 | - |
| 86519 | VS2 | 1/2 | 10.944 | 0.033 | 0.0 | 0.0 | 45.0* |
| 151974 | Y2I2 | 1/2 | 32.795 | -0.029 | 0.0 | 0.0 | - |
| 9009131 | Ni3Br6 | 1 | 6.736 | -0.175 | 0.76 | 0.8 | - |
| 9009111 | MnO2 | 3/2 | 0.509 | 0.305 | 1.13 | 1.29 | 19.0 |
| 1536707 | V6Cl18 | 1 | 42.957 | -0.346 | 0.0 | 0.0 | - |
| 1539696 | Mg2Mn2Ge2 | 1 | 11.524 | 0.604 | 0.0 | 0.0 | 73.0 |
| 9012135 | Cr3H3O6 | 3/2 | 2.348 | 0.147 | 0.46 | 0.65 | 44.0 |

| | | | | | | | |
|---------|-------------|-----|--------|--------|------|------|-------|
| 51016 | NiRe2O8 | 1 | 2.016 | 1.294 | 1.57 | 1.57 | 36.0 |
| 2106381 | Fe2Cl2O2 | 1/2 | 8.498 | 0.38 | 0.0 | 0.0 | - |
| 1539705 | Ca2Mn2Si2 | 1 | 3.344 | 0.415 | 0.0 | 0.0 | 29.0 |
| 1534386 | Cr2Br2O2 | 3/2 | 0.349 | -0.049 | 0.5 | 0.95 | - |
| 1527676 | Mn4O16Se4 | 3/2 | 12.129 | -0.178 | 0.02 | 0.12 | - |
| 626810 | Cr6Si6Te18 | 3/2 | 3.416 | 0.307 | 0.26 | 0.46 | 36.0 |
| 641335 | K3Ti3S6 | 1/2 | 10.314 | -0.017 | 0.0 | 0.0 | - |
| 2106692 | V2Cl2O2 | 1 | 5.08 | 0.077 | 0.0 | 0.0 | 26.0 |
| 24381 | V2Br4O2 | 1/2 | 19.485 | 0.536 | 0.0 | 0.18 | - |
| 32551 | Fe6Ga6S15 | 1 | 0.0 | -0.095 | 0.0 | 0.0 | - |
| 77990 | Rb3Ti3S6 | 1/2 | 18.64 | 0.063 | 0.0 | 0.0 | 75.0* |
| 643239 | Mn6P6Se18 | 1 | 0.715 | -0.18 | 0.0 | 0.0 | - |
| 33288 | Co3Cl6O24 | 3/2 | 0.243 | 0.419 | 0.72 | 0.8 | 13.0 |
| 1537583 | V2Br2O2 | 1 | 6.641 | 0.301 | 0.0 | 0.0 | 42.0 |
| 28318 | Cr2Cl2O2 | 3/2 | 1.036 | 0.069 | 0.65 | 1.13 | 16.0 |
| 1531759 | Ca4Co2O6 | 3/2 | 4.494 | 3.527 | 0.04 | 0.06 | 103.0 |
| 631804 | Fe2Ga2S5 | 1 | 0.001 | -0.113 | 0.0 | 0.0 | - |
| 2002027 | Fe2Ta2Te6 | 1 | 42.478 | -0.627 | 0.0 | 0.0 | - |
| 33289 | Ni3Cl6O24 | 1 | 0.476 | -0.075 | 1.54 | 1.55 | - |
| 1543733 | Cr6Ge6Te18 | 3/2 | 5.935 | -0.02 | 0.0 | 0.23 | - |
| 626052 | CrGa2S4 | 2 | 1.828 | 0.086 | 0.0 | 0.0 | 51.0 |
| 1001053 | Cr2Ta4O12 | 1 | 35.544 | -0.619 | 0.22 | 0.21 | - |
| 1541091 | Li2Ni2P4S12 | 1/2 | 8.122 | -0.292 | 0.0 | 0.12 | - |
| 2014296 | V2C8F2H8O12 | 1 | 21.586 | 0.487 | 0.0 | 0.0 | - |
| 7227895 | NiC6Cl2H4N2 | 1 | 8.499 | -0.063 | 0.85 | 0.82 | - |

Table 5.3: **Screening AFM materials.** List of 2D anti-ferromagnetic materials obtained from screening ICSD+COD. The *id* number indicates the unique identification number in the online database[124, 121] and the structure respects the stoichiometry of the bulk system to avoid confusion. The spin S is expressed in terms of Bohr magneton μ_B , while energies are reported in meV and eV for Heisenberg parameters and optical band gap respectively. Highlighted entries are robust insulating system (optical band gap $E_{GAP,FM(AFM)} > 0.1$ eV).

| id | Struct | S | J_{corr} | Δ | $E_{GAP,FM}$ | $E_{GAP,AFM}$ |
|---------|---|-----|-------------------|----------|--------------|---------------|
| 2241796 | Nb ₂ F ₈ | 1/2 | -57.689 | 1.306 | 0.0 | 0.19 |
| 9009110 | MnI ₂ | 5/2 | -0.532 | 0.017 | 0.88 | 1.36 |
| 9009109 | MnBr ₂ | 5/2 | -0.535 | 0.036 | 1.48 | 1.83 |
| 246906 | VBr ₂ | 3/2 | -2.695 | 0.031 | 1.26 | 1.26 |
| 9009100 | CoI ₂ | 1/2 | -19.577 | -0.304 | 0.0 | 0.0 |
| 1535971 | TiBr ₂ | 1 | -4.341 | 0.428 | 0.0 | 0.0 |
| 165398 | Ru ₂ F ₈ | 1 | -0.409 | -6.69 | 0.59 | 0.7 |
| 9009130 | Mn ₃ Cl ₆ | 5/2 | -0.569 | 0.014 | 1.79 | 2.05 |
| 1539645 | V ₂ F ₈ | 1/2 | -11.881 | -0.053 | 0.45 | 0.77 |
| 626718 | CrSe ₂ | 1 | -1.186 | -1.047 | 0.0 | 0.0 |
| 603582 | VTe ₂ | 1/2 | -0.655 | 0.223 | 0.0 | 0.0 |
| 67500 | Mn ₃ Br ₆ | 5/2 | -0.539 | 0.036 | 1.48 | 1.83 |
| 1528165 | VCl ₂ | 3/2 | -4.773 | 0.028 | 1.36 | 1.36 |
| 9009104 | FeO ₂ | 1 | -0.076 | -1.247 | 0.0 | 0.0 |
| 162900 | Mn ₂ Se ₂ | 1/2 | -53.032 | 1.094 | 0.0 | 0.0 |
| 1509332 | AgSnF ₆ | 1/2 | -0.778 | 0.003 | 0.52 | 0.6 |
| 2104863 | Ni ₂ As ₂ O ₇ | 1 | -3.287 | 0.078 | 0.78 | 0.9 |
| 608511 | Al ₆ Mn ₃ S ₁₂ | 5/2 | -10.181 | 0.116 | 0.0 | 0.0 |

| | | | | | | |
|---------|---|-----|---------|--------|------|------|
| 1539711 | Ca ₂ Mn ₂ Ge ₂ | 1 | -26.673 | 0.846 | 0.0 | 0.0 |
| 634664 | Ga ₂ Mn ₂ S ₅ | 5/2 | -3.578 | 0.065 | 0.0 | 0.15 |
| 24380 | V ₂ Cl ₄ O ₂ | 1/2 | -2.929 | -0.009 | 0.0 | 0.0 |
| 7210230 | Bi ₆ Mn ₃ Te ₁₂ | 5/2 | -0.515 | 1.146 | 0.14 | 0.16 |
| 1539720 | Mn ₂ Sr ₂ Ge ₂ | 1 | -29.763 | 0.854 | 0.0 | 0.0 |
| 634670 | Ga ₆ Mn ₃ S ₁₂ | 2 | -11.497 | 0.102 | 0.0 | 0.0 |
| 634901 | Ga ₂ NiS ₄ | 1 | -10.886 | -0.251 | 0.16 | 0.15 |
| 1539717 | Ca ₂ Mn ₂ Sn ₂ | 2 | -14.406 | 0.185 | 0.0 | 0.06 |
| 639980 | In ₆ Mn ₃ Se ₁₂ | 5/2 | -2.856 | 0.062 | 0.0 | 0.0 |
| 74810 | Mn ₄ H ₈ O ₁₆ S ₄ | 5/2 | -0.671 | 0.006 | 2.04 | 2.5 |
| 109965 | Cu ₂ C ₄ H ₄ O ₈ | 1/2 | -0.044 | -1.359 | 1.07 | 1.55 |
| 408099 | Co ₄ H ₈ O ₁₆ Se ₄ | 3/2 | -1.589 | 0.208 | 0.48 | 0.64 |
| 1529142 | Fe ₄ Sr ₆ Br ₄ O ₁₀ | 2 | -20.388 | 0.072 | 0.0 | 0.0 |
| 7112837 | Mn ₂ C ₁₂ N ₈ Se ₄ | 1 | -21.216 | 0.171 | 0.0 | 0.0 |
| 418858 | Co ₂ Br ₄ O ₆ Sb ₄ | 3/2 | -4.703 | -0.704 | 0.65 | 0.82 |
| 7221295 | Fe ₂ Sr ₄ Br ₂ O ₆ | 2 | -0.136 | 0.171 | 0.0 | 0.0 |
| 7016115 | Co ₂ C ₈ Cl ₄ H ₈ N ₄ | 1/2 | -14.67 | 0.031 | 0.31 | 0.48 |
| 1528341 | Co ₄ C ₄ H ₁₂ O ₁₆ P ₄ | 3/2 | -0.949 | 0.482 | 0.56 | 0.76 |
| 4509073 | Ni ₂ C ₈ H ₁₆ N ₄ O ₈ | 1 | -12.899 | 0.1 | 1.35 | 1.78 |

CHAPTER 6

Conclusions and Outlook

In this thesis, we showed how we can employ *ab-initio* methods and statistical simulations to extract relevant parameters of magnetic 2D materials.

Many other topics, like topological insulator, Kosterlitz-Thouless transitions for in-plane magnetization, intra-layer anti-ferromagnetic and Dzialoshinsky-Morya interactions from first-principles have been taken into consideration and investigated as well during the last three years. However, at the moment, didn't yield conclusive and publishable results. For this reason they are not showed in this thesis. The project also involved original code writing in Python and a significant amount of time has been spent in relative debugging, testing and optimization of the code. Specifically, we conducted a a systematic search for out-of-plane ferromagnetic monolayers with high critical temperature.

Since the recent synthesis of the 2D systems with intrinsic long range order, the field has received a lot of interest and a search for novel candidates is expanding. High-throughput methods are still among the fastest and most accurate routes. Some of them are based on a pool of 2D or 3D materials computationally generated with hypothetical structure[127, 128, 90], other from databases of experimentally known compounds[129, 122, 123]. In literature there are other examples of screening for 2D magnetic materials analogous to the one presented here. For example, in [130], a similar approach using a DFT+U functional lead to the identification of 8 ferromagnetic mono-layers, obtained after geometrical and chemical screening of ICSD database. However, no relaxation of the structure has been carried out after the structural exfoliation and critical temperatures have been extrapolated with Monte Carlo simulations based on 2D Ising model, and thus highly overestimated. In [131] a screening of magnetic materials from existing 3D compounds [129] has been carried out with GGA+U functionals. Classical Monte Carlo simulations based on Ising Hamiltonian with nearest and next-nearest neighboring coupling of on-site spins have been used to predict high critical temperatures. Among the 8 ferromagnetic materials individuated, they found TMDH crystals, namely CrSBr with $T_C > 200K$, and CrSI, CrSCl, CrSeBr with $T_C > 500K$. However, as noticed before, the Ising model tends to overestimate and according to our calculations based on Heisenberg model, the critical temperatures are remarkably lower ($\approx 150K$, see Paper IV). In addition, in Paper IV we report non negligible in-plane anisotropies for these structures, which are not taken into account in the Ising model.

Inevitably, in any screening-based method, one needs to find a compromise between target accuracy and manageability of calculations. In most cases the outputs are only qualitative and serve as suggestion for a further investigations. For this reason, most works in literature, focus on the investigation of a small subset of materials, generally only one prototype and few atomic substitution, but with deeper insights. For the discussion of individual materials, the reader can find more references and a more exhaustive analysis in section 3 of Paper III, but in general, we notice a good agreement with other similar works in literature based on the same models.

With this thesis we hope to have provided a fast and reliable method to characterized 2D magnetic materials based on classical Monte Carlo results. It can be applied on top of the DFT + Eergy Mapping scheme and despite its simplicity, it is able to account for many quantum-mechanical effects occurring when strongly correlated systems are investigated at low temperature and low dimensionality.

Our systematic search, as the same time, cannot be considered exhaustive as well. The number of hypothetical prototypes considered in this study is just a subset of the number one can imagine. Furthermore, we tried to keep manageable the computational workload of the screening by adopting restrictions on the number and on the nature of atoms in the unit cells. In particular we focus on transition metals but others element as rare earth, can host magnetism. Moreover, only one AFM configuration has been taken into consideration when predicting the magnetic ground state, namely the total AFM configurations when this was possible (for square and honeycomb lattices,

while for the triangular lattice the striped AFM has been compared to the FM configuration). While being a good guess, since it minimises the energy for AFM exchanges, frustrations and geometrical deformation (Jahn-Teller distortion) could fix a different ground state reachable only adopting a bigger unit cell. The work focused only on square, triangular and honeycomb lattice, being the most common magnetic lattice and those for which numerical results are more accessible. Finally, adopting a simple Hamiltonian with only few free parameters to describe 2D systems is often necessary because of the heavy computational tasks these kind of simulations require and to avoid spurious overfitting. However, some systems may require specific analysis and the inclusion of new relevant interactions, such as anti-symmetric exchange interactions, or framework, like XY model.

We think that in future a similar workflow-based method can be easily implemented and employed for *ab-initio* screening of new parameters, so to provide a clear picture of the mechanisms that originate and prevent magnetic phase, and guide experimental investigations toward the next revolution in material science.

CHAPTER 7

Papers

- 7.1 Paper I: Calculating critical temperatures for ferromagnetic order in two-dimensional materials

2D Materials



RECEIVED
20 August 2018

REVISED
6 November 2018

ACCEPTED FOR PUBLICATION
13 November 2018

PUBLISHED
17 December 2018

PAPER

Calculating critical temperatures for ferromagnetic order in two-dimensional materials

Daniele Torelli and Thomas Olsen

CAMD, Department of Physics, Technical University of Denmark, 2820 Kgs. Lyngby, Denmark

E-mail: tolsen@fysik.dtu.dk

Keywords: ferromagnetism, 2D materials, critical temperature, first principles calculations

Abstract

Magnetic order in two-dimensional (2D) materials is intimately coupled to magnetic anisotropy (MA) since the Mermin–Wagner theorem implies that rotational symmetry cannot be spontaneously broken at finite temperatures in 2D. Large MA thus comprises a key ingredient in the search for magnetic 2D materials that retains the magnetic order above room temperature. Magnetic interactions are typically modeled in terms of Heisenberg models and the temperature dependence on magnetic properties can be obtained with the random phase approximation (RPA), which treats magnon interactions at the mean-field level. In the present work we show that large MA gives rise to strong magnon–magnon interactions that leads to a drastic failure of the RPA. We then demonstrate that classical Monte Carlo (MC) simulations correctly describe the critical temperatures in the large MA limit and agree with RPA when the MA becomes small. A fit of the MC results leads to a simple expression for the critical temperatures as a function of MA and exchange coupling constants, which significantly simplifies the theoretical search for new 2D magnetic materials with high critical temperatures. The expression is tested on a monolayer of CrI₃, which were recently observed to exhibit ferromagnetic order below 45 K and we find excellent agreement with the experimental value.

1. Introduction

In 2017 it was demonstrated that a monolayer of CrI₃ exhibits ferromagnetic order with a Curie temperature of 45 K [1]. The discovery comprises the first example of magnetism in a two-dimensional (2D) material and it was subsequently shown that the magnetic properties of few layers of CrI₃ can be controlled with an electric field [2–5] and act as spin-filters [6, 7]. The observation has initiated a vast amount of interest in the subject [8–14] and a few other 2D materials have been shown to exhibit promising magnetic properties as well. For example, it has been shown that ferromagnetic order persists down to the bilayer limit in Cr₂Ge₂Te₆ [15] and room temperature magnetic order has been observed for monolayers of VSe₂ on a van der Waals substrate [16]. However, the description of magnetic order in 2D is more demanding than in three dimensions and it is currently a difficult task to predict the critical temperature of a given material. While it is well-known that magnetic order in 2D is driven by magnetic anisotropy (MA) there is no simple descriptor for the critical temperature and one has to

rely on complex simulations in order to obtain reliable estimates.

Magnetic order in crystalline solids is an inherently correlated effect that arises as a consequence of Pauli exclusion and electron–electron interactions. The theoretical description thus comprises a highly challenging topic and a series of approximations are required in order to derive various quantities related to the magnetic properties of solids. Typically, the problem is mapped onto a Heisenberg model of the form [17]

$$H = -\frac{1}{2} \sum_{ij} J_{ij} \mathbf{S}_i \cdot \mathbf{S}_j, \quad (1)$$

where \mathbf{S}_i is the spin operator at site j and J_{ij} is the magnetic coupling between spins at site i and j , that account for both direct exchange and superexchange [18, 19]. Still, a quantum mechanical treatment of equation (1) is non-trivial and the eigenstates cannot be obtained by analytical means in general. A direct numerical treatment is also out of the question due to the vast Hilbert space required for solids.

If one is interested in the critical temperature, a simple expression can be obtained from mean field

theory, where it is assumed that each spin only couples to the average magnetic field of the crystal. In the ferromagnetic case where all sites carry the same spin one obtains [17]

$$T_c^{\text{MF}} = \frac{S(S+1)}{3k_B} J_0, \quad (2)$$

where k_B is Boltzmann's constant, S is the maximum eigenvalue of S_z and $J_0 = \sum_j J_{ij}$. Correlation effects are completely neglected in mean field theory and the present expression does not in general yield quantitative agreement with experiments. However, for three-dimensional materials it does provide a rough estimate of T_c and has been widely applied to predict critical temperature and to extract exchange coupling constants from measured values of T_c [20–23]. In contrast, the Mermin–Wagner theorem implies that magnetic order in a 2D material cannot persist at finite temperatures unless MA is present. Since the derivation of equation (2) does not make any assumptions of dimensionality of the problem, a direct consequence of the Mermin–Wagner theorem is that mean field theory cannot be applied in 2D. The main purpose of the present work is to obtain a simple equivalent of equation (2) that can be applied to obtain the Curie temperature of 2D ferromagnetic materials for a given set of anisotropy and exchange parameters.

Another approach to analyzing the Heisenberg model is based on a Holstein–Primakoff transformation of the spin operators. In that case the Hamiltonian can be written as power series in bosonic field operators and the leading quadratic part is then straightforward to diagonalize. The excitations can be interpreted as non-interacting spin-waves and provide a good approximation for the spectrum at low temperatures. The remaining terms in the Hamiltonian represent spin-wave interactions and need to be taken into account at finite temperatures where many spin-waves are typically present. This is not a trivial task, however, but one can include the quartic term in a Hartree–Fock type of approximation, which gives rise to a temperature dependent renormalization of the spin-waves. In the present work we will refer to this as the random phase approximation (RPA) [17], but we note that this terminology is also sometimes used for the time-dependent susceptibility in the Hartree–Fock approximation. For 3D materials Curie temperatures obtained from RPA provide a more accurate estimate than those obtained from mean field theory and tend to provide a lower bound for the exact value, whereas mean field theory provides an upper bound [24, 25]. More importantly, RPA respects the Mermin–Wagner theorem and gives rise to vanishing critical temperatures in the absence of magnetic anisotropy. RPA thus appears to comprise the simplest method that can provide quantitative agreement with experiment. However, as will be shown in the present work, the RPA fails dramatically in systems with large anisotropy. For 2D materials it is expected that large anisotropy is exactly

the property needed if one is searching for materials with high critical temperatures and RPA is not a suitable approximation in such cases.

A third approach to the problem is based on the fact that at large temperatures quantum effects tend to be quenched by thermal fluctuations and one can consider a classical approximation for the model. Critical temperatures can then be obtained by performing Monte Carlo simulations of the model at different temperatures and identify the point where the average magnetization vanishes. While such an approach includes all correlation in the model, it is in general difficult to assess the importance of the neglected quantum effects. In particular, for systems with $S = 1/2$ quantum effects are likely to be important even at elevated temperatures. Nevertheless, classical Monte Carlo simulations have been shown to provide excellent agreement with experimental critical temperatures for diluted magnetic semiconductors [25] and Heusler alloys [24]. Moreover, the classical treatment has the important property that it correctly approaches the Ising limit for large anisotropies.

The classical simulations are, however, rather demanding in terms of computational load and it would be highly desirable to have an analytical expression that replaces equation (2) for two-dimensional materials with anisotropy. In the present paper we obtain such an expression by fitting the results of Monte Carlo simulations in anisotropic two-dimensional systems to an analytical expression. We perform the simulations for honeycomb, quadratic, and hexagonal lattices and provide a universal expression that only depends on the number of nearest neighbors and the critical temperature of the corresponding Ising model. We then consider a monolayer of CrI_3 as a test example and obtain good agreement with the experimental value of T_c using Heisenberg parameters obtained from first principles calculations.

2. Theory

The starting point of our calculations is the Heisenberg model with nearest neighbor exchange interactions J , single ion anisotropy A , and nearest neighbor anisotropic exchange B . Typically, 2D materials are isotropic in-plane and magnetic order is therefore only possible if the easy axis (here chosen as the z -axis) is perpendicular to the plane of the material. We thus consider the model Hamiltonian

$$H = -\frac{1}{2} \sum_{ij} J_{ij} \mathbf{S}_i \cdot \mathbf{S}_j - A \sum_i (S_i^z)^2 - \frac{1}{2} \sum_{ij} B_{ij} S_i^z S_j^z, \quad (3)$$

with $J_{ij}, A, B_{ij} > 0$. The sums run over all magnetic sites and $J_{ij} = J, B_{ij} = B$ if i and j are nearest neighbors and zero otherwise. The maximum value of S_i^z is denoted by S . Without MA, all eigenenergies are proportional to J and the model does not contain any fundamental interaction parameters. This implies that the amount

of correlation only depends on the lattice and the value of S . In contrast, when MA is present, the last terms in equation (3) introduces additional correlations, which is quantified by the dimensionless coupling constants A/J and B/J . Importantly, it should be noted that in the limit of $A/J \rightarrow \infty$, all excitations will have spins aligned along the easy axis and the model becomes equivalent to the Ising model with coupling parameter $J^{\text{Ising}} = J + B$.

The critical temperature is defined as the temperature at which the magnetic order vanishes. For a ferromagnetic system it can be determined by calculating the magnetization as

$$M(T) = \frac{1}{Z} \sum_{\{s\}} M_s e^{-E_s/k_B T}, \quad (4)$$

where Z is the partition function, s denotes eigenstates of equation (3), and M_s are the corresponding magnetic moments. From equation (3) it is clear T_c/J must be a function of A/J , B/J , and S as well as the lattice. A common approach to obtain approximate solutions to equation (3) is the Holstein–Primakoff transformation that replaces the spin operators by bosonic raising and lowering operators [17, 26]. The Hamiltonian can then be written as

$$H = E_0 + S\tilde{H}_0 + \tilde{H}_1 + \frac{1}{S}\tilde{H}_2 + \dots \quad (5)$$

where E_0 is the ground state energy. $S\tilde{H}_0$ is quadratic in raising and lowering operators, \tilde{H}_1 is quartic in raising and lowering operators, \tilde{H}_2 contains sixth order terms and so forth. The terms beyond \tilde{H}_0 thus introduce interactions between the Holstein–Primakoff bosons. We note that the anisotropy constants A and B only enters in E_0 , \tilde{H}_0 and \tilde{H}_1 . With periodic boundary conditions, all excitations can be labeled by a Bloch momentum \mathbf{q} and all terms in the Hamiltonian can be written in terms of $a_{\nu\mathbf{q}}^\dagger$ and $a_{\nu\mathbf{q}}$, which create and annihilate Holstein–Primakoff bosons for the sublattice ν at wavevector \mathbf{q} . Since the bosons carry spin-1, the magnetization per site can be written as

$$M(T) = M_0 - \frac{1}{nN_{\mathbf{q}}} \sum_{n\mathbf{q}} n_B(E_{n\mathbf{q}}, T), \quad (6)$$

where M_0 is the ground state magnetization per site, $N_{\mathbf{q}}$ is the number of unit cells, n is a band index, n_B is the Bose distribution, and $E_{n\mathbf{q}}$ are the eigenenergies of the Hamiltonian.

For simplicity we will restrict ourselves to a single site per unit cell in the following. If one neglects the interactions, the dispersion is readily obtained yielding

$$\varepsilon_{\mathbf{q}} = \varepsilon_{\mathbf{q}}^0 + A(2S - 1) + SBN_{nn}, \quad (7)$$

where N_{nn} is the number of nearest neighbors and $\varepsilon_{\mathbf{q}}^0$ is the dispersion of spinwaves without anisotropy, which satisfies $\varepsilon_{\mathbf{0}}^0 = 0$. Magnetic order at finite temperature in 2D is only possible if the spectrum is gapped and thus depends on the presence of MA. The expression becomes exact in the limit of vanishing

temperature and we see that the single-ion anisotropy will introduce a gap in the spectrum if $S > 1/2$. For $S = 1/2$ the single-ion anisotropy alone does not introduce a gap and finite critical temperatures are only possible with non-vanishing anisotropic exchange. In general magnetic order will be possible if $A(2S - 1) + SBN_{nn} > 0$. The interacting part of the anisotropy terms in the Hamiltonian (5) to fourth order in the field operators becomes

$$\tilde{H}_1^{\text{Ani}} = -\frac{1}{2N_{\mathbf{q}}} \sum_{\mathbf{q}\mathbf{q}'\mathbf{q}''} [2A + \tilde{B}(\mathbf{q}'' - \mathbf{q})] a_{\mathbf{q}'}^\dagger a_{\mathbf{q}''}^\dagger a_{\mathbf{q}} a_{\mathbf{q}+\mathbf{q}'-\mathbf{q}''} \quad (8)$$

with

$$\tilde{B}(\mathbf{q}) = B \sum_j \cos(\mathbf{q} \cdot \mathbf{R}_j), \quad (9)$$

where the sum runs over the set of smallest lattice vectors. The single-ion anisotropy thus introduces attractive interactions between the Holstein–Primakoff bosons, whereas the sign of the anisotropic exchange interaction depends on the value of \mathbf{q} .

Whereas \tilde{H}_0 is readily diagonalized, the interaction terms require some level of approximation. Taking the Hartree–Fock approximation for \tilde{H}_1 leads to the random phase approximation (RPA), which has previously been shown to provide good estimates of the Curie temperatures in 3D where the MA is usually neglected. The temperature dependent corrections to the spectrum without anisotropy $\Delta\varepsilon_{\mathbf{q}}$ is well-known and can be found in [17]. In the presence of anisotropy the RPA spectrum (for a single site per unit cell) acquires the additional temperature dependent terms

$$\Delta\varepsilon_{\mathbf{q}}^{\text{Ani}} = -\frac{1}{N_{\mathbf{q}}} \sum_{\mathbf{q}'} [4A + \tilde{B}(\mathbf{q} - \mathbf{q}') + \tilde{B}(\mathbf{0})] n_B(E_{\mathbf{q}'}^{\text{RPA}}, T) \quad (10)$$

with $E_{\mathbf{q}}^{\text{RPA}} = \varepsilon_{\mathbf{q}} + \Delta\varepsilon_{\mathbf{q}} + \Delta\varepsilon_{\mathbf{q}}^{\text{Ani}}$. The RPA dispersion and resulting magnetization at a given temperature thus have to be calculated self-consistently. It should be mentioned that the procedure of calculating the critical temperature as the point where equation (6) vanishes appears to be ill-defined in the RPA, since the renormalized spin gap approached zero before the magnetization vanishes. In particular, if we take $B = 0$ it can be seen from equations (7) and (10) that the gap should close when $\langle n \rangle = (2S - 1)/4$, which is always smaller than $M_0 = S$. However, the average number of bosons in the system diverges as the gap approaches zero, and the magnetization is not well-defined at this point. Nevertheless, since the average number of bosons diverge as the gap closes we have that $dM(T)/dT \rightarrow -\infty$ as $\Delta\varepsilon_{\mathbf{0}} + \Delta\varepsilon_{\mathbf{0}}^{\text{Ani}} \rightarrow 0$. We can thus calculate the magnetization up to arbitrarily small values of the spin gap, where the magnetization acquires a large negative slope as a function of temperature and we may simply identify the critical temperature as the point where the renormalized spin wave gap closes.

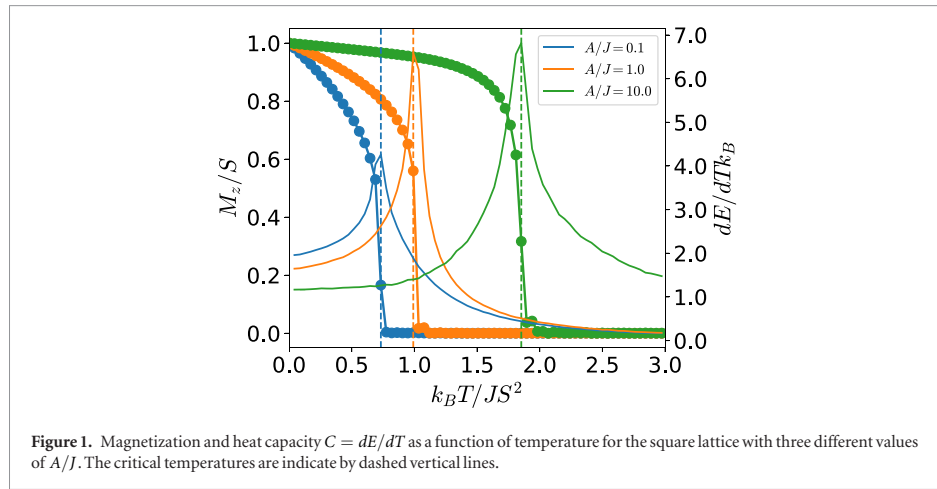


Figure 1. Magnetization and heat capacity $C = dE/dT$ as a function of temperature for the square lattice with three different values of A/J . The critical temperatures are indicate by dashed vertical lines.

In the case of large MA the RPA provides qualitatively wrong results since the Hartree–Fock level of theory cannot correctly capture the strong correlation introduced by the additional interaction term. This is inherited from the non-interacting spin-wave theory, where the breakdown can be seen as follows: assuming a quadratic dispersion of the form $\varepsilon_q = aq^2 + \Delta$ the magnetization becomes

$$\begin{aligned} M(T) &= M_0 - \frac{L^2}{(2\pi)^2} \int \frac{d^2q}{e^{(aq^2 + \Delta)/k_B T} - 1} \\ &= M_0 - k_B T \frac{L^2}{\pi a} \int_{\Delta/k_B T} \frac{dx}{e^x - 1} \\ &= M_0 + k_B T \frac{L^2}{\pi a} \log(1 - e^{-\Delta/k_B T}). \end{aligned} \quad (11)$$

At the critical temperature the magnetization vanishes, which implies

$$1 - e^{-\Delta/k_B T_c} = e^{-\alpha/k_B T_c}, \quad (12)$$

where $\alpha = \pi a M_0 / L^2$. This equation allows for arbitrarily large solutions for T_c if Δ is taken large enough (high anisotropy). In RPA one obtains a similar picture, since the average treatment of interactions simply introduces a temperature dependent rescaling of Δ . The fact that T_c diverges for large values of the anisotropy signals a breakdown of the RPA, since for a fixed value of B the critical temperature has to approach the Ising limit asymptotically as we take $A \rightarrow \infty$.

3. Results

3.1. Single-ion anisotropy

We now turn to the Monte Carlo simulations of the classical Heisenberg model at different temperatures. We start by considering only single-ion anisotropy and thus set $B = 0$. It is expected that the classical treatment is unreliable at low temperature where quantum fluctuations may dominate but at large temperatures the quantum fluctuation will be quenched by thermal

fluctuations. A major advantage of this approach is the fact that the Ising limit is naturally satisfied and the classical approximation will thus become asymptotically exact when $A/J \rightarrow \infty$ and $S \neq 1/2$. In figure 1 we show examples of the MC simulations for the square lattice using three different values of A/J . The critical temperature can be extracted as the point where the magnetization vanishes or as the temperature where the heat capacity $C = dE/dT$ diverges. The two-approaches gives identical results for the critical temperature.

In figure 2 we compare the critical temperature obtained from the RPA with classical MC simulations on a quadratic lattice. For the classical model the critical temperature can be written as $k_B T_c^{\text{Cl}} = S^2 f_{\text{Cl}}(A/J)$, where f is a universal function that do not depend on S . For the RPA one has $k_B T_c^{\text{RPA}} = S^2 f_{\text{RPA}}(S, A/J)$, but it is clear from figure 2 that $f_{\text{RPA}}(S, A/J)$ is nearly independent of S . The RPA clearly violates the Ising limit as noted above and we expect that T_c^{RPA} becomes unreliable when $A \sim J$. The MC simulations reveal that the Ising limit is approached rather slowly as A/J is increased and we can conclude that the materials with large anisotropies that will typically be referred to as Ising type ferromagnets are poorly described by the Ising model.

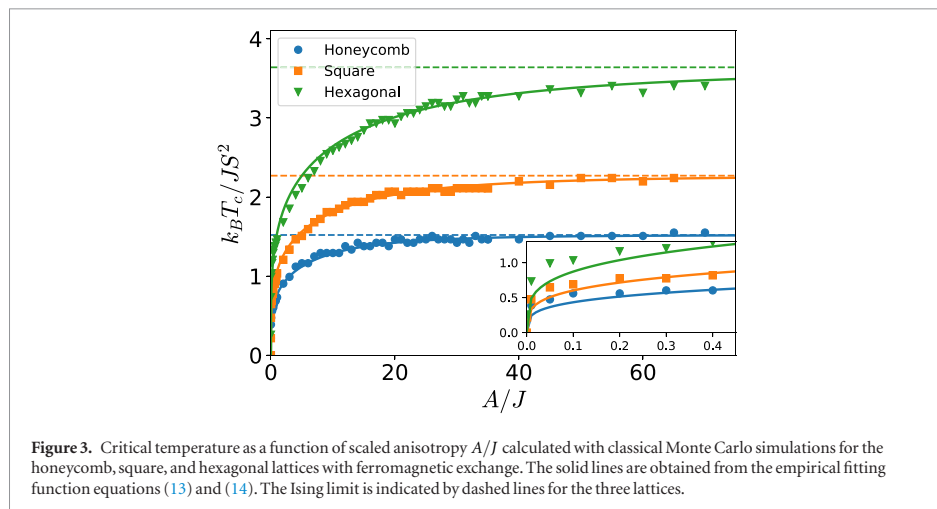
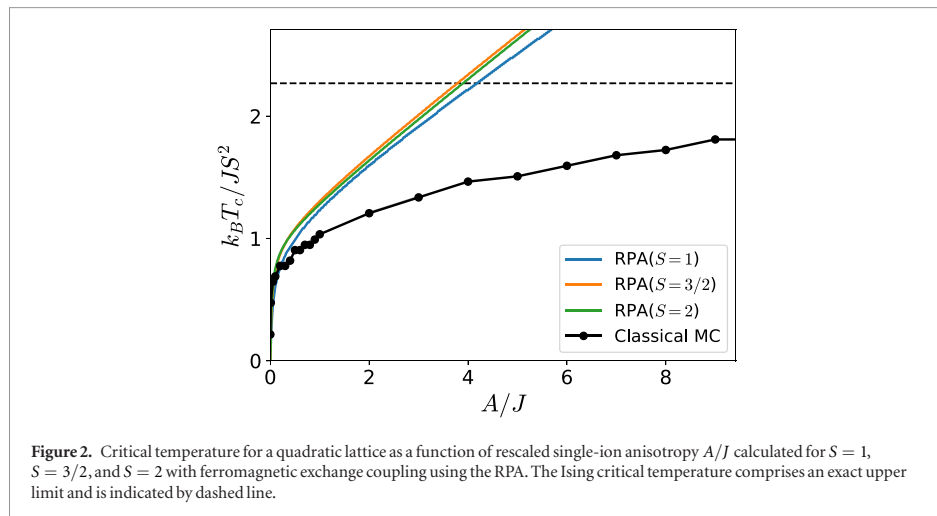
We can fit the classical simulations to an analytical function of the form.

$$T_c = T_c^{\text{Ising}} f(A/J), \quad (13)$$

with

$$f(x) = \tanh^{1/4} \left[\frac{6}{N_{nn}} \log(1 + \gamma x) \right] \quad (14)$$

where N_{nn} is the number of nearest neighbors and $\gamma = 0.033$. T_c^{Ising} is the critical temperatures for the corresponding Ising model, which can be written as $T_c^{\text{Ising}} = S^2 \tilde{T}_c / k_B$, where \tilde{T}_c is a dimensionless critical temperature with values of 1.52, 2.27, 2.27, and 3.64 for the honeycomb, quadratic, Kagomé, and hexagonal lattices respectively [27]. The fit was obtained by



noting that the critical temperature has a logarithmic dependence on the anisotropy at low temperature. It is thus natural to base the fit on the $\tanh(x)$ function, which Taylor expands to its arguments for $x \ll 1$ and approaches unity for $x \rightarrow \infty$. The exponent of $1/4$, γ and the factor of 6 in front of the log function were obtained by fitting. The comparison of the fit and classical MC simulations for the honeycomb, quadratic, and hexagonal lattices are shown in figure 3. It should be noted that the fit gives slightly lower values than the simulations at low values of A/J . However, for low values of A/J the classical simulations overestimate the critical temperatures compared with RPA and we expect that RPA is more accurate in this limit. Equations (13) and (14) are the main result of the present work and comprises a simple analytical approximation for Curie temperatures of 2D materials with single-ion anisotropy.

3.2. Anisotropic exchange

The situation become slightly more complicated when anisotropic exchange is also present ($B \neq 0$). To exemplify the qualitative differences between anisotropic exchange and single-ion anisotropy we start by considering the case of $A = 0$ for a quadratic lattice. The critical temperatures obtained with RPA and MC simulations are shown in figure 4 as a function of the anisotropic exchange parameter B . In the case of $B \gg J$ one obtains $H \approx \frac{B+J}{2} \sum S_i^z S_j^z$, which is equivalent to the Ising model when $S = 1/2$. However, for $S \geq 1$, the critical temperature is lowered compared to the Ising model due to the non-binary nature of S^z . In the limit of $B \gg J$, it may be argued that the values of $\pm S^z$ are favored for all sites, but when the critical temperature is approached the magnetization vanishes in a manner that is quite

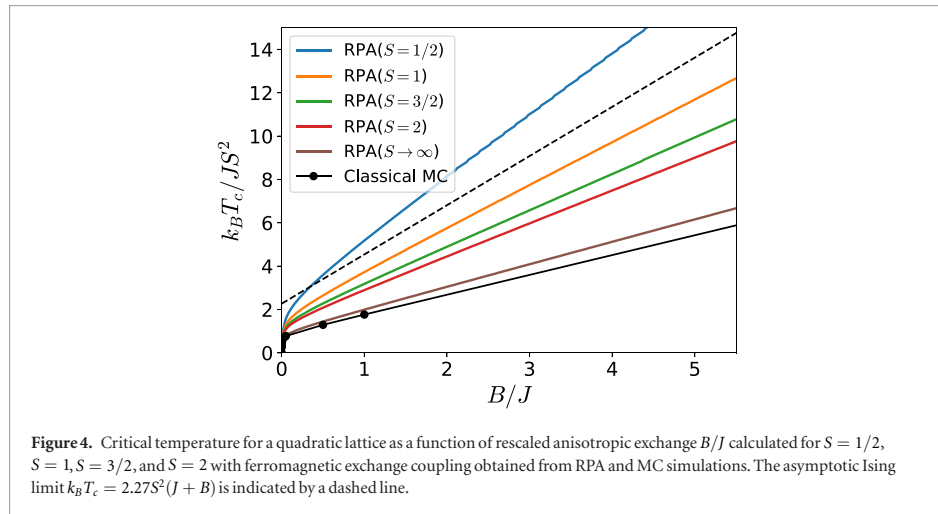


Figure 4. Critical temperature for a quadratic lattice as a function of rescaled anisotropic exchange B/J calculated for $S = 1/2$, $S = 1$, $S = 3/2$, and $S = 2$ with ferromagnetic exchange coupling obtained from RPA and MC simulations. The asymptotic Ising limit $k_B T_c = 2.27 S^2 (J + B)$ is indicated by a dashed line.

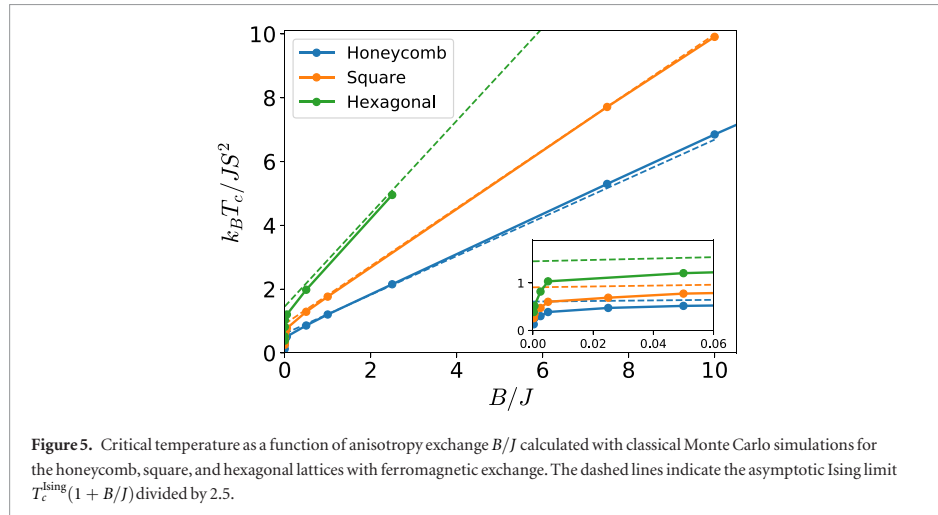


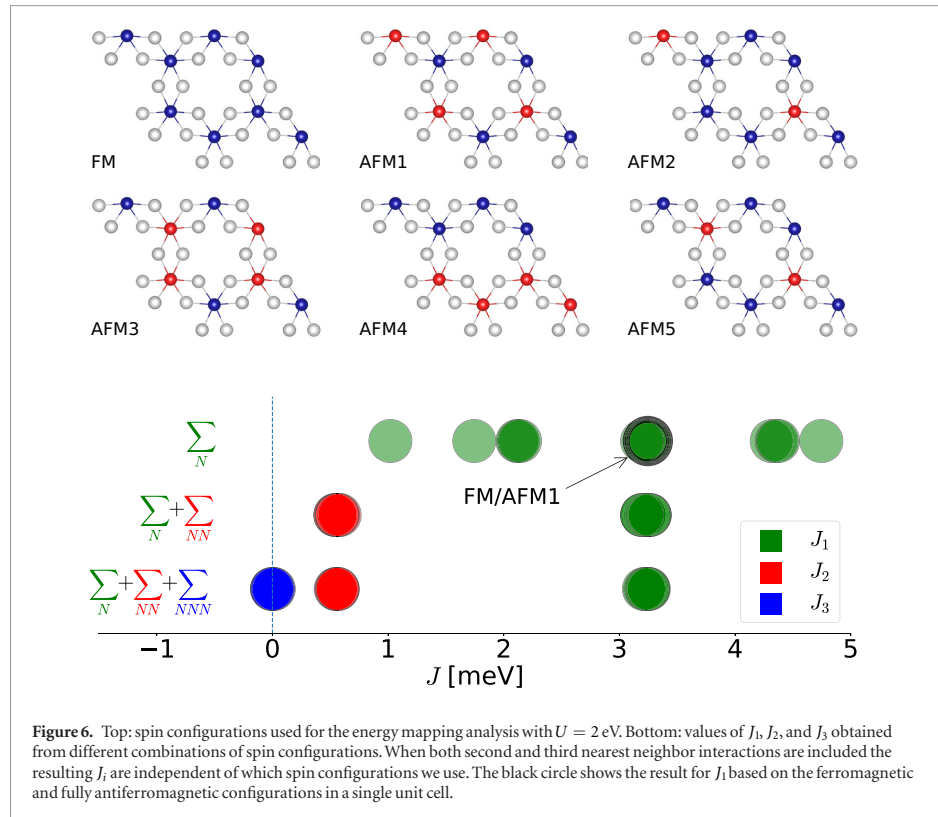
Figure 5. Critical temperature as a function of anisotropic exchange B/J calculated with classical Monte Carlo simulations for the honeycomb, square, and hexagonal lattices with ferromagnetic exchange. The dashed lines indicate the asymptotic Ising limit $T_c^{\text{sing}}(1 + B/J)$ divided by 2.5.

different from the Ising model, since the magnetization per site is allowed to decrease in addition to the effect of domain formation. From figure 4, it can be seen that RPA overestimates the asymptotic behavior of T_c as $B/J \rightarrow \infty$ due to the mean-field approximation for correlation effects. However, the classical limit of $S \rightarrow \infty$ is accurately captured by RPA, which agrees well with classical MC simulations. This is in sharp contrast to the case of single-ion anisotropy, where RPA fails completely in the classical limit.

The fact that the model becomes asymptotically equivalent to an Ising type model with continuous spin variables indicate that the asymptotic critical temperatures should resemble those of the Ising model but with an effective value of S that is smaller than the maximum value that enters in the Heisenberg model. For example, taking a spherical average of S_z such that $S^2 \rightarrow \langle S_z^2 \rangle_\Omega = S^2/3$ one obtains a decrease in the critical temperature by a factor

of three compared to the corresponding Ising model. By inspection of the classical simulations we find that $S^2 \rightarrow S^2/2.5$ provides good agreement with our simulations. This is shown in figure 5 for the honeycomb, square, and hexagonal lattices. However, we note that this is a strictly classical result and for $S = 1/2$ one should reproduce the Ising limit without any rescaling. For finite values of S , we expect a rescaling between unity and 2.5.

In order to include the anisotropic exchange in the one-parameter expression (13), we note that for $B = 0$, one can express the single-ion anisotropy in terms of the zero-temperature gap Δ as $A = \Delta/(2S - 1)$ (see equation (7)). For $B \neq 0$ the situation is more complicated due to the additional dispersion introduced by the anisotropic exchange. Nevertheless, if we choose to regard the zero temperature gap as the primary descriptor for the critical temperature we can write the critical temperature for $S \neq 1/2$ as



$$T_c = T_c^{\text{ising}} f\left(\frac{\Delta}{J(2S-1)}\right), \quad (15)$$

with

$$\Delta = A(2S-1) + BSN_m \quad (16)$$

and $f(x)$ given by equation (14).

3.3. Application to CrI_3

As a test example for the derived expression we consider a monolayer of CrI_3 , which has recently been shown to exhibit ferromagnetic order below 45 K [1]. We have extracted the Heisenberg model parameters from first principles in the framework of density functional theory. All calculations were performed using the GPAW code [28, 29] and the Perdew–Burke–Ernzerhof (PBE) functional [30] for exchange–correlation energies. We have included a Hubbard U correction to properly account for the localization of Cr d-orbitals. A cut-off energy of 800 eV for the plane wave basis and a Γ -centered Monkhorst–Pack k -point grid with a density of 6 \AA^{-3} have been used to ensure converged results. Monolayers were separated by 15 \AA vacuum and the atomic structure relaxed until all forces declined below 0.01 eV \AA^{-1} .

Magnetic moments of $3 \mu_B$ are localized on the Cr atoms and each Cr atom has three nearest neighbors. The exchange coupling constant can be extracted from

the energy differences between various spin configurations of the monolayer [31–36]. In order to calculate the nearest neighbor coupling constant J_1 , two configurations are required. However, it is important to check that the results are independent of, which configurations are used. We have thus considered a 2×2 unit cell and considered a total of 6 different spin configurations. Taking different combinations of these produce values of J_1 that range from 1 to 5 meV. Including the next nearest neighbor interaction J_2 reduces the spread somewhat and give values of J_1 in the range 3.1–3.3 meV. Finally including the third nearest neighbor interaction J_3 produces converged results that are independent of which spin configurations that we use. Five different combinations of the six spin configurations (four structures are needed to extract three parameters) all produce $J_1 = 3.24$ meV, $J_2 = 0.56$ meV and $J_3 = 0.001$ meV. If we simply consider the two possible magnetic configurations in a single unit cell we obtain $J_1 = 3.25$ meV (black ring in figure 6), which is very close to the converged result. Although J_2 and J_3 are required in order to obtain converged results these parameters are much smaller than J_1 and we expect that they will have small influence on the critical temperature. We will thus neglect the second and third nearest neighbor interaction in the following and simply use $J = J_1$ when applying the model (15).

The anisotropy parameters can be extracted by a calculations with spin–orbit coupling [37] by comparing the energies in-plane and out-of-plane spin configurations [12]. In particular

$$A = \frac{\Delta E_{\text{FM}} + \Delta E_{\text{AFM}}}{2S^2} \quad (17)$$

$$B = \frac{\Delta E_{\text{FM}} - \Delta E_{\text{AFM}}}{N_{nn}S^2}, \quad (18)$$

where $\Delta E_{\text{FM(AFM)}} = E_{\text{FM(AFM)}}^{(x)} - E_{\text{FM(AFM)}}^{(z)}$ are the energy differences per atom between in-plane and out-of-plane spin configurations for the ferromagnetic and antiferromagnetic structures and $N_{nn} = 3$ is the number of nearest neighbors. Using $U = 2$ eV we find

$$A^{\text{CrI}_3} = 0.056 \text{ meV}, \quad (19)$$

$$B^{\text{CrI}_3} = 0.22 \text{ meV}, \quad (20)$$

and from equation (16)

$$\Delta^{\text{CrI}_3} = 1.08 \text{ meV}, \quad (21)$$

which yields

$$T_c^{\text{CrI}_3} = 42 \text{ K}, \quad (22)$$

from equations (14)–(16). This is in excellent agreement with the experimental value of 45 K [1]. However, the result is somewhat sensitive to the choice of U and calculations with $U = 0$, $U = 1$, and $U = 3$ eV gives $T_c = 32$, $T_c = 37$, $T_c = 47$ K respectively. In general we observe that J and B increases while A decreases, when U is increased and the critical temperature is largely linear in U with $dT_c/dU = 5$ K eV⁻¹. In [12] the authors found $A = 0$, $B = 0.09$ meV, $J = 2.2$ meV and $\Delta = 0.4$ meV from GGA + U calculations, which is in somewhat disagreement with the present results. In particular, we find that single-ion anisotropy and anisotropic exchange contribute equal amounts to spin gap whereas in [12] it was found that single-ion anisotropy is negligible. The reasons for this discrepancy is presently unclear.

4. Discussion

To summarize, we have calculated the critical temperatures of various 2D lattices using the RPA and classical MC simulations as a function of single-ion anisotropy and anisotropic exchange. We find that RPA generally tend to overestimate critical temperatures and fails dramatically for large single-ion anisotropies. In contrast, the MC simulations capture the asymptotic Ising limit correctly and agrees reasonably well with RPA at small values of the anisotropy. We used the calculations to obtain an analytical fit for the critical temperature that only depends on the anisotropy constants, nearest neighbor exchange parameter and the (known) critical temperature of the Ising model for the lattices. Since all parameters are easily obtainable from first principles calculations, we expect that the expression will be highly useful for predicting critical

temperatures of novel 2D materials as well as verify the microscopic mechanism that underlie magnetic order in experimentally observed 2D ferromagnets.

It should be noted that other approximations to the Heisenberg model, might be better suited than the mean field approximation of the Holstein–Primakoff bosons considered in here. For example, a mean field treatment of the Schwinger bosons approach [38] has been successfully applied to describe the properties of ferrimagnetic systems [39] and antiferromagnetic Kagome lattices [40] and it would be very interesting to investigate the performance of such methods in future works.

The present results obtained from classical Monte Carlo simulations are largely based on classical simulations and are not expected to be valid for the the important case of $S = 1/2$ systems. Even for $S = 1$ and $S = 3/2$, it is hard to argue that a classical approach is reliable and the only evidence for the validity so far is the good agreement with the experimentally observed Curie temperature for CrI₃. To verify the reliability of the method it would thus be highly desirable to obtain accurate results based on either many-body techniques beyond the RPA [41] or quantum Monte Carlo simulations of the anisotropic Heisenberg model. Moreover, the first principles evaluation of the Heisenberg parameters seems to be rather sensitive to the exact approach used to calculate them and the exact values of the parameters are still debated [12]. Whereas spin waves [20] and critical exponents [42] have been measured in bulk CrI₃ there is not yet any direct measurements for a monolayer of CrI₃ and it is currently not possible to determine the Heisenberg parameters experimentally.

Presently, there are very few known purely 2D magnetic materials, which severely limits the possibilities of benchmarking *ab initio* calculations and models for magnetism in 2D against experimental observations. However, with the rapid developments in synthesis, characterization, and prediction of 2D materials [43–45], it is likely that several new magnetic 2D materials will be observed in the near future.

Acknowledgments

This work was supported by the Independent Research Fund Denmark, grant number 6108-00464A.

ORCID iDs

Thomas Olsen  <https://orcid.org/0000-0001-6256-9284>

References

- [1] Huang B *et al* 2017 *Nature* **546** 270
- [2] Jiang S, Shan J and Mak K F 2018 *Nat. Mater.* **17** 406
- [3] Huang C, Du Y, Wu H, Xiang H, Deng K and Kan E 2018 *Phys. Rev. Lett.* **120** 147601
- [4] Huang B *et al* 2018 *Nat. Nanotechnol.* **13** 544

- [5] Jiang S, Li L, Wang Z, Mak K F and Shan J 2018 *Nat. Nanotechnol.* **13** 549
- [6] Song T *et al* 2018 *Science* **360** 1214
- [7] Klein D R *et al* 2018 *Science* **360** 1218
- [8] Sachs B, Wehling T O, Novoselov K S, Lichtenstein A I and Katsnelson M I 2013 *Phys. Rev. B* **88** 201402
- [9] Zhuang H L and Hennig R G 2016 *Phys. Rev. B* **93** 1
- [10] McGuire M A 2017 *Crystals* **7** 121
- [11] Seyler K L *et al* 2017 *Nat. Phys.* **14** 277
- [12] Lado J L and Fernández-Rossier J 2017 *2D Mater.* **4** 035002
- [13] Miao N, Xu B, Zhu L, Zhou J and Sun Z 2018 *J. Am. Chem. Soc.* **140** 2417
- [14] Ersan F, Vatansever E, Sarikurt S, Yüksel Y, Kadioglu Y, Ozaydin H D, Aktürk O Ü, Akinci U and Aktürk E 2018 (arXiv: 1804.01560)
- [15] Gong C *et al* 2017 *Nature* **546** 265
- [16] Bonilla M, Kolekar S, Ma Y, Diaz H C, Kalappattil V, Das R, Eggers T, Gutierrez H R, Phan M-H and Batzill M 2018 *Nat. Nanotechnol.* **13** 289
- [17] Yosida K 1996 *Theory of Magnetism* (Berlin: Springer)
- [18] Anderson P W 1950 *Phys. Rev.* **79** 350
- [19] Anderson P W 1959 *Phys. Rev.* **115** 2
- [20] Samuelsen E J, Silbergliitt R, Shirane G and Remeika J P 1971 *Phys. Rev. B* **3** 157
- [21] Ami T, Crawford M K, Harlow R L, Wang Z R, Johnston D C, Huang Q and Erwin R W 1995 *Phys. Rev. B* **51** 5994
- [22] Bose S K and Kudrnovský J 2010 *Phys. Rev. B* **81** 054446
- [23] Johnston D C, McQueeney R J, Lake B, Honecker A, Zhitomirsky M E, Nath R, Furukawa Y, Antropov V P and Singh Y 2011 *Phys. Rev. B* **84** 094445
- [24] Rusz J, Bergqvist L, Kudrnovský J and Turek I 2006 *Phys. Rev. B* **73** 1
- [25] Bergqvist L, Eriksson O, Kudrnovský J, Drchal V, Korzhavyi P and Turek I 2004 *Phys. Rev. Lett.* **93** 137202
- [26] Bruno P 1991 *Phys. Rev. B* **43** 6015
- [27] Malarz K, Zborek M and Wrobel B 2005 *TASK Q.* **9** 475
- [28] Enkovaara J *et al* 2010 *J. Phys.: Condens. Matter* **22** 253202
- [29] Hjorth Larsen A *et al* 2017 *J. Phys.: Condens. Matter* **29** 273002
- [30] Perdew J P, Burke K and Ernzerhof M 1996 *Phys. Rev. Lett.* **77** 3865
- [31] Illas F and Martin R L 1998 *J. Chem. Phys.* **108** 2519
- [32] Ködderitzsch D, Hergert W, Temmerman W M, Szotek Z, Ernst A and Winter H 2002 *Phys. Rev. B* **66** 064434
- [33] Filippetti A and Fiorentini V 2005 *Phys. Rev. Lett.* **95** 086405
- [34] Xiang H, Lee C, Koo H-J, Gong X and Whangbo M-H 2013 *Dalton Trans.* **42** 823
- [35] Babkevich P *et al* 2016 *Phys. Rev. Lett.* **117** 237203
- [36] Olsen T 2017 *Phys. Rev. B* **96** 125143
- [37] Olsen T 2016 *Phys. Rev. B* **94** 235106
- [38] Auerbach A and Arovas D P 1998 *J. Appl. Phys.* **67** 5734
- [39] Wu C, Chen B C, Dai X, Yu Y and Su Z-B 1999 *Phys. Rev. B* **60** 1057
- [40] Mondal K and Kadolkar C 2017 *Phys. Rev. B* **95** 134404
- [41] Pershoguba S S, Banerjee S, Lashley J, Park J, Ågren H, Aepli G and Balatsky A V 2018 *Phys. Rev. X* **8** 011010
- [42] Liu Y and Petrovic C 2018 *Phys. Rev. B* **97** 014420
- [43] Zhou J *et al* 2018 *Nature* **556** 355
- [44] Mounet N *et al* 2018 *Nat. Nanotechnol.* **13** 246
- [45] Hastrup S *et al* 2018 *2D Mater.* **5** 042002

7.2 Paper II: The Computational 2D Materials Database: high-throughput modeling and discovery of atomically thin crystals

2D Materials

OPEN ACCESS

TOPICAL REVIEW



RECEIVED
28 March 2018

REVISED
8 June 2018

ACCEPTED FOR PUBLICATION
28 June 2018

PUBLISHED
7 September 2018

Original content from this work may be used under the terms of the [Creative Commons Attribution 3.0 licence](#).

Any further distribution of this work must maintain attribution to the author(s) and the title of the work, journal citation and DOI.



The Computational 2D Materials Database: high-throughput modeling and discovery of atomically thin crystals

Sten Hastrup¹, Mikkel Strange¹, Mohnish Pandey¹, Thorsten Deilmann¹, Per S Schmidt¹, Nicki F Hinsche¹, Morten N Gjerding^{1,2}, Daniele Torelli¹, Peter M Larsen¹, Anders C Riis-Jensen¹, Jakob Gath¹, Karsten W Jacobsen¹, Jens Jørgen Mortensen¹, Thomas Olsen¹ and Kristian S Thygesen^{1,2}

¹ CAMD, Department of Physics, Technical University of Denmark, 2800 Kgs. Lyngby, Denmark

² Center for Nanostructured Graphene (CNG), Technical University of Denmark, 2800 Kgs. Lyngby, Denmark

E-mail: thygesen@fysik.dtu.dk

Keywords: ab initio calculations, opto-electronic properties, database, materials discovery, materials design, 2D materials, many-body perturbation theory

Abstract

We introduce the Computational 2D Materials Database (C2DB), which organises a variety of structural, thermodynamic, elastic, electronic, magnetic, and optical properties of around 1500 two-dimensional materials distributed over more than 30 different crystal structures. Material properties are systematically calculated by state-of-the-art density functional theory and many-body perturbation theory (G_0W_0 and the Bethe–Salpeter equation for ~ 250 materials) following a semi-automated workflow for maximal consistency and transparency. The C2DB is fully open and can be browsed online (<http://c2db.fysik.dtu.dk>) or downloaded in its entirety. In this paper, we describe the workflow behind the database, present an overview of the properties and materials currently available, and explore trends and correlations in the data. Moreover, we identify a large number of new potentially synthesisable 2D materials with interesting properties targeting applications within spintronics, (opto-)electronics, and plasmonics. The C2DB offers a comprehensive and easily accessible overview of the rapidly expanding family of 2D materials and forms an ideal platform for computational modeling and design of new 2D materials and van der Waals heterostructures.

1. Introduction

Over the past decade, atomically thin two-dimensional (2D) materials have made their way to the forefront of several research areas including batteries, (electro-) catalysis, electronics, and photonics [1, 2]. This development was prompted by the intriguing and easily tunable properties of atomically thin crystals and has been fueled by the constant discovery of new 2D materials and the emergent concepts of lateral [3] and vertical [4] 2D heterostructures, which opens completely new possibilities for designing materials with tailored and superior properties.

So far more than fifty compounds have been synthesised or exfoliated as single layers (see figure 7). These include the well known mono-elemental crystals (Xenes, e.g. graphene, phosphorene) [5] and their ligand functionalised derivatives (Xanes, e.g. CF, GeH) [6], transition metal dichalcogenides (TMDCs, e.g. MoS_2 , TaSe_2) [7], transition metal carbides and -nitrides (MXenes, e.g. Ti_2CO_2) [8], group III–V

semiconductors and insulators (e.g. GaN, BN) [9, 10], transition metal halides (e.g. CrI_3) [11, 12], post-transition metal chalcogenides (e.g. GaS and GaSe) [13, 14] and organic-inorganic hybrid perovskites (e.g. $\text{Pb}(\text{C}_4\text{H}_9\text{NH}_3)_2\text{I}_4$) [15]. However, the already known monolayers are only the tip of a much larger iceberg. Indeed, recent data mining studies indicate that several hundred 2D materials could be exfoliated from known layered bulk crystals [16–19]. In the present work we take a complementary approach to 2D materials discovery based on combinatorial lattice decoration and identify another few hundred previously unknown and potentially synthesisable monolayers.

In the search for new materials with tailored properties or novel functionalities, first-principles calculations are playing an increasingly important role. The continuous increase in computing power and significant advancements of theoretical methods and numerical algorithms have pushed the field to a point where first-principles calculations are comparable to experiments in terms of accuracy and greatly

surpass them in terms of speed and cost. For more than a century, experimental databases on e.g. structural, thermal, and electronic properties, have been a cornerstone of materials science, and in the past decade, the experimental data have been augmented by an explosion of computational data obtained from first-principles calculations. Strong efforts are currently being focused on storing and organising the computational data in open repositories [20, 21]. Some of the larger repositories, together containing millions of material entries, are the Materials Project [22], the Automatic Flow for Materials Discovery (AFLOW-LIB) [23], the Open Quantum Materials Database (OQMD) [24, 25], and the Novel Materials Discovery (NOMAD) Repository [26].

The advantages of computational materials databases are many. Most obviously, they facilitate open sharing and comparison of research data whilst reducing duplication of efforts. In addition, they underpin the development and benchmarking of new methods by providing easy access to common reference systems [27]. Finally, the databases enable the application of machine learning techniques to identify deep and complex correlations in the materials space and to use them for designing materials with tailored properties and for accelerating the discovery of new materials [28–30]. Among the challenges facing the computational databases is the quality of the stored data, which depends both on the numerical precision (e.g. the employed k -point grid and basis set size) and the accuracy of the employed physical models (e.g. the exchange-correlation functional). Most of the existing computational databases store results of standard density functional theory (DFT) calculations. While such methods, when properly conducted, are quite reliable for ground state properties such as structural and thermodynamic properties, they are generally not quantitatively accurate for excited state properties such as electronic band structures and optical absorption spectra.

Compared to databases of bulk materials, databases of 2D materials are still few and less developed. Early work used DFT to explore the stability and electronic structures of monolayers of group III–V honeycomb lattices [31, 32] and the class of MX_2 transition metal dichalcogenides and oxides [33]. Later, by data-filtering the inorganic crystal structure database (ICSD), 92 experimentally known layered crystals were identified and their electronic band structures calculated at the DFT level [34]. Another DFT study, also focused on stability and band structures, explored around one hundred 2D materials selected from different structure classes [35]. To overcome the known limitations of DFT, a database with many-body G_0W_0 band structures for 50 semiconducting TMDCs was established [36]. Very recently, data mining of the Materials Project and experimental crystal structure databases in the spirit of [34], led to the identification of close to one thousand experimentally known layered crystals from which single layers could potentially be exfoliated

[16–19]. These works also computed basic energetic, structural and electronic properties of the monolayers (or at least selected subsets) at the DFT level.

In this paper, we introduce the open Computational 2D Materials Database (C2DB) which organises a variety of *ab initio* calculated properties for more than 1500 different 2D materials. The key characteristics of the C2DB are:

- **Materials:** the database focuses entirely on 2D materials, i.e. isolated monolayers, obtained by combinatorial lattice decoration of known crystal structure prototypes.
- **Consistency:** all properties of all materials are calculated using the same code and parameter settings following the same workflow for maximum transparency, reproducibility, and consistency of the data.
- **Properties:** the database contains a large and diverse set of properties covering structural, thermodynamic, magnetic, elastic, electronic, dielectric and optical properties.
- **Accuracy:** Hybrid functionals (HSE06) as well as beyond-DFT many-body perturbation theory (G_0W_0) are employed to obtain quantitatively accurate band structures, and optical properties are obtained from the random phase approximation (RPA) and Bethe–Salpeter equation (BSE).
- **Openness:** the database is freely accessible and can be directly downloaded and browsed online using simple and advanced queries.

The systematic combinatorial approach used to generate the structures in the database inevitably produces many materials that are unstable and thus unrealistic and impossible to synthesise in reality. Such ‘hypothetical’ structures may, however, still be useful in a number of contexts, e.g. for method development and benchmarking, testing and training of machine learning algorithms, identification of trends and structure-property relationships, etc. For this reason we map out the properties of all but the most unstable (and thus chemically unreasonable) compounds. Nevertheless, the reliable assessment of stability and synthesisability of the candidate structures is an essential issue. Using the 55 materials in the C2DB, which have been experimentally synthesised in monolayer form, as a guideline, we set down the criteria that a hypothesised 2D material should fulfill in order for it to be ‘likely synthesisable’. On the basis of these criteria, we introduce a simple *stability scale* to quantify a candidate material’s dynamic and thermodynamic stability. Out of an initial set of around 1900 monolayers distributed over 32 different crystal structures, we find 350 in the most stable category. In addition to the 55 experimentally synthesised monolayers, this set also includes around 80 monolayers from experimentally known vdW layered bulk materials, and thus around 200 completely new and potentially synthesisable 2D materials.

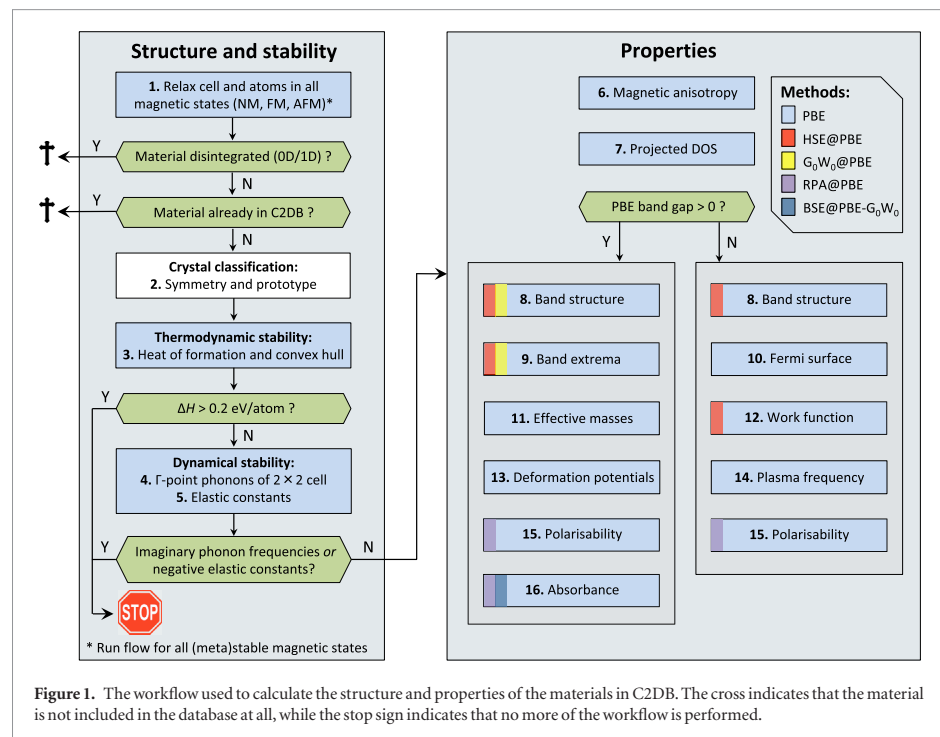


Figure 1. The workflow used to calculate the structure and properties of the materials in C2DB. The cross indicates that the material is not included in the database at all, while the stop sign indicates that no more of the workflow is performed.

In section 2, we describe the computational workflow behind the database. The structure and properties of the materials are calculated using well established state-of-the-art methodology. Technical descriptions of the different steps in the workflow are accompanied by illustrative examples and comparisons with literature data. Since *documentation and validation* is the main purpose of the section, we deliberately focus on well known 2D materials like the Xenex and transition metal dichalcogenides where plenty of both computational and experimental reference data is available. It should be clear that the novelty of the present work does not lie in the employed methodology nor in the type of materials properties that we calculate (we note, however, that to the best of our knowledge the present compilation of GW and BSE calculations represents the largest of its kind reported so far). The significance of our work is rather reflected by the fact that when large and consistently produced data sets are organised and made easily accessible, new scientific opportunities arise. As outlined below, this paper presents several examples of this effect.

In section 3 we give an overview of the materials and the data contained in the C2DB and provide some specific examples to illustrate its use. Using an extensive set of many-body G_0W_0 calculations as a reference, we establish the performance of various DFT xc-functionals for predicting band gaps, band edge positions, and band alignment at hetero-interfaces, and we propose an optimal strategy for obtaining accurate band energies at low computational cost. Similarly,

the 250 BSE calculations allow us to explore trends in exciton binding energies and perform a statistically significant and unbiased assessment of the accuracy and limitations of the widely used Mott–Wannier model for 2D excitons. From the data on more than 600 semiconductor monolayers, we present strong empirical evidence against an often employed relation between effective masses and band gaps derived from $\mathbf{k} \cdot \mathbf{p}$ perturbation theory. Inspired by the potential of using 2D materials as building blocks for plasmonics and photonics, we propose a model to predict the plasmon dispersion relations in 2D metals from the (intraband) plasma frequency and the onset of interband transitions and use it to identify 2D metals with plasmons in the optical frequency regime. We propose several new magnetic 2D materials (including both metals and semiconductors) with ferromagnetic or anti-ferromagnetic ordering and significant out-of-plane magnetic anisotropy. Finally, we point to new high-mobility 2D semiconductors including some with band gaps in the range of interest for (opto)electronic applications.

In section 4 we provide our conclusions together with an outlook discussing some opportunities and possible future directions for the C2DB.

2. Workflow

The workflow used to generate the data in the C2DB is illustrated in figure 1. It consists of two parts: In the first part (left panel) the unit cell and atom positions

are optimised for different magnetic configurations: non-magnetic (NM), ferro-magnetic (FM) and antiferro-magnetic (AFM). Materials satisfying certain stability and geometry criteria (indicated by green boxes) are subject to the second part (right panel) where the different properties are computed using DFT and many-body methods. The G_0W_0 band structure and BSE absorbance calculations have been performed only for semiconducting materials with up to four atoms in the unit cell. Per default, properties shown in the online database include spin-orbit coupling (SOC); however, to aid comparison with other calculations, most properties are also calculated and stored without SOC.

All DFT and many-body calculations are performed with the projector augmented wave code GPAW [37] using plane wave basis sets and PAW potentials version 0.9.2. The workflow is managed using the Python based atomic simulation environment (ASE) [38]. We have developed a library of robust and numerically accurate (convergence verified) ASE-GPAW scripts to perform the various tasks of the workflow, and to create the database afterwards. The library is freely available, under a GPL license.

Below we describe all steps of the workflow in detail. As the main purpose is to document the workflow, the focus is on technical aspects, including numerical convergence and benchmarking. An overview of the most important parameters used for the different calculations is provided in table 1.

2.1. Structure relaxation

The workflow is initiated with a crystal structure defined by its unit cell (Bravais lattice and atomic basis). The crystal lattice is typically that of an experimentally known prototype (the ‘seed structure’) decorated with atoms picked from a subset of the periodic table, see figure 2. We refer to materials by the chemical formula of their unit cell followed by the crystal structure. The latter is indicated by a representative material of that prototype, as described in section 3.1. For example, monolayer MoS_2 in the hexagonal H and T phases are denoted $\text{MoS}_2\text{-MoS}_2$ and $\text{MoS}_2\text{-CdI}_2$, respectively. Now, MoS_2 is in fact not stable in the T phase, but undergoes a 2×1 distortion to the so-called T’ phase. Because the T’ phase is the thermodynamically stable phase of WTe_2 , we denote MoS_2 in the distorted T phase by $\text{Mo}_2\text{S}_4\text{-WTe}_2$. In the following, we shall refer to the unit cell with which the workflow is initiated, i.e. the unit cell of the seed structure, as the primitive cell or the 1×1 cell, even if this cell is not dynamically stable for the considered material (see section 2.4).

The unit cell and internal coordinates of the atoms are relaxed in both a spin-paired (NM), ferromagnetic (FM), and anti-ferromagnetic (AFM) configuration. Calculations for the AFM configuration are performed only for unit cells containing at least two metal atoms.

The symmetries of the initial seed structure are kept during relaxation. All relevant computational details are provided in table 1.

After relaxation, we check that the structure has remained a covalently connected 2D material and not disintegrated into 1D or 0D clusters. This is done by defining clusters of atoms using the covalent radius [39] + 30% as a measure for covalent bonds between atoms. The dimensionality of a cluster is obtained from the scaling of the number of atoms in a cluster upon repetition of the unit cell following the method described by Ashton *et al* [16]. Only materials containing exactly one cluster of dimensionality 2 are given further consideration (an exception is made for the metal-organic perovskites (prototype PbA_2I_4) for which the metal atom inside the octahedron represents a 0D cluster embedded in a 2D cluster). To illustrate the effect of the covalent radius + 30% threshold, figure 3 shows the distribution of the candidate structures in the database as a function of the covalent factor needed to fully connect the structure. Most materials have a critical covalent factor below 1.3 and fall in the green shaded region. There is, however, a tail of around 100 disconnected materials (red region); these materials are not included in the database (see first green box in figure 1).

We also check that the material is not already contained in the database (second green box in figure 1). This is done by measuring the root mean square distance (RMSD) [40] relative to all other materials in the C2DB with the same reduced chemical formula. A threshold of 0.01 Å is used for this test.

In case of multiple metastable magnetic configurations (in practice, if both a FM and AFM ground state are found), these are regarded as different phases of the same material and will be treated separately throughout the rest of the workflow. To indicate the magnetic phase we add the extensions ‘FM’ or ‘AFM’ to the material name. The total energy of the spin-paired ground state is always stored, even when it is not the lowest. If the energy of the non-magnetic state is higher than the most stable magnetic state by less than 10 meV/atom, the workflow is also performed for the non-magnetic state. This is done in recognition of the finite accuracy of DFT for predicting the correct energetic ordering of different magnetic states.

We have compared the lattice constants of 29 monolayers with those reported in [41], which were obtained with the VASP code using PBE and very similar numerical settings and find a mean absolute deviation of 0.024 Å corresponding to 0.4%. The small yet finite deviations are ascribed to differences in the employed PAW potentials.

2.2. Crystal structure classification

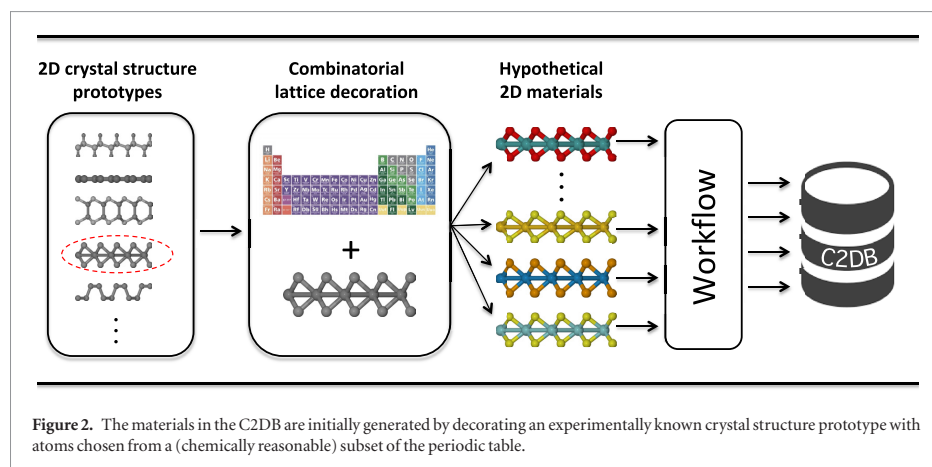
2.2.1. Symmetry

To classify the symmetries of the crystal structure the 3D space group is determined using the crystal

Table 1. Overview of the methods and parameters used for the different steps of the workflow. If a parameter is not specified at a given step, its value equals that of the last step where it was specified.

| Workflow step(s) | Parameters |
|---|---|
| Structure and energetics (1–4) ^a | vacuum = 15 Å; k -point density = $6.0/\text{Å}^{-3}$; Fermi smearing = 0.05 eV; PW cutoff = 800 eV; xc functional = PBE; maximum force = 0.01 eV/Å; maximum stress = $0.002 \text{ eV}/\text{Å}^3$; phonon displacement = 0.01 Å |
| Elastic constants (5) | k -point density = $12.0/\text{Å}^{-3}$; strain = $\pm 1\%$ |
| Magnetic anisotropy (6) | k -point density = $20.0/\text{Å}^{-3}$; spin-orbit coupling = True |
| PBE electronic properties (7–10 and 12) | k -point density = $12.0/\text{Å}^{-3}$ ($36.0/\text{Å}^{-3}$ for step 7) |
| Effective masses (11) | k -point density = $45.0/\text{Å}^{-3}$; finite difference |
| Deformation potential (13) | k -point density = $12.0/\text{Å}^{-3}$; strain = $\pm 1\%$ |
| Plasma frequency (14) | k -point density = $20.0/\text{Å}^{-3}$; tetrahedral interpolation |
| HSE band structure (8–12) | HSE06@PBE; k -point density = $12.0/\text{Å}^{-3}$ |
| G_0W_0 band structure (8, 9) | G_0W_0 @PBE; k -point density = $5.0/\text{Å}^{-3}$; PW cutoff = ∞ (extrapolated from 170, 185 and 200 eV); full frequency integration; analytical treatment of $W(q)$ for small q ; truncated Coulomb interaction |
| RPA polarisability (15) | RPA@PBE; k -point density = $20.0/\text{Å}^{-3}$; PW cutoff = 50 eV; truncated Coulomb interaction; tetrahedral interpolation |
| BSE absorbance (16) | BSE@PBE with G_0W_0 scissors operator; k -point density = $20.0/\text{Å}^{-3}$; PW cutoff = 50 eV; truncated Coulomb interaction; at least 4 occupied and 4 empty bands |

^a For the cases with convergence issues, we set a k -point density of 9.0 and a smearing of 0.02 eV.



symmetry library Spglib [42] on the 3D supercell with a tolerance of 10^{-4} Å.

2.2.2. Prototypes

The materials are classified into crystal structure prototypes based on the symmetry of the crystals. For two materials to belong to the same prototype, we require that they have the same space group, the same stoichiometry, and comparable thicknesses. The last requirement is included to distinguish between materials with the same symmetry and stoichiometry but with different number of atomic layers, see for example monolayer BN and GaS in figure 4. Each prototype is labelled by a specific representative material. For prototypes which have been previously

investigated, we comply with the established conventions. However, since the field of 2D materials is still young and because C2DB contains a large number of never-synthesised materials, some of the considered crystal structures fall outside the known prototypes. In these cases we have chosen the representative material to be the one with the lowest energy with respect to the convex hull. Some of the crystal structure prototypes presently contained in the C2DB are shown in figure 4.

2.3. Thermodynamic stability

The heat of formation, ΔH , is defined as the energy of the material with respect to the standard states of its constituent elements. For example, the heat of formation per atom of a binary compound, A_xB_y , is

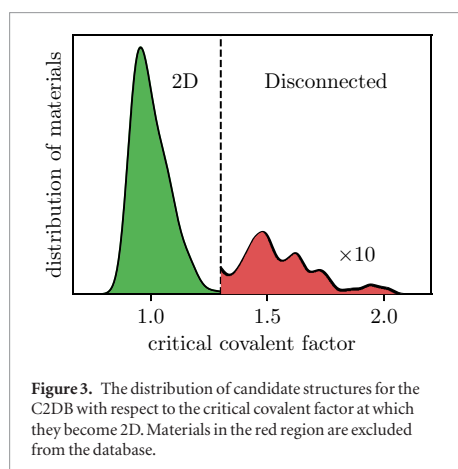


Figure 3. The distribution of candidate structures for the C2DB with respect to the critical covalent factor at which they become 2D. Materials in the red region are excluded from the database.

$$\Delta H = (E(A_xB_y) - xE(A) - yE(B))/(x + y), \quad (1)$$

where $E(A_xB_y)$ is the total energy of the material A_xB_y , and $E(A)$ and $E(B)$ are the total energies of the elements A and B in their standard state. When assessing the stability of a material in the C2DB, it should be kept in mind that the accuracy of the PBE functional for the heat of formation is only around 0.2 eV/atom on average [43]. Other materials databases, e.g. OQMD, Materials Project, and AFLOW, employ fitted elementary reference energies (FERE) [44] and apply a Hubbard U term [45] for the rare earth and transition metal atoms (or a selected subset of them). While such correction schemes in general improve ΔH they also introduce some ambiguity, e.g. the dataset from which the FERE are determined or the exact form of the orbitals on which the U term is applied. Thus in order not to compromise the transparency and reproducibility of the data we use the pure PBE energies.

For a material to be thermodynamically stable it is necessary but not sufficient that $\Delta H < 0$. Indeed, thermodynamic stability requires that ΔH be negative not only relative to its pure elemental phases but relative to all other competing phases, i.e. its energy must be below the *convex hull* [46]. We stress, however, that in general, but for 2D materials in particular, this definition cannot be directly applied as a criterion for stability and synthesizability. The most important reasons for this are (i) the intrinsic uncertainty on the DFT energies stemming from the approximate xc-functional (ii) substrate interactions or other external effects that can stabilise the monolayer (iii) kinetic barriers that separate the monolayer from other lower energy phases rendering the monolayer (meta)stable for all practical purposes.

We calculate the energy of the 2D material relative to the convex hull of competing bulk phases, ΔH_{hull} . The convex hull is currently constructed from the 2836 most stable binary bulk compounds which were obtained from the OQMD [24]. The energies of the

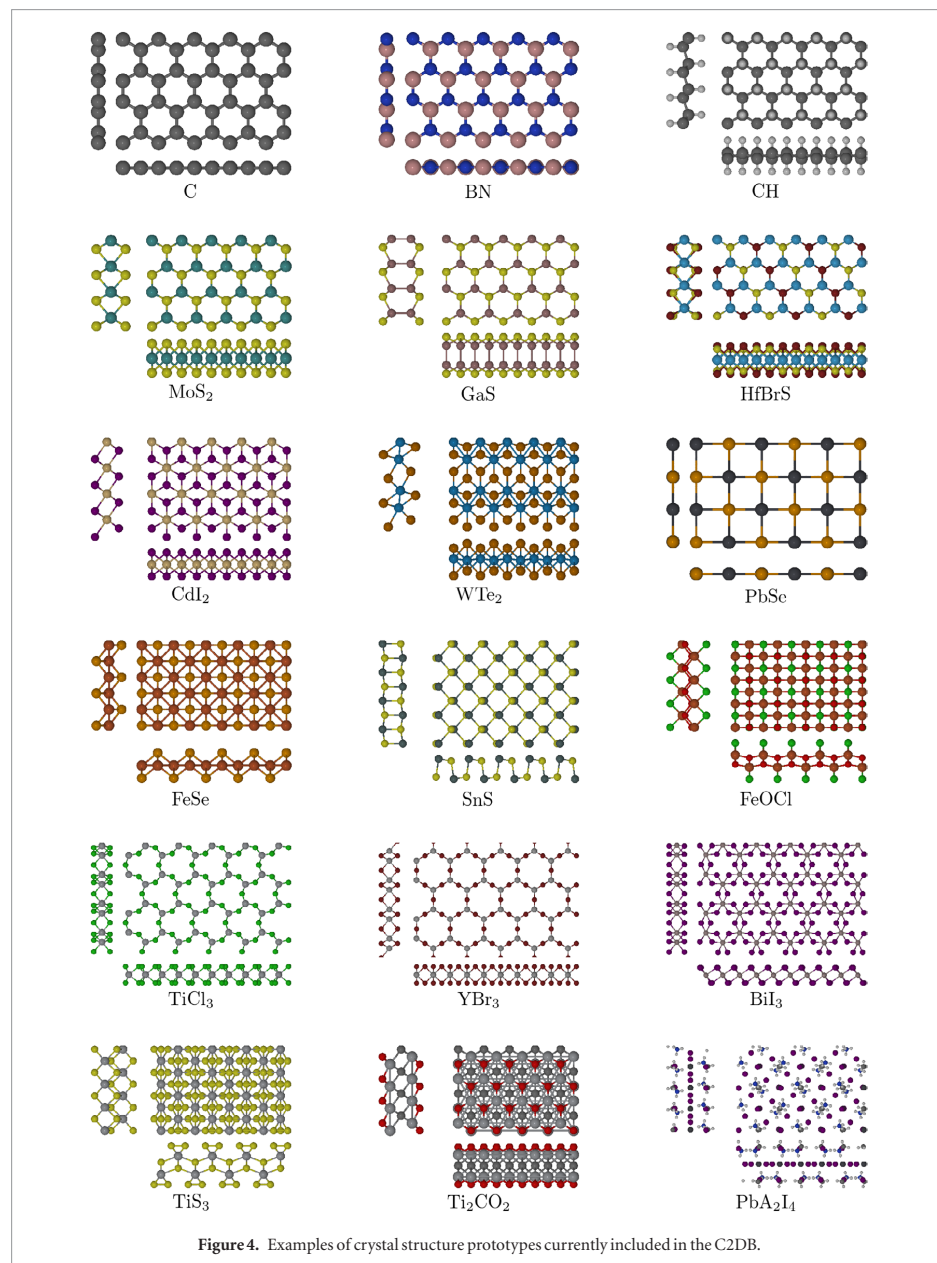
bulk phases were recalculated with GPAW using the PBE xc-functional and the same numerical settings as applied for the 2D materials (but the structure was not re-optimised). Because the bulk reference structures from OQMD were optimised with the VASP code and with Hubbard U corrections for materials containing 3d elements, and because the PBE misses attractive vdW interaction, the bulk energies could be slightly overestimated relative to the monolayers. As a consequence, monolayers that also exist in a layered bulk phase could have $\Delta H_{\text{hull}} < 0$, even if the layered bulk phase is part of the convex hull and thus should be energetically more stable than the monolayer. Comparing our ΔH_{hull} values for 35 compounds with the exfoliation energies calculated in [18] employing vdW compliant xc-functionals for both bulk and monolayer, we estimate the errors in the convex hull energies to be below 0.1 eV/atom.

As an example, the convex hull for $\text{Fe}_x\text{Se}_{1-x}$ is shown in figure 5. The convex hull as defined by the bulk binaries is indicated by the blue lines. The labels for the 2D materials refer to the crystal prototype and magnetic order. Clearly, most 2D materials lie above the convex hull and are thus predicted to be thermodynamically unstable in freestanding form under standard conditions. However, as mentioned above, depending on the material, errors on the PBE formation energies can be sizable and thus the hull diagram should only be taken as guideline. Nevertheless, in the present example we find that FeSe (which is itself a prototype) with anti-ferromagnetic ordering lies slightly below the convex hull and is thus predicted to be thermodynamically stable. This prediction is consistent with the recent experimental observation that monolayer FeSe deposited on SrTiO_3 exhibits AFM order [47].

2.4. Phonons and dynamic stability

Due to the applied symmetry constraints and/or the limited size of the unit cell, there is a risk that the structure obtained after relaxation does not represent a local minimum of the potential energy surface, but only a saddle point. We test for dynamical stability by calculating the Γ -point phonons of a 2×2 repeated cell (without re-optimising the structure) as well as the elastic constants (see section 2.5). These quantities represent second-order derivatives of the total energy with respect to atom displacements and unit cell lengths, respectively, and negative values for either quantity indicate a structural instability.

The Γ -point phonons of the 2×2 supercell are obtained using the finite displacement method [48]. We displace each atom in the primitive cell by $\pm 0.01 \text{ \AA}$, and calculate the forces induced on all the atoms in the supercell. From the forces we construct the dynamical matrix, which is diagonalised to obtain the Γ -point phonons of the 2×2 cell (or equivalently the Γ -point and zone boundary phonons of the primitive cell). The eigenvalues of the dynamical matrix correspond to the



square of the mass-renormalised phonon frequencies, $\tilde{\omega}$. Negative eigenvalues are equivalent to imaginary frequencies and signal a saddle point.

Our procedure explicitly tests for stability against local distortions of periodicities up to 2×2 and thus provides a necessary, but not sufficient condition for dynamic stability. We stress, however, that even in cases where a material would spontaneously relax into a structure with periodicity larger than 2×2 , the Γ -point dynamical matrix of the 2×2 cell could

exhibit negative eigenvalues. Our test is thus more stringent than it might seem at first glance. In principle, a rigorous test for dynamic stability would require the calculation of the full phonon band structure. Mathematically, the instabilities missed by our approach are those that result in imaginary phonons in the interior of the BZ but *not* at the zone boundary. Physically, such modes could be out of plane buckling or charge density wave-driven reconstructions with periodicities of several unit cells. In general, however, these types of

instabilities are typically rather weak (as measured by the magnitude of the imaginary frequency) as compared to more local distortions such as the T to T' distortion considered below. Moreover, they could well be a special property of the isolated monolayer and become stabilised by the ubiquitous interactions of the 2D material with its environment, e.g. substrates. This is in fact supported by the full phonon calculations by Mounet *et al* for ~ 250 isolated monolayers predicted to be easily exfoliable from experimentally known layered bulk phases [18]. Indeed, most of the instabilities revealed by their calculations are of the type described above and would thus be missed by our test. However, these instabilities cannot be too critical as the monolayers are known to be stable in the vdW bonded layered bulk structure.

As an example, figure 6 compares the dynamical stability of a subset of transition metal dichalcogenides and -oxides in the T and T' phases (CdI₂ and WTe₂ prototypes). The two upper panels show the smallest eigenvalue of the Γ -point dynamical matrix of the 2×2 cell. Only materials above the dashed line are considered dynamically stable (for this example we do not consider the sign of the elastic constants which could further reduce the set of dynamically stable materials). Since the unit cell of the T' phase contains that of the T phase it is likely that a material initially set up in the T' phase relaxes back to the T phase. To identify these cases, and thereby avoid the presence of duplicates in the database, the third panel shows the root mean square distance (RMSD) between the structures obtained after relaxations starting in the T- and T' phase, respectively. Structures below the dashed line are considered identical. The color of each symbol refers to the four different potential energy surfaces illustrated at the bottom of the figure.

2.4.1. Stability criteria

To assess the stability of the materials in the C2DB, we turn to the set of experimentally synthesised/exfoliated monolayers. For these materials, the calculated energy above the convex hull and minimum eigenvalue of the dynamical matrix are shown on figure 7. It is clear that all but five known monolayers have a hull energy below 0.2 eV/atom, and three of these have only been synthesised on a metal substrate. Turning to the dynamical stability, all but one of the experimentally known monolayers have a minimum eigenvalue of the dynamical matrix above -2 eV \AA^{-2} , and 70% have a minimum eigenvalue above $-1 \times 10^{-5} \text{ eV \AA}^{-2}$.

Guided by these considerations, we assign each material in the C2DB a stability level (low, medium or high) for both dynamical and thermodynamic stability, as illustrated in table 2. For ease of reference, we also define the overall stability level of a given material as the lower of the dynamical and thermodynamic stability levels. If a material has 'low' overall stability (marked by bold in the table), we consider it unstable and do not carry out the rest of the workflow. Materials

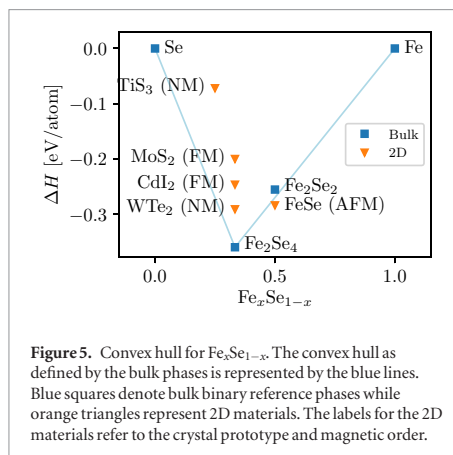


Figure 5. Convex hull for $\text{Fe}_x\text{Se}_{1-x}$. The convex hull as defined by the bulk phases is represented by the blue lines. Blue squares denote bulk binary reference phases while orange triangles represent 2D materials. The labels for the 2D materials refer to the crystal prototype and magnetic order.

with 'high' overall stability are considered likely to be stable and thus potentially synthesisable. Materials in the 'medium' stability category, while unlikely to be stable as freestanding monolayers, cannot be discarded and might be metastable and possible to synthesise under the right conditions. For example, freestanding silicene has a heat of formation of 0.66 eV/atom, but can be grown on a silver substrate. Likewise, the T' phase of MoS₂ (WTe₂ prototype) has an energy of 0.27 eV/atom higher than the thermodynamically stable H phase, but can be stabilised by electron doping.

2.5. Elastic constants

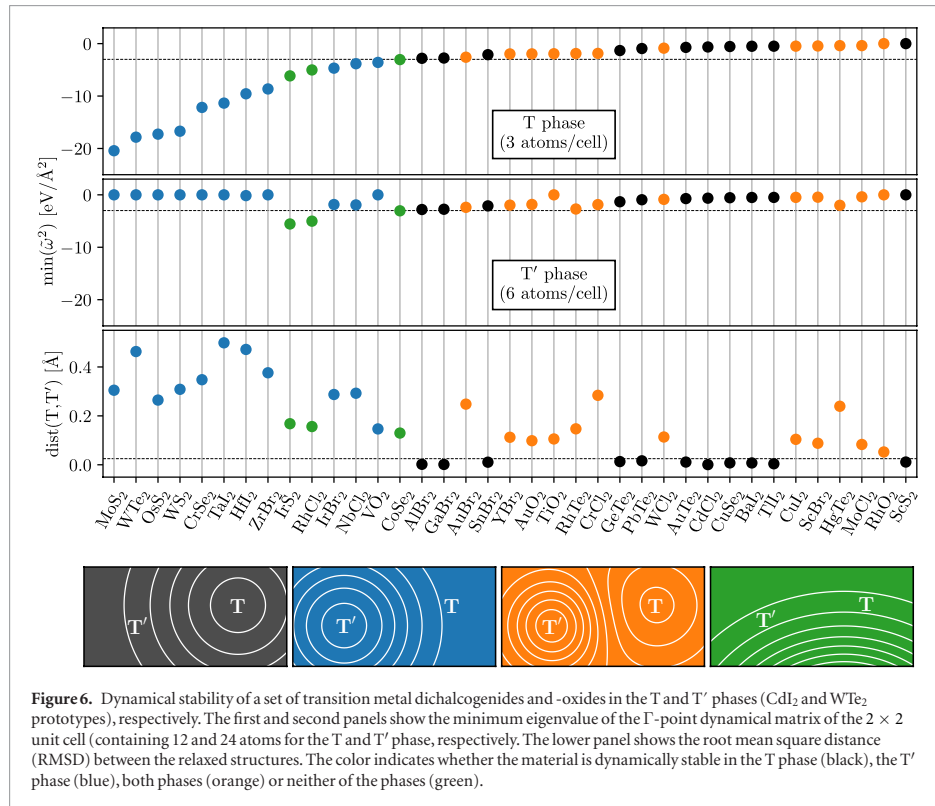
The elastic constants of a material are defined by the generalised Hooke's law,

$$\sigma_{ij} = C_{ijkl}\varepsilon_{kl} \quad (2)$$

where σ_{ij} , C_{ijkl} and ε_{kl} are the stress, stiffness and strain tensors, respectively, and where we have used the Einstein summation convention. In two dimensions, the stress and strain tensors have three independent components, namely planar stress/strain in the x and y directions, as well as shear stress/strain. The stiffness tensor is a symmetric linear map between these two tensors, and therefore has up to six independent components. Disregarding shear deformations, the relationship between planar strain and stress is

$$\begin{bmatrix} \sigma_{xx} \\ \sigma_{yy} \end{bmatrix} = \begin{bmatrix} C_{11} & C_{12} \\ C_{12} & C_{22} \end{bmatrix} \begin{bmatrix} \varepsilon_{xx} \\ \varepsilon_{yy} \end{bmatrix}. \quad (3)$$

For all materials in the C2DB, we calculate the planar elastic stiffness coefficients C_{11} , C_{22} , and C_{12} . These are calculated using a central difference approximation to the derivative of the stress tensor: the material is strained along one of the coordinate axes, x or y , and the stress tensor is calculated after the ions have relaxed. We use strains of $\pm 1\%$ which we have found to be sufficiently large to eliminate effects of numerical



noise and sufficiently small to stay within the linear response regime.

Table 3 shows the calculated planar stiffness coefficients of a set of 2D materials. As can be seen the values from the C2DB are in very good agreement with previously published PBE results. For the isotropic materials MoS₂, WSe₂ and WS₂, C₁₁ and C₂₂ should be identical, and we see a variation of up to 0.6%. This provides a test of how well converged the values are with respect to numerical settings.

2.6. Magnetic anisotropy

The energy dependence on the direction of magnetisation, or magnetic anisotropy (MA), arises from spin-orbit coupling (SOC). According to the magnetic force theorem [96] this can be evaluated from the eigenvalue differences such that the correction to the energy becomes

$$\Delta E(\hat{\mathbf{n}}) = \sum_{\mathbf{kn}} f(\varepsilon_{\mathbf{kn}}^{\hat{\mathbf{n}}}) \varepsilon_{\mathbf{kn}}^{\hat{\mathbf{n}}} - \sum_{\mathbf{kn}} f(\varepsilon_{\mathbf{kn}}^0) \varepsilon_{\mathbf{kn}}^0, \quad (4)$$

where $\varepsilon_{\mathbf{kn}}^{\hat{\mathbf{n}}}$ and $f(\varepsilon_{\mathbf{kn}}^{\hat{\mathbf{n}}})$ are the eigenenergies and occupation numbers, respectively, obtained by diagonalising the Kohn–Sham Hamiltonian including SOC in a basis of collinear spinors aligned along the direction $\hat{\mathbf{n}}$, while $\varepsilon_{\mathbf{kn}}^0$ and $f(\varepsilon_{\mathbf{kn}}^0)$ are the bare Kohn–Sham eigenenergies and occupation numbers without SOC.

For all magnetic materials we have calculated the energy difference between out-of-plane and in-plane magnetisation $E_{\text{MA}}(i) = \Delta E(\hat{\mathbf{z}}) - \Delta E(i)$, ($i = \hat{\mathbf{x}}, \hat{\mathbf{y}}$). Negative values of $E_{\text{MA}}(i)$ thus indicate that there is an out-of-plane easy axis of magnetisation.

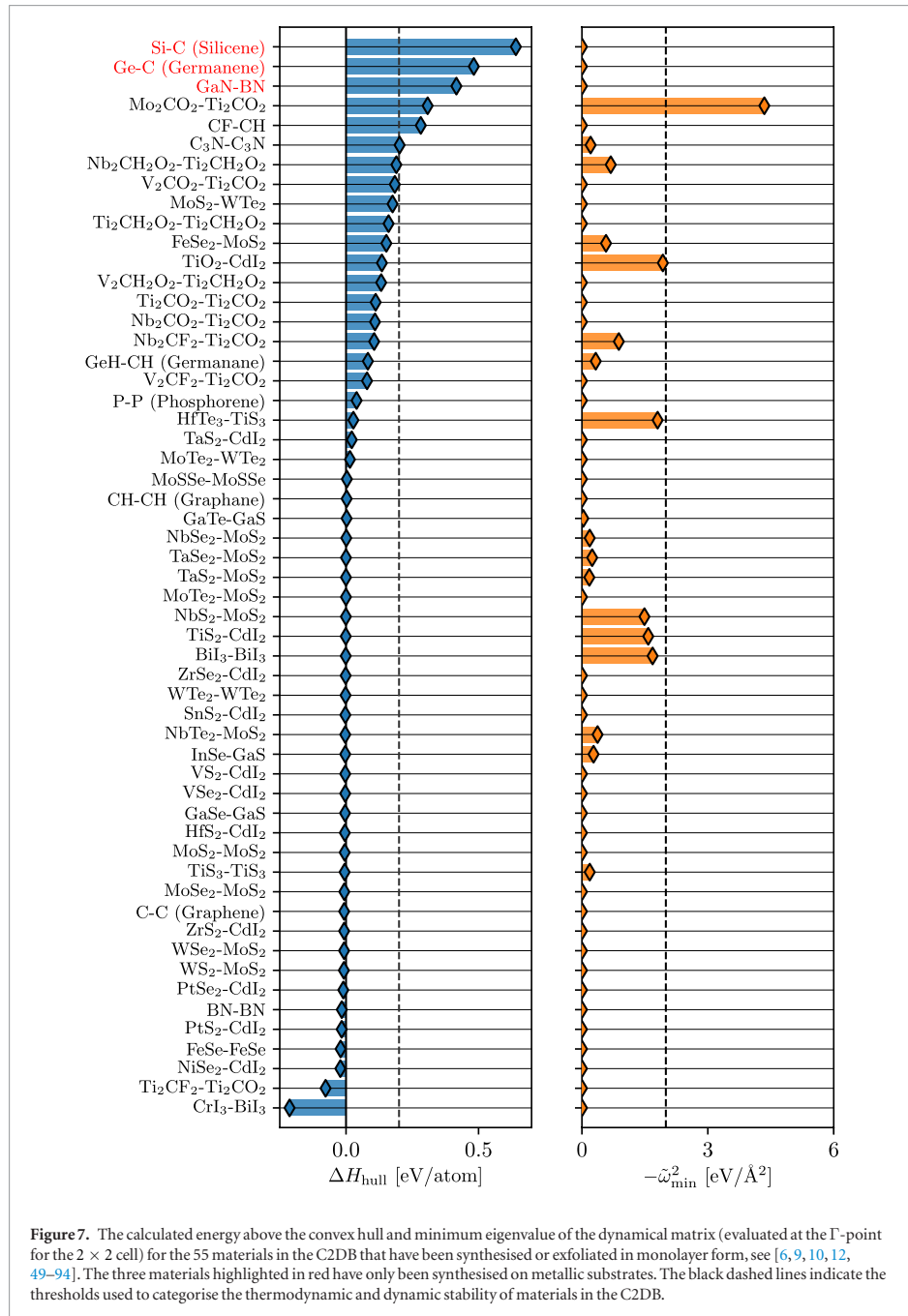
Calculations for the ground state have been performed with plane-wave cutoff and energetic convergence threshold set to 800 eV and 0.5 meV/atom respectively. For all calculations we have used a Γ -centered Monkhorst–Pack k -point with a density of $20/\text{\AA}^{-3}$. The SOC contribution is introduced via a non-self-consistent diagonalisation of the Kohn–Sham Hamiltonian evaluated in the projector-augmented wave formalism [97].

2.7. Projected density of states

The projected density of states (PDOS) is a useful tool for identifying which atomic orbitals comprise a band. It is defined as

$$\rho_i^S(\varepsilon) = \sum_{a \in S} \sum_{\mathbf{kn}} \sum_m |\langle \phi_{l,m}^a | \psi_{\mathbf{kn}} \rangle|^2 \delta(\varepsilon - \varepsilon_{\mathbf{kn}}), \quad (5)$$

where $\psi_{\mathbf{kn}}$ are the Kohn–Sham wave functions with eigenvalues $\varepsilon_{\mathbf{kn}}$ and $\phi_{l,m}^a$ are the spin-paired Kohn–Sham orbitals of atomic species S with angular momentum l (s, p, d, f). We sum over all atoms belonging to species S so every atomic species has one



entry per angular momentum channel. In the PAW formalism this can be approximated as

$$\rho_l^S(\varepsilon) = \sum_{a \in S} \sum_{\mathbf{k}\mathbf{n}} \sum_m |\langle \tilde{p}_{l,m}^a | \tilde{\psi}_{\mathbf{k}\mathbf{n}} \rangle|^2 \delta(\varepsilon - \varepsilon_{\mathbf{k}\mathbf{n}}) \quad (6)$$

where $\tilde{\psi}_{\mathbf{k}\mathbf{n}}$ are the pseudo wave functions and $\tilde{p}_{l,m}^a$ are the PAW projectors associated with the atomic orbitals

$\phi_{l,m}^a$. The PDOS is calculated from equation (6) using linear tetrahedron interpolation [98] (LTI) of energy eigenvalues obtained from a ground state calculation with a k -point sampling of $36/\text{\AA}^{-3}$. In contrast to other techniques for calculating the PDOS using smearing, the PDOS yielded by the LTI method returns exactly zero at energies with no states. Examples of PDOS

Table 2. The materials in the C2DB distributed over the nine stability categories defined by the three levels (high, medium and low) of dynamical stability (columns) and thermodynamic stability (rows). The overall stability of the materials is defined as the lower of the two separate stability scales. Materials with low overall stability (bold) are considered unstable.

| Thermodynamic stability (eV/atom) | Dynamic stability ($\text{eV}\text{\AA}^{-2}$) | | | Total |
|--------------------------------------|--|--|--|--------------|
| | $ \tilde{\omega}_{\min}^2 > 2$ or $C_{ii} < 0$ | $10^{-5} < \tilde{\omega}_{\min}^2 < 2$, $C_{ii} > 0$ | $ \tilde{\omega}_{\min}^2 < 10^{-5}$, $C_{ii} > 0$ | |
| $\Delta H > 0.2$ | 6.0% | 4.2% | 1.7% | 12.0% |
| $\Delta H < 0.2$ | 14.9% | 10.9% | 6.4% | 32.2% |
| $\Delta H_{\text{hull}} < 0.2$ | 11.4% | 24.1% | 20.3% | 55.8% |
| Total | 32.3% | 39.2% | 28.5% | |

Table 3. Planar elastic stiffness coefficients (in N m^{-1}) calculated at the PBE level. The results of this work are compared to previous calculations from the literature and the mean absolute deviation (MAD) is shown.

| | C_{11} (N m^{-1}) | | C_{22} (N m^{-1}) | | C_{12} (N m^{-1}) | |
|------------------|--------------------------------|------------|--------------------------------|------------|--------------------------------|------------|
| | C2DB | Literature | C2DB | Literature | C2DB | Literature |
| P (phosphorene) | 101.9 | 105.2 [95] | 25.1 | 26.2 [95] | 16.9 | 18.4 [95] |
| MoS ₂ | 131.4 | 132.6 [19] | 131.3 | 132.6 [19] | 32.6 | 32.7 [19] |
| WSe ₂ | 120.6 | 119.5 [19] | 121.3 | 119.5 [19] | 22.8 | 22.7 [19] |
| WS ₂ | 146.3 | 145.3 [19] | 146.7 | 145.3 [19] | 32.2 | 31.5 [19] |
| MAD | 1.7 | — | 1.4 | — | 0.6 | — |

are shown in figure 9 (right) for respectively the ferromagnetic metal VO₂ and the semiconductor WS₂ in the H phase (MoS₂ prototype).

2.8. Band structures

Electronic band structures are calculated along the high symmetry paths shown in figure 8 for the five different types of 2D Bravais lattices. The band energies are computed within DFT using three different xc-functionals, namely PBE, HSE06, and GLLBSC. These single-particle approaches are complemented by many-body G_0W_0 calculations for materials with a finite gap and up to four atoms in the unit cell (currently around 250 materials). For all methods, SOC is included by non-selfconsistent diagonalisation in the full basis of Kohn–Sham eigenstates. Band energies always refer to the vacuum level defined as the asymptotic limit of the Hartree potential, see figure 12. Below we outline the employed methodology while section 3.2.1 provides an overview and comparison of the band energies obtained with the different methods.

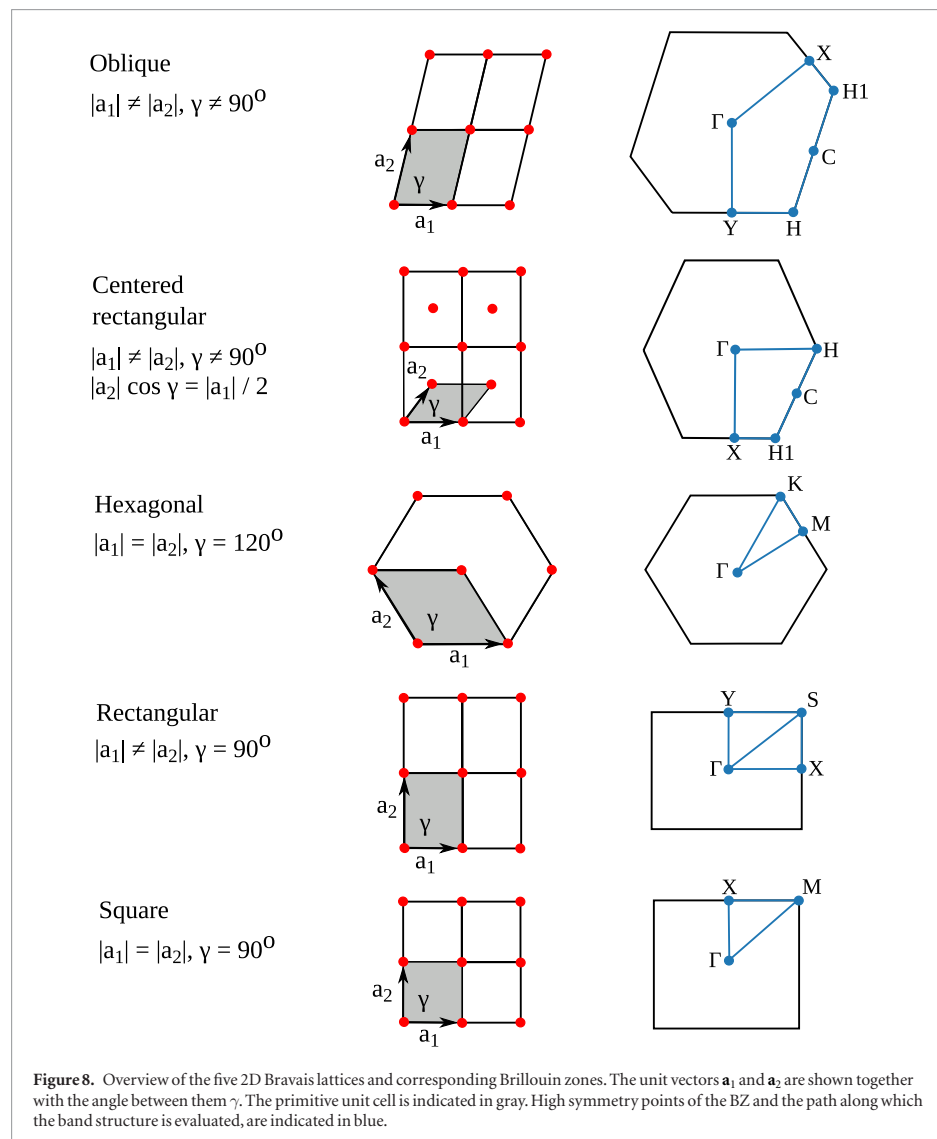
2.8.1. PBE band structure

The electron density is determined self-consistently on a uniform k -point grid of density $12.0/\text{\AA}^{-3}$. From this density, the PBE band structure is computed non-selfconsistently at 400 k -points distributed along the band path (see figure 8). Examples of PBE band structures are shown in figure 9 for the ferromagnetic metal VO₂ and the semiconductor WS₂ both in the MoS₂ prototype structure. The expectation value of the out-of-plane spin component, $\langle \chi_{nk\sigma} | \hat{S}_z | \chi_{nk\sigma} \rangle$, is evaluated for each spinorial wave

function, $\chi_{nk\sigma} = (\psi_{nk\uparrow}, \psi_{nk\downarrow})$, and is indicated by the color of the band. For materials with inversion symmetry, the SOC cannot induce band splitting, meaning that $\langle \chi_{nk\sigma} | \hat{S}_z | \chi_{nk\sigma} \rangle$ is ill-defined and no color coding is used. The band structure without SOC is indicated by a dashed grey line. We have compared our PBE + SOC band gaps of 29 different monolayers with those obtained with the VASP code in [41] and find a mean absolute deviation of 0.041 eV.

2.8.2. HSE band structure

The band structure is calculated non-selfconsistently using the range-separated hybrid functional HSE06 [99] on top of a PBE calculation with k -point density $12.0/\text{\AA}^{-3}$ and 800 eV plane wave cutoff. We have checked for selected systems that the HSE band structure is well converged with these settings. The energies along the band path are obtained by spline interpolation from the uniform k -point grid. As an example, the HSE band structure of WS₂ is shown in the left panel of figure 10 (black line) together with the PBE band structure (grey dashed). The PBE band gap increases from 1.52 eV to 2.05 eV with the HSE06 functional in good agreement with earlier work reporting band gaps of 1.50 eV (PBE) and 1.90 eV (HSE) [100] and 1.55 eV (PBE) and 1.98 eV (HSE) [101], respectively. A more systematic comparison of our results with the HSE + SOC band gaps obtained with the VASP code in [41] for 29 monolayers yield a mean absolute deviation of 0.14 eV. We suspect this small but non-zero deviation is due to differences in the employed PAW potentials and the non-selfconsistent treatment of the HSE in our calculations.

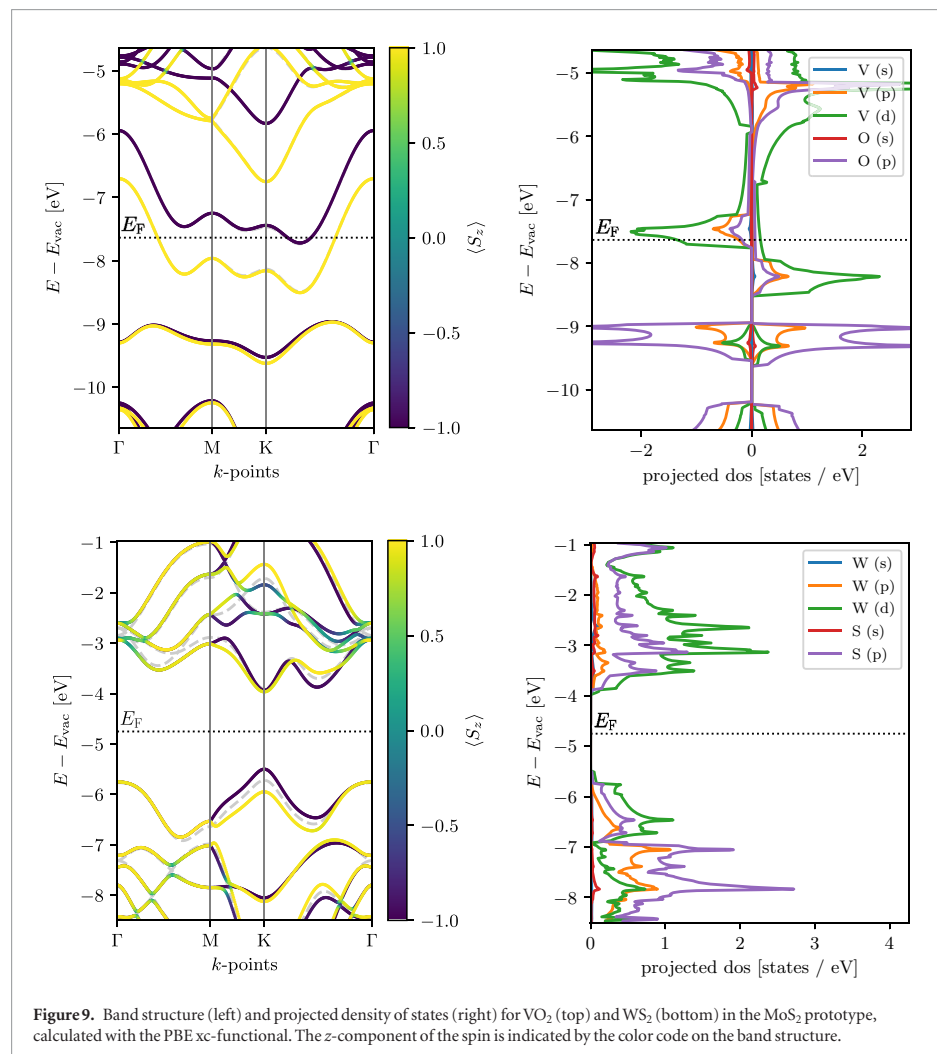


2.8.3. GLLBSC fundamental gap

For materials with a finite PBE band gap, the fundamental gap (i.e. the difference between the ionisation potential and electron affinity) also sometimes referred to as the quasiparticle gap, is calculated self-consistently using the GLLBSC [102] xc-functional with a Monkhorst–Pack k -point grid of density $12.0/\text{\AA}^{-1}$. The GLLBSC is an orbital-dependent exact exchange-based functional, which evaluates the fundamental gap as the sum of the Kohn–Sham gap and the xc-derivative discontinuity, $E_{\text{gap}} = \varepsilon_{\text{gap}}^{\text{KS}} + \Delta_{\text{xc}}$. The method has been shown to yield excellent quasiparticle band gaps at very low

computational cost for both bulk [102, 103] and 2D semiconductors [36].

In the exact Kohn–Sham theory, $\varepsilon_{\text{v}}^{\text{KS}}$ should equal the exact ionisation potential and thus Δ_{xc} should be used to correct only the conduction band energies [104]. Unfortunately, we have found that in practice this procedure leads to up-shifted band energies (compared with the presumably more accurate G_0W_0 results, see figure 20). Consequently, we store only the fundamental gap and Δ_{xc} in the database. However, as will be shown in section 3.2.1 the center of the gap is in fact reasonably well described by PBE suggesting that efficient and fairly accurate predictions of the absolute



band edge energies can be obtained by a symmetric GLLBSC correction of the PBE band edges.

2.8.4. G_0W_0 band structure

For materials with finite PBE band gap the quasiparticle (QP) band structure is calculated using the G_0W_0 approximation on top of PBE following our earlier work [105, 106]. Currently, this resource demanding step is performed only for materials with up to four atoms in the unit cell. The number of plane waves and the number of unoccupied bands included in the calculation of the non-interacting density response function and the GW self-energy are always set equal. The individual QP energies are extrapolated to the infinite basis set limit from calculations at plane wave cutoffs of 170, 185 and 200 eV, following the standard $1/N_G$ dependence [107, 108], see figure 11 (right). The screened Coulomb interaction is represented on a non-linear real frequency grid ranging from 0 eV to

230 eV and includes around 250 frequency points. The exchange contribution to the self-energy is calculated using a Wigner–Seitz truncation scheme [109] for a more efficient treatment of the long range part of the exchange potential. For the correlation part of the self-energy, a 2D truncation of the Coulomb interaction is used [110, 111]. We stress that the use of a truncated Coulomb interaction is essential to avoid unphysical screening from periodically repeated layers which otherwise leads to significant band gap reductions.

Importantly, the use of a truncated Coulomb interaction leads to much slower k -point convergence because of the strong q -dependence of the 2D dielectric function around $q = 0$. We alleviate this problem by using an analytical expression for the screened interaction when performing the BZ integral around $q = 0$ [106]. This allows us to obtain well converged results with a relatively low k -point density of $5.0/\text{\AA}^{-1}$ (corresponding to

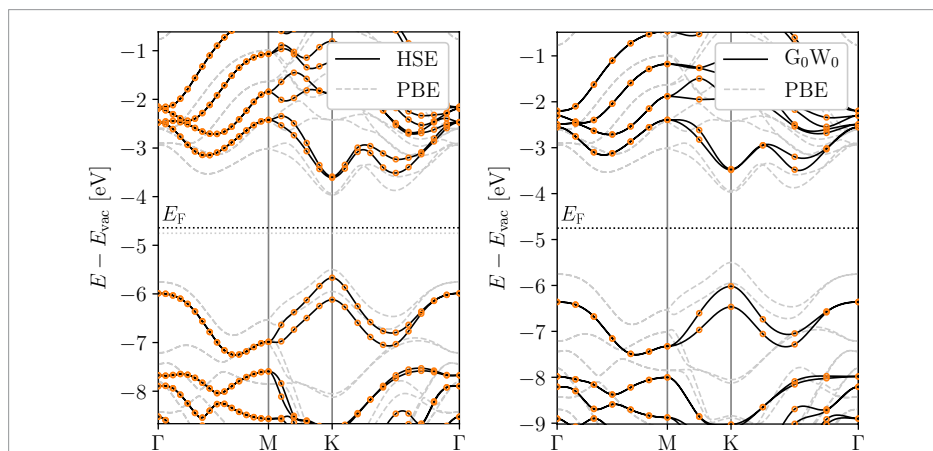
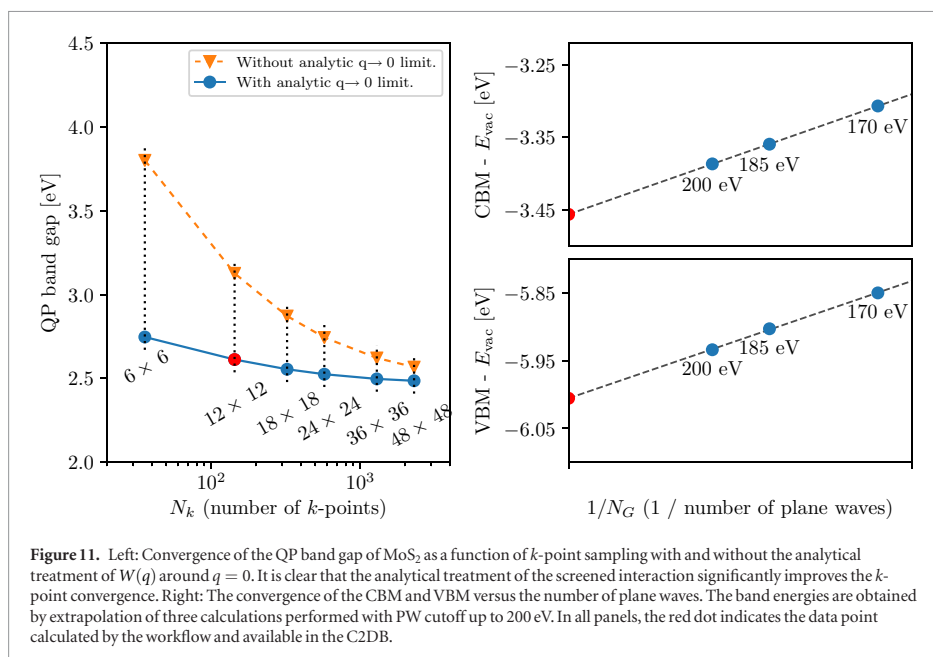


Figure 10. Band structure of WS_2 calculated with the HSE06 functional (left) and G_0W_0 (right). For comparison the PBE result is also shown (grey dashed). Spin-orbit coupling (SOC) is included in all calculations. The band energies refer to the vacuum level. The points show the calculated eigenvalues from which the band structure is interpolated. The relatively coarse k -point grid used for G_0W_0 is justified by the analytical treatment of the screened interaction $W(q)$ around $q = 0$, see figure 11.



12×12 k -points for MoS_2). For example, with this setting the G_0W_0 band gap of MoS_2 is converged to within 0.05 eV, see figure 11 (left). In comparison, standard BZ sampling with no special treatment of the $q = 0$ limit, requires around 40×40 k -points to reach the same accuracy.

Figure 10 (right) shows the PBE and G_0W_0 band structures of WS_2 (including SOC). The G_0W_0 self-energy opens the PBE band gap by 1.00 eV and the HSE gap by 0.47 eV, in good agreement with previous stud-

ies [112]. We note in passing that our previously published G_0W_0 band gaps for 51 monolayer TMDCs [36] are in good agreement with the results obtained using the workflow described here. The mean absolute error between the two data sets is around 0.1 eV and can be ascribed to the use of PBE rather than LDA as starting point and the use of the analytical expression for W around $q = 0$.

A detailed comparison of our results with previously published G_0W_0 data is not meaningful because

Table 4. Comparison between calculated and experimental band gaps for four freestanding monolayers. The experimental values have been corrected for substrate screening. MAD refers to the mean absolute deviation between the predicted values and the measured values.

| Material | Band gap (eV) | | | | Experiment |
|-----------------------|---------------|-------|--------|-------------------------------|------------|
| | PBE | HSE06 | GLLBSC | G ₀ W ₀ | |
| MoS ₂ | 1.58 | 2.09 | 2.21 | 2.53 | 2.50 [125] |
| MoSe ₂ | 1.32 | 1.80 | 1.88 | 2.12 | 2.31 [126] |
| WS ₂ | 1.53 | 2.05 | 2.16 | 2.53 | 2.72 [127] |
| P (phosphorene) | 0.90 | 1.51 | 1.75 | 2.03 | 2.20 [124] |
| MAD w.r.t. experiment | 1.10 | 0.57 | 0.43 | 0.15 | — |

of the rather large differences in the employed implementations/parameter settings. In particular, most reported calculations do not employ a truncated Coulomb interaction and thus suffer from spurious screening effects, which are then corrected for in different ways. Moreover, they differ in the amount of vacuum included in the supercell, the employed k -point grids and basis sets, the in-plane lattice constants, and the DFT starting points. For example, published values for the QP band gap of monolayer MoS₂ vary from from 2.40 to 2.90 eV [113–120] (see [119] for a detailed overview). The rather large variation in published GW results for 2D materials is a result of the significant numerical complexity of such calculations and underlines the importance of establishing large and consistently produced benchmark data sets like the present.

For bulk materials, self-consistency in the Green's function part of the self-energy, i.e. the G₀W₀ method, has been shown to increase the G₀W₀ band gaps and improve the agreement with experiments [121]. The trend of band gap opening is also observed for 2D materials [106, 120, 120, 122], however, no systematic improvement with respect to experiments has been established [122]. For both bulk and 2D materials, the fully self-consistent GW self-energy systematically overestimates the band gap [121, 122] due to the neglect of vertex corrections [122, 123]. In G₀W₀ the neglect of vertex corrections is partially compensated by the smaller band gap of the non-interacting Kohn–Sham Green's function compared to the true interacting Green's function. In this case, the vertex corrections will affect mainly the absolute position of the bands relative to vacuum while the effect on the band gap is relatively minor [122].

In table 4 we compare calculated band gaps from C2DB with experimental band gaps for three monolayer TMDCs and phosphorene. The experimental data has been corrected for substrate interactions [122, 124], but not for zero-point motion, which is expected to be small (<0.1 eV). The G₀W₀ results are all within 0.2 eV of the experiments. A further (indirect) test of the G₀W₀ band gaps against experimental values is provided by the comparison of our BSE spectra against experimental photoluminescence data in table 7, where we have used a G₀W₀ scissors operator. Finally, we stress that the employed PAW potentials are not norm-conserving, and this can lead to errors for bands with highly localised states (mainly 4*f* and 3*d* orbitals),

as shown in [108]. Inclusion of vertex corrections and use of norm conserving potentials will be the focus of future work on the C2DB.

2.9. Band extrema

For materials with a finite band gap, the positions of the valence band maximum (VBM) and conduction band minimum (CBM) within the BZ are identified together with their energies relative to the vacuum level. The latter is defined as the asymptotic value of the electrostatic potential, see figure 12. The PBE electrostatic potential is used to define the vacuum level in the non-selfconsistent HSE and G₀W₀ calculations. For materials with an out-of-plane dipole moment, a dipole correction is applied during the selfconsistent DFT calculation, and the vacuum level is defined as the average of the asymptotic electrostatic potentials on the two sides of the structure. The PBE vacuum level shift is also stored in the database.

2.10. Fermi surface

The Fermi surface is calculated using the PBE xc-functional including SOC for all metallic compounds in the database. Based on a ground state calculation with a k -point density of at least $20/\text{\AA}^{-3}$, the eigenvalues are interpolated with quadratic splines and plotted within the first BZ. Figure 13 (left) shows an example of the Fermi surface for VO₂-MoS₂ with color code indicating the out-of-plane spin projection $\langle S_z \rangle$. The band structure refers to the ferromagnetic ground state of VO₂-MoS₂, which has a magnetic moment of $0.70 \mu_B$ per unit cell, characterised by alternating spin-polarised lobes with $\langle S_z \rangle = \pm 1$.

2.11. Effective masses

For materials with a finite PBE gap, the effective electron and hole masses are calculated from the PBE eigenvalues; initially these are calculated on an ultrafine k -point mesh of density $45.0/\text{\AA}^{-3}$ uniformly distributed inside a circle of radius 0.015\AA^{-1} centered at the VBM and CBM, respectively. The radius is chosen to be safely above the noise level of the calculated eigenvalues but still within the harmonic regime; it corresponds to a spread of eigenvalues of about 1 meV within the circle for an effective mass of $1 m_0$. For each band within an energy window of 100 meV above/below the CBM/VBM, the band

curvature is obtained by fitting a third order polynomial. Even though the masses represent the second derivative of the band energies, we have found that the inclusion of 3rd order terms stabilises the fitting procedure and yields masses that are less sensitive to the details of the employed k -point grids. For each band the mass tensor is diagonalised to yield heavy and light masses in case of anisotropic band curvatures. The masses (in two directions) and the energetic splitting of all bands within 100 meV of the band extremum are calculated both with and without SOC and stored in the database. Other approaches exist for calculating effective masses, such as $\mathbf{k} \cdot \mathbf{p}$ perturbation theory (see e.g. [128] and references therein); the present scheme was chosen for its simplicity and ease of application to a wide range of different materials.

In addition to the effective masses at the VBM and CBM, the exciton reduced mass is calculated by applying the above procedure to the direct valence-conduction band transition energies, $\varepsilon_{v-c}(\mathbf{k}) = \varepsilon_c(\mathbf{k}) - \varepsilon_v(\mathbf{k})$. For direct band gap materials the exciton reduced mass is related to the electron and hole masses by $1/\mu_{ex} = 1/m_e^* + 1/m_h^*$, but in the more typical case of indirect band gaps, this relation does not hold.

As an example, figure 14 shows a zoom of the band structure of SnS-GeSe around the VBM and CBM (upper and lower panels). The second order fits to the band energies (extracted from the fitted 3rd order polynomial) are shown by red dashed lines. It can be seen that both the conduction and valence bands are anisotropic leading to a heavy and light mass direction (left and right panels, respectively). The valence band is split by the SOC resulting in two bands separated by ~ 10 meV and with slightly different curvatures. The conduction band exhibits a non-trivial band splitting in one of the two directions. The peculiar band splitting is due to a Rashba effect arising from the combination of spin-orbit coupling and the finite perpendicular electric field created by the permanent dipole of the SnS structure where Sn and S atoms are displaced in the out of plane direction leading to a sizable vacuum level difference of 1.13 eV, see figure 12.

Table 5 shows a comparison between selected effective masses from the C2DB and previously published data also obtained with the PBE xc-correlation functional and including SOC. Overall, the agreement is very satisfactory.

2.12. Work function

For metallic compounds, the work function is obtained as the difference between the Fermi energy and the asymptotic value of the electrostatic potential in the vacuum region, see figure 12. The work function is determined for both PBE and HSE band structures (both including SOC) on a uniform k -point grid of density $12.0/\text{\AA}^{-3}$. Since the SOC is evaluated non-selfconsistently, the Fermi energy is adjusted afterwards based on a charge neutrality condition.

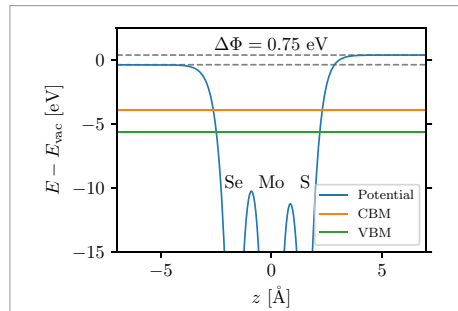


Figure 12. Electrostatic potential profile perpendicular to monolayer MoSSe (averaged in plane). The position of the VBM and CBM are indicated together with the splitting of the vacuum levels caused by the out-of-plane dipole moment of the MoSSe layer.

2.13. Deformation potentials

For semiconductors, the deformation potentials quantify the shift in band edge energies (VBM or CBM) upon a linear deformation of the lattice. The uniaxial absolute deformation potential along axis i ($i = x, y$) is defined as [129, 130]

$$D_{ii}^{\alpha} = \frac{\Delta E_{\alpha}}{\varepsilon_{ii}}, \quad \alpha = \text{VBM, CBM} \quad (7)$$

where ΔE_{α} is the energy shift upon strain and ε_{ii} are the strains in the i -directions.

The deformation potentials are important physical quantities as they provide an estimate of the strength of the (acoustic) electron-phonon interaction, see section 3.2.2. Moreover, they are obviously of interest in the context of strain-engineering of band gaps and they can be used to infer an error bar on the band gap or band edge positions due to a known or estimated error bar on the lattice constant.

The calculation of D_{ii}^{α} is based on a central difference approximation to the derivative. A strain of $\pm 1\%$ is applied separately in the x and y directions and the ions are allowed to relax while keeping the unit cell fixed. Calculations are performed with the PBE xc-functional, a plane wave cutoff of 800 eV, and a k -point density of $12/\text{\AA}^{-3}$.

The change in band energy, ΔE_{α} , is measured relative to the vacuum level. In cases with nearly degenerate bands, care must be taken to track the correct bands as different bands might cross under strain. In this case, we use the expectation value $\langle \hat{S}_z \rangle$ to follow the correct band under strain. Figure 15 shows how the band structure of MoS₂ changes as a function of strain. Both the VBM and the CBM shift down (relative to the vacuum level) when tensile strain is applied in the x direction, but the conduction band shows a much larger shift, leading to an effective band gap closing under tensile strain.

Table 6 shows a comparison between the deformation potentials in the C2DB, and literature values obtained using similar methods. There is generally

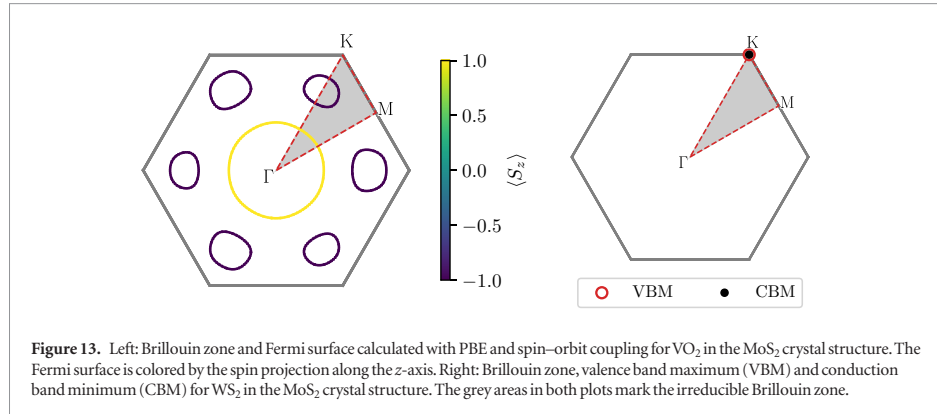


Figure 13. Left: Brillouin zone and Fermi surface calculated with PBE and spin–orbit coupling for VO₂ in the MoS₂ crystal structure. The Fermi surface is colored by the spin projection along the z-axis. Right: Brillouin zone, valence band maximum (VBM) and conduction band minimum (CBM) for WS₂ in the MoS₂ crystal structure. The grey areas in both plots mark the irreducible Brillouin zone.

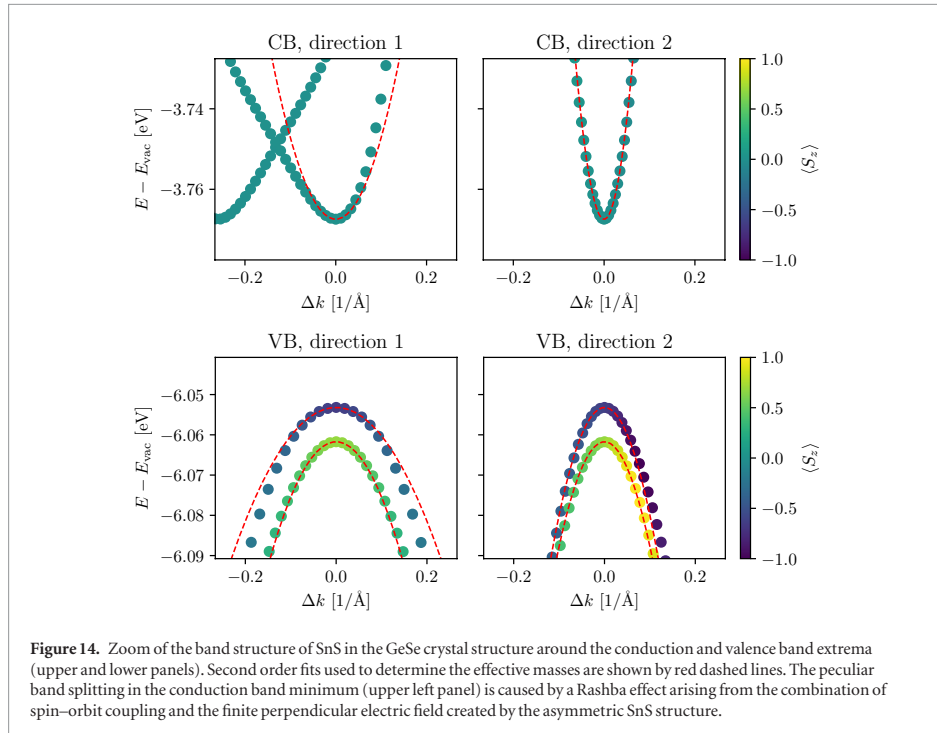


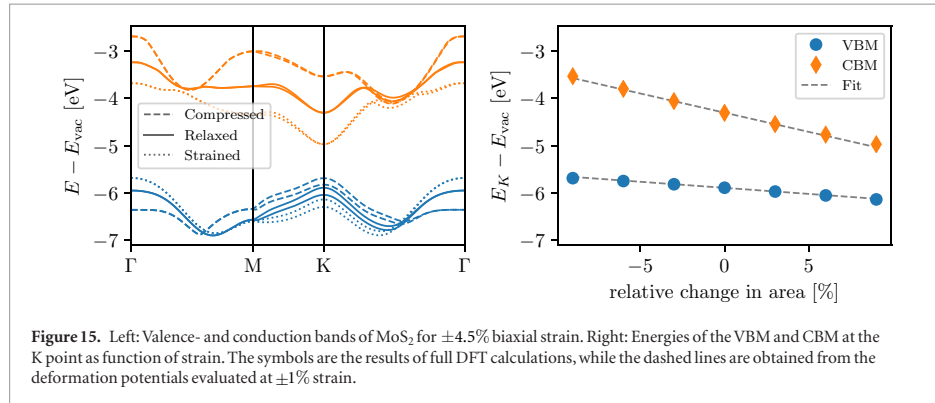
Figure 14. Zoom of the band structure of SnS in the GeSe crystal structure around the conduction and valence band extrema (upper and lower panels). Second order fits used to determine the effective masses are shown by red dashed lines. The peculiar band splitting in the conduction band minimum (upper left panel) is caused by a Rashba effect arising from the combination of spin–orbit coupling and the finite perpendicular electric field created by the asymmetric SnS structure.

Table 5. Calculated PBE effective masses (in units of m_0), for the highest valence band and lowest conduction band, for different 2D materials. All C2DB values are calculated including spin–orbit coupling.

| Material | k -point | Electron mass (m_0) | | Hole mass (m_0) | |
|------------------------|------------|-------------------------|------------|---------------------|------------|
| | | C2DB | Literature | C2DB | Literature |
| MoS ₂ | K | 0.42 | 0.44 [128] | 0.53 | 0.54 [128] |
| WSe ₂ | K | 0.46 | 0.40 [128] | 0.35 | 0.36 [128] |
| Phosphorene (zig-zag) | Γ | 1.24 | 1.24 [95] | 6.56 | 6.48 [95] |
| Phosphorene (armchair) | Γ | 0.14 | 0.13 [95] | 0.13 | 0.12 [95] |
| MAD | | 0.02 | — | 0.03 | — |

Table 6. Absolute deformation potentials (in eV) of the VBM and CBM for different materials. All results are based on the PBE xc-functional.

| Material | k -point | Valence band | | Conduction band | |
|-------------------|------------|--------------|------------|-----------------|------------|
| | | C2DB | Ref. [131] | C2DB | Ref. [131] |
| MoSe ₂ | K | -1.43 | -1.86 | -5.57 | -5.62 |
| WS ₂ | K | -1.25 | -1.59 | -6.66 | -6.76 |
| WSe ₂ | K | -1.21 | -1.43 | -6.21 | -6.35 |
| hBN | K | -1.57 | -1.63 | -4.55 | -4.62 |
| MAD | | 0.26 | — | 0.14 | — |

**Figure 15.** Left: Valence- and conduction bands of MoS₂ for $\pm 4.5\%$ biaxial strain. Right: Energies of the VBM and CBM at the K point as function of strain. The symbols are the results of full DFT calculations, while the dashed lines are obtained from the deformation potentials evaluated at $\pm 1\%$ strain.

good agreement, and part of the discrepancy can be ascribed to the fact that, in contrast to [131], our numbers include spin-orbit coupling.

2.14. Plasma frequencies

The dielectric response of a 2D material is described by its 2D polarisability, α^{2D} (see section 2.15 for a general introduction of this quantity). For metals, it can be separated into contributions from intraband and interband transitions, i.e. $\alpha^{2D} = \alpha^{2D,\text{intra}} + \alpha^{2D,\text{inter}}$. We have found that local field effects (LFEs) are negligible for the intraband component, which consequently can be treated separately and evaluated as an integral over the Fermi surface. Specifically, this leads to the Drude expression for the polarisability in the long wave length limit $\alpha^{2D,\text{intra}}(\omega) = -\omega_{\text{p},2D}^2 / (2\pi\omega^2)$ where $\omega_{\text{p},2D}$ is the 2D plasma frequency, which in atomic units is given by

$$\omega_{\text{p},2D}^2 = \frac{4\pi}{A} \sum_{snk} |\hat{\mathbf{q}} \cdot \mathbf{v}_{snk}|^2 \delta(\varepsilon_{snk} - \varepsilon_F), \quad (8)$$

where $\mathbf{v}_{snk} = \langle snk | \hat{\mathbf{p}} / m_0 | snk \rangle$ is a velocity matrix element (with m_0 the electron mass), $\hat{\mathbf{q}} = \mathbf{q} / q$ is the polarisation direction, s, n, \mathbf{k} denote spin, band and momentum indices, and A is the supercell area. The 2D plasma frequency is related to the conventional 3D plasma frequency by $\omega_{\text{p},2D}^2(\omega) = \omega_{\text{p},3D}^2(\omega) L / 2$ where L is the supercell height.

The plasma frequency defined above determines the intraband response of the 2D metal to external fields.

In particular, it determines the dispersion relation of plasmon excitations in the metal. The latter are defined by the condition $\varepsilon^{2D}(\omega_{\text{p}}) = 1 + 2\pi q \alpha^{2D}(\omega_{\text{p}}) = 0$, where q is the plasmon wave vector. Neglecting interband transitions (the effect of which is considered in section 3.2.4), the 2D plasmon dispersion relation becomes

$$\omega_{\text{p}}(q) = \omega_{\text{p},2D} \sqrt{q}. \quad (9)$$

The plasma frequencies, $\omega_{\text{p},2D}$, for polarisation in the x and y directions, respectively, are calculated for all metals in the C2DB using the linear tetrahedron method [98] to interpolate matrix elements and eigenvalues based on a PBE band structure calculation with a k -point density of $20/\text{\AA}^{-3}$.

2.15. Electronic polarisability

The polarisability tensor α_{ij} is defined by

$$P_i(\mathbf{q}, \omega) = \sum_j \alpha_{ij}(\mathbf{q}, \omega) E_j(\mathbf{q}, \omega), \quad (10)$$

where P_i is the i 'th component of the induced polarisation averaged over a unit cell and E_j is the j 'th component of the macroscopic electric field. Using that $P_i = (D_i - E_i) / (4\pi) = \sum_j (\epsilon_{ij} - \delta_{ij}) E_j / (4\pi)$ one observes that $\alpha_{ij} = (\epsilon_{ij} - \delta_{ij}) / (4\pi)$, where ϵ_{ij} is the dielectric function. In contrast to the dielectric function, whose definition for a 2D material is not straightforward [119], the polarisability allows for a natural generalisation to 2D by considering the induced dipole moment per unit area,

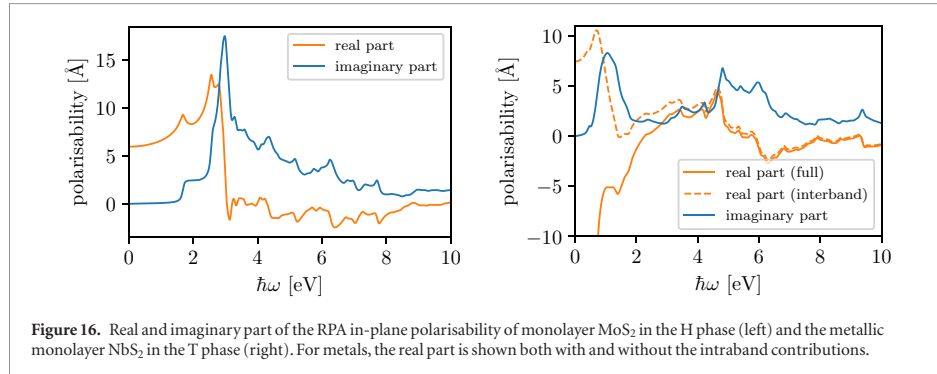


Figure 16. Real and imaginary part of the RPA in-plane polarisability of monolayer MoS₂ in the H phase (left) and the metallic monolayer NbS₂ in the T phase (right). For metals, the real part is shown both with and without the intraband contributions.

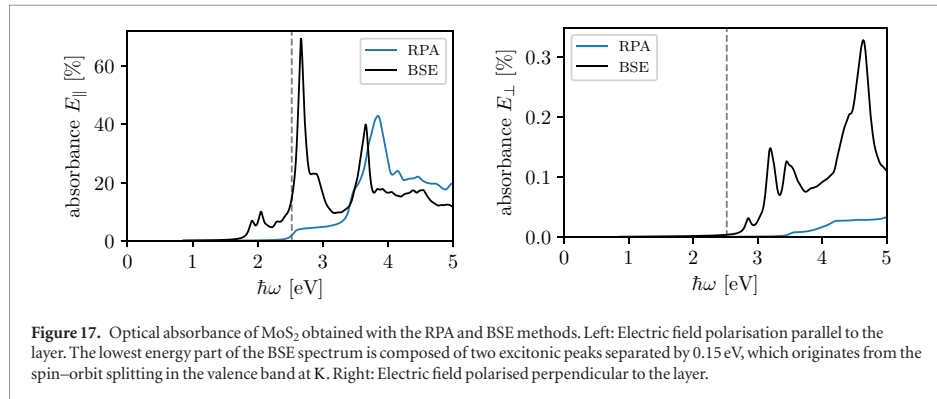


Figure 17. Optical absorbance of MoS₂ obtained with the RPA and BSE methods. Left: Electric field polarisation parallel to the layer. The lowest energy part of the BSE spectrum is composed of two excitonic peaks separated by 0.15 eV, which originates from the spin-orbit splitting in the valence band at K. Right: Electric field polarised perpendicular to the layer.

$$P_i^{2D}(\mathbf{q}, \omega) = \sum_j \alpha_{ij}^{2D}(\mathbf{q}, \omega) E_j(\mathbf{q}, \omega). \quad (11)$$

Since the P_i is a full unit cell average and P_i^{2D} is integrated in the direction orthogonal to the slab, we have $P_i^{2D} = LP_i$ and $\alpha_{ij}^{2D} = L\alpha_{ij}$, where L is the length of the unit cell in the direction orthogonal to the slab.

In the following, we focus on the longitudinal components of the polarisability and dielectric tensors, which are simply denoted by α and ϵ . These are related to the density-density response function, χ , via the relations

$$\alpha^{2D}(\mathbf{q}, \omega) = \frac{L}{4\pi} (\epsilon(\mathbf{q}, \omega) - 1), \quad (12)$$

$$\epsilon^{-1}(\mathbf{q}, \omega) = 1 + \langle v_c(\mathbf{q}) \chi(\omega) \rangle_{\mathbf{q}}, \quad (13)$$

where v_c is the Coulomb interaction and

$$\langle v_c \chi(\omega) \rangle_{\mathbf{q}} = \frac{1}{V} \int_{\text{Cell}} d\mathbf{r} d\mathbf{r}' d\mathbf{r}'' v_c(\mathbf{r}, \mathbf{r}') \chi(\mathbf{r}', \mathbf{r}'', \omega) e^{-i\mathbf{q}(\mathbf{r}-\mathbf{r}'')}, \quad (14)$$

where Cell is the supercell with volume V . The response function, χ , satisfies the Dyson equation [132] $\chi = \chi^{\text{irr}} + \chi^{\text{irr}} v_c \chi$, where χ^{irr} is the irreducible density-density response function. In the random phase approximation (RPA) χ^{irr} is replaced by the non-interacting response function, χ^0 , whose plane wave representation is given by [133, 134]

$$\chi_{\mathbf{G}\mathbf{G}'}^0(\mathbf{q}, \omega) = \frac{1}{\Omega} \sum_{\mathbf{k} \in \text{BZ}} \sum_{mn} (f_{n\mathbf{k}} - f_{m\mathbf{k}+\mathbf{q}}) \times \frac{\langle \psi_{n\mathbf{k}} | e^{-i(\mathbf{q}+\mathbf{G}) \cdot \mathbf{r}} | \psi_{m\mathbf{k}+\mathbf{q}} \rangle \langle \psi_{m\mathbf{k}+\mathbf{q}} | e^{i(\mathbf{q}+\mathbf{G}') \cdot \mathbf{r}} | \psi_{n\mathbf{k}} \rangle}{\hbar\omega + \epsilon_{n\mathbf{k}} - \epsilon_{m\mathbf{k}+\mathbf{q}} + i\eta}, \quad (15)$$

where \mathbf{G}, \mathbf{G}' are reciprocal lattice vectors and Ω is the crystal volume.

For all materials in the database, we calculate the polarisability within the RPA for both in-plane and out-of-plane polarisation in the optical limit $\mathbf{q} \rightarrow 0$. For metals, the interband contribution to the polarisability is obtained from equation (15) while the intraband contribution is treated separately as described in section 2.14. The single-particle eigenvalues and eigenstates used in equation (15) are calculated with PBE, a k -point density of $20/\text{\AA}^{-3}$ (corresponding to a k -point grid of 48×48 for MoS₂ and 60×60 for graphene), and 800 eV plane wave cutoff. The Dyson equation is solved using a truncated Coulomb potential [105, 111] to avoid spurious interactions from neighboring images. We use the tetrahedron method to interpolate the eigenvalues and eigenstates and a peak broadening of $\eta = 50$ meV. Local field effects are accounted for by including \mathbf{G} -vectors up to 50 eV. For the band summation we include 5 times as many unoccupied bands as occupied bands, which roughly corresponds to an

energy cutoff of 50 eV. The calculations are performed without spin–orbit coupling.

In figure 16 we show the real and imaginary part of α^{2D} for the semiconductor MoS₂. The PBE band gap of this material is 1.6 eV and we see the onset of dissipation at that energy. We also see that the initial structure of $\text{Im } \alpha$ is a constant, which is exactly what would be expected from the density of states in a 2D material with parabolic dispersion. Finally, we note that the static polarisability $\text{Re } \alpha|_{\omega=0} \approx 6 \text{ \AA}$, which can easily be read off the figure. The polarisability is also shown for the metallic 1T-NbS₂ where we display the real part with and without the intraband Drude contribution $\omega_{\text{P,2D}}^2/(\hbar\omega + i\eta)^2$.

2.16. Optical absorbance

The power absorbed by a 2D material under illumination of a monochromatic light field with polarisation $\hat{\mathbf{e}}$ is quantified by the dimensionless absorbance:

$$\text{Abs}(\omega) = 4\pi\omega\alpha^{2D}(q\hat{\mathbf{e}} \rightarrow 0, \omega)/c, \quad (16)$$

where c is the speed of light. In section 2.15 we gave a prescription for evaluating α^{2D} in the RPA. However, absorption spectra of 2D semiconductors often display pronounced excitonic effects, which are not captured by the RPA. The Bethe–Salpeter equation (BSE) is a well-known method capable of describing excitonic effects and has been shown to provide good agreement with experimental absorption spectra for a wide range of materials [135].

For materials with finite band gap and up to four atoms per unit cell, we have calculated the RPA and the BSE absorption spectra for electric fields polarised parallel and perpendicular to the layers. The calculations are performed on top of PBE eigenstates and eigenvalues with spin–orbit coupling included and all unoccupied band energies shifted by a constant in order to reproduce the G_0W_0 quasiparticle gap (the scissors operator method). If the G_0W_0 gap is not available we use the GLLBSC gap for non-magnetic materials and the HSE gap for magnetic materials (since GLLBSC is not implemented in GPAW for spin-polarised systems). The screened interaction entering the BSE Hamiltonian is calculated within the RPA using a non-interacting response function evaluated from equation (15) with local field effects (i.e. \mathbf{G} -vectors) included up to 50 eV and 5 times as many unoccupied bands as occupied bands for the sum over states. We apply a peak broadening of $\eta = 50 \text{ meV}$ and use a truncated Coulomb interaction. The BSE Hamiltonian is constructed from the four highest occupied and four lowest unoccupied bands on a k -point grid of density of $20/\text{\AA}^{-1}$, and is diagonalised within the Tamm–Dancoff approximation. We note that the Tamm–Dancoff approximation has been found to be very accurate for bulk semiconductors [136]. For monolayer MoS₂ we have checked that it reproduces

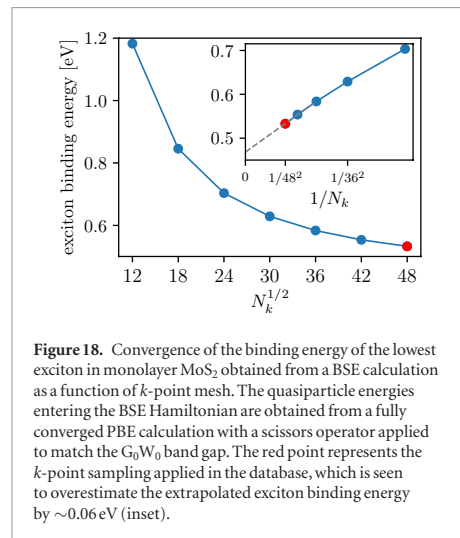


Figure 18. Convergence of the binding energy of the lowest exciton in monolayer MoS₂ obtained from a BSE calculation as a function of k -point mesh. The quasiparticle energies entering the BSE Hamiltonian are obtained from a fully converged PBE calculation with a scissors operator applied to match the G_0W_0 band gap. The red point represents the k -point sampling applied in the database, which is seen to overestimate the extrapolated exciton binding energy by $\sim 0.06 \text{ eV}$ (inset).

the full solution of the BSE, but its general validity for 2D materials, in particular those with small band gaps, should be more thoroughly tested.

In figure 17 we show the optical absorption spectrum of MoS₂ obtained with the electric field polarised parallel and perpendicular to the layer, respectively. Both RPA and BSE spectra are shown (the in-plane RPA absorbance equals the imaginary part of the RPA polarisability, see figure 16 (left), apart from the factor $4\pi\omega$ and the scissors operator shift). The low energy part of the in-plane BSE spectrum is dominated by a double exciton peak (the so-called A and B excitons) and is in excellent agreement with experiments [55].

In general, calculations of electronic excitations of 2D materials converge rather slowly with respect to k -points due to the non-analytic behavior of the dielectric function in the vicinity of $q = 0$ [119, 137, 138]. In figure 18 we show the k -point dependence of the binding energy of the A exciton in MoS₂ obtained as the difference between the direct band gap and the position of the first peak in figure 17. We observe a strong overestimation of the exciton binding energy at small k -point samplings, which converges slowly to a value of $\sim 0.5 \text{ eV}$ at large k -point samplings. For 48×48 k -points, corresponding to the k -point sampling used for the BSE calculations in the database, the exciton binding energy is 0.53 eV, whereas a $1/N_k^2$ extrapolation to infinite k -point sampling gives 0.47 eV (see inset in figure 18). In general, the exciton binding energy decreases with increasing k -point sampling, and thus the exciton binding energies reported in the C2DB might be slightly overestimated. However, since G_0W_0 band gaps also decrease when the k -point sampling is increased (see figure 11) the two errors tend to cancel such that the absolute position of the absorption peak from BSE- G_0W_0 converges faster than the band gap or exciton binding energy alone.

Table 7. Comparison between calculated and experimental positions of the first excitonic peak for four different transition metal dichalcogenide monolayers and phosphorene.

| Material | Energy of the first bright exciton (eV) | |
|-----------------------|---|------------------------------------|
| | BSE@PBE- G_0W_0 | Experiment |
| MoS ₂ | 2.00 | 1.83 [140], 1.86 [141], 1.87 [142] |
| MoSe ₂ | 1.62 | 1.57 [140], 1.57 [143], 1.58 [144] |
| WS ₂ | 2.07 | 1.96 [141], 2.02 [144] |
| WSe ₂ | 1.71 | 1.64 [142], 1.66 [143] |
| P (phosphorene) | 1.45 | 1.45 [145], 1.75 [146] |
| MAD w.r.t. experiment | 0.066 | — |

The BSE- G_0W_0 method has previously been shown to provide good agreement with experimental photoluminescence and absorption measurements on 2D semiconductors. In table 7 we show that our calculated position of the first excitonic peak agree well with experimental observations for four different TMDCs and phosphorene. Experimentally, the monolayers are typically supported by a substrate, which may alter the screening of excitons. However the resulting decrease in exciton binding energies is largely cancelled by a reduced quasiparticle gap such that the positions of the excitons are only slightly red-shifted as compared with the case of pristine monolayers [139].

3. Database overview

Having described the computational workflow, we now turn to the content of the database itself. We first present a statistical overview of all the materials in the C2DB (i.e. without applying any stability filtering) by displaying their distribution over crystal structure prototypes and their basic properties. We also provide a short list with some of the most stable materials, which to our knowledge have not been previously studied. Next, the predicted stability of the total set of materials is discussed and visualised in terms of the descriptors for thermodynamic and dynamic stability introduced in section 2.4.1. In section 3.2 we analyse selected properties in greater detail focusing on band gaps and band alignment, effective masses and mobility, magnetic properties, plasmons, and excitons. Throughout the sections we explore general trends and correlations in the data and identify several promising materials with interesting physical properties.

3.1. Materials

In table 8 we list the major classes of materials currently included in the database. The materials are grouped according to their prototype, see section 2.2.2. For each prototype we list the corresponding space group, the total number of materials, and the number of materials satisfying a range of different conditions. The atomic structure of some of the different prototypes were shown in figure 4. The vast majority of the 2D materials that have been experimentally synthesised in monolayer

form are contained in the C2DB (the 55 materials in figure 7 in addition to seven metal-organic perovskites). These materials are marked in the database and a literature reference is provided. Additionally, 80 of the monolayers in the C2DB could potentially be exfoliated from experimentally known layered bulk structures [16–19]. These materials are also marked and the ID of the bulk compound in the relevant experimental crystal structure database is provided.

To illustrate how all the materials are distributed in terms of stability, we show the energy above the convex hull plotted against $\bar{\omega}_{\min}^2$ in figure 19. It can be seen that the structures naturally sort themselves into two clusters according to the dynamic stability. The points have been colored according to the three levels for dynamic stability introduced in section 2.4. The lower panel shows the distribution of the materials in the grey region on a linear scale. While most of the experimentally known materials (red and black dots) have high dynamic stability, a significant part of them fall into the medium stability category. The marginal distributions on the plot show that the more dynamically stable materials are also more thermodynamically stable. The mean energy above the convex hull is 0.12 eV for the materials with high dynamical stability, while it is 0.25 eV for the others.

In table 9 we show the key properties of a selected set of stable materials, distributed across a variety of different crystal structure prototypes. To our knowledge, these materials are not experimentally known, and they are therefore promising candidates further study and experimental synthesis.

3.2. Properties: example applications

In the following sections we present a series of case studies focusing on different properties of 2D materials including band gaps and band alignment, effective masses and mobility, magnetic order, plasmons and excitons. The purpose is not to provide an in-depth nor material specific analysis, but rather to explore trends and correlations in the data and showcase some potential applications of the C2DB. Along the way, we report some of the novel candidate materials revealed by this analysis, which could be interesting to explore closer in the future.

Table 8. Overview of the materials currently in the C2DB. The table shows the number of compounds listed by their crystal structure prototype and selected properties. $E_{\text{gap}} > 0$ and ‘direct gap’ refer to the PBE values, ‘high stability’ refers to the stability scale defined in section 2.4.1, and the last three columns refer to the magnetic state, see section 2.1. In this overview, separate magnetic phases of the same structure are considered different materials.

| Prototype | Symmetry | Number of materials | | | | | | |
|--|--------------------|---------------------|----------------------|------------|----------------|------|-----|-----|
| | | Total | $E_{\text{gap}} > 0$ | Direct gap | High stability | NM | FM | AFM |
| C | P6/mmm | 4 | 4 | 3 | 1 | 4 | 0 | 0 |
| CH | P $\bar{3}$ m1 | 8 | 7 | 6 | 1 | 8 | 0 | 0 |
| CH ₂ Si | P3m1 | 2 | 2 | 2 | 1 | 2 | 0 | 0 |
| BN | P $\bar{3}$ m2 | 10 | 9 | 5 | 1 | 10 | 0 | 0 |
| GaS | P $\bar{3}$ m2 | 125 | 34 | 95 | 8 | 100 | 18 | 7 |
| FeSe | P4/nmm | 103 | 13 | 90 | 26 | 74 | 18 | 11 |
| GeSe | P3m1 | 20 | 19 | 5 | 6 | 20 | 0 | 0 |
| PbSe | P4/mmm | 44 | 6 | 38 | 1 | 33 | 8 | 3 |
| P | Pmna | 9 | 9 | 0 | 1 | 9 | 0 | 0 |
| MoS ₂ | P $\bar{3}$ m2 | 241 | 85 | 176 | 53 | 156 | 85 | 0 |
| CdI ₂ | P $\bar{3}$ m1 | 315 | 95 | 231 | 90 | 218 | 80 | 17 |
| WTe ₂ | P2 ₁ /m | 75 | 29 | 48 | 34 | 57 | 13 | 5 |
| FeOCl | Pmmn | 443 | 92 | 385 | 65 | 328 | 63 | 52 |
| MoSSe | P3m1 | 9 | 6 | 6 | 5 | 8 | 1 | 0 |
| C ₃ N | P6/mmm | 25 | 1 | 24 | 0 | 25 | 0 | 0 |
| YBr ₃ | P6/mmm | 57 | 11 | 51 | 0 | 21 | 24 | 12 |
| TiCl ₃ | P $\bar{3}$ 2m | 69 | 35 | 51 | 2 | 32 | 23 | 14 |
| BiI ₃ | P $\bar{3}$ m1 | 123 | 69 | 66 | 15 | 48 | 54 | 21 |
| TiS ₃ | Pmmn | 34 | 8 | 28 | 5 | 31 | 2 | 1 |
| MnTe ₃ | P2 ₁ /m | 29 | 3 | 27 | 1 | 22 | 4 | 3 |
| Cr ₃ WS ₈ | Pmm2 | 35 | 34 | 18 | 8 | 35 | 0 | 0 |
| CrWS ₄ | Pmm2 | 18 | 17 | 7 | 8 | 18 | 0 | 0 |
| Ti ₂ CO ₂ | P $\bar{3}$ m1 | 28 | 8 | 20 | 12 | 19 | 6 | 3 |
| Ti ₂ CH ₂ O ₂ | P $\bar{3}$ m1 | 13 | 3 | 12 | 3 | 10 | 2 | 1 |
| Ti ₃ C ₂ | P $\bar{3}$ m2 | 12 | 0 | 12 | 0 | 7 | 5 | 0 |
| Ti ₃ C ₂ O ₂ | P $\bar{3}$ m2 | 26 | 0 | 26 | 0 | 20 | 6 | 0 |
| Ti ₃ C ₂ H ₂ O ₂ | P $\bar{3}$ m2 | 14 | 0 | 14 | 0 | 10 | 4 | 0 |
| PbA ₂ I ₄ | P1 | 27 | 27 | 27 | 0 | 27 | 0 | 0 |
| Sum | | 1918 | 626 | 151 | 347 | 1352 | 416 | 150 |

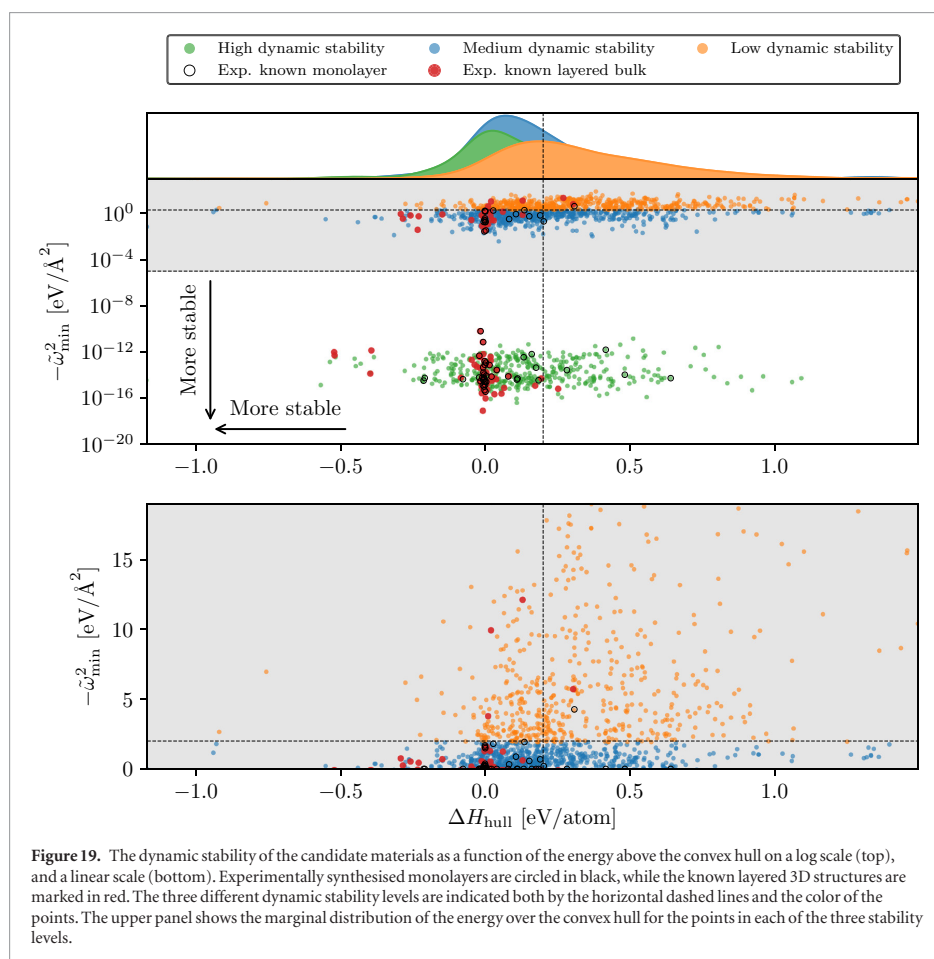
3.2.1. Band gaps and band alignment

The band gaps and band edge positions of all semiconductors and insulators in the C2DB have been calculated with the PBE, HSE06, and GLLBSC xc-functionals while G_0W_0 calculations have been performed for the ~ 250 simplest materials. The relatively large size of these datasets and the high degree of consistency in the way they are generated (all calculations performed with the same code using same PAW potentials and basis set etc) provide a unique opportunity to benchmark the performance of the different xc-functionals against the more accurate G_0W_0 method.

Figure 20 compares the size and center of the band gaps obtained with the density functionals to the G_0W_0 results. Relative to G_0W_0 the PBE functional underestimates the gaps by 45%, i.e. on average the PBE values must be scaled by 1.83 to reproduce the G_0W_0 results. The HSE06 band gaps are closer to G_0W_0 but are nevertheless systematically underesti-

mated by more than 20%. On the other hand, GLLBSC shows very good performance with band gaps only 2% smaller than G_0W_0 on average. Table 10 shows the mean absolute deviations of the DFT methods relative to G_0W_0 . We note that although GLLBSC provides an excellent description of the G_0W_0 band gaps *on average* the spread is sizable with a mean absolute deviation of 0.4 eV.

We note a handful of outliers in figure 20 with large HSE band gaps compared to PBE and G_0W_0 . For one of these, namely the ferromagnetic CoBr₂-CdI₂, we obtain the band gaps: 0.30 eV (PBE), 3.41 eV (HSE), and 0.91 eV (G_0W_0). For validation, we have performed GPAW and QuantumEspresso calculations with the norm-conserving HGH pseudopotentials and plane wave cutoff up to 1600 eV. The converged band gaps are 0.49 eV (GPAW-HGH-PBE), 0.51 eV (QE-HGH-PBE) and 3.69 eV (GPAW-HGH-HSE), 3.52 eV (QE-HGH-HSE), which are all in reasonable



agreement with the C2DB results. It should be interesting to explore the reason for the anomalous behavior of the HSE band gap in these materials.

Compared to the band gaps, the gap centers predicted by PBE and HSE06 are in overall better agreement with the G_0W_0 results. This implies that, on average, the G_0W_0 correction of the DFT band energies is symmetric on the valence and conduction band. In contrast, the GLLBSC predicts less accurate results for the gap center. This suggests that an accurate and efficient prediction of absolute band energies is obtained by combining the GLLBSC band gap with the PBE band gap center.

Next, we consider the band alignment at the interface between different 2D materials. Assuming that the bands line up with a common vacuum level and neglecting hybridisation/charge transfer at the interface, the band alignment is directly given by the VBM and CBM positions relative to vacuum.

We focus on pairs of 2D semiconductors for which the G_0W_0 band alignment is either Type II ($\Delta E > 0$) or Type III ($\Delta E < 0$), see figure 21 (left). Out of approximately 10 000 bilayers predicted to have Type II band alignment by G_0W_0 , the PBE and HSE06 functionals

predict qualitatively wrong band alignment (i.e. Type III) in 44% and 21% cases, respectively (grey shaded areas). In particular, PBE shows a sizable and systematic underestimation of ΔE as a direct consequence of the underestimation of the band gaps in both monolayers.

3.2.2. Effective masses and mobilities

The carrier mobility relates the drift velocity of electrons or holes to the strength of an applied electric field and is among the most important parameters for a semiconductor material. In general, the mobility is a sample specific property which is highly dependent on the sample purity and geometry, and (for 2D materials) interactions with substrate or embedding layers. Here we consider the phonon-limited mobility, which can be considered as the intrinsic mobility of the material, i.e. the mobility that would be measured in the absence of any sample specific- or external scattering sources.

The effective masses of the charge carriers have been calculated both with and without SOC for ~ 600 semiconductors. Figure 22 shows the electron mass plotted against the hole mass. The data points are scat-

Table 9. Key properties of selected stable materials in the C2DB, which have not been previously synthesised. The calculated properties are the magnetic state, formation energy, energy above the convex hull, work function, PBE gap and and the nature of the gap (direct or indirect).

| Prototype | Formula | Magnetic state | ΔH (eV) | ΔH_{hull} (eV) | Φ (eV) | PBE gap (eV) | Direct gap |
|---------------------------------|---------------------------------|----------------|-----------------|-------------------------------|-------------|--------------|------------|
| BiI ₃ | VI ₃ | FM | -0.51 | -0.15 | 5.3 | | |
| | CoCl ₃ | NM | -0.65 | -0.21 | | 1.13 | No |
| | CoBr ₃ | NM | -0.41 | -0.16 | | 0.96 | No |
| | CoI ₃ | NM | -0.14 | -0.14 | | 0.53 | No |
| CdI ₂ | FeO ₂ | FM | -1.14 | -0.36 | 7.31 | | |
| | MnSe ₂ | FM | -0.47 | -0.18 | 5.09 | | |
| | MnS ₂ | FM | -0.57 | -0.12 | 5.74 | | |
| | PdO ₂ | NM | -0.40 | -0.08 | | 1.38 | No |
| | CaBr ₂ | NM | -2.09 | -0.02 | | 4.86 | No |
| FeOCl | RhClO | NM | -0.65 | -0.18 | 5.49 | | |
| | NiClO | AFM | -0.64 | -0.17 | 6.32 | | |
| | NiBrO | AFM | -0.52 | -0.16 | 5.78 | | |
| | ScIS | NM | -1.68 | -0.14 | | 1.66 | Yes |
| FeSe | CoSe | FM | -0.27 | 0.02 | 4.22 | | |
| | RuS | NM | -0.38 | 0.05 | 4.72 | | |
| | MnSe | AFM | -0.50 | -0.20 | | 0.90 | No |
| | MnS | AFM | -0.64 | -0.19 | | 0.78 | No |
| GaS | AlSe | NM | -0.72 | -0.02 | | 2.00 | No |
| | AlS | NM | -0.89 | 0.00 | | 2.09 | No |
| GeSe | GeSe | NM | -0.19 | 0.04 | | 2.22 | No |
| | GeS | NM | -0.22 | 0.05 | | 2.45 | No |
| | GeTe | NM | -0.01 | 0.09 | | 1.47 | No |
| | SnSe | NM | -0.33 | 0.10 | | 2.15 | No |
| MoS ₂ | VS ₂ | FM | -0.88 | -0.02 | 5.95 | | |
| | ScBr ₂ | FM | -1.59 | -0.40 | | 0.16 | No |
| | YBr ₂ | FM | -1.73 | -0.23 | | 0.34 | No |
| | FeCl ₂ | FM | -0.67 | -0.16 | | 0.35 | Yes |
| | TiBr ₂ | NM | -1.14 | -0.04 | | 0.76 | No |
| | ZrBr ₂ | NM | -1.34 | -0.04 | | 0.83 | No |
| Ti ₂ CO ₂ | Zr ₂ CF ₂ | NM | -2.36 | -0.08 | 3.92 | | |
| | Hf ₂ CF ₂ | NM | -2.26 | 0.03 | 3.62 | | |
| | Y ₂ CF ₂ | NM | -2.50 | -0.17 | | 1.12 | No |
| WTe ₂ | NbI ₂ | NM | -0.37 | 0.04 | 3.01 | | |
| | HfBr ₂ | NM | -1.16 | -0.18 | | 0.85 | No |
| | OsSe ₂ | NM | -0.17 | 0.00 | | 0.57 | No |

tered, with no clear correlation between the electron and hole masses. Overall, the electron masses are generally slightly smaller than the hole masses. The mean electron mass is $0.9 m_0$, while the mean hole mass is $1.1 m_0$, and 80% of the electron masses are below m_0 while the fraction is only 65% for the holes. This is not too surprising, since, on average, the energetically lower valence band states are expected to be more localised and thus less dispersive than the conduction band states.

The right panel of figure 22 shows the effective mass for electrons and holes plotted as a function of the inverse band gap. It can be seen that there is no clear correlation between the two quantities, which is confirmed by calculating the cross-correlation coefficient:

for both electrons and holes it is less than 0.02. This provides empirical evidence against the linear relation between effective masses and inverse band gaps derived from $\mathbf{k} \cdot \mathbf{p}$ perturbation theory. The relation is based on the assumption that the perturbative expansion is dominated by the conduction and valence band and that the momentum matrix element between these states, $\langle u_c | \hat{\mathbf{p}} | u_v \rangle$, does not vary too much as function of the considered parameter (here the type of material). These assumptions clearly do not hold across a large set of different semiconductors. If we focus on a specific class of materials, e.g. sulfides in the MoS₂ structure indicated by the highlighted symbols, we see a slightly improved trend but still with significant fluctuations.

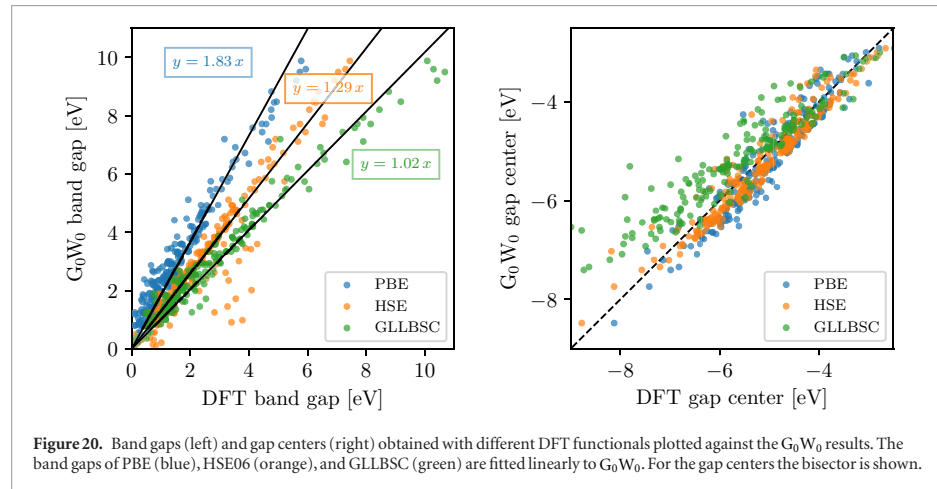


Figure 20. Band gaps (left) and gap centers (right) obtained with different DFT functionals plotted against the G_0W_0 results. The band gaps of PBE (blue), HSE06 (orange), and GLLBSC (green) are fitted linearly to G_0W_0 . For the gap centers the bisector is shown.

Table 10. The mean absolute deviation (in eV) of the band gap and band gap center calculated with three different xc-functionals with respect to G_0W_0 .

| | PBE | HSE06 | GLLBSC |
|----------------------------------|------|-------|--------|
| MAD w.r.t. G_0W_0 (band gap) | 1.49 | 0.82 | 0.38 |
| MAD w.r.t. G_0W_0 (gap center) | 0.37 | 0.32 | 0.76 |

If one assumes energetically isolated and parabolic bands, the intrinsic mobility limited only by scattering on acoustic phonons can be estimated from the Takagi formula [147],

$$\mu_i = \frac{e\hbar^3 \rho v_i^2}{k_B T m_i^* m_d^* D_i^2}. \quad (17)$$

Here i refers to the transport direction, ρ is the mass density, v_i is the speed of sound in the material, m_i^* is the carrier mass, m_d^* is the equivalent isotropic density-of-state mass defined as $m_d^* = \sqrt{m_x^* m_y^*}$, and D_i is the deformation potential. We stress that the simple Takagi formula is only valid for temperatures high enough that the acoustic phonon population can be approximated by the Rayleigh–Jeans law, $n \approx \hbar\omega_{ac}/k_B T$, but low enough that scattering on optical phonons can be neglected.

For the semiconductors in the C2DB we have found that the denominator of equation (17) varies more than the numerator. Consequently, a small product of deformation potential and effective mass is expected to correlate with high mobility. Figure 23 shows the deformation potential plotted against the carrier mass for the valence and conduction bands, respectively. The shaded area corresponds, somewhat arbitrarily, to the region for which $m_i^* D_i < m_0(1 \text{ eV})$. The 2D semiconductors which have been synthesised in monolayer form are indicated with orange symbols while those which have been used in field effect transistors are labeled. Consistent with experimental findings, phosphorene (P) is predicted to be among the

materials with the highest mobility for both electrons and holes.

Interestingly, a number of previously unknown 2D materials lie in this shaded region and could be candidates for high mobility 2D semiconductors. Table 11 lists a few selected materials with high intrinsic mobility according to equation (17), which all have ‘high’ overall stability (see section 2.4.1). In the future, it will be interesting to explore the transport properties of these candidate materials in greater detail.

To put the numbers in table 11 to scale, we consider the well studied example of MoS_2 . For this material we obtain an electron mobility of $240 \text{ cm}^2 \text{ V}^{-1} \text{ s}^{-1}$ while a full *ab initio* calculation found a phonon-limited mobility of $400 \text{ cm}^2 \text{ V}^{-1} \text{ s}^{-1}$ (in good agreement with experiments on hBN encapsulated MoS_2 [148]), with the acoustic phonon contribution corresponding to a mobility of $1000 \text{ cm}^2 \text{ V}^{-1} \text{ s}^{-1}$. Similarly, for the series MX_2 ($M = \text{W}, \text{Mo}, X = \text{S}, \text{Se}$), we calculate room-temperature electron mobilities between $200 \text{ cm}^2 \text{ V}^{-1} \text{ s}^{-1}$ and $400 \text{ cm}^2 \text{ V}^{-1} \text{ s}^{-1}$, which are all within 50% of the *ab initio* results [149]. Presumably, as in the case for MoS_2 , the good quantitative agreement is partly a result of error cancellation between an overestimated acoustic phonon scattering and the neglect of optical phonon scattering. Importantly, however, the relative ordering of the mobilities of the four MX_2 monolayers is correctly predicted by equation (17) for all but one pair (MoS_2 and WSe_2) out of the six pairs. These results illustrate that equation (17) should only be used for ‘order of magnitude’ estimates of the mobility but that relative comparisons of mobilities in different materials are probably reliable.

3.2.3. Magnetic properties

Recently, a single layer of CrI_3 was reported to exhibit ferromagnetic order with a Curie temperature of 45 K [12]. This comprises the first example of a pure 2D material exhibiting magnetic order and there is

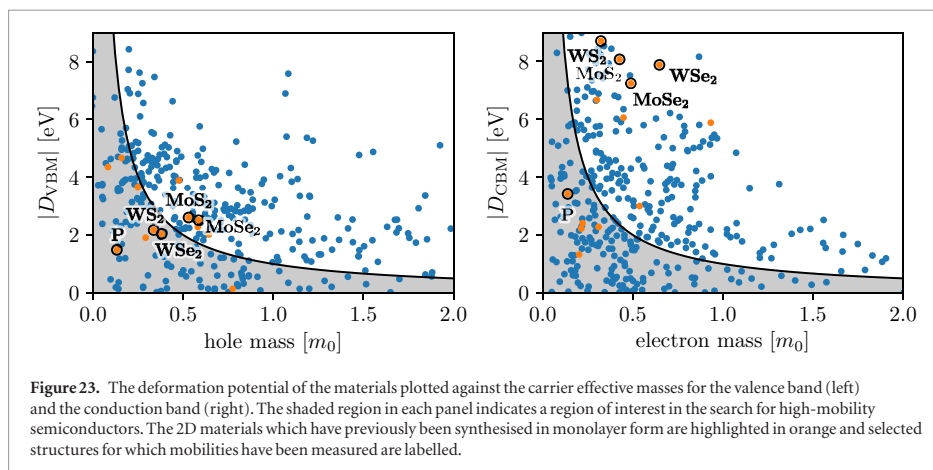
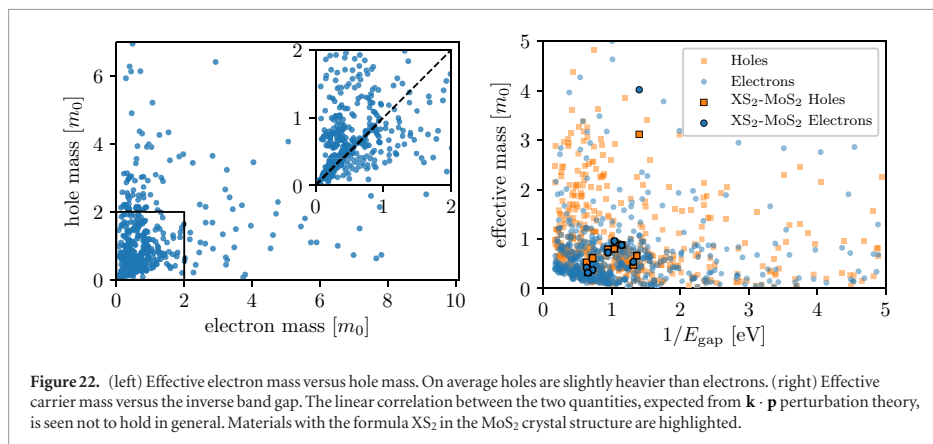
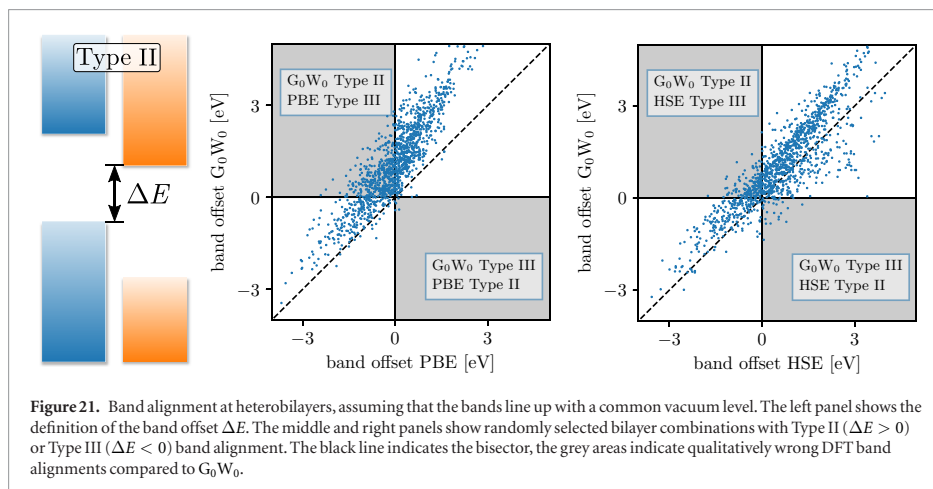
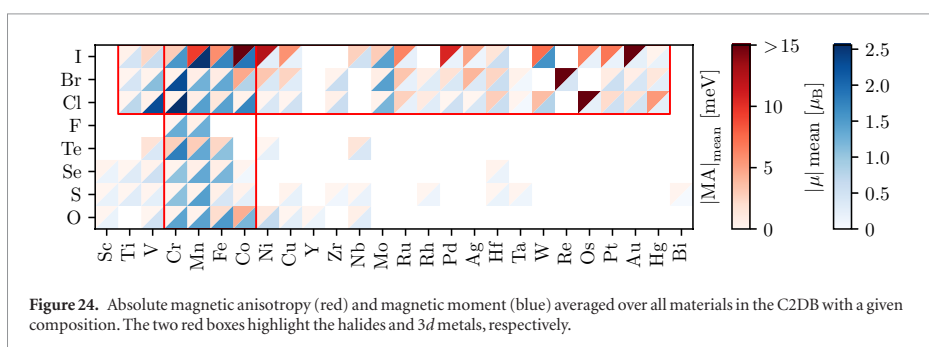


Table 11. Key transport properties of selected materials with high intrinsic room-temperature mobility according to equation (17). All the materials shown have ‘high’ overall stability as defined in section 2.4.1. μ_{high} is the larger value of the mobilities in the x or y directions, m^* is the corresponding effective mass, and $\mu_{\text{high}}/\mu_{\text{low}}$ is the ratio of the mobilities in the two directions.

| Carrier | Formula | Prototype | PBE gap (eV) | μ_{high} ($\text{cm}^2 \text{V}^{-1} \text{s}^{-1}$) | m^* (m_0) | $\frac{\mu_{\text{high}}}{\mu_{\text{low}}}$ |
|-----------|-------------------|------------------|--------------|---|-----------------|--|
| Holes | PbS ₂ | MoS ₂ | 1.39 | 30 000 | 0.62 | 1.4 |
| | OsO ₂ | WTe ₂ | 0.17 | 23 000 | 0.23 | 3.0 |
| | ZrCl ₂ | MoS ₂ | 0.98 | 12 000 | 0.43 | 1.1 |
| | WSSe | MoSSe | 1.40 | 5500 | 0.37 | 1.0 |
| Electrons | PtTe ₂ | CdI ₂ | 0.30 | 9600 | 0.17 | 1.3 |
| | GaO | GaS | 1.56 | 7200 | 0.32 | 1.0 |
| | NiS ₂ | CdI ₂ | 0.58 | 6000 | 0.29 | 1.5 |
| | RuTe ₂ | WTe ₂ | 0.64 | 4600 | 1.55 | 8.5 |



currently an intense search for new 2D materials with magnetic order persisting above room temperature [150–152].

For 2D materials, magnetic order will only persist at finite temperatures in the presence of magnetic anisotropy (MA). Indeed, by virtue of the Mermin–Wagner theorem, magnetic order is impossible in 2D unless the rotational symmetry of the spins is broken [153]. A finite MA with an out-of-plane easy axis breaks the assumption behind the Mermin–Wagner theorem and makes magnetic order possible at finite temperature. The critical temperature for magnetic order in 2D materials will thus have a strong dependence on the anisotropy.

The MA originates from spin–orbit coupling and is here defined as the energy difference between in-plane and out-of-plane orientation of the magnetic moments, see equation (4). With our definition, a negative MA corresponds to an out-of-plane easy axis. We note that most of the materials in the C2DB are nearly isotropic in-plane. Consequently, if the easy axis lies in the plane, the spins will exhibit an approximate in-plane rotational symmetry, which prohibits magnetic order at finite temperatures. Since spin–orbit coupling becomes large for heavy elements, we generally expect to find larger MA for materials containing heavier elements. In general the magnitude of the MA is small. For example, for a monolayer of CrI₃ with a Curie temperature of 45 K [12] we find a MA of -0.85 meV per Cr atom in agreement with previous

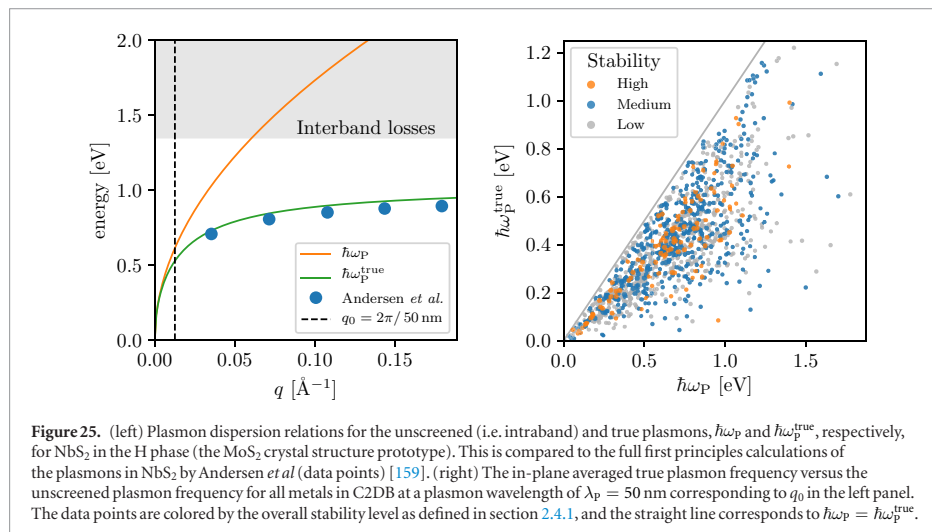
calculations [154]. Although small, the MA is, however, crucial for magnetic order to emerge at finite temperature.

In figure 24 we show the magnitude of the magnetic anisotropy (red triangles) and the magnetic moment per metal atom (blue triangles) averaged over all materials with a given chemical composition. The plot is based on data for around 1200 materials in the medium to high stability categories (see table 2) out of which around 350 are magnetic. It is interesting to note that while the magnetic moment is mainly determined by the metal atom, the MA depends strongly on the non-metal atom. For example, the halides (Cl, Br, I) generally exhibit much larger MAs than the chalcogenides (S, Se, Te). Overall, iodine (I) stands out as the most significant element for a large MA while the 3d metals Cr, Mn, Fe, Co are the most important elements for a large magnetic moment. Since the MA is driven by spin–orbit coupling (SOC) and the spin is mainly located on the metal atom, one would expect a large MA to correlate with a heavy metal atom. However, it is clear from the figure that it is not essential that the spin-carrying metal atom should also host the large SOC. For example, we find large MA for several 3d metal-iodides despite of the relatively weak SOC on the 3d metals. This shows that the MA is governed by a rather complex interplay between the spins, orbital hybridisation and crystal field.

A selection of materials predicted to have high overall stability (see section 2.4.1) and high out-of-plane magnetic anisotropy ($\text{MA} < -0.3$ meV/

Table 12. Selection of magnetic materials with a negative MA per magnetic atom. The prototype, the magnetic moment of the magnetic atom, the energy gap calculated with PBE xc-functional and the magnetic state are also shown. The experimentally synthesised ferromagnetic monolayer CrI₃ is highlighted.

| Formula | Prototype | Magnetic moment (μ_B) | PBE gap (eV) | MA (meV/atom) | Magnetic state | ΔH_{hull} (eV/atom) |
|------------------------|------------------------|-----------------------------|--------------|---------------|----------------|------------------------------------|
| OsI ₃ | BiI ₃ | 0.9 | 0.0 | -3.17 | FM | 0.18 |
| CrTe | FeSe | 2.6 | 0.0 | -1.85 | AFM | 0.15 |
| FeCl ₃ | BiI ₃ | 1.0 | 0.01 | -1.84 | FM | -0.08 |
| FeTe | FeSe | 1.9 | 0.0 | -1.06 | FM | 0.08 |
| MnTe ₂ | CdI ₂ | 2.7 | 0.0 | -0.94 | FM | -0.10 |
| FeBr ₃ | BiI ₃ | 1.0 | 0.04 | -0.88 | FM | -0.04 |
| CrI₃ | BiI₃ | 3.0 | 0.90 | -0.85 | FM | -0.21 |
| MnTe | FeSe | 3.8 | 0.69 | -0.75 | AFM | -0.15 |
| NiO | PbSe | 1.1 | 0.0 | -0.53 | FM | 0.05 |
| FeBrO | FeOCl | 1.1 | 0.0 | -0.47 | FM | -0.05 |
| CrISe | FeOCl | 3.0 | 0.0 | -0.45 | FM | -0.10 |
| MnSe ₂ | CdI ₂ | 2.8 | 0.0 | -0.40 | FM | -0.18 |
| CrIS | FeOCl | 3.0 | 0.35 | -0.36 | FM | -0.10 |
| MnO ₂ | CdI ₂ | 3.0 | 1.13 | -0.36 | FM | 0.02 |
| VCl ₃ | BiI ₃ | 2.0 | 0.0 | -0.35 | FM | -0.01 |
| MnSe | FeSe | 3.7 | 0.90 | -0.31 | AFM | -0.20 |
| CrSe | FeSe | 2.0 | 0.0 | -0.31 | AFM | 0.12 |



magnetic atom) is listed in table 12. We find several semiconductors with anisotropies comparable to CrI₃ and some metals with higher values. If we also look at materials with medium overall stability, we find semiconductors with anisotropies up to 2 meV/atom. It is likely that some of these materials will have Curie temperatures similar to, or even higher than, CrI₃.

In addition to the MA, the critical temperature depends sensitively on the magnetic exchange couplings. We are presently developing a workflow for systematic calculation of exchange coupling constants, which will allow us to estimate the Curie temperature of all the magnetically ordered 2D materials. The database contains several 2D materials with antiferromagnetic order. As a note of caution, we mention

that the magnetic interactions in AFM materials typically arise from the super-exchange mechanism, which is poorly described by PBE and requires a careful verification using a PBE + U scheme [155].

3.2.4. Plasmons

The unique optical properties of 2D materials make them highly interesting as building blocks for nanophotonic applications [156, 157]. Many of these applications involve electron rich components which can capture, focus, and manipulate light via plasmons or plasmon-polaritons. Graphene sheets can host plasmons that are long lived, can be easily tuned via electrostatic or chemical doping, and can be used to confine light to extremely small volumes [158].

Table 13. Selection of 2D metals with high plasmon energies ω_p^{true} for a plasmon wavelength of $\lambda_p = 50$ nm. The interband screening $\alpha^{2\text{D,inter}}$ at $\omega = 0$ and the in-plane averaged 2D plasma frequency $\omega_{p,2\text{D}}$, which are required to reproduce ω_p^{true} , are also reported.

| Prototype | Formula | Magnetic state | ω_p^{true} (eV) | $\alpha^{2\text{D,inter}}$ (Å) | $\omega_{p,2\text{D}}$ (eV Å ^{0.5}) |
|------------------|-------------------|----------------|----------------------------------|-----------------------------------|--|
| TiS ₃ | TaSe ₃ | NM | 0.99 | 12.54 | 12.48 |
| FeOCl | PdClS | NM | 0.93 | 4.13 | 9.52 |
| FeOCl | NiClS | NM | 0.90 | 5.60 | 9.66 |
| CdI ₂ | TaS ₂ | NM | 0.82 | 5.59 | 8.79 |
| FeOCl | ZrIS | NM | 0.75 | 7.68 | 8.43 |
| CdI ₂ | NbS ₂ | NM | 0.73 | 8.2 | 8.42 |
| FeOCl | ZrClS | NM | 0.73 | 13.6 | 9.35 |
| TiS ₃ | TaS ₃ | NM | 0.73 | 34.22 | 12.44 |
| PbSe | NiO | FM | 0.72 | 2.9 | 7.16 |

However, due to the limited charge carrier density achievable in graphene, its plasmons are limited to the mid-infrared regime. Here we show that some metallic monolayers support plasmons with significantly higher energies than graphene and could potentially push 2D plasmonics into the optical regime.

Figure 25 (left) shows the plasmon dispersion for monolayer NbS₂ in the MoS₂ crystal structure. The effect of interband transitions on the plasmon is significant as can be seen by comparison to the pure intraband plasmon ($\hbar\omega_p$). The true plasmon energies are obtained from the poles of the (long wave length limit) dielectric function including the interband transitions, $\epsilon = 1 + 2\pi q(\alpha^{2\text{D,intra}} + \alpha^{2\text{D,inter}})$, yielding $\omega_p^{\text{true}} = \omega_{p,2\text{D}} q^{1/2} [1 + 2\pi q \alpha^{2\text{D,inter}} (\omega_p^{\text{true}})]^{-1/2}$. For simplicity we ignore the frequency dependence of the interband polarisability, i.e. we set $\alpha^{2\text{D,inter}}(\omega_p^{\text{true}}) \approx \alpha^{2\text{D,inter}}(\omega = 0)$, which should be valid for small plasmon energies (far from the onset of interband transitions). The validity of this approximation is confirmed by comparing to the full *ab initio* calculations of Andersen *et al* (blue dots) which include the full q - and ω -dependence [159]. The figure shows that interband screening generally reduces the plasmon energy and becomes increasingly important for larger q .

Figure 25 (right) shows the in-plane averaged true plasmon energy of all metals in the C2DB plotted against the intraband plasmon energy at a fixed plasmon wavelength of $\lambda_p = 50$ nm (corresponding to q_0 at the dashed vertical line in the left panel). For comparison, the plasmon energy of freestanding graphene at this wavelength and for the highest achievable doping level ($E_F = \pm 0.5$ eV relative to the Dirac point) is around 0.4 eV. The data points are colored according to the overall stability level as defined in section 2.4.1. Table 13 shows a selection of the 2D metals with ‘high’ overall stability (see section 2.4.1) and large plasmon frequencies. We briefly note the interesting band structures of the metals in the FeOCl prototype (not shown) which exhibits band gaps above or below the partially occupied metallic band(s), which is likely to lead to reduced losses in plasmonic applications [160].

A detailed study of the plasmonic properties of the lead candidate materials will be published elsewhere. However, from figure 25 (right) it is already clear that several of the 2D metals have plasmon energies around 1 eV at $\lambda_p = 50$ nm, which significantly exceeds the plasmon energies in highly doped graphene.

3.2.5. Excitons

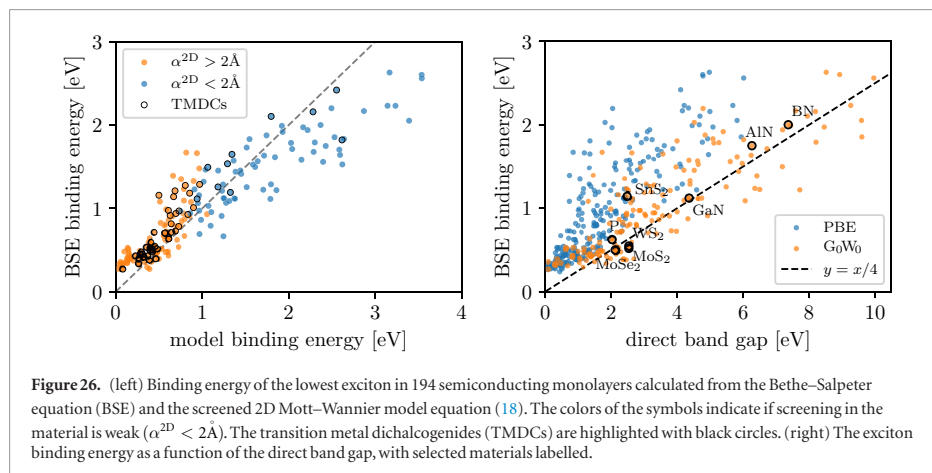
Two-dimensional materials generally exhibit pronounced many-body effects due to weak screening and strong quantum confinement. In particular, exciton binding energies in monolayers are typically an order of magnitude larger than in the corresponding layered bulk phase and it is absolutely crucial to include excitonic effects in order to reproduce experimental absorption spectra.

The electronic screening is characterised by the in-plane 2D polarisability, see equation (12). For a strictly 2D insulator, the screened Coulomb potential can be written as $W^{2\text{D}}(q) = v_c^{2\text{D}}(q)/\epsilon^{2\text{D}}(q)$ with $\epsilon^{2\text{D}}(q) = 1 + 2\pi\alpha^{2\text{D}}q$ and $v_c^{2\text{D}}(q) = 2\pi/q$ is the 2D Fourier transform of the Coulomb interaction. The q -dependence of $\epsilon^{2\text{D}}$ indicates that the screening is non-local, i.e. it cannot be represented by a q -independent dielectric constant, and that Coulomb interactions tend to be weakly screened at large distances (small q vectors) [119, 161, 162]. This is in sharp contrast to the case of 3D semiconductors/insulators where screening is most effective at large distances where its effect can be accounted for by a q -independent dielectric constant. For a two-band model with isotropic parabolic bands, the excitons can be modeled by a 2D Hydrogen-like (Mott–Wannier) Hamiltonian where the Coulomb interaction is replaced by $W = 1/\epsilon r$ and the electron mass is replaced by a reduced excitonic mass μ_{ex} derived from the curvature of conduction and valence bands. It has previously been shown that the excitonic Rydberg series of a 2D semiconductor can be accurately reproduced by this model if the dielectric constant, ϵ , is obtained by averaging $\epsilon^{2\text{D}}(q)$ over the extent of the exciton in reciprocal space [163]. For the lowest exciton ($n = 1$), the binding energy can then be expressed as

$$E_B = \frac{8\mu_{\text{ex}}}{(1 + \sqrt{1 + 32\pi\alpha^{2\text{D}}\mu_{\text{ex}}/3})^2}. \quad (18)$$

It has furthermore been demonstrated that this expression gives excellent agreement with a numerical solution of the Mott–Wannier model employing the full q -dependent dielectric function, $\epsilon^{2\text{D}}(q) = 1 + 2\pi\alpha^{2\text{D}}q$, for 51 transition metal dichalcogenides [163]. We note that the previous calculations were based on LDA and we generally find that the PBE values for $\alpha^{2\text{D}}$ obtained in the present work are 10–20% smaller compared with LDA.

In figure 26, we compare the binding energy of the lowest exciton obtained from BSE-PBE with G_0W_0 scissors operator and the Mott–Wannier model equation (18), respectively. Results are shown for the 194



non-magnetic semiconductors out of the total set of ~ 250 materials for which BSE calculations have been performed. We focus on the optically active zero-momentum excitons and compute the exciton masses by evaluating the curvature of the band energies at the *direct gap*, see section 2.11. For anisotropic materials we average the heavy and light exciton masses as well as the x and y components of the polarisability, α^{2D} , to generate input parameters for the isotropic model equation (18).

Although a clear correlation with the BSE results is observed, it is also evident that the Mott–Wannier model can produce significant errors. The mean absolute deviation between BSE and the model is 0.28 eV for all materials and 0.20 eV for the subset of transition metal dichalcogenides (TMDCs). Furthermore, the Mott–Wannier model seems to overestimate E_B for more strongly bound excitons while the opposite trend is seen for weakly bound excitons. As explained below these trends are a consequence of systematic errors in the Mott–Wannier model which can be traced to two distinct sources.

(i) *Weak screening*: If α^{2D} is small (on the order of 1 Å), the exciton becomes strongly localised and the orbital character of the states comprising the exciton plays a significant role. In general, the Mott–Wannier model tends to overestimate the exciton binding energy in this case as can be seen from the relatively large deviation of points with model binding energies >2.0 eV in figure 26. The overestimated binding energy results from the homogeneous electron and hole distributions implicitly assumed in the Mott–Wannier model. In reality, the short range variation of the electron and hole distributions is determined by the shape of the conduction and valence band states. In general these will differ leading to a reduced spatial overlap of the electron and hole and thus a lower Coulomb interaction. For example, SrCl₂ in the CdI₂ prototype ($\alpha^{2D} = 0.68$ Å) has a BSE binding

energy of 2.1 eV and a model binding energy of 3.4 eV. From the PDOS of this material (see the C2DB webpage) it is evident that the electron and hole are mainly residing on the Sr and Cl atoms, respectively.

(ii) *Breakdown of the parabolic band approximation*: Materials with small band gaps often exhibit hyperbolic rather than parabolic band structures in the vicinity of the band gap. This typically happens in materials with small band gaps such as BSb in the BN prototype. In figure 26 these materials can be identified as the cluster of points with model binding energies <0.25 eV and BSE binding energies >0.25 eV. A similar situation occurs if the conduction and valence bands flatten out away from the band gap region. In both of these cases, the excitons tend to be delocalised over a larger area in the Brillouin zone than predicted by the parabolic band approximation of the Mott–Wannier model. Typically, such delocalisation will result in larger binding energies than predicted by the model. For example, FeI₂ in the CdI₂ prototype exhibits shallow band minima in a ring around the Γ -point and has a BSE binding energy of 1.1 eV and a model binding energy of 0.5 eV because the model assumes that the exciton will be located in the vicinity of the shallow minimum (and thus more delocalised in real space). A detailed inspection reveals that such break down of the parabolic band approximation is responsible for most of the cases where the model underestimates the binding energy.

Other sources of errors come from contributions to the exciton from higher/lower lying bands, i.e. breakdown of the two-band approximation, and anisotropic exciton masses not explicitly accounted for by equation (18).

Based on this comprehensive and unbiased assessment of the Mott–Wannier model, we conclude that while the model can be useful for understand-

ing trends and qualitative properties of excitons, its quantitative accuracy is rather limited when applied to a broad set of materials without any parameter tuning. For quantitative estimates α^{2D} should not be too small (certainly not less than 2 Å) and the validity of the effective mass approximation should be carefully checked by inspection of the band structure.

It has been argued that there should exist a robust and universal scaling between the exciton binding energy and the quasiparticle band gap of 2D semiconductors, namely $E_B \approx E_{\text{gap}}/4$ [164]. This scaling relation was deduced empirically based on BSE-GW calculations for around 20 monolayers and explained from equation (18) and the relation $\alpha^{2D} \propto 1/E_{\text{gap}}$ from $\mathbf{k} \cdot \mathbf{p}$ perturbation theory. Another work observed a similar trend [165] but explained it from the $1/E_{\text{gap}}$ dependence of the exciton effective mass expected from $\mathbf{k} \cdot \mathbf{p}$ perturbation theory. Based on our results we can completely refute the latter explanation (see figure 22 (right)). In figure 26 (right) we show the exciton binding energy plotted versus the direct PBE and G_0W_0 band gaps, respectively. While there is a correlation, it is by no means as clear as found in [164].

4. Conclusions and outlook

The C2DB is an open database with calculated properties of two-dimensional materials. It currently contains more than 1500 materials distributed over 32 different crystal structures. A variety of structural, elastic, thermodynamic, electronic, magnetic and optical properties are computed following a high-throughput, semi-automated workflow employing state of the art DFT and many-body methods. The C2DB is growing continuously as new structures and properties are being added; thus the present paper provides a snapshot of the present state of the database. The C2DB can be browsed online using simple and advanced queries, and it can be downloaded freely at <https://c2db.fysik.dtu.dk/> under a Creative Commons license.

The materials in the C2DB comprise both experimentally known and not previously synthesised structures. They have been generated in a systematic fashion by combinatorial decoration of different 2D crystal lattices. The full property workflow is performed only for structures that are found to be dynamically stable and have a negative heat of formation. We employ a liberal stability criterion in order not to exclude potentially interesting materials that could be stabilised by external means like substrate interactions or doping even if they are unstable in freestanding form. As an important and rather unique feature, the C2DB employs beyond-DFT methods, such as the many-body GW approximation, the random phase approximation (RPA) and the Bethe–Salpeter equation (BSE). Such methods are essential for obtaining quantitatively accurate descriptions of key properties like band gaps and optical spectra. This is particularly important for 2D materials due the weak dielectric

screening in reduced dimensions, which tends to enhance many-body effects. For maximal transparency and reproducibility of the data in the C2DB, all relevant parameters have been provided in this paper. Additionally, all scripts used to generate the data are freely available for download under a GPL license.

Beyond its obvious use as a look-up table, the C2DB offers access to numerous well documented, high-quality calculations, making it ideally suited for benchmarking and comparison of different codes and methodologies. The large set of different available properties makes the C2DB interesting as a playground for exploring structure-property relations and for applying and advancing machine learning approaches in materials science. Moreover, the C2DB should be useful as a stepping stone towards the development of theoretical models for more complex 2D structures such as van der Waals heterostructures (see below).

As reported in this work, based on the combinatorial screening approach, we have identified a number of new, potentially synthesisable 2D materials with interesting properties including ferromagnets with large magnetic anisotropy, semiconductors with high intrinsic carrier mobility, and metals with plasmons in the visible frequency range. These predictions are all based on the computed properties of the perfect crystalline materials. While the pristine crystal constitutes an important baseline reference it remains an idealised model of any real material. In the future, it would be interesting to extend the database to monolayers with adsorbed species and/or point defects. Not only would this allow for a more realistic assessment of the magnetic and (opto)electronic properties, it would also facilitate the design and discovery of 2D materials for e.g. battery electrodes and (electro)catalysis [166, 167].

The C2DB should also be useful as a platform for establishing parametrisations of computationally less expensive methods such as tight-binding models [168] and $\mathbf{k} \cdot \mathbf{p}$ perturbation theory [128]. Such methods are required e.g. for device modeling, description of magnetic field effects, and van der Waals heterostructures. The database already provides band structures, spin orbit-induced band splittings, and effective masses, which can be directly used to determine model parameters. It would be straightforward to complement these with momentum matrix elements at band extrema for modeling of optical properties and construction of full $\mathbf{k} \cdot \mathbf{p}$ Hamiltonians. Similarly, the spread functional required as input for the construction of Wannier functions e.g. by the ASE [38] or the Wannier90 [169] packages, could be easily and systematically produced. This would enable direct construction of minimal basis set Hamiltonians and would allow for the calculation of Born charges and piezoelectric coefficients as well as certain topological invariants [170]. A workflow to calculate exchange couplings of magnetic 2D materials is currently being developed with the aim of predicting magnetic phase transitions and critical temperatures.

Of specific interest is the modeling of the electronic and optical properties of vdW heterostructures. Due to lattice mismatch or rotational misalignment between stacked 2D layers, such structures are difficult or even impossible to treat by conventional *ab initio* techniques. Different simplified models have been proposed to describe the electronic bands, including tight-binding Hamiltonians derived from strained lattice configurations [171] and perturbative treatments of the interlayer coupling [172]. In both cases, the data in the C2DB represents a good starting point for constructing such models. The effect of dielectric screening in vdW heterostructures can be incorporated e.g. by the quantum electrostatic heterostructure (QEH) model [173] which computes the dielectric function of the vdW heterostructure from the polarisabilities of the isolated monolayers. The latter are directly available in the C2DB, at least in the long wavelength limit.

Finally, it would be relevant to supplement the current optical absorbance spectra by other types of spectra, such as Raman spectra, infrared absorption or XPS, in order to assist experimentalists in characterising their synthesised samples. The automatic first-principles calculation of such spectra is, however, not straightforward and will require significant computational investments.

Acknowledgments

The Center for Nanostructured Graphene is sponsored by the Danish National Research Foundation, Project DNRF103. The project also received funding from the European Unions Horizon 2020 research and innovation programme under Grant Agreement No. 676580 with The Novel Materials Discovery (NOMAD) Laboratory, a European Center of Excellence. This work was also supported by a research grant (9455) from VILLUM FONDEN. This project has received funding from the European Research Council (ERC) under the European Union's Horizon 2020 research and innovation programme (grant agreement No 773122, LIMA).

ORCID iDs

Sten Hastrup  <https://orcid.org/0000-0003-3696-0356>

Mohnish Pandey  <https://orcid.org/0000-0002-1715-0617>

Thorsten Deilmann  <https://orcid.org/0000-0003-4165-2446>

Nicki F Hinsche  <https://orcid.org/0000-0002-0176-6038>

Morten N Gjerding  <https://orcid.org/0000-0002-5256-660X>

Kristian S Thygesen  <https://orcid.org/0000-0001-5197-214X>

References

- [1] Ferrari A C *et al* 2015 Science and technology roadmap for graphene, related two-dimensional crystals and hybrid systems *Nanoscale* **7** 4598–810
- [2] Bhimanapati G R *et al* 2015 Recent advances in two-dimensional materials beyond graphene *ACS Nano* **9** 11509–39
- [3] Huang C, Wu S, Sanchez A M, Peters J J, Beanland R, Ross J S, Rivera P, Yao W, Cobden D H and Xu X 2014 Lateral heterojunctions within monolayer mose2–wse2 semiconductors *Nat. Mater.* **13** 1096–101
- [4] Geim A K and Grigorieva I V 2013 Van der waals heterostructures *Nature* **499** 419–25
- [5] Molle A, Goldberger J, Houssa M, Xu Y, Zhang S-C and Akinwande D 2017 Buckled two-dimensional xene sheets *Nat. Mater.* **16** 163–9
- [6] Bianco E, Butler S, Jiang S, Restrepo O D, Windl W and Goldberger J E 2013 Stability and exfoliation of germanane: a germanium graphene analogue *ACS Nano* **7** 4414–21
- [7] Wang Q H, Kalantar-Zadeh K, Kis A, Coleman J N and Strano M S 2012 Electronics and optoelectronics of two-dimensional transition metal dichalcogenides *Nat. Nanotechnol.* **7** 699–712
- [8] Naguib M, Mashtalir O, Carle J, Presser V, Lu J, Hultman L, Gogotsi Y and Barsoum M W 2012 Two-dimensional transition metal carbides *ACS Nano* **6** 1322–31
- [9] Ci L *et al* 2010 Atomic layers of hybridized boron nitride and graphene domains *Nat. Mater.* **9** 430–5
- [10] Al Balushi Z Y *et al* 2016 Two-dimensional gallium nitride realized via graphene encapsulation *Nat. Mater.* **15** 1166
- [11] Lin S-H and Kuo J-L 2014 Towards the ionic limit of two-dimensional materials: monolayer alkaline earth and transition metal halides *Phys. Chem. Chem. Phys.* **16** 20763–71
- [12] Huang B *et al* 2017 Layer-dependent ferromagnetism in a van der Waals crystal down to the monolayer limit *Nature* **546** 270
- [13] Dattatray J *et al* 2012 Gas and gase ultrathin layer transistors *Adv. Mater.* **24** 3549–54
- [14] Hu P, Wen Z, Wang L, Tan P and Xiao K 2012 Synthesis of few-layer gase nanosheets for high performance photodetectors *ACS Nano* **6** 5988–94
- [15] Dou L *et al* 2015 Atomically thin two-dimensional organic-inorganic hybrid perovskites *Science* **349** 1518–21
- [16] Ashton M, Paul J, Sinnott S B and Hennig R G 2017 Topology-scaling identification of layered solids and stable exfoliated 2d materials *Phys. Rev. Lett.* **118** 106101
- [17] Cheon G, Duerloo K-A N, Sendek A D, Porter C, Chen Y and Reed E J 2017 Data mining for new two- and one-dimensional weakly bonded solids and lattice-commensurate heterostructures *Nano Lett.* **17** 1915–23
- [18] Mounet N, Gibertini M, Schwaller P, Merkys A, Castelli I E, Cepellotti A, Pizzi G and Marzari N 2018 Novel two-dimensional materials from high-throughput computational exfoliation of experimentally known compounds *Nat. Nanotechnol.* **13** 246–52
- [19] Choudhary K, Kalish I, Beams R and Tavazza F 2017 High-throughput identification and characterization of two-dimensional materials using density functional theory *Sci. Rep.* **7** 5179
- [20] Jain A, Persson K A and Ceder G 2016 Research update: the materials genome initiative: data sharing and the impact of collaborative *ab initio* databases *APL Mater.* **4** 053102
- [21] Thygesen K S and Jacobsen K W 2016 Making the most of materials computations *Science* **354** 180–1
- [22] Jain A, Ong S P, Hautier G, Chen W, Richards W D, Dacek S, Cholia S, Gunter D, Skinner D, Ceder G and Persson K A 2013 The materials project: a materials genome approach to accelerating materials innovation *APL Mater.* **1** 011002
- [23] Curtarolo S *et al* 2012 Aflo: an automatic framework for high-throughput materials discovery *Comput. Mater. Sci.* **58** 218–26
- [24] Saal J E, Kirklin S, Aykol M, Meredig B and Wolverton C 2013 Materials design and discovery with high-throughput density

- functional theory: the open quantum materials database (oqmd) *JOM* **65** 1501–9
- [25] Kirklın S, Saal J E, Meredig B, Thompson A, Doak J W, Aykol M, Ruehl S and Wolverton C 2015 The open quantum materials database (oqmd): assessing the accuracy of dft formation energies *NPJ Comput. Mater.* **1** 15010
- [26] <http://nomad-repository.eu>; <https://nomad-coe.eu>
- [27] Lejaeghere K *et al* 2016 Reproducibility in density functional theory calculations of solids *Science* **351** aad3000
- [28] Hautier G, Fischer C C, Jain A, Mueller T and Ceder G 2010 Finding nature's missing ternary oxide compounds using machine learning and density functional theory *Chem. Mater.* **22** 3762–7
- [29] Ghiringhelli L M, Vybiral J, Levchenko S V, Draxl C and Scheffler M 2015 Big data of materials science: critical role of the descriptor *Phys. Rev. Lett.* **114** 105503
- [30] Ward L and Wolverton C 2017 Atomistic calculations and materials informatics: a review *Curr. Opin. Solid State Mater. Sci.* **21** 167–76
- [31] Şahin H, Cahangirov S, Topsakal M, Bekaroglu E, Akturk E, Senger R T and Ciraci S 2009 Monolayer honeycomb structures of group-IV elements and III–V binary compounds: first-principles calculations *Phys. Rev. B* **80** 155453
- [32] Ciraci S and Cahangirov S 2017 *2D Materials: Properties and Devices* ed P Avouris *et al* (Cambridge: Cambridge University Press) pp 472–84
- [33] Ataca C, Şahin H and Ciraci S 2012 Stable, single-layer mx₂ transition-metal oxides and dichalcogenides in a honeycomb-like structure *J. Phys. Chem. C* **116** 8983–99
- [34] Lebègue S, Björkman T, Klintonberg M, Nieminen R M and Eriksson O 2013 Two-dimensional materials from data filtering and *ab initio* calculations *Phys. Rev. X* **3** 031002
- [35] Miro P, Audiffred M and Heine T 2014 An atlas of two-dimensional materials *Chem. Soc. Rev.* **43** 6537–54
- [36] Rasmussen F A and Thygesen K S 2015 Computational 2d materials database: electronic structure of transition-metal dichalcogenides and oxides *J. Phys. Chem. C* **119** 13169–83
- [37] Enkovaara J *et al* 2010 Electronic structure calculations with gpaw: a real-space implementation of the projector-augmented-wave method *J. Phys.: Condens. Matter* **22** 253202
- [38] Larsen A *et al* 2017 The atomic simulation environment—a python library for working with atoms *J. Phys.: Condens. Matter* **29** 273002
- [39] Cordero B, Gomez V, Platero-Prats A E, Reves M, Echeverria J, Cremades E, Barragan F and Alvarez S 2008 Covalent radii revisited *Dalton Trans.* **37** 2832–8
- [40] Larsen P M 2017 Structural analysis algorithms for nanomaterials *PhD Thesis* Department of Physics, DTU
- [41] Özçelik V O, Azadani J G, Yang C, Koester S J and Low T 2016 Band alignment of two-dimensional semiconductors for designing heterostructures with momentum space matching *Phys. Rev. B* **94** 035125
- [42] Togo A 2009 Spglib <https://atztogo.github.io/spglib/>
- [43] Pandey M and Jacobsen K W 2015 Heats of formation of solids with error estimation: the mbeef functional with and without fitted reference energies *Phys. Rev. B* **91** 235201
- [44] Stevanović V, Lany S, Zhang X and Zunger A 2012 Correcting density functional theory for accurate predictions of compound enthalpies of formation: fitted elemental-phase reference energies *Phys. Rev. B* **85** 115104
- [45] Anisimov V and Gunnarsson O 1991 Density-functional calculation of effective coulomb interactions in metals *Phys. Rev. B* **43** 7570
- [46] Kuhar K, Crovetto A, Pandey M, Thygesen K S, Seger B, Vesborg P C K, Hansen O, Chorkendorff I and Jacobsen K W 2017 Sulfide perovskites for solar energy conversion applications: computational screening and synthesis of the selected compound lays3 *Energy Environ. Sci.* **10** 2579–93
- [47] Zhou Y *et al* 2018 Antiferromagnetic order in epitaxial fese films on srto3 *Phys. Rev. Lett.* **120** 097001
- [48] Alfe D 2009 Phon: a program to calculate phonons using the small displacement method *Comput. Phys. Commun.* **180** 2622–33
- [49] Novoselov K S, Geim A K, Morozov S V, Jiang D, Zhang Y, Dubonos S V, Grigorieva I V and Firsov A A 2004 Electric field effect in atomically thin carbon films *Science* **306** 666–9
- [50] Sone J, Yamagami T, Aoki Y, Nakatsuji K and Hirayama H 2014 Epitaxial growth of silicene on ultra-thin ag (1 1 1) films *New J. Phys.* **16** 095004
- [51] Dávila M, Xian L, Cahangirov S, Rubio A and Le Lay G 2014 Germanene: a novel two-dimensional germanium allotrope akin to graphene and silicene *New J. Phys.* **16** 095002
- [52] Li L, Yu Y, Ye G J, Ge Q, Ou X, Wu H, Feng D, Chen X H and Zhang Y 2014 Black phosphorus field-effect transistors *Nat. Nanotechnol.* **9** 372
- [53] Yang S *et al* 2017 C_{3n}—a 2d crystalline, hole-free, tunable-narrow-bandgap semiconductor with ferromagnetic properties *Adv. Mater.* **29** 1605625
- [54] Kappera R, Voiry D, Yalcin S E, Branch B, Gupta G, Mohite A D and Chhowalla M 2014 Phase-engineered low-resistance contacts for ultrathin MoS₂ transistors *Nat. Mater.* **13** 1128
- [55] Mak K F, Lee C, Hone J, Shan J and Heinz T F 2010 Atomically thin MoS₂: a new direct-gap semiconductor *Phys. Rev. Lett.* **105** 136805
- [56] Tonndorf P *et al* 2013 Photoluminescence emission and raman response of monolayer MoS₂, mo₂ e and w₂ e *Opt. Express* **21** 4908–16
- [57] Lu A-Y *et al* 2017 Janus monolayers of transition metal dichalcogenides *Nat. Nanotechnol.* **12** 744
- [58] Naylor C H *et al* 2016 Monolayer single-crystal 1T-mote₂ grown by chemical vapor deposition exhibits weak antilocalization effect *Nano Lett.* **16** 4297–304
- [59] Wang Y *et al* 2017 Structural phase transition in monolayer mote₂ driven by electrostatic doping *Nature* **550** 487
- [60] Okada M, Sawazaki T, Watanabe K, Taniguchi T, Hibino H, Shinohara H and Kitaura R 2014 Direct chemical vapor deposition growth of WS₂ atomic layers on hexagonal boron nitride *ACS Nano* **8** 8273–7
- [61] Fei Z, Palomaki T, Wu S, Zhao W, Cai X, Sun B, Nguyen P, Finney J, Xu X and Cobden D H 2017 Edge conduction in monolayer wte₂ *Nat. Phys.* **13** 677
- [62] Xi X, Zhao L, Wang Z, Berger H, Forró L, Shan J and Mak K F 2015 Strongly enhanced charge-density-wave order in monolayer nbse₂ *Nat. Nanotechnol.* **10** 765
- [63] Wang X, Lin J, Zhu Y, Luo C, Suenaga K, Cai C and Xie L 2017 Chemical vapor deposition of trigonal prismatic nbs₂ monolayers and 3r-polytype few-layers *Nanoscale* **9** 16607–11
- [64] Zhang M *et al* 2015 Controlled synthesis of zrs₂ monolayer and few layers on hexagonal boron nitride *J. Am. Chem. Soc.* **137** 7051–4
- [65] Mañas-Valero S, García-López V, Cantarero A and Galbiati M 2016 Raman spectra of zrs₂ and zrse₂ from bulk to atomically thin layers *Appl. Sci.* **6** 264
- [66] Xu K, Wang Z, Wang F, Huang Y, Wang F, Yin L, Jiang C and He J 2015 Ultrasensitive phototransistors based on few-layered hfs₂ *Adv. Mater.* **27** 7881–7
- [67] Fu W *et al* 2016 Controlled synthesis of atomically thin 1t-tas₂ for tunable charge density wave phase transitions *Chem. Mater.* **28** 7613–8
- [68] Ryu H *et al* 2018 Persistent charge-density-wave order in single-layer tase₂ *Nano Lett.* **8** 689–94
- [69] Zhao W, Dong B, Guo Z, Su G, Gao R, Wang W and Cao L 2016 Colloidal synthesis of VSe₂ single-layer nanosheets as novel electrocatalysts for the hydrogen evolution reaction *Chem. Commun.* **52** 9228–31
- [70] Feng J, Sun X, Wu C, Peng L, Lin C, Hu S, Yang J and Xie Y 2011 Metallic few-layered VS₂ ultrathin nanosheets: high two-dimensional conductivity for in-plane supercapacitors *J. Am. Chem. Soc.* **133** 17832–8
- [71] Wang Y *et al* 2015 Monolayer ptse₂, a new semiconducting transition-metal-dichalcogenide, epitaxially grown by direct selenization of pt *Nano Lett.* **15** 4013–8
- [72] Zhao Y, Qiao J, Yu B, Hu Z, Lin Z, Lau S P, Liu Z, Ji W and Chai Y 2016 Extraordinarily strong interlayer interaction in 2d layered pts₂ *Adv. Mater.* **28** 2399–407

- [73] Wan C *et al* 2015 Flexible n-type thermoelectric materials by organic intercalation of layered transition metal dichalcogenide *Nat. Mater.* **14** 622
- [74] Shao Y *et al* 2017 Epitaxial fabrication of two-dimensional NiSe_2 on $\text{Ni}(111)$ substrate *Appl. Phys. Lett.* **111** 113107
- [75] Tongay S *et al* 2014 Monolayer behaviour in bulk res_2 due to electronic and vibrational decoupling *Nat. Commun.* **5** 3252
- [76] Oyedele A D *et al* 2017 PdSe_2 : pentagonal two-dimensional layers with high air stability for electronics *J. Am. Chem. Soc.* **139** 14090–7
- [77] Zhou L *et al* 2018 InSe monolayer: synthesis, structure and ultra-high second-harmonic generation *2D Mater.* **5** 025019
- [78] Del Pozo-Zamudio O *et al* 2015 Photoluminescence of two-dimensional gate and gas films *2D Mater.* **2** 035010
- [79] Zhou Y, Nie Y, Liu Y, Yan K, Hong J, Jin C, Zhou Y, Yin J, Liu Z and Peng H 2014 Epitaxy and photoresponse of two-dimensional gas crystals on flexible transparent mica sheets *ACS Nano* **8** 1485–90
- [80] Island J O, Buscema M, Barawi M, Clamagirand J M, Ares J R, Sánchez C, Ferrer I J, Steele G A, van der Zant H S and Castellanos-Gomez A 2014 Ultrahigh photoresponse of few-layer TiS_3 nanoribbon transistors *Adv. Opt. Mater.* **2** 641–5
- [81] Wang Y-Q *et al* 2016 Tunable electronic structures in wrinkled 2d transition-metal-trichalcogenide (tmt) hftc_3 films *Adv. Electron. Mater.* **2** 1600324
- [82] Song C-L, Wang Y-L, Jiang Y-P, Li Z, Wang L, He K, Chen X, Ma X-C and Xue Q-K 2011 Molecular-beam epitaxy and robust superconductivity of stoichiometric fese crystalline films on bilayer graphene *Phys. Rev. B* **84** 020503
- [83] Liu H-J *et al* 2016 A metal–insulator transition of the buried mno_2 monolayer in complex oxide heterostructure *Adv. Mater.* **28** 9142–51
- [84] Cai L, McClellan C J, Koh A L, Li H, Yalon E, Pop E and Zheng X 2017 Rapid flame synthesis of atomically thin moo_3 down to monolayer thickness for effective hole doping of wse_2 *Nano Lett.* **17** 3854–61
- [85] Xu S *et al* 2015 van der Waals epitaxial growth of atomically thin Bi_2Se_3 and thickness-dependent topological phase transition *Nano Lett.* **15** 2645–51
- [86] Kong D, Dang W, Cha J J, Li H, Meister S, Peng H, Liu Z and Cui Y 2010 Few-layer nanoplates of Bi_2Se_3 and Bi_2Te_3 with highly tunable chemical potential *Nano Lett.* **10** 2245–50
- [87] Mashtalir O, Lukatskaya M R, Zhao M-Q, Barsoum M W and Gogotsi Y 2015 Amine-assisted delamination of Nb_2C mxene for Li-ion energy storage devices *Adv. Mater.* **27** 3501–6
- [88] Liu F, Zhou J, Wang S, Wang B, Shen C, Wang L, Hu Q, Huang Q and Zhou A 2017 Preparation of high-purity V_2C mxene and electrochemical properties as Li-ion batteries *J. Electrochem. Soc.* **164** A709–13
- [89] Lukatskaya M R, Mashtalir O, Ren C E, Dall' Agnese Y, Rozier P, Taberna P L, Naguib M, Simon P, Barsoum M W and Gogotsi Y 2013 Cation intercalation and high volumetric capacitance of two-dimensional titanium carbide *Science* **341** 1502–5
- [90] Melchior S A, Raju K, Ike I S, Erasmus R M, Kabongo G, Sigalas I, Iyuke S E and Ozoemena K I 2018 High-voltage symmetric supercapacitor based on 2d titanium carbide (mxene, ti_2ctx)/carbon nanosphere composites in a neutral aqueous electrolyte *J. Electrochem. Soc.* **165** A501–11
- [91] Liu G, Li Z, Hasan T, Chen X, Zheng W, Feng W, Jia D, Zhou Y and Hu P 2017 Vertically aligned two-dimensional sn_2 nanosheets with a strong photon capturing capability for efficient photoelectrochemical water splitting *J. Mater. Chem. A* **5** 1989–95
- [92] Li J, Guan X, Wang C, Cheng H-C, Ai R, Yao K, Chen P, Zhang Z, Duan X and Duan X 2017 Synthesis of 2d layered bi_3 nanoplates, bi_3/wse_2 van der Waals heterostructures and their electronic, optoelectronic properties *Small* **13** 1701034
- [93] Elias D C *et al* 2009 Control of graphene's properties by reversible hydrogenation: evidence for graphane *Science* **323** 610–3
- [94] Nair R R *et al* 2010 Fluorographene: a two-dimensional counterpart of teflon *Small* **6** 2877–84
- [95] Wang L, Kutana A, Zou X and Yakobson B I 2015 Electro-mechanical anisotropy of phosphorene *Nanoscale* **7** 9746–51
- [96] Wang X, Wang D S, Ruqian W and Freeman A J 1996 Validity of the force theorem for magnetocrystalline anisotropy *J. Magn. Magn. Mater.* **159** 337–41
- [97] Olsen T 2016 Designing in-plane heterostructures of quantum spin hall insulators from first principles: 1 T-MoS₂ with adsorbates *Phys. Rev. B* **94** 235106
- [98] MacDonald A H, Vosko S H and Coleridge P T 1979 Extensions of the tetrahedron method for evaluating spectral properties of solids *J. Phys. C: Solid State Phys.* **12** 2991–3002
- [99] Heyd J, Scuseria G E and Ernzerhof M 2003 Hybrid functionals based on a screened coulomb potential *J. Chem. Phys.* **118** 8207–15
- [100] Kořmider K and Fernández-Rossier J 2013 Electronic properties of the MoS₂-WS₂ heterojunction *Phys. Rev. B* **87** 075451
- [101] Kang J, Tongay S, Zhou J, Li J and Wu J 2013 Band offsets and heterostructures of two-dimensional semiconductors *Appl. Phys. Lett.* **102** 012111
- [102] Kuisma M, Ojanen J, Enkovaara J and Rantala T T 2010 Kohn–Sham potential with discontinuity for band gap materials *Phys. Rev. B* **82** 115106
- [103] Castelli I E, Olsen T, Datta S, Landis D D, Dahl S, Thygesen K S and Jacobsen K W 2012 Computational screening of perovskite metal oxides for optimal solar light capture *Energy Environ. Sci.* **5** 5814–9
- [104] Baerends E 2017 From the Kohn–Sham band gap to the fundamental gap in solids. an integer electron approach *Phys. Chem. Chem. Phys.* **19** 15639–56
- [105] Hüser F, Olsen T and Thygesen K S 2013 Quasiparticle GW calculations for solids, molecules and two-dimensional materials *Phys. Rev. B* **87** 235132
- [106] Rasmussen F A, Schmidt P S, Winther K T and Thygesen K S 2016 Efficient many-body calculations for two-dimensional materials using exact limits for the screened potential: band gaps of MoS₂, h-BN, and phosphorene *Phys. Rev. B* **94** 155406
- [107] Tiago M L, Ismail-Beigi S and Louie S G 2004 Effect of semicore orbitals on the electronic band gaps of Si, Ge and GaAs within the GW approximation *Phys. Rev. B* **69** 125212
- [108] Klimeš J, Kaltak M and Kresse G 2014 Predictive GW calculations using plane waves and pseudopotentials *Phys. Rev. B* **90** 075125
- [109] Sundaraman R and Arias T A 2013 Regularization of the coulomb singularity in exact exchange by wigner-seitz truncated interactions: towards chemical accuracy in nontrivial systems *Phys. Rev. B* **87** 165122
- [110] Ismail-Beigi S 2006 Truncation of periodic image interactions for confined systems *Phys. Rev. B* **73** 233103
- [111] Rozzi C A, Varsano D, Marini A, Gross E K U and Rubio A 2006 Exact coulomb cutoff technique for supercell calculations *Phys. Rev. B* **73** 205119
- [112] Lee J, Huang J, Sumpter B G and Yoon M 2017 Strain-engineered optoelectronic properties of 2d transition metal dichalcogenide lateral heterostructures *2D Mater.* **4** 021016
- [113] Ramasubramaniam A 2012 Large excitonic effects in monolayers of molybdenum and tungsten dichalcogenides *Phys. Rev. B* **86** 115409
- [114] Cheiwchanhannangij T and Lambrecht W R L 2012 Quasiparticle band structure calculation of monolayer, bilayer and bulk MoS₂ *Phys. Rev. B* **85** 205302
- [115] Komsa H-P and Krasheninnikov A V 2012 Effects of confinement and environment on the electronic structure and exciton binding energy of MoS₂ from first principles *Phys. Rev. B* **86** 241201
- [116] Molina-Sánchez A, Sangalli D, Hummer K, Marini A and Wirtz L 2013 Effect of spin–orbit interaction on the optical spectra of single-layer, double-layer and bulk MoS₂ *Phys. Rev. B* **88** 045412
- [117] Shi H, Pan H, Zhang Y-W and Yakobson B I 2013 Quasiparticle band structures and optical properties of strained monolayer MoS₂ and WS₂ *Phys. Rev. B* **87** 155304
- [118] Conley H J, Wang B, Ziegler J I, Haglund R F, Pantelides S T and Bolotin K I 2013 Bandgap engineering of strained monolayer and bilayer MoS₂ *Nano Lett.* **13** 3626–30

- [119] Hüser F, Olsen T and Thygesen K S 2013 How dielectric screening in two-dimensional crystals affects the convergence of excited-state calculations: monolayer MoS₂ *Phys. Rev. B* **88** 245309
- [120] Qiu D Y, Felipe H and Louie S G 2016 Screening and many-body effects in two-dimensional crystals: monolayer MoS₂ *Phys. Rev. B* **93** 235435
- [121] Shishkin M and Kresse G 2007 Self-consistent *g w* calculations for semiconductors and insulators *Phys. Rev. B* **75** 235102
- [122] Schmidt P S, Patrick C E and Thygesen K S 2017 Simple vertex correction improves *g w* band energies of bulk and two-dimensional crystals *Phys. Rev. Lett.* **99** 246403
- [123] Shishkin M, Marsman M and Kresse G 2007 Accurate quasiparticle spectra from self-consistent GW calculations with vertex corrections *Phys. Rev. Lett.* **99** 246403
- [124] Wang X, Jones A M, Seyler K L, Tran V, Jia Y, Zhao H, Wang H, Yang L, Xu X and Xia F 2015 Highly anisotropic and robust excitons in monolayer black phosphorus *Nat. Nanotechnol.* **10** 517
- [125] Klots A *et al* 2014 Probing excitonic states in suspended two-dimensional semiconductors by photocurrent spectroscopy *Sci. Rep.* **4** 6608
- [126] Ugeda M M *et al* 2014 Giant bandgap renormalization and excitonic effects in a monolayer transition metal dichalcogenide semiconductor *Nat. Mater.* **13** 1091
- [127] Hill H M, Rigosi A F, Rim K T, Flynn G W and Heinz T F 2016 Band alignment in MoS₂/WS₂ transition metal dichalcogenide heterostructures probed by scanning tunneling microscopy and spectroscopy *Nano Lett.* **16** 4831–7
- [128] Kormanyos A, Burkard G, Gmitra M, Fabian J, Zolyomi V, Drummond N D and Fal'ko V 2015 *k*·*p* theory for two-dimensional transition metal dichalcogenide semiconductors *2D Mater.* **2** 022001
- [129] Van De Walle C and Martin R 1989 Absolute deformation potentials—formulation and *ab initio* calculations for semiconductors *Phys. Rev. Lett.* **62** 2028–31
- [130] Resta R, Colombo L and Baroni S 1990 Absolute deformation potentials in semiconductors *Phys. Rev. B* **41** 12358–61
- [131] Wiktor J and Pasquarello A 2016 Absolute deformation potentials of two-dimensional materials *Phys. Rev. B* **94** 245411
- [132] Marques M, Ullrich C, Nogueira F, Rubio A and Gross E 2006 Time-dependent density functional theory (<https://doi.org/10.1007/B11767107>)
- [133] Hybertsen M S and Louie S G 1987 *Ab initio* static dielectric matrices from the density-functional approach. I. Formulation and application to semiconductors and insulators *Phys. Rev. B* **35** 5585–601
- [134] Yan J, Mortensen J J, Jacobsen K W and Thygesen K S 2011 Linear density response function in the projector augmented wave method: applications to solids, surfaces and interfaces *Phys. Rev. B* **83** 245122
- [135] Onida G, Reining L and Rubio A 2002 Electronic excitations: density-functional versus many-body Green's-function approaches *Rev. Mod. Phys.* **74** 601–59
- [136] Sander T, Maggio E and Kresse G 2015 Beyond the tamm-dancoff approximation for extended systems using exact diagonalization *Phys. Rev. B* **92** 045209
- [137] Latini S, Olsen T and Thygesen K S 2015 Excitons in van der Waals heterostructures: the important role of dielectric screening *Phys. Rev. B* **92** 245123
- [138] Da Jornada F H, Qiu D Y and Louie S G 2017 Nonuniform sampling schemes of the Brillouin zone for many-electron perturbation-theory calculations in reduced dimensionality *Phys. Rev. B* **95**
- [139] Drueppel M, Deilmann T, Krueger P and Rohlfing M 2017 Diversity of trion states and substrate effects in the optical properties of an MoS₂ monolayer *Nat. Commun.* **8** 2117
- [140] Mouri S, Zhang W, Kozawa D, Miyauchi Y, Eda G and Matsuda K 2017 Thermal dissociation of inter-layer excitons in MoS₂/MoSe₂ hetero-bilayers *Nanoscale* **9** 6674–9
- [141] Chen H, Wen X, Zhang J, Wu T, Gong Y, Zhang X, Yuan J, Yi C, Lou J, Ajayan P M, Zhuang W, Zhang G and Zheng J 2016 Ultrafast formation of interlayer hot excitons in atomically thin MoS₂/WS₂ heterostructures *Nat. Commun.* **7** 1–8
- [142] Fang H *et al* 2014 Strong interlayer coupling in van der Waals heterostructures built from single-layer chalcogenides *Proc. Natl Acad. Sci.* **111** 6198–202
- [143] Wilson N R, Nguyen P V, Seyler K, Rivera P, Marsden A J, Laker Z P, Constantinescu G C, Kandyba V, Barinov A, Hine N D, Xu X and Cobden D H 2017 Determination of band offsets, hybridization and exciton binding in 2D semiconductor heterostructures *Sci. Adv.* **3** e1601832
- [144] Ceballos F, Bellus M Z, Chiu H-Y and Zhao H 2015 Probing charge transfer excitons in a MoSe₂-WS₂ van der Waals heterostructure *Nanoscale* **7** 17523–8
- [145] Liu H, Neal A T, Zhu Z, Luo Z, Xu X, Tománek D and Ye P D 2014 Phosphorene: an unexplored 2D semiconductor with a high hole mobility *ACS Nano* **8** 4033–41
- [146] Yang J, Xu R, Pei J, Myint Y W, Wang F, Wang Z, Zhang S, Yu Z and Lu Y 2015 Optical tuning of exciton and trion emissions in monolayer phosphorene *Light Sci. Appl.* **4** 1–7
- [147] Takagi S, Toriumi A and Iwase M 1994 On the universality of inversion layer mobility in Si MOSFET's: part I-effects of substrate impurity concentration *IEEE Trans. Electron Dev.* **41** 2357–62
- [148] Cui X *et al* 2015 Multi-terminal transport measurements of MoS₂ using a van der Waals heterostructure device platform *Nat. Nanotechnol.* **10** 534–40
- [149] Jin Z, Li X, Mullen J T and Kim K W 2014 Intrinsic transport properties of electrons and holes in monolayer transition-metal dichalcogenides *Phys. Rev. B* **90** 045422
- [150] Gong C *et al* 2017 Discovery of intrinsic ferromagnetism in two-dimensional van der Waals crystals *Nature* **546** 265–9
- [151] Bonilla M *et al* 2018 Strong room-temperature ferromagnetism in VSe₂ monolayers on van der Waals substrates *Nat. Nanotechnol.* **13** 289–93
- [152] Huang C, Du Y, Wu H, Xiang H, Deng K and Kan E 2018 Prediction of intrinsic ferromagnetic ferroelectricity in a transition-metal halide monolayer *Phys. Rev. Lett.* **120** 147601
- [153] Mermin N D and Wagner H 1966 Absence of ferromagnetism or antiferromagnetism in one- or two-dimensional isotropic Heisenberg models *Phys. Rev. Lett.* **17** 1133–6
- [154] Lado J L and Fernández-Rossier J 2017 On the origin of magnetic anisotropy in two dimensional CrI₃ *2D Mater.* **4** 035002
- [155] Olsen T 2017 Assessing the performance of the random phase approximation for exchange and superexchange coupling constants in magnetic crystalline solids *Phys. Rev. B* **96** 125143
- [156] Low T, Chaves A, Caldwell J D, Kumar A, Fang N X, Avouris P, Heinz T F, Guinea F, Martin-Moreno L and Koppens F 2017 Polaritons in layered two-dimensional materials *Nat. Mater.* **16** 182
- [157] Gjerding M N, Petersen R, Pedersen T, Mortensen N A and Thygesen K S 2017 Layered van der Waals crystals with hyperbolic light dispersion *Nat. Commun.* **8** 320
- [158] Chen J *et al* 2012 Optical nano-imaging of gate-tunable graphene plasmons *Nature* **487** 77
- [159] Andersen K and Thygesen K S 2013 Plasmons in metallic monolayer and bilayer transition metal dichalcogenides *Phys. Rev. B* **88** 155128
- [160] Gjerding M N, Pandey M and Thygesen K S 2017 Band structure engineered layered metals for low-loss plasmonics *Nat. Commun.* **8** 15133
- [161] Cudazzo P, Tokatly I V and Rubio A 2011 Dielectric screening in two-dimensional insulators: implications for excitonic and impurity states in graphene *Phys. Rev. B* **84** 085406
- [162] Chernikov A, Berkelbach T C, Hill H M, Rigosi A, Li Y, Aslan O B, Reichman D R, Hybertsen M S and Heinz T F 2014 Exciton binding energy and nonhydrogenic rydberg series in monolayer WS₂ *Phys. Rev. Lett.* **113** 076802

- [163] Olsen T, Latini S, Rasmussen F and Thygesen K S 2016 Simple screened hydrogen model of excitons in two-dimensional materials *Phys. Rev. Lett.* **116** 056401
- [164] Jiang Z, Liu Z, Li Y and Duan W 2017 Scaling universality between band gap and exciton binding energy of two-dimensional Semiconductors *Phys. Rev. Lett.* **118** 266401
- [165] Choi J-H, Cui P, Lan H and Zhang Z 2015 Linear scaling of the exciton binding energy versus the band gap of two-dimensional materials *Phys. Rev. Lett.* **115** 066403
- [166] Seh Z W, Fredrickson K D, Anasori B, Kibsgaard J, Strickler A L, Lukatskaya M R, Gogotsi Y, Jaramillo T F and Vojvodic A 2016 Two-dimensional molybdenum carbide (mxene) as an efficient electrocatalyst for hydrogen evolution *ACS Energy Lett.* **1** 589–94
- [167] Xie J, Zhang H, Li S, Wang R, Sun X, Zhou M, Zhou J, Lou X W D and Xie Y 2013 Defect-rich MoS₂ ultrathin nanosheets with additional active edge sites for enhanced electrocatalytic hydrogen evolution *Adv. Mater.* **25** 5807–13
- [168] Ridolfi E, Le D, Rahman T, Mucciolo E and Lewenkopf C 2015 A tight-binding model for MoS₂ monolayers *J. Phys.: Condens. Matter* **27** 365501
- [169] Mostofi A A, Yates J R, Lee Y-S, Souza I, Vanderbilt D and Marzari N 2008 Wannier90: a tool for obtaining maximally-localised wannier functions *Comput. Phys. Commun.* **178** 685–99
- [170] Taherinejad M, Garrity K F and Vanderbilt D 2014 Wannier center sheets in topological insulators *Phys. Rev. B* **89** 115102
- [171] Bokdam M, Amlaki T, Brocks G and Kelly P J 2014 Band gaps in incommensurable graphene on hexagonal boron nitride *Phys. Rev. B* **89** 201404
- [172] Tritsaris G A, Shirodkar S N, Kaxiras E, Cazeaux P, Luskin M, Plecháč P and Cancès E 2016 Perturbation theory for weakly coupled two-dimensional layers *J. Mater. Res.* **31** 959–66
- [173] Andersen K, Latini S and Thygesen K S 2015 Dielectric genome of van der Waals heterostructures *Nano Lett.* **15** 4616–21


7.3 Paper III: Discovering two-dimensional topological insulators from high-throughput computations

Discovering two-dimensional topological insulators from high-throughput computations

Thomas Olsen,^{1,*} Erik Andersen,¹ Takuya Okugawa,¹ Daniele Torelli,¹ Thorsten Deilmann,¹ and Kristian S. Thygesen^{1,2}

¹Computational Atomic-Scale Materials Design (CAMD), Technical University of Denmark, DK-2800 Kgs. Lyngby, Denmark

²Center for Nanostructured Graphene (CNG), Department of Physics, Technical University of Denmark, DK-2800 Kgs. Lyngby, Denmark

 (Received 17 December 2018; published 28 February 2019)

We have performed a computational screening of topological two-dimensional (2D) materials from the Computational 2D Materials Database (C2DB) employing density functional theory. A full *ab initio* scheme for calculating hybrid Wannier functions directly from the Kohn-Sham orbitals has been implemented and the method was used to extract \mathbb{Z}_2 indices, Chern numbers, and mirror Chern numbers of 3331 2D systems including both experimentally known and hypothetical 2D materials. We have found a total of 48 quantum spin Hall insulators, seven quantum anomalous Hall insulators, and 21 crystalline topological insulators. Roughly 75% are predicted to be dynamically stable and one-third was known prior to the screening. The most interesting of the topological insulators are investigated in more detail. We show that the calculated topological indices of the quantum anomalous Hall insulators are highly sensitive to the approximation used for the exchange-correlation functional and reliable predictions of the topological properties of these materials thus require methods beyond density functional theory. We also performed *GW* calculations, which yield a gap of 0.65 eV for the quantum spin Hall insulator PdSe₂ in the MoS₂ crystal structure. This is significantly higher than any known 2D topological insulator and three times larger than the Kohn-Sham gap.

DOI: [10.1103/PhysRevMaterials.3.024005](https://doi.org/10.1103/PhysRevMaterials.3.024005)

I. INTRODUCTION

The concept of topological band theory was initially developed in order to explain the quantum Hall effect, which was observed experimentally in 1980 [1]. The measurements were soon interpreted as a topological effect arising from the phases of Bloch states winding around the boundary of the magnetic Brillouin zone [2] and is thus closely related to the k -space Berry phase [3]. In 1988, Haldane proposed a model system that exhibited the quantum Hall effect without an external magnetic field, but with intrinsically broken time-reversal symmetry [4]. Such materials are referred to as quantum anomalous Hall insulators (QAHI) and the first experimental demonstration of the effect was reported in 2013—25 years after it was proposed. In the meantime, Kane and Mele had showed that any time-reversal invariant two-dimensional (2D) insulator can be characterized by a \mathbb{Z}_2 topological index ν . Time-reversal invariant materials with nontrivial topology ($\nu = 1$) are known as quantum spin Hall insulators (QSHI) and the effect was observed immediately after a theoretical prediction of the effect in HgTe quantum wells [5,6]. Subsequently, the concepts have been generalized to bulk 3D systems [7,8] and several well-known materials have been shown to comprise examples of topological insulators [9]. Most notably, Sb₂Te₃, Bi₂Se₃, and Bi₂Te₃ [10,11], but also several 2D materials have been shown to exhibit a nontrivial band topology. In fact, graphene comprised the first theoretical prediction for a QSHI and while it is still believed that graphene has a nontrivial band topology it is practically impossible to verify experimentally due to the small band

gap. However, several other 2D materials have been shown to comprise examples of QSHIs. For example, the graphene-like materials silicene [12,13], germanene [14,15], and stanene [16] are all predicted to be QSHIs [17] and so are several of the transition metal dichalcogenides in the 1T' phase [18,19].

While the quantum spin Hall effect has been observed in a wide range of both 2D and 3D materials, the quantum anomalous Hall effect has proven more elusive and has so far only been observed in a few \mathbb{Z}_2 topological insulators, where time-reversal symmetry is broken by introducing magnetic impurities [20,21]. There have been a few proposals for pristine 2D materials that are predicted to be intrinsic QAHI by first principles calculations [22–26], but the effect has not yet been confirmed experimentally for any of the materials and the topological properties seem to be somewhat sensitive to the details of the calculations. Moreover, first principles calculations typically only pertain to the case of zero kelvin, but for 2D materials magnetic order is highly fragile to finite temperature effects and can only be stabilized in the presence of magnetic anisotropy [27,28]. Realistic theoretical predictions of 2D QAHI thus have to take into account that the magnetic order must persist at experimentally relevant temperatures—preferably room temperature.

Since the discovery of topological classifications of solids, the field has witnessed a tremendous development of the theoretical concepts, which have been extended to include topological semimetals [29], topological crystalline insulators [30,31], and higher order topological effects [32–35]. In addition to QAHI and QSHI we will focus on a particular class of topological insulators in the present work, namely, the topological crystalline insulators where the topology is protected by mirror symmetry in a plane parallel to the 2D material [36,37]. It is particularly easy to understand the

*tolsen@fysik.dtu.dk

topology in this case since the topological index is simply defined as the difference between the quantum anomalous Hall conductance of the two eigenspaces of the mirror operator. Moreover, the fact that the mirror plane coincides with the plane of the materials implies that any edge that conserves the mirror symmetry will host gapless states that are protected from elastic backscattering by the topology.

Although topological properties are in principle derivable from the ground state of bulk materials, the observable consequences are very limited in bulk. It is, for example, not possible to distinguish a nontrivial topological state from a trivial one by looking at the band structure alone. However, any interface between materials belonging to different topological classes is guaranteed to host gapless states that are localized at the boundary. Since the boundary states are protected by topology, they are extremely stable and have been proposed as candidates for dissipationless electronics circuits. Moreover, since the spin of boundary states are locked to the direction of propagation in QSHIs, such materials are promising for spintronics applications [38].

A crucial ingredient for operating topological insulators at room temperature is a sizable band gap. Typically, the band gap in topological insulators is determined by the strength of spin-orbit coupling and common values of the gap are on the order of 0.1–0.2 eV. With such small band gaps it becomes hard to maintain full control of the gapless boundary states and the applicability of the materials becomes questionable. It would thus be highly desirable to find new topological insulators with large band gaps. Large-scale screening studies based on first principles computations have previously been performed for 3D materials [39,40] and very recently for 2D materials based on experimentally known van der Waals bonded crystals [41]. The latter study predicted a 2D material in the Jacutingaite prototype to be a QSHI with a band gap of 0.5 eV [42]. Remarkably, the PBE gap of the material was only 0.15 eV, but a quasiparticle gap 0.5 eV was obtained with the G_0W_0 approximation. It is thus far from obvious that the simple Kohn-Sham gap provides a good estimate of the quasiparticle gap in 2D topological insulators.

Finally, we emphasize that it has not yet been possible to demonstrate the quantum anomalous Hall effect in a pristine 2D material. This is perhaps not so surprising since a magnetically ordered ground state is a minimal requirement for the effect and until very recently magnetic order had not been observed in 2D [43]. The discovery of the first pristine 2D QAHI, which exhibits magnetic order at reasonable temperatures, thus comprises a tremendous challenge and it is highly likely that theoretical predictions may aid this quest by significantly decreasing the number of relevant materials to investigate.

In the present work we have screened more than 3000 hypothetical 2D materials using first principles simulations and identified 61 2D topological insulators. We have focused on three topological classes. (1) QAHI, which require a magnetically ordered ground state and are characterized by the Chern number C that may take any integer value. (2) QSHIs, which require time-reversal symmetry and are classified by the binary \mathbb{Z}_2 index. (3) Mirror crystalline topological insulators, where the topology is protected by mirror symmetry and the ground state is classified according to the mirror Chern number C_M , which may take any integer value. In order to

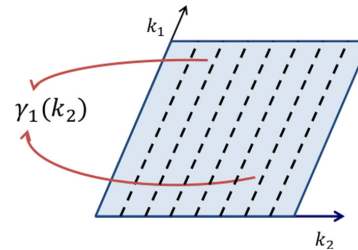


FIG. 1. Colored area indicate the unit cell in reciprocal space. For each value of k_2 , the Berry space is calculated by parallel transporting the Bloch states along k_1 (indicated by dashed lines).

extract the topological properties we have implemented a full calculation of k -space Berry phases that allow us to extract the topological indices in a semi-automated way and does not depend on a mapping to tight binding models through Wannier functions [44].

The paper is organized as follows. In Sec. II, we describe the Berry-phase implementation and exemplify how the topological indices are extracted for the three cases described above. In Sec. III, we present the computational details and provide a comprehensive list of all the 2D materials with nontrivial topology that have been found in the screening. We then analyze the topological properties of a few representative materials in more detail and investigate the effect of the approximations for exchange-correlation energy and G_0W_0 calculations. In Sec. IV we provide a discussion of the results.

II. BERRY PHASES AND HYBRID WANNIER FUNCTIONS

In this section we will briefly introduce the notion of parallel transport and show how it can be applied to obtain the Berry phase matrix of a closed path in k space. We will closely follow the discussions in Refs. [44–46]. We consider a minimal unit cell in reciprocal space spanned by the reciprocal lattice vectors \mathbf{b}_1 and \mathbf{b}_2 . A generic point in the reciprocal unit cell can then be written as

$$\mathbf{k} = k_1 \mathbf{b}_1 + k_2 \mathbf{b}_2, \quad (1)$$

where $0 \leq k_i < 1$ are the reciprocal fractional coordinates. We wish to calculate the Berry phase obtained by transporting the occupied Bloch states along k_1 through the reciprocal unit cell at a fixed value of k_2 (see Fig. 1). In a numerical treatment of the Bloch Hamiltonian $H(\mathbf{k})$, one obtains a set of occupied eigenstates $|u_{n\mathbf{k}}\rangle$ at different \mathbf{k} points and each set of eigenstates come with an arbitrary set of phases. In fact, any unitary rotation in the space of occupied states leaves the ground state invariant and in order to evaluate the phases picked up along a closed path in k space one needs to construct eigenstates with phases that are smooth along the path. This can be accomplished by the so-called parallel transport gauge. For a single occupied state we fix the phase along the path by requiring that $\langle u_{\mathbf{k}} | \partial_{k_1} u_{\mathbf{k}} \rangle = 0$, which enforces that the change in the state along the path is orthogonal to the state itself. When the Bloch states are calculated at a string of N \mathbf{k} points with fixed k_2 and $k_1 = 0, 1/N, 2/N, \dots$, the parallel

transport condition can be implemented by requiring that $\langle u_{\mathbf{k}} | u_{\mathbf{k}+\mathbf{b}_1/N} \rangle$ is real at any point along the path. Thus for an initial state at \mathbf{k} on the path we can fix all phases on the path sequentially by the parallel transport condition, which will result in a smooth phase along the path. The phase at $k_1 = 1$ can then be obtained by imposing the periodic gauge such that $|u_{\mathbf{k}+\mathbf{b}_1}\rangle = e^{-i\mathbf{r}\cdot\mathbf{b}_1} |u_{\mathbf{k}}\rangle$ and the Berry phase is obtained as the phase difference between $k_1 = 0$ and $k_1 = 1$.

In the case of multiple occupied bands, the condition is generalized by requiring that the matrix $M_{mn\mathbf{k}} = \langle u_{n\mathbf{k}} | u_{m\mathbf{k}+\mathbf{b}_1/N} \rangle$ is Hermitian. This uniquely fixes the unitary rotation among the occupied states at all points along the path in terms of an initial set of occupied states at particular point \mathbf{k} on the path. This is due to the fact that a single value decomposition yields $M = V\Sigma W^\dagger = V\Sigma V^\dagger V W^\dagger$, where V and W are unitary matrices and Σ is diagonal and real. We can thus take $|u_{n\mathbf{k}+\mathbf{b}_1/N}\rangle \rightarrow W V^\dagger |u_{n\mathbf{k}+\mathbf{b}_1/N}\rangle$, which renders M Hermitian and completely fixes the gauge at $\mathbf{k} + \mathbf{b}_1/N$. This procedure is continued along the path until the states at $\mathbf{k} + \mathbf{b}_1$ are obtained using the periodic gauge where $|u_{n\mathbf{k}+\mathbf{b}_1}\rangle = e^{-i\mathbf{r}\cdot\mathbf{b}_1} |u_{n\mathbf{k}}\rangle$. Finally, the eigenvalues of the unitary matrix relating the states at \mathbf{k} and $\mathbf{k} + \mathbf{b}_1$ are the Berry phases acquired by the individual bands.

The method can also be used to obtain the individual states $|\tilde{u}_{n\mathbf{k}}\rangle$ that are parallel transported without mixing and thus acquire the distinct eigenvalues of the Berry phase matrix [45]. Since these are smooth, one may construct hybrid Wannier functions (HWFs) localized along the direction parallel to \mathbf{b}_1 as

$$|W_{njk_2}\rangle = \int_0^1 dk_1 e^{-i\mathbf{k}\cdot(\hat{\mathbf{r}}+\hat{\mathbf{R}}_j)} |\tilde{u}_{n\mathbf{k}}\rangle. \quad (2)$$

Writing $\mathbf{r} = x_1\mathbf{a}_1 + x_2\mathbf{a}_2$ with $\mathbf{a}_i \cdot \mathbf{b}_j = 2\pi\delta_{ij}$, one can show that [47]

$$x_{1,n}(k_2) \equiv \langle W_{n0k_2} | \hat{x}_1 | W_{n0k_2} \rangle = \gamma_{1,n}(k_2)/2\pi, \quad (3)$$

with

$$\gamma_{1,n}(k_2) = i \int_0^1 dk_1 \langle \tilde{u}_{n\mathbf{k}} | \partial_{k_1} \tilde{u}_{n\mathbf{k}} \rangle. \quad (4)$$

Except for a factor of 2π , the Berry phases obtained from the parallel transport gauge are thus the charge centers of the HWFs. This construction allows one to calculate various properties associated with the individual phases. For example, the spin expectation value

$$S_n^{(z)}(k_2) \equiv \langle W_{n0k_2} | \hat{S}^{(z)} | W_{n0k_2} \rangle, \quad (5)$$

which will serve as a useful tool for analyzing the topological properties of 2D materials below.

The Berry phases will be smooth functions of k_2 , which implies that one can track the evolution of the phases while k_2 is cycled through the reciprocal space unit cell. The dispersion of the spectrum of Berry phases gives rise to topological classifications as explained below. We will provide examples of *ab initio* calculations of the Berry phase spectrum for the three topological classes considered in the present work, but postpone a compilation of the computational details until Sec. III.

A. Quantum anomalous Hall insulators

The Hall conductance σ_{xy} relates an electric current in the x direction to a uniform field in the y direction by $J_x = \sigma_{xy} E_y$. A finite Hall conductance requires broken time-reversal symmetry and it follows from the Kubo formula that it can be written in terms of the k -space Berry curvature $\Omega_c(\mathbf{k})$ as [48]

$$\sigma_{xy} = -\frac{e^2}{h} \int_{BZ} \frac{d^2k}{2\pi} \Omega(\mathbf{k}), \quad (6)$$

with

$$\Omega(\mathbf{k}) = i \sum_{ijn} f_{n\mathbf{k}} \varepsilon_{ij} \partial_{k_i} \langle u_{n\mathbf{k}} | \partial_{k_j} u_{n\mathbf{k}} \rangle. \quad (7)$$

Here i, j runs over x and y , ε is the two-dimensional Levi-Civita symbol, and $f_{n\mathbf{k}}$ are occupation factors.

For insulators, the integral can be shown to yield an integer known as the Chern number C and the Hall conductance becomes

$$\sigma_{xy} = -C \frac{e^2}{h}, \quad C \in \mathbb{Z}. \quad (8)$$

In 2D metals, a gap can be opened due to the Landau levels emerging when an external magnetic field is introduced and the value of the Chern number can be controlled by the magnitude of magnetic field. That is the quantum Hall effect. Moreover, as shown by Haldane [4], materials with spontaneously broken time-reversal symmetry can exhibit intrinsic quantum Hall effect without an external magnetic field. Such materials are known as quantum anomalous Hall insulators (QAHI) (or Chern insulators) and have a finite Chern number and a nontrivial band topology.

We now briefly discuss how the k -space Berry phase calculations outlined above can be related to the Chern number in QAHI. A constant electric field in the y direction of magnitude E_0 can be included in the Bloch Hamiltonian by the substitution $k_y \rightarrow k_y - eE_0t/\hbar$. Clearly the physical properties of the Bloch Hamiltonian are restored after a period $T = 2\pi\hbar/eE_0$. If E_0 is sufficiently small, the system will evolve adiabatically and the charge transported in the x direction in the time interval is $Q = \int_0^T J_x dt = T \sigma_{xy} E_0 = h\sigma_{xy}/e$. Expressing the Hall conductance as $\sigma_{xy} = -Ce^2/h$, we see that the transferred charge is $Q = -eC$. One can thus obtain the Chern number as the number of Wannier charge centers that are transported by a unit cell in the x direction, while k_y is cycled through the reciprocal space unit cell in the backward direction. This argument comprises a modified version [7] of the explanation originally provided by Laughlin to account for the quantum Hall effect [49]. This also explains the appearance of gapless edge states in QAHI. For a bulk system an adiabatic cycling of k_2 through a reciprocal unit vector will return the system to itself by transferring C charges by one lattice vector. However, in the presence of an edge charges will pile up at the edge and the argument breaks down unless there is a different mechanism that can remove the charges from the edge. One may thus conclude that any edge has to host chiral gapless states that connect the valence band with the conduction band, such that C units of charge are transferred out of the valence bands at the edge while k_2 is cycled by a unit.

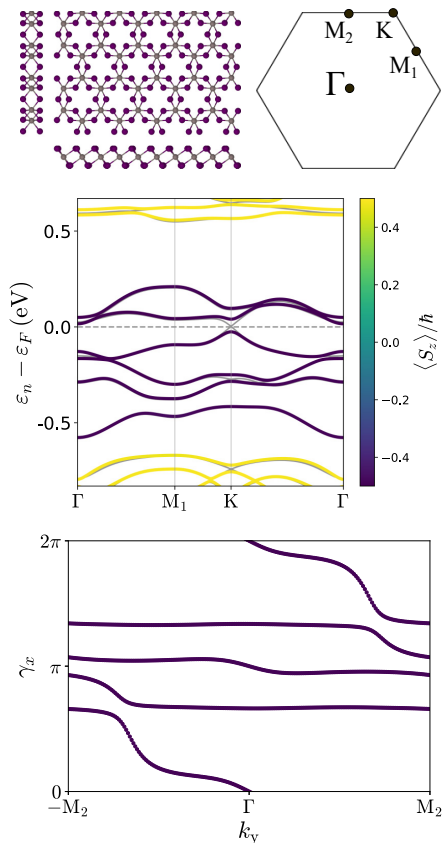


FIG. 2. Top: structure and Brillouin zone of FeBr_3 in the BiI_3 crystal structure. Middle: band structure of FeBr_3 with colors denoting the expectation value of S_z . The band PBE gap is 42 meV. Bottom: Berry phases of the four highest occupied states of FeBr_3 calculated as a function of k in the direction of M_2 .

In Fig. 2 we show the Berry phases of FeBr_3 in the BiI_3 crystal structure. Due to Eq. (3), the vertical axis in the plot can be regarded as the unit cell in the x direction and it is clear that at any horizontal line there will be a total of one state crossing in the downward direction. We can thus calculate the Chern number as the total number of chiral crossings—that is, the number of crossing points with negative slope minus the number of crossing points with positive slope at any horizontal line and we conclude that $C = 1$. We have confirmed this result by a direct integration of the Berry curvature Ω_z over the Brillouin zone.

B. Quantum spin Hall insulators

Materials with time-reversal symmetry must have a vanishing Hall conductance and thus cannot have a nonzero Chern number. From the Berry phase perspective this is due to the fact that any phase at \mathbf{k} will be accompanied by an equal

phase at $-\mathbf{k}$, which excludes the possibility of having a finite number of chiral crossings at a horizontal line. Nevertheless, as shown by Kane and Mele [50,51] all 2D time-reversal invariant insulators belong to one of two topological classes and can thus be characterized by a \mathbb{Z}_2 topological index. The simplest way to understand the \mathbb{Z}_2 index is by considering a system where S_z is a good quantum number. Then one can calculate the Chern numbers of the two spin states and obtain $C_\uparrow = -C_\downarrow$, since $C = C_\uparrow + C_\downarrow = 0$. Due to time-reversal symmetry all Berry phases have Kramers degenerate partners at time-reversal invariant points such as M and Γ . If one introduces spin-mixing (but time-reversal conserving) perturbations in the Hamiltonian, the two Chern numbers are no longer well defined but two distinct ways of connecting phases between time-reversal invariant points remain, which gives rise to a \mathbb{Z}_2 topological classification. In particular, if C_\uparrow is even in the case where S_z is a good quantum number, there will be an even number of Kramers pairs at Γ and M that may hybridize and open a gap in the Berry phase spectrum, once spin-mixing terms are introduced. In contrast, if C_\uparrow is odd, there will be an odd number of Kramers pairs at M and Γ and the Berry phase spectrum must remain gapless when spin-mixing terms are included. In general the \mathbb{Z}_2 index distinguishes whether there is an odd or even number of Berry phases crossing any horizontal line in half the Brillouin zone.

In Fig. 3 we show the band structure and Berry phase spectrum for stanene (Sn), which comprises an example of a quantum spin Hall insulator. Due to inversion symmetry in stanene, all bands are doubly degenerate and cannot be colored according to spin. However, the degeneracy of the Berry phases are split due to spin-orbit coupling, which will allow the spectrum to exhibit a single crossing in half the Brillouin zone. Qualitatively, the spin-down electrons are transported upwards, while the spin-up electrons are transported downwards indicating that one would be able to assign spin Chern numbers of $C_\uparrow = -C_\downarrow = 1$ if the Hamiltonian of the system could be continuously connected to a Hamiltonian that commutes with S_z without closing the gap.

C. Mirror crystalline topological insulators

As shown by Fu [30], crystal symmetries alone may give rise to a topologically nontrivial band structure. However, the consequences (gapless boundary states) are only observable at edges or surfaces that conserve the crystal symmetry. In this respect, mirror symmetry comprises a particularly simple type of crystal symmetry that gives rise to an integer topological classification. Whenever a material has mirror symmetry all the occupied states may be labeled according to their mirror eigenvalues $\pm i$ and one can define Chern numbers C_\pm for these subsets of bands. The total Chern number is then $C = C_+ + C_-$, but we might as well consider the $\mathbb{Z} \times \mathbb{Z}$ classification based on C_+ and C_- . In the case where the total Chern number vanishes the topology can be specified by the mirror Chern number $C_M = (C_+ - C_-)/2$, which is readily verified to be an integer.

For 2D materials, mirror symmetry in the plane of the material plays a special role, since any clean edge of the material will conserve the symmetry. A 2D material with nonvanishing

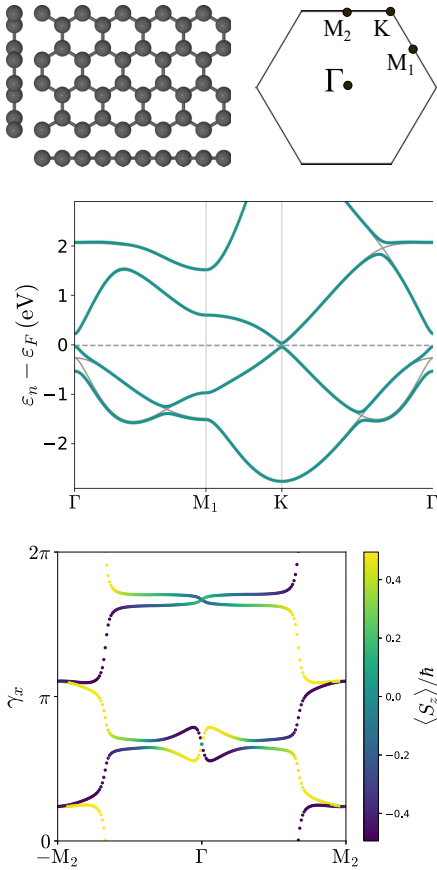


FIG. 3. Top: structure and Brillouin zone of stanene. Middle: band structure of stanene. Bottom: Berry phases of the four highest occupied states of stanene calculated as a function of k in the direction of M_2 with colors denoting the expectation value of S_z .

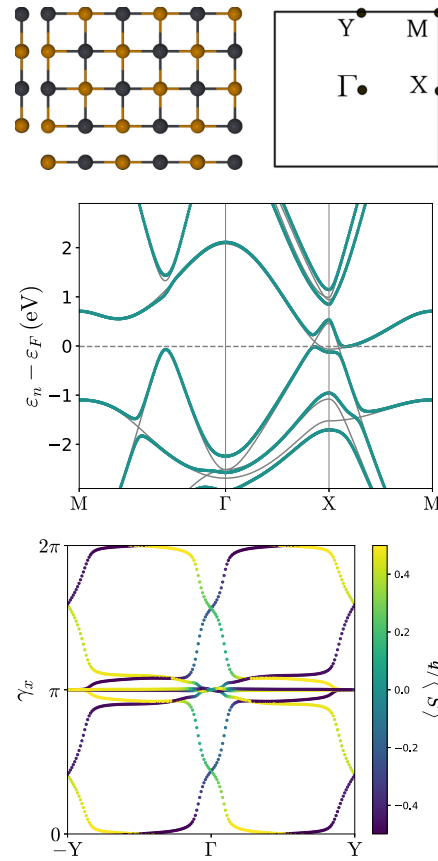


FIG. 4. Top: structure and Brillouin zone of SnTe in the PbSe crystal structure. Middle: band structure of SnTe. Bottom: Berry phases of the eight highest occupied states of FeBr₃ calculated as a function of k in the direction of Y with colors denoting the expectation value of S_z .

mirror Chern number is thus guaranteed to host gapless edge states and gapless boundary states if the material is interfaced with a topologically trivial material that exhibits mirror symmetry in the plane. Strictly speaking, the interface or edge itself may break the symmetry by reconstruction or adsorption of atoms or molecules and as such the gapless edge states are more fragile than in the case of QSHI where the topology is defined by time-reversal symmetry. If $C = 0$ an edge will host C_M edge states of positive chirality and C_M edge states of negative chirality. In Fig. 4 we show the Berry phase spectrum of SnTe, which is an example of a mirror crystalline topological insulator with $C_M = 2$ [36]. We note that the spinorial part of the mirror operator in the z plane is represented as $i\sigma_z$ and the mirror eigenvalues thus closely follow the spin of the hybrid Wannier functions. This is evident in Fig. 4, where the spin up states are largely transported downward ($C_+ = 2$) and the spin down states ($C_- = -2$) are largely transported

upward. This is of course only a qualitative argument, since the mirror operator also affects the orbital part, but the spin structure of the hybrid Wannier functions does allow one to obtain an intuitive picture of the (mirror-resolved) charge transport.

It is interesting to note that, in the presence of time-reversal symmetry, the \mathbb{Z}_2 index can be obtained as $C_M \bmod 2$. This is due to the fact that time-reversal symmetry enforces mirror symmetry on the Berry phase spectrum around the vertical axis at the Γ point. In particular, we can represent the time-reversal symmetry operator as $T = \sigma_y K$, where K denotes complex conjugation and the mirror symmetry operator by $M_z = i\sigma_z$. Due to the fact that σ_y and σ_z anticommute, it follows that if $|u_+\rangle$ is an eigenstate of M_z with eigenvalue $+i$ then $T|u_+\rangle$ will be an eigenstate of M_z with eigenvalue $-i$. The Berry phase spectrum of the negative eigenvalue sector can thus be obtained from that of the positive mirror

eigenvalues by reflection through the vertical line at Γ . This results in an odd number of crossings in half the Brillouin zone if C_M is odd and an even number of crossings if C_M is even. Materials with odd mirror Chern number and time-reversal symmetry thus have a dual topological character such that the edge states will remain protected if either mirror symmetry or time-reversal symmetry is broken. This can be regarded as a 2D analog of the dual topological character in Bi_2Se_3 [52,53]. In that case the strong topological index can be calculated from the Chern-Simons axion coupling θ , which is restricted to the values of zero and π in the presence of either mirror symmetry or time-reversal symmetry.

III. RESULTS

A. Computational details

All the calculations presented in this work were based on the Computational 2D Materials Database (C2DB), which currently contains DFT calculations for 3331 2D materials [54]. The calculations were performed with the electronic structure software package GPAW [55], which is based on the projector augmented wave method [56] combined with the atomic simulation environment (ASE) [57]. All materials have been fully relaxed with the PBE functional [58] and treated according to a strict work flow and a wide range of properties are calculated for materials that are both dynamically and thermodynamically stable. We refer to Ref. [54] for details on the calculations. The database can be browsed online or the full database can be downloaded from the repository.

As a first screening for 2D materials with nontrivial topology, we have sorted the C2DB for insulators with direct PBE band gaps below 0.7 eV. This primary criterion is based on the fact that the topological gaps are driven by spin-orbit coupling and we do not expect spin-orbit coupling to open band gaps by more than 0.7 eV. For all these materials, we carried out the parallel transport described in Sec. II and identified topological insulators as the materials with a gapless Berry phase spectrum. The procedure is highly convenient for automated screening, because no reference to the type of topological insulator is needed for the calculations and one can simply sort out whether a given material is a QAH, QSHI, or a crystalline topological insulator (protected by mirror symmetry) afterwards.

The only nonstandard ingredient in the procedure is the calculation of the matrix elements

$$M_{mn}(\mathbf{k}, \mathbf{k} + \delta\mathbf{k}) = \langle u_m(\mathbf{k}) | u_n(\mathbf{k} + \delta\mathbf{k}) \rangle = \langle \psi_m(\mathbf{k}) | e^{-i\delta\mathbf{k}\cdot\hat{\mathbf{r}}} | \psi_n(\mathbf{k} + \delta\mathbf{k}) \rangle, \quad (9)$$

which is needed for the parallel transport algorithm. Within the PAW formalism the all-electron wave functions are written as

$$|\psi_n\rangle = |\tilde{\psi}_n\rangle + \sum_{ai} [\tilde{p}_i^a |\tilde{\psi}_n\rangle][|\phi_i^a\rangle - |\tilde{\phi}_i^a\rangle], \quad (10)$$

where $|\tilde{\psi}_n\rangle$ are soft pseudowave functions, $|\phi_i^a\rangle$ are atomic orbitals of atom a , and $|\tilde{p}_i^a\rangle$ are projector functions satisfying $\langle \tilde{p}_i^a | \tilde{\phi}_j^a \rangle = \delta_{ij}$. Denoting the position of atom a by \mathbf{r}_a the

TABLE I. Overview of known topological materials found by computational screening. The topology is specified by either the Chern number C , the \mathbb{Z}_2 index ν , or the mirror Chern number C_M . We also state the calculated Kohn-Sham gap (KS gap).

| Material | Prototype | Topology | KS gap (meV) |
|----------------------|----------------|--------------------|--------------|
| C_2 [51] | C_2 | $\nu = 1, C_M = 1$ | 0.3 |
| Si_2 [59] | C_2 | $\nu = 1$ | 1.6 |
| Ge_2 [59] | C_2 | $\nu = 1$ | 25 |
| Sn_2 [59] | C_2 | $\nu = 1$ | 65 |
| SnF [60] | CH | $\nu = 1$ | 316 |
| HgSe [61] | GeSe | $\nu = 1$ | 90 |
| HgTe [61] | GeSe | $\nu = 1$ | 156 |
| MoS_2 [18] | WTe_2 | $\nu = 1$ | 51 |
| MoSe_2 [18] | WTe_2 | $\nu = 1$ | 41 |
| WSe_2 [18] | WTe_2 | $\nu = 1$ | 32 |
| OsCl_3 [24] | BiI_3 | $C = 1$ | 64 |
| GeTe_2 [62] | MnS_2 | $\nu = 1$ | 32 |
| SnS [36] | PbS | $C_M = 2$ | 67 |
| SnSe [36] | PbS | $C_M = 2$ | 84 |
| SnTe [36] | PbS | $C_M = 2$ | 28 |
| PbS [36] | PbS | $C_M = 2$ | 422 |
| PbSe [36] | PbS | $C_M = 2$ | 478 |
| PbTe [36] | PbS | $C_M = 2$ | 271 |

matrix elements can thus be written as

$$M_{mn}(\mathbf{k}, \mathbf{k} + \delta\mathbf{k}) = \langle \tilde{\psi}_m(\mathbf{k}) | e^{-i\delta\mathbf{k}\cdot\hat{\mathbf{r}}} | \tilde{\psi}_n(\mathbf{k} + \delta\mathbf{k}) \rangle + \sum_{aij} e^{-i\delta\mathbf{k}\cdot\mathbf{r}_a} \langle \tilde{\psi}_m(\mathbf{k}) | \tilde{p}_i^a \rangle \times [\langle \phi_i^a | \phi_j^a \rangle - \langle \tilde{\phi}_i^a | \tilde{\phi}_j^a \rangle] \langle \tilde{p}_j^a | \tilde{\psi}_n(\mathbf{k} + \delta\mathbf{k}) \rangle, \quad (11)$$

where we assumed that $\langle \phi_i^a | e^{-i\delta\mathbf{k}\cdot\hat{\mathbf{r}}} | \phi_j^a \rangle = e^{-i\delta\mathbf{k}\cdot\mathbf{r}_a} \langle \phi_i^a | \phi_j^a \rangle$, since the partial waves $|\phi_i^a\rangle$ are localized at the atom a and $e^{-i\delta\mathbf{k}\cdot\mathbf{r}}$ is a slowly varying function when $\delta\mathbf{k}$ is small. All quantities entering in Eq. (11) are calculated during standard DFT calculations with GPAW and are thus readily available for Berry phase calculations.

B. Overview of topological insulators in C2DB

In Tables I–IV we provide an overview of all the topological insulators found in the screening. We emphasize again that all these were simply identified by looking for materials with a gapless Berry phase spectrum. The topological indices ν , C , and C_M , relevant for QSHIs, QAHs and MCTIs respectively, were then assigned to the different materials afterwards.

Table I contains known topological 2D materials. We find most of the materials that have previously been predicted to exhibit a nontrivial band topology. For example, graphene [51] and its derivatives silicene, germanene, and stanene [59], as well as the transition metal dichalcogenides MoS_2 , MoSe_2 , and WSe_2 in the $1T'$ phase (WTe_2 crystal structure) [18]. However, some well-known 2D topological insulators are missing from this table, for example, WTe_2 and WS_2 in the $1T'$ phase. These materials are present in C2DB, but are semimetals in the PBE approximation [18]

TABLE II. Overview of novel QSHIs without mirror symmetry. All the materials have a \mathbb{Z}_2 index of $\nu = 1$. We also state the calculated Kohn-Sham gap (KS gap), the heat of formation (HOF), and the energy above the convex hull (EACH). The dynamically stable materials are shown in boldface.

| Material | Prototype | Topology | KS gap (meV) | HOF (eV) | EACH (eV) |
|------------------|------------------|-----------|--------------|----------|-----------|
| AuCl | FeSe | $\nu = 1$ | 20 | 0.10 | 0.30 |
| CrAsBi | BiTeI | $\nu = 1$ | 35 | 0.31 | 0.46 |
| IrSe | GaSe | $\nu = 1$ | 134 | 0.18 | 0.45 |
| TiTe | GaSe | $\nu = 1$ | 109 | -0.08 | 0.63 |
| ZrTe | GaSe | $\nu = 1$ | 207 | -0.28 | 0.65 |
| AuI ₃ | BiI ₃ | $\nu = 1$ | 109 | 0.10 | 0.10 |
| TiIN | FeOCl | $\nu = 1$ | 62 | -1.18 | -0.26 |
| TiClSe | FeOCl | $\nu = 1$ | 27 | -0.36 | 0.32 |
| TiS | CH | $\nu = 1$ | 54 | -1.13 | 0.31 |
| TiCl | CH | $\nu = 1$ | 13 | -0.64 | 0.45 |
| ZrS | CH | $\nu = 1$ | 132 | -1.16 | 0.26 |
| ZrSe | CH | $\nu = 1$ | 20 | -0.91 | 0.25 |
| ZrCl | CH | $\nu = 1$ | 37 | -0.59 | 0.73 |
| ZrBr | CH | $\nu = 1$ | 45 | -0.34 | 0.68 |
| SbCl | CH | $\nu = 1$ | 434 | -0.46 | 0.13 |
| SbBr | CH | $\nu = 1$ | 442 | -0.31 | 0.10 |
| SbI | CH | $\nu = 1$ | 584 | -0.12 | 0.13 |
| HfS | CH | $\nu = 1$ | 158 | -0.89 | 0.43 |
| HfSe | CH | $\nu = 1$ | 42 | -0.64 | 0.54 |
| ReS | CH | $\nu = 1$ | 309 | 0.10 | 0.54 |
| HgCl | CH | $\nu = 1$ | 129 | -0.37 | 0.23 |
| HgBr | CH | $\nu = 1$ | 188 | -0.25 | 0.22 |
| PbF | CH | $\nu = 1$ | 116 | -1.43 | 0.45 |

and are therefore excluded from the present compilation. In addition CoBr₂ in the CdI₂ crystal structure has previously been predicted to be a QAHI based on PBEsol [26], which we have confirmed but the material is metallic within PBE and is therefore not included here. On the other hand, we find both HgSe and HgTe to be QSHIs although these materials have previously been reported to be trivial insulators based on calculations with a modified Becke-Johnson LDA functional [61].

Tables II–IV contain all the topological insulators that to our knowledge have not been reported prior to this work. The dynamically stable compounds (shown in boldface) are likely to be the only ones that are experimentally relevant, but we include all materials that we have found for completeness.

We find 27 time-reversal invariant topological insulators that are dynamically stable and have not been reported previously (Tables II and III). We start by noting that the list is dominated by 15 materials in the CH crystal structure (graphane),

TABLE III. Overview of novel crystalline topological insulators protected by mirror symmetry. The topology is specified the mirror Chern number C_M . All the materials are invariant under time-reversal symmetry and the associated \mathbb{Z}_2 index thus becomes $\nu = 1$ if C_M is odd and $\nu = 0$ if C_M is even. We also state the calculated Kohn-Sham gap (KS gap), the heat of formation (HOF), and the energy above the convex hull (EACH). The dynamically stable materials are shown in boldface.

| Material | Prototype | Topology | KS gap (meV) | HOF (eV) | EACH (eV) |
|-------------------------|-------------------|--------------------|--------------|----------|-----------|
| HgO | BN | $\nu = 1, C_M = 1$ | 302 | -0.15 | 0.21 |
| PdSe₂ | MoS ₂ | $\nu = 1, C_M = 1$ | 229 | -0.02 | 0.27 |
| AuTe | GaS | $\nu = 1, C_M = 1$ | 37 | 0.03 | 0.11 |
| WO | GaS | $\nu = 1, C_M = 1$ | 53 | -1.01 | 0.49 |
| RhO | GaS | $\nu = 1, C_M = 3$ | 67 | -0.38 | 0.25 |
| IrO | GaS | $\nu = 1, C_M = 3$ | 122 | -0.16 | 0.51 |
| ReI ₃ | AgBr ₃ | $\nu = 1, C_M = 1$ | 141 | 0.37 | 0.43 |
| ReCl ₃ | TiCl ₃ | $\nu = 1, C_M = 1$ | 220 | -0.18 | 0.52 |
| WI₃ | TiCl ₃ | $\nu = 1, C_M = 1$ | 222 | 0.19 | 0.19 |
| GeTe₂ | MnS ₂ | $\nu = 1, C_M = 1$ | 32 | 0.27 | 0.33 |
| RuTe₂ | MnS ₂ | $\nu = 1, C_M = 1$ | 157 | 0.34 | 0.68 |
| OsS₂ | MnS ₂ | $\nu = 0, C_M = 2$ | 111 | 0.25 | 0.63 |
| OsSe ₂ | MnS ₂ | $\nu = 0, C_M = 2$ | 144 | 0.51 | 0.68 |
| OsTe ₂ | MnS ₂ | $\nu = 0, C_M = 2$ | 117 | 0.70 | 0.77 |

TABLE IV. Overview of novel QAHI found by computational screening. The topology is specified by either the Chern number C . We also state the calculated Kohn-Sham gap (KS gap), the heat of formation (HOF), and the energy above the convex hull (EACH). The dynamically stable materials are shown in boldface.

| Material | Prototype | Topology | KS gap (meV) | HOF (eV) | EACH (eV) |
|-------------------------|-------------------|----------|--------------|----------|-----------|
| PdF₂ | GeS ₂ | $C = -2$ | 27 | -0.83 | 0.38 |
| FeCl₃ | BiI ₃ | $C = 1$ | 13 | -0.66 | -0.08 |
| FeBr₃ | BiI ₃ | $C = 1$ | 42 | -0.38 | -0.04 |
| PdI₃ | BiI ₃ | $C = -1$ | 36 | -0.13 | 0.06 |
| CoBr₃ | AgBr ₃ | $C = -2$ | 27 | -0.21 | -0.16 |
| MoS₂ | MnS ₂ | $C = 2$ | 133 | 0.10 | 1.05 |

the antimony halides exhibiting band gaps exceeding 0.4 eV. Among the remaining materials, PdSe₂ in the MoS₂ crystal structure is the one with the largest band gap of 0.23 eV. However, it is situated 0.25 eV/atom above the convex hull with two other materials of the same stoichiometry being more stable. Nevertheless, the difference in stability is similar to the difference between MoS₂ in the 2H phase and the 1T' phase, which are both accessible by modern synthesis techniques. To test the reliability of the topological gap obtained with PBE, we have calculated LDA and *GW* band structures fully including spin-orbit coupling in the self-energy [63]. The result is shown in Fig. 5. The LDA gap is 0.225 eV, which is very similar to the PBE value. However, the *GW* gap is 0.65 eV, which nearly comprises a threefold increase of the Kohn-Sham gap. In fact, to our knowledge this is one of the largest gaps reported for a two-dimensional topological insulator. A similar dramatic increase was recently reported for a Jacutingaite crystal structure where PBE yielded a gap of 0.15 eV and *GW* predicted a gap of 0.5 eV [42]. Such a large increase in band gap has not been reported for three-dimensional topological insulators and could be related to the reduced screening in 2D. In principle, the predicted topology of the materials may depend on the approximation used to obtain the eigenstates. For example, in Ref. [64] it was shown that DFT can lead to a false-positive conclusion for the nontrivial topology of certain 3D materials and *GW* calculations may reverse the band inversion leading to the predicted nontrivial topology in DFT. However, we will not perform full *GW* calculations (with spin-orbit coupling) for all the materials in the present work, but note that false positives could be a caveat for the present method. We discuss this issue further below in the context of QAHI.

In addition to the six well-known mirror crystalline topological insulators displayed in Table I, we also find three osmium dichalcogenides in the MnS₂ crystal structure with a mirror Chern number of $C_M = 2$, which are displayed in Table III. Only one of these—OsO₂—is stable though. As noted previously, any \mathbb{Z}_2 odd topological insulator with mirror symmetry must have an odd Chern number. In those cases the \mathbb{Z}_2 index does not exhaust the topological properties and we may distinguish the topological classes corresponding to $C_M = 1$ and $C_M = 3$, for example, as in the case of RhO and AuTe in the GaS crystal structure. Again the physical consequences only emerge when considering an edge where the difference in Chern numbers would yield the number of protected gapless edge states. In general, one would not expect

an interface between two \mathbb{Z}_2 topological insulators ($\nu = 1$) to exhibit gapless interface modes. However, any interface between RhO and AuTe that conserves the mirror symmetry would host four topologically protected gapless edge modes—two for each mirror sector.

We would also like to emphasize that the screening has resulted in six candidates for quantum anomalous Hall insulators, which are displayed in Table IV. This is of particular interest, since an experimental demonstration of the quantum anomalous Hall effect in a pristine 2D material is still lacking. Specifically, the materials FeCl₃ and FeBr₃ are highly stable and situated less than 0.1 eV/atom above the convex hull. However, the band structure of FeBr₃ shown in Fig. 2 exhibits rather flat bands and indicates that the electrons in these materials are strongly correlated. It is thus likely that the PBE band gap provides a poor estimate of the fundamental gap of the material and even the topological properties could be wrong if PBE does not describe the band inversion correctly. In order to test the reliability of PBE we have tested the topological properties with various semilocal functionals and with PBE+*U*. Using LDA, RPBE, and PBEsol yield a trivial topology, whereas PBE and revPBE predicts a QAHI with $C = 1$. Using PBE+*U* we obtain a QAHI for values of *U* below 0.18 eV and a trivial insulator for $U > 0.18$ eV. In all cases the geometry was optimized with the given functional. The topological properties of FeBr₃ are thus highly sensitive to the method used and with the methodology applied here it is not possible to determine whether or not the material is a QAHI.

C. Magnetic anisotropy

The quantum anomalous Hall effect is driven by spin-orbit mediated band inversion in magnetic materials. Moreover, as a consequence of the Mermin-Wagner theorem magnetic order cannot exist without magnetic anisotropy in 2D materials and spin-orbit effects thus have another crucial role to play for these materials. In fact, the Curie temperature in a 2D ferromagnet is strongly dependent on the anisotropy as well as the exchange coupling constants and the first example of 2D ferromagnetic order was only observed very recently in the trivial insulator CrI₃. Some of the present authors have shown that the Curie temperatures in 2D can be obtained from Monte Carlo simulations [28] based on the classical

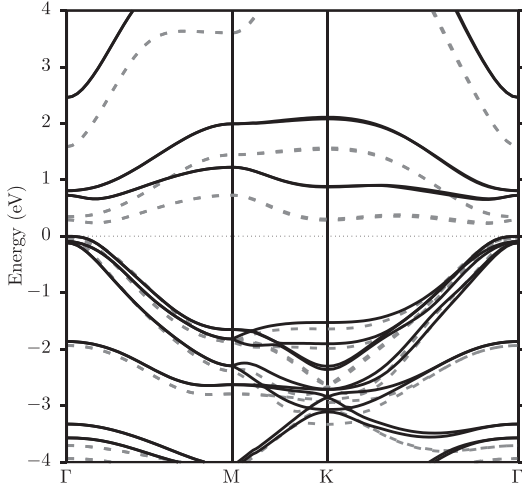


FIG. 5. LDA (dashed) and GW (solid) band structures of PdSe₂ in the MoS₂ prototype. In both cases the energy of the top of the valence band has been set to zero.

Heisenberg model

$$H = -\frac{1}{2}J \sum_{\langle ij \rangle} \mathbf{S}_i \cdot \mathbf{S}_j - A \sum_i (S_i^z)^2 - \frac{1}{2}B \sum_{\langle ij \rangle} S_i^z S_j^z, \quad (12)$$

where $\langle ij \rangle$ denotes the sum over nearest neighbors. The exchange and anisotropy constants J , A , and B can be obtained from first principles calculations combined with an energy mapping scheme that assumes magnetic moments to be located on transition metal atoms [28,65]. Since the magnetic structure is typically isotropic in the plane of the material a minimal requirement for magnetic order at finite temperatures is an out-of-plane easy axis. For the magnetic materials in Table IV we find $T_c = 2$ K and $T_c = 274$ K, respectively, for FeBr₃ and CoBr₃. The remaining magnetic materials are predicted to lack magnetic order at any finite temperature due to an in-plane easy axis or, more precisely, a negative spin-wave gap [28]. From these calculations CoBr₃ appears highly promising. However, additional calculations show that this material is more stable in the BiI₃ crystal structure (similar to CrI₃), which is nonmagnetic and a trivial insulator. We note that the materials with an in-plane easy axis that are excluded here could in general give rise to a finite critical temperature if there is additional small in-plane anisotropy such that the rotational symmetry is explicitly broken. It is, however, rather difficult to predict the critical temperature in those cases and we expect critical temperatures to be low due to the approximate in-plane anisotropy. One exception to this may be provided by OsCl₃ [24], which has a rather large magnetic anisotropy of ~ 40 meV per Os atom.

It is interesting to note that small gap magnetic insulators with large spin-orbit coupling may undergo topological phase transitions upon a rotation of the spin structure. As an example, we take OsO₂ in the CdI₂ crystal structure, which has an in-plane easy axis and is not found in Table IV because it

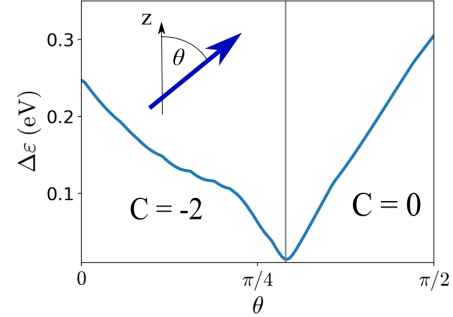


FIG. 6. Band gap as a function of magnetization angle with the out-of-plane axis in OsO₂. The material undergoes a topological transition for $C = 0$ to $C = -2$ when the gap closes in the vicinity of $\pi/4$.

is a trivial insulator. However, if the magnetic moments are rotated out of plane to align with the axis perpendicular to the plane of the material it becomes a QAHI with a Chern number of $C = -2$. This is only possible if the band gap closes at some point when the magnetic moments are rotated from the in-plane to the out-of-plane configuration. In Fig. 6 we show the band gap as a function of the polar angle θ that the magnetic moments form with the z axis. The band gap is seen to close in the vicinity of $\theta = \pi/4$, where the system undergoes a topological phase transition from $C = 0$ to $C = 2$. Such a rotation can be accomplished by applying a magnetic field and comprises a mechanism under which the gapless edge states can switched on or off by external means.

IV. DISCUSSION

We have implemented and performed an automated search for topologically nontrivial 2D materials in the Computational 2D Database. The method is based on a direct evaluation of Berry phases from the Kohn-Sham states and circumvents the common mapping to tight binding models via Wannier functions [44] that can sometimes make automation cumbersome.

In addition to several well-known topological insulators we have found 45 materials of which 18 are predicted to be stable. Of particular interest are the six magnetic QAHI. The experimental demonstration of the quantum anomalous Hall effect in a pristine 2D material would constitute a major breakthrough in the field of topological materials science. However, even if any of these materials could be synthesized the experimental verification of the effect will be highly tricky, since all of the experimentally relevant QAHI have band gaps below 0.1 eV. Moreover, we have shown that the theoretical prediction of the topological properties is nontrivial due to strong correlation and the predictions based on PBE calculations may not be reliable as we exemplified in the case of FeBr₃. Nevertheless, the PBE predictions for QAHI presented here provide indications that some of these materials could be highly interesting to put under experimental scrutiny. Most notable CoBr₃ in the AgBr₃ crystal structure, which we predict to have a Curie temperature of 274 K, but which is also

predicted to be less stable compared to the similar BiI_3 crystal structure.

The 10 stable QSHIs found have PBE band gaps between 0.05 and 0.23 eV. We have only performed full spinorial *GW* calculations for PdSe_2 where we found a threefold increase of the band gap. It would be highly interesting to perform carefully converged spinorial *GW* calculations for all the topological insulators presented in Tables I–IV, but this is beyond the scope of the present work. However, based on the cases of PdSe_2 and jacutegaite [42] we believe it is likely that several of the materials could have significantly larger gaps than predicted by PBE. None of the materials in Tables II–IV have been synthesized yet. But considering the rapid pace at which experimental techniques are currently evolving, we

expect an experimental realization of one or several of the predicted topological insulators should be within reach in the near future.

ACKNOWLEDGMENTS

This project has received funding from the European Research Council (ERC) under the European Union’s Horizon 2020 research and innovation programme (Grant No. 773122, LIMA). T.O. and D.T. were supported by the Independent Research Fund Denmark, Grant No. 6108-00464A. T.O. acknowledges support from the Scandinavia-Japan Sasakawa Foundation. T.D. acknowledges financial support from the Villum foundation.

- [1] K. von Klitzing, *Rev. Mod. Phys.* **58**, 519 (1986).
- [2] D. J. Thouless, M. Kohmoto, M. P. Nightingale, and M. den Nijs, *Phys. Rev. Lett.* **49**, 405 (1982).
- [3] M. V. Berry, *Proc. R. Soc. A Math. Phys. Eng. Sci.* **392**, 45 (1984).
- [4] F. D. M. Haldane, *Phys. Rev. Lett.* **61**, 2015 (1988).
- [5] B. A. Bernevig, T. L. Hughes, and S.-C. Zhang, *Science* **314**, 1757 (2006).
- [6] M. König, S. Wiedmann, C. Brüne, A. Roth, H. Buhmann, L. W. Molenkamp, X.-L. Qi, and S.-C. Zhang, *Science* **318**, 766 (2007).
- [7] X.-L. Qi, T. L. Hughes, and S.-C. Zhang, *Phys. Rev. B* **78**, 195424 (2008).
- [8] J. C. Y. Teo, L. Fu, and C. L. Kane, *Phys. Rev. B* **78**, 045426 (2008).
- [9] M. Z. Hasan and C. L. Kane, *Rev. Mod. Phys.* **82**, 3045 (2010).
- [10] D. Hsieh, Y. Xia, D. Qian, L. Wray, F. Meier, J. H. Dil, J. Osterwalder, L. Patthey, A. V. Fedorov, H. Lin, A. Bansil, D. Grauer, Y. S. Hor, R. J. Cava, and M. Z. Hasan, *Phys. Rev. Lett.* **103**, 146401 (2009).
- [11] H. Zhang, C.-X. Liu, X.-L. Qi, X. Dai, Z. Fang, and S.-C. Zhang, *Nat. Phys.* **5**, 438 (2009).
- [12] M. Ezawa, *Phys. Rev. Lett.* **109**, 055502 (2012).
- [13] M. Ezawa, *Phys. Rev. B* **87**, 155415 (2013).
- [14] L. Zhang, P. Bampoulis, A. N. Rudenko, Q. Yao, A. van Houselt, B. Poelsema, M. I. Katsnelson, and H. J. W. Zandvliet, *Phys. Rev. Lett.* **116**, 256804 (2016).
- [15] T. Amlaki, M. Bokdam, and P. J. Kelly, *Phys. Rev. Lett.* **116**, 256805 (2016).
- [16] P. Tang, P. Chen, W. Cao, H. Huang, S. Cahangirov, L. Xian, Y. Xu, S.-C. Zhang, W. Duan, and A. Rubio, *Phys. Rev. B* **90**, 121408 (2014).
- [17] A. Molle, J. Goldberger, M. Houssa, Y. Xu, S.-C. Zhang, and D. Akinwande, *Nat. Mater.* **16**, 163 (2017).
- [18] X. Qian, J. Liu, L. Fu, and J. Li, *Science* **346**, 1344 (2014).
- [19] T. Olsen, *Phys. Rev. B* **94**, 235106 (2016).
- [20] C. Z. Chang, J. Zhang, X. Feng, J. Shen, Z. Zhang, M. Guo, K. Li, Y. Ou, P. Wei, L. L. Wang, Z. Q. Ji, Y. Feng, S. Ji, X. Chen, J. Jia, X. Dai, Z. Fang, S. C. Zhang, K. He, Y. Wang, L. Lu, X. C. Ma, and Q. K. Xue, *Science* **340**, 167 (2013).
- [21] M. Mogi, M. Kawamura, R. Yoshimi, A. Tsukazaki, Y. Kozuka, N. Shirakawa, K. S. Takahashi, M. Kawasaki, and Y. Tokura, *Nat. Mater.* **16**, 516 (2017).
- [22] W.-K. Tse, Z. Qiao, Y. Yao, A. H. MacDonald, and Q. Niu, *Phys. Rev. B* **83**, 155447 (2011).
- [23] K. F. Garrity and D. Vanderbilt, *Phys. Rev. B* **90**, 121103 (2014).
- [24] X.-I. Sheng and B. K. Nikolić, *Phys. Rev. B* **95**, 201402 (2017).
- [25] M. Wu, *2D Mater.* **4**, 021014 (2017).
- [26] P. Chen, J.-Y. Zou, and B.-G. Liu, *Phys. Chem. Chem. Phys.* **19**, 13432 (2017).
- [27] N. D. Mermin and H. Wagner, *Phys. Rev. Lett.* **17**, 1133 (1966).
- [28] D. Torelli and T. Olsen, *2D Mater.* **6**, 015028 (2019).
- [29] N. Armitage, E. Mele, and A. Vishwanath, *Rev. Mod. Phys.* **90**, 015001 (2018).
- [30] L. Fu, *Phys. Rev. Lett.* **106**, 106802 (2011).
- [31] T. H. Hsieh, H. Lin, J. Liu, W. Duan, A. Bansil, and L. Fu (unpublished).
- [32] W. A. Benalcazar, B. A. Bernevig, and T. L. Hughes, *Phys. Rev. B* **96**, 245115 (2017).
- [33] W. A. Benalcazar, B. A. Bernevig, and T. L. Hughes, *Science* **357**, 61 (2017).
- [34] F. Schindler, A. M. Cook, M. G. Vergniory, Z. Wang, S. S. P. Parkin, B. A. Bernevig, and T. Neupert, *Sci. Adv.* **4**, eaat0346 (2018).
- [35] F. Schindler, Z. Wang, M. G. Vergniory, A. M. Cook, A. Murani, S. Sengupta, A. Y. Kasumov, R. Deblock, S. Jeon, I. Drozdov, H. Bouchiat, S. Guéron, A. Yazdani, B. A. Bernevig, and T. Neupert, *Nat. Phys.* **14**, 918 (2018).
- [36] J. Liu, X. Qian, and L. Fu, *Nano Lett.* **15**, 2657 (2015).
- [37] C. Niu, P. M. Buhl, G. Bihlmayer, D. Wortmann, S. Blügel, and Y. Mokrousov, *Nano Lett.* **15**, 6071 (2015).
- [38] D. Pesin and A. H. MacDonald, *Nat. Mater.* **11**, 409 (2012).
- [39] K. Yang, W. Setyawan, S. Wang, M. Buongiorno Nardelli, and S. Curtarolo, *Nat. Mater.* **11**, 614 (2012).
- [40] Z. Zhang, R.-W. Zhang, X. Li, K. Koepfner, Y. Yao, and H. Zhang, *J. Phys. Chem. Lett.* **9**, 6224 (2018).
- [41] N. Mounet, M. Gibertini, P. Schwaller, D. Campi, A. Merkys, A. Marrazzo, T. Sohier, I. E. Castelli, A. Cepellotti, G. Pizzi, and N. Marzari, *Nat. Nanotechnol.* **13**, 246 (2018).
- [42] A. Marrazzo, M. Gibertini, D. Campi, N. Mounet, and N. Marzari, *Phys. Rev. Lett.* **120**, 117701 (2018).
- [43] B. Huang, G. Clark, E. Navarro-Moratalla, D. R. Klein, R. Cheng, K. L. Seyler, D. Zhong, E. Schmidgall, M. A. McGuire, D. H. Cobden, W. Yao, D. Xiao, P. Jarillo-Herrero, and X. Xu, *Nature (London)* **546**, 270 (2017).

- [44] D. Gresch, G. Autès, O. V. Yazyev, M. Troyer, D. Vanderbilt, B. A. Bernevig, and A. A. Soluyanov, *Phys. Rev. B* **95**, 075146 (2017).
- [45] N. Marzari and D. Vanderbilt, *Phys. Rev. B* **56**, 12847 (1997).
- [46] M. Taherinejad, K. F. Garrity, and D. Vanderbilt, *Phys. Rev. B* **89**, 115102 (2014).
- [47] N. Marzari, A. A. Mostofi, J. R. Yates, I. Souza, and D. Vanderbilt, *Rev. Mod. Phys.* **84**, 1419 (2012).
- [48] N. Nagaosa, J. Sinova, S. Onoda, A. H. MacDonald, and N. P. Ong, *Rev. Mod. Phys.* **82**, 1539 (2010).
- [49] R. B. Laughlin, *Phys. Rev. B* **23**, 5632 (1981).
- [50] C. L. Kane and E. J. Mele, *Phys. Rev. Lett.* **95**, 146802 (2005).
- [51] C. L. Kane and E. J. Mele, *Phys. Rev. Lett.* **95**, 226801 (2005).
- [52] T. Rauch, M. Flieger, J. Henk, I. Mertig, and A. Ernst, *Phys. Rev. Lett.* **112**, 016802 (2014).
- [53] T. Olsen, M. Taherinejad, D. Vanderbilt, and I. Souza, *Phys. Rev. B* **95**, 075137 (2017).
- [54] S. Haastруп, M. Strange, M. Pandey, T. Deilmann, P. S. Schmidt, N. F. Hinsche, M. N. Gjerding, D. Torelli, P. M. Larsen, A. C. Riis-Jensen, J. Gath, K. W. Jacobsen, J. Jørgen Mortensen, T. Olsen, and K. S. Thygesen, *2D Mater.* **5**, 042002 (2018); <https://c2db.fysik.dtu.dk>.
- [55] J. Enkovaara, C. Rostgaard, J. J. Mortensen, J. Chen, M. Dulak, L. Ferrighi, J. Gavnholt, C. Glinsvad, V. Haikola, H. a. Hansen, H. H. Kristoffersen, M. Kuisma, a. H. Larsen, L. Lehtovaara, M. Ljungberg, O. Lopez-Acevedo, P. G. Moses, J. Ojanen, T. Olsen, V. Petzold, N. a. Romero, J. Stausholm-Møller, M. Strange, G. a. Tritsarlis, M. Vanin, M. Walter, B. Hammer, H. Häkkinen, G. K. H. Madsen, R. M. Nieminen, J. K. Nørskov, M. Puska, T. T. Rantala, J. Schiøtz, K. S. Thygesen, and K. W. Jacobsen, *J. Phys.: Condens. Matter* **22**, 253202 (2010).
- [56] P. E. Blöchl, *Phys. Rev. B* **50**, 17953 (1994).
- [57] A. Hjorth Larsen, J. Jørgen Mortensen, J. Blomqvist, I. E. Castelli, R. Christensen, M. Dulak, J. Friis, M. N. Groves, B. Hammer, C. Hargus, E. D. Hermes, P. C. Jennings, P. Bjerre Jensen, J. Kermode, J. R. Kitchin, E. Leonhard Kolsbjerg, J. Kubal, K. Kaasbjerg, S. Lysgaard, J. Bergmann Maronsson, T. Maxson, T. Olsen, L. Pastewka, A. Peterson, C. Rostgaard, J. Schiøtz, O. Schütt, M. Strange, K. S. Thygesen, T. Vegge, L. Vilhelmsen, M. Walter, Z. Zeng, and K. W. Jacobsen, *J. Phys.: Condens. Matter* **29**, 273002 (2017).
- [58] J. P. Perdew, K. Burke, and M. Ernzerhof, *Phys. Rev. Lett.* **77**, 3865 (1996).
- [59] M. Ezawa, *J. Phys. Soc. Jpn.* **84**, 121003 (2015).
- [60] Y. Xu, B. Yan, H.-J. Zhang, J. Wang, G. Xu, P. Tang, W. Duan, and S.-C. Zhang, *Phys. Rev. Lett.* **111**, 136804 (2013).
- [61] J. Li, C. He, L. Meng, H. Xiao, C. Tang, X. Wei, J. Kim, N. Kioussis, G. Malcolm Stocks, and J. Zhong, *Sci. Rep.* **5**, 14115 (2015).
- [62] R.-W. Zhang, C.-C. Liu, D.-S. Ma, and Y. Yao, *Phys. Rev. B* **97**, 125312 (2018).
- [63] M. Rohlfing, P. Krüger, and J. Pollmann, *Phys. Rev. B* **48**, 17791 (1993).
- [64] J. Vidal, X. Zhang, L. Yu, J.-W. Luo, and A. Zunger, *Phys. Rev. B* **84**, 041109 (2011).
- [65] T. Olsen, *Phys. Rev. B* **96**, 125143 (2017).

7.4 Paper IV: High throughput computational screening for 2D ferromagnetic materials: the critical role of anisotropy and local correlations

N.B.: Tab. 2 needs an update, as explained in sec. 5.4

2D Materials



PAPER

High throughput computational screening for 2D ferromagnetic materials: the critical role of anisotropy and local correlations

RECEIVED
8 April 2019

REVISED
11 June 2019

ACCEPTED FOR PUBLICATION
24 June 2019

PUBLISHED
16 July 2019

Daniele Torelli¹, Kristian S Thygesen^{1,2} and Thomas Olsen^{1,3}

¹ Department of Physics, Computational Atomic-scale Materials Design (CAMD), Technical University of Denmark, DK-2800 Kgs. Lyngby, Denmark

² Center for Nanostructured Graphene (CNG), Department of Physics, Technical University of Denmark, DK-2800 Kongens Lyngby, Denmark

³ Author to whom any correspondence should be addressed.

E-mail: tolsen@fysik.dtu.dk

Keywords: ferromagnetism, 2D materials, critical temperature, first principle calculations

Abstract

The recent observation of ferromagnetic order in two-dimensional (2D) materials has initiated a booming interest in the subject of 2D magnetism. In contrast to bulk materials, 2D materials can only exhibit magnetic order in the presence of magnetic anisotropy. In the present work we have used the computational 2D materials database (C2DB) to search for new ferromagnetic 2D materials using the spinwave gap as a simple descriptor that accounts for the role of magnetic anisotropy. In addition to known compounds we find 17 novel insulating materials that exhibit magnetic order at finite temperatures. For these we evaluate the critical temperatures from classical Monte Carlo simulations of a Heisenberg model with exchange and anisotropy parameters obtained from first principles. Starting from 150 stable ferromagnetic 2D materials we find ten candidates that are predicted to have critical temperatures exceeding that of CrI₃. We also study the effect of Hubbard corrections in the framework of DFT + U and find that the value of U can have a crucial influence on the prediction of magnetic properties. Our work provides new insight into 2D magnetism and identifies a new set of promising monolayers for experimental investigation.

1. Introduction

The nature of magnetic order in two-dimensional (2D) materials is fundamentally different from the three-dimensional case. In 3D, magnetic order arises from spontaneously broken symmetry of the magnetization direction and the magnetic anisotropy only plays a marginal role. In 2D, however, the Mermin–Wagner theorem [1] prohibits a broken symmetry phase at finite temperatures and the spin rotational symmetry has to be broken explicitly by magnetic anisotropy.

In 2017, two examples of 2D ferromagnetic insulators were discovered experimentally: a monolayer of CrI₃ that exhibits magnetic order below 45 K [2] and a bilayer of Cr₂Ge₂Te₆ with a Curie temperature of 20 K [3]. In the case of CrI₃ the magnetic order is driven by a strong out-of-plane magnetic anisotropy—a case that is often referred to as Ising-type ferromagnet. In contrast, Cr₂Ge₂Te₆ has a rather weak magnetic anisotropy and the magnetic order is maintained in bilayer structures by interlayer exchange couplings. Subsequently, ferromagnetic order at room temperature has

been reported in monolayers of MnSe₂ [4] and VSe₂ [5]. Both of these are itinerant (metallic) ferromagnets and the origin of magnetism in these materials is still not completely clarified. In particular, VSe₂ has an easy plane, which implies lack of magnetic order by virtue of the Mermin–Wagner theorem. However, such a two-dimensional spin system may comprise an example of a Kosterlitz–Thouless phase [6], which is known to display magnetic order due to finite size effects [7]. More recently, Fe₃GeTe₂ [8] was reported to host itinerant ferromagnetic order below 130 K, which originates from strong out-of-plane magnetic anisotropy. Several other 2D materials have been predicted to exhibit either ferromagnetic or anti-ferromagnetic order based on first principles calculations, but in most cases the predictions have not yet been confirmed by experiments [9] and estimates of the critical temperatures are often unjustified or very crude.

Two-dimensional CrI₃ has proven to comprise a highly versatile material. For example, an applied electric field can induce Dzyaloshinskii–Moriya interactions [10], and switch the magnetic state in bilayer

samples [11, 12]. In addition, it has been demonstrated that one can obtain control of in-plane conductivity and valley polarization by constructing heterostructures of CrI₃/graphene [13] and CrI₃/WSe₂ [14] respectively. van der Waals heterostructures of 2D materials involving magnetic layers thus constitute a highly flexible platform for designing spin tunnel junctions and could provide new ways to build nanostructured spintronics devices [9, 15, 16]. However, in order to make 2D magnetism technologically relevant there is a pressing need to find new 2D materials that exhibit magnetic order at higher temperatures.

A theoretical search for materials with particular properties may be based on either experimental databases such as the inorganic crystal structure database (ICSD) or computational databases where first principles simulations are employed to predict new stable materials. The former approach has been applied to predict new 2D materials from exfoliation energies of 3D materials in the ICSD [17–19] and several materials was found to have a magnetically ordered ground state (at $T = 0$ K). An example of the latter approach is the computational 2D materials database (C2DB) [20, 21]; presently containing 3712 2D materials of which 20% are predicted to be stable. One advantage of using a theoretical database is that the search is not restricted to materials that are experimentally known in a 3D parent van der Waals structure. However, materials predicted from theoretical databases may pose severe challenges with respect to synthesis and experimental characterization; even if they are predicted to be stable by first principles calculations.

Regarding the magnetic properties of materials, a major difficulty stems from the fact that standard first principles methods can only predict whether or not magnetic order is present at $T = 0$ K. For 2D materials the Mermin–Wagner theorem implies that magnetic order at $T = 0$ vanishes at any finite temperature in the absence of magnetic anisotropy. A first principles prediction of magnetic order at $T = 0$ is therefore irrelevant unless other properties of the material are taken into account. The question then arises: how to calculate the critical temperature for magnetic order given a set of exchange and anisotropy parameters for a particular material. It is clear that the Mermin–Wagner theorem disqualifies any standard mean-field approach because such methods neglect the fluctuations that are responsible for deteriorating magnetic order at finite temperatures in the absence of magnetic anisotropy. On the other hand, the importance of having magnetic anisotropy and an easy axis for the magnetization (as opposed to an easy plane) has led many authors to derive the magnetic properties from an Ising model for which the critical temperatures are known for all Archimedean lattices [22, 23]. However, the Ising model only provides a good magnetic model in the limit of infinite single-ion anisotropy and simply provides an upper bound for the critical temperature in general [24]. For example, in the case of CrI₃, which is regarded as an Ising-type ferromagnet, the Ising model overesti-

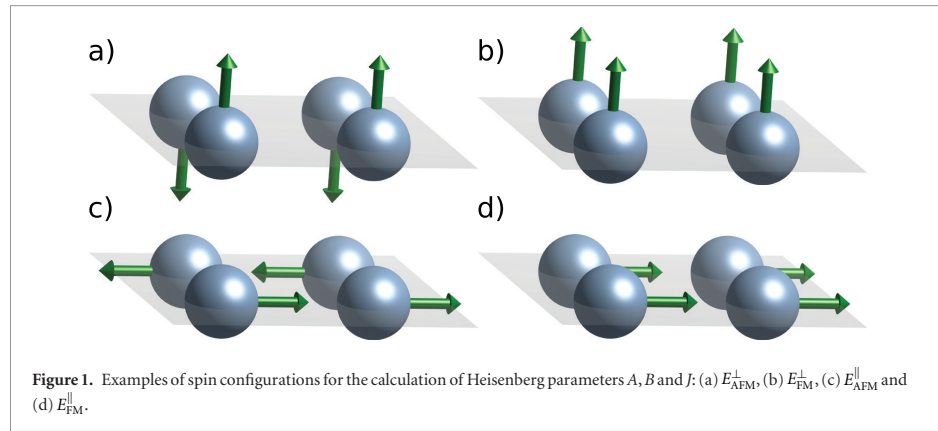
mates the critical temperature by a factor of three. The effect of finite anisotropy was analyzed in [24], where Monte Carlo simulations and renormalized spin-wave theory were applied to obtain a simple expression for the critical temperature of Ising-type ferromagnets. The expression only depends on the number of nearest neighbors, the nearest neighbor exchange interactions, and two anisotropy parameters. In the present work we have applied this expression to search the C2DB for ferromagnetic materials with finite critical temperatures. For some materials in the C2DB, the magnetic structure is not well approximated by an Ising-type ferromagnet and we have performed full Monte Carlo simulations to obtain the critical temperatures of these materials.

The paper is organized as follows. In section 2 we summarize the computational details and discuss the Heisenberg model, which forms the basis for calculations of critical temperatures in the present work. In section 3 we present the magnetic materials found by searching the C2DB and discuss and compare the calculated critical temperatures with previous works. Section 4 contains a conclusion and outlook.

2. Method and computational details

The materials in C2DB have been found by performing first principles calculations on isolated monolayers obtained by combinatorial lattice decoration of known 2D crystal structure prototypes in the framework of density functional theory (DFT). All results have been obtained using the Perdew–Burke–Ernzerhof (PBE) exchange–correlation functional and the electronic structure package GPAW [25, 26]. The geometry of all materials are fully optimized and the dynamical stability is assessed based on phonon frequencies at the center and corners of the Brillouin zone using the finite displacement method for a 2×2 supercell [20]. The heat of formation is calculated with respect to standard references [20] and a material is regarded as thermodynamically stable if it situated less than 0.2 eV above the convex hull defined by the 2807 most stable binary bulk compounds from the open quantum materials database (OQMD) [27, 28]. We find that more than 700 materials in the C2DB are predicted to have a ferromagnetic ground state and ~ 150 of these are thermodynamically and dynamically stable. The DFT calculations show whether or not the materials have a ferromagnetic ground state at $T = 0$ and for insulators the critical temperature can then be obtained from the descriptor derived in [24] or Monte Carlo simulations. The procedure requires knowledge of exchange and anisotropy parameters, which can be obtained from an energy mapping analysis including spin–orbit coupling [29]. We will briefly outline the approach below.

The magnetic properties of a system of localized spins are commonly analyzed in terms of the Heisenberg model. The most basic ingredient in the model is the isotropic exchange interactions arising between neighboring spins as a consequence of Coulomb



repulsion and Pauli exclusion. In addition, spin-orbit coupling may lead to magnetic anisotropy, which manifests itself through anisotropic exchange interactions [30] as well as single-ion anisotropy. 2D materials often exhibit (nearly) isotropic magnetic interactions in the plane of the materials and in the following we will restrict ourselves to models of the form

$$H = -\frac{1}{2} \sum_{i \neq j} J_{ij} \mathbf{S}_i \cdot \mathbf{S}_j - \sum_i A_i (S_i^z)^2 - \frac{1}{2} \sum_{i \neq j} B_{ij} S_i^z S_j^z, \quad (1)$$

where the sums over i and j run over all magnetic sites. J_{ij} denotes the isotropic exchange between spins at site i and j , B_{ij} is the anisotropic exchange for spins pointing out of the plane (here assumed to be the z -direction), and A_i is the single-ion anisotropy. We will also assume that the model is composed of a single kind of magnetic atom (as is the case for all the magnetic materials listed in the current version of C2DB), which is characterized by a half-integer S , yielding the maximum possible eigenvalue of S_z for any site. The most general form of the exchange interaction between sites i and j can be written as $\sum_{\alpha\beta} S_i^\alpha J_{ij}^{\alpha\beta} S_j^\beta$, where $J_{ij}^{\alpha\beta}$ is a 3×3 tensor for a given pair of i and j . This includes the Dzyaloshinskii-Moriya interactions as the anti-symmetric part as well as symmetric off-diagonal components that give rise to Kitaev interactions [30]. Such terms are neglected in the present work since, we are mainly interested in critical temperatures which is dominated by the terms included in equation (1). However, we emphasize that the neglect of such terms as well as the assumption of in-plane magnetic isotropy is an approximation we will make to reduce the set of parameters needed for the identification of promising candidates. Below we discuss a few important exceptions exemplified by materials with large critical temperatures that are not well described by the model (1).

In order to obtain the magnetic properties of a given material based on the model (1), one needs to extract the parameters J_{ij} , A_i and B_{ij} . In the case of a single magnetic element we have $A_i = A$ and restrict-

ing ourselves to nearest neighbor interactions we take $J_{ij} = J$ and $B_{ij} = B$ if i, j are nearest neighbors and $J_{ij} = B_{ij} = 0$ otherwise. The parameters can then be obtained by mapping the model to first principles calculations based on density functional theory [31]. In particular, the three parameters can be obtained from the total energies of the four spin configurations $E_{FM}^{\perp(\parallel)}$ and $E_{AFM}^{\perp(\parallel)}$, where E_{FM} is the energy of a fully ferromagnetic configuration and E_{AFM} is an anti-ferromagnetic state that involves anti-parallel spin alignment. The superscripts \perp and \parallel indicates whether the spinors are lying in the plane of the materials or perpendicular to the plane. A ferromagnetic material with $E_{FM}^{\perp} < E_{FM}^{\parallel}$, will thus have an out-of-plane easy axis. The four configurations are illustrated in figure 1. All energies are evaluated with the geometry obtained from the relaxed ferromagnetic ground state. For materials with a single magnetic atom in the unit cell, we have doubled the unit cell in order to accommodate the anti-ferromagnetic configuration. Comparing with equation (1) and approximating the spin operators by classical vectors we can obtain the parameters as

$$A = \frac{\Delta E_{FM} (1 - \frac{N_{AFM}}{N_{AFM}}) + \Delta E_{AFM} (1 + \frac{N_{AFM}}{N_{AFM}})}{2S^2}, \quad (2)$$

$$B = \frac{\Delta E_{FM} - \Delta E_{AFM}}{N_{AFM} S^2}, \quad (3)$$

$$J = \frac{E_{AFM}^{\parallel} - E_{FM}^{\parallel}}{N_{AFM} S^2}, \quad (4)$$

where $\Delta E_{FM(AFM)} = E_{FM(AFM)}^{\parallel} - E_{FM(AFM)}^{\perp}$ are the energy differences between in-plane and out-of-plane spin configurations for ferromagnetic(anti-ferromagnetic) structures and $N_{FM(AFM)}$ is the number of nearest neighbors with aligned(anti-aligned) spins in the anti-ferromagnetic configuration. For bipartite lattices $N_{FM} = 0$ and N_{AFM} is simply the number of nearest neighbors. In contrast, the triangular magnetic lattices (for example the MoS_2 crystal structure) have

no natural anti-ferromagnetic configurations and one has to consider a frustrated configuration where each atom has aligned as well as anti-aligned nearest neighbors. In the present work we have evaluated the exchange coupling constants Eq. (4) from the bare FM and AFM DFT energies without spin-orbit coupling, since the energy difference entering equation (4) can be tricky to converge properly when spin-orbit coupling is included.

Once the parameters have been determined the Curie temperatures can be calculated from an expression obtained in [24], which was derived by fitting to classical Monte Carlo (MC) simulations of the model (1) combined with renormalized spinwave theory. This simplifies the procedure significantly compared to running MC calculations for all materials and still assures a good reliability compared to available experimental data [24]. The expression for the Curie temperature is

$$T_C = \frac{S^2 J T_C^{\text{Ising}}}{k_B} f\left(\frac{\Delta}{J(2S-1)}\right) \quad (5)$$

where

$$f(x) = \tanh^{1/4} \left[\frac{6}{N_{nn}} \log(1 + \gamma x) \right] \quad (6)$$

is a fitted function with $\gamma = 0.033$ and N_{nn} the number of nearest neighbors. T_C^{Ising} is the critical temperature of the corresponding Ising model (in units of $J S^2 / k_B$), which has been tabulated for all the Archimedean lattices [22], and are given by 1.52, 2.27, and 3.64 for honeycomb, square and triangular lattices respectively.

$$\Delta = A(2S-1) + B S N_{nn} \quad (7)$$

is the spinwave gap, which is the smallest energy required for a magnetic excitation. It follows from the Mermin-Wagner theorem that a positive spinwave gap is a minimal requirement for out-of-plane magnetic order in 2D, and Δ thus provides a crucial parameter that can be used for a rough screening for materials that exhibit magnetic order at finite temperature. The spinwave gap was calculated by taking the ground state to have an out-of-plane ferromagnetic magnetization and compared to an in-plane ferromagnetic magnetization. A negative spinwave gap thus implies that the material can only exhibit in-plane magnetic order.

It should be noted that for $S = 1/2$, the single-ion anisotropy alone cannot open a gap in the spinwave spectrum and magnetic order thus requires anisotropic exchange. We note that the present approach can lead to situations where a material with an out-of-plane easy axis ($\Delta E_{\text{FM}} > 0$) has a negative spinwave gap indicating that the ground state is unstable. For example, for a honeycomb lattice with $N_{nn} = N_{\text{AFM}} = 3$ and $S = 1$ equations (2)–(4) one obtains $\Delta < 0$ if $\Delta E_{\text{AFM}} > 3\Delta E_{\text{FM}}$. This is due to the factor of $2S - 1$, which replaces a factor of $2S$ when

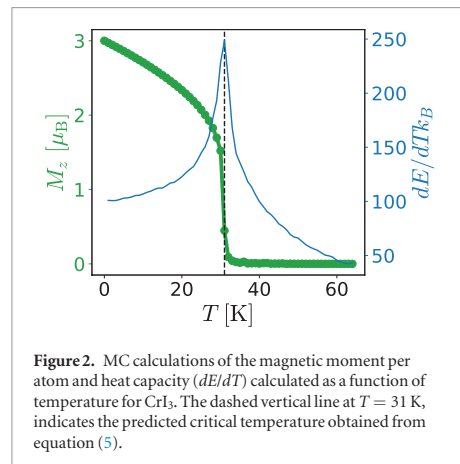
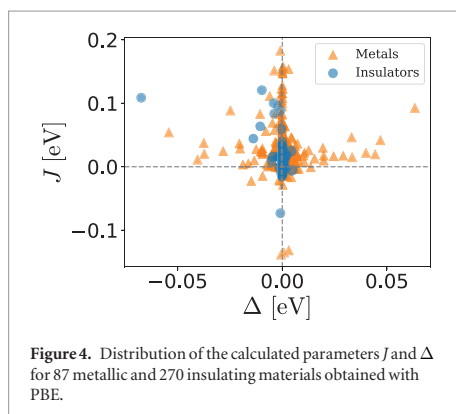
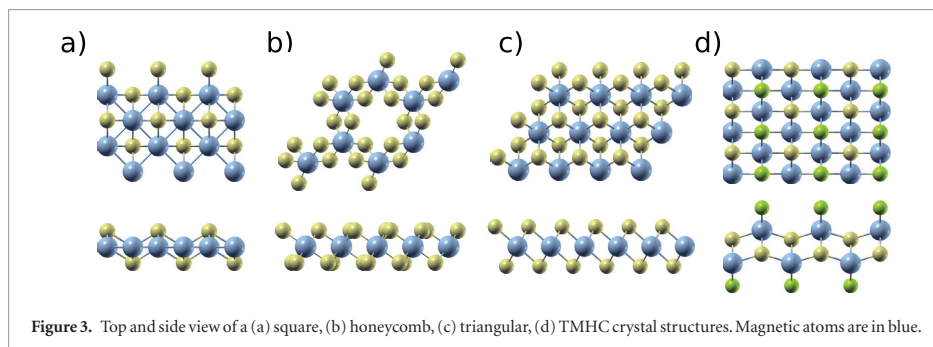


Figure 2. MC calculations of the magnetic moment per atom and heat capacity (dE/dT) calculated as a function of temperature for CrI_3 . The dashed vertical line at $T = 31$ K, indicates the predicted critical temperature obtained from equation (5).

quantum corrections to the anisotropy terms are taken into account in *renormalized* spinwave theory [3, 24]. In principle this is inconsistent with the energy mapping approach, which is based on a classical treatment of the Heisenberg model. However, a full quantum mechanical energy mapping analysis is beyond the scope of the present work. In figure 2 we compare the magnetization and heat capacity obtained from MC calculations of CrI_3 as well as the model result from equation (5). The critical temperature can be obtained from the position of the peak in the heat capacity.

The parameters A , B , and J (equations (2)–(4)) and critical temperatures (equations (5)–(7)) have been calculated for the nearly 550 materials listed in the C2DB database, which display honeycomb, square or triangular magnetic lattices, including stable as well as unstable materials. The calculations were performed with the same plane wave cutoff and k -point sampling as used for the magnetic anisotropy calculations in the database [20]. Examples of such structures are shown in figure 3 and includes the transition metal dichalcogenides (TMD) in the 1T phase and in the 2H phase (triangular magnetic lattice), compounds adopting the FeSe crystal structure (square magnetic lattice), and transition metal trihalides such as CrI_3 (honeycomb magnetic lattice). In figure 4 we show all the calculated parameters J and Δ for insulators and metals with triangular, square or honeycomb lattice.

The transition metal halogen chalcogen (TMHC) comprises another crystal structure that deserves an additional comment here. These materials display an atomic structure that resembles a distorted hexagonal magnetic lattice arranged over two layers. Although at least two comparable—but distinct—exchange paths are identifiable, MC calculations show that we can obtain rough estimates of the critical temperatures from the model (5) by treating it as a hexagonal lattice with a single effective nearest neighbour coupling obtained from the energy mapping analysis. For example, for CrI_3 we obtain $T_C = 118$ K from the model (5), which is in decent agreement with the MC results of



140 K including both nearest and next-nearest neighbour exchange interactions.

3. Results and discussion

In figure 5 we show the exchange coupling J and spinwave gap Δ for the stable ferromagnetic materials with $\Delta > 0$, grouped by structure prototypes. Relevant details about the prototypes and parameters used in equations (2)–(4) are listed in table 1.

We have performed the calculations for insulating as well as metallic materials. For metals, the value of S is ill-defined and here we have simply used the magnetic moment localized on the magnetic atoms, which is obtained by integrating the magnetization density over the PAW spheres. Moreover, the Heisenberg model is not a reliable starting point for itinerant magnets and to our knowledge there is no simple method to obtain critical temperatures for metallic ferromagnetic materials. For this reason we will not discuss metallic materials any further in the present work, but simply note that large anisotropies and exchange couplings indicate that metallic compounds such as CoBr_3 , VBr_3 , NiI_3 , and NiBr_3 could potentially exhibit very high critical temperatures. In general we observe that most compounds contain transition metal atoms with $3d$ valence electrons. In particular Cr, Mn, Fe, Ni and Co, which are all well-known elements in magnetic materials. In addition, most of the compounds contain

halides, albeit with a few important exceptions (for example MnO_2). In table 2 we show a list of all the insulating ferromagnetic materials and the calculated critical temperatures. The top part of the table contains the stable materials and in the lower part we have included a few examples of materials that exhibit very high critical temperatures but which are predicted to be unstable in their pristine form.

3.1. FeCl_2

The largest Curie temperature is found for FeCl_2 in the MoS_2 crystal structure where we obtain $T_C = 202$ K. The main reason for the high value of T_C is the large magnetic moment of $4 \mu_B$ per Fe atom and an exchange coupling of $J = 15$ meV, which is one of the largest values found in the present study. Previous *ab initio* calculations have reported that FeCl_2 in the CdI_2 crystal structure (which is metallic) is more stable compared to the MoS_2 crystal structure [32,33] and the Curie temperature was estimated to 17 K based on mean-field theory [32]. Our calculations confirm the stability hierarchy and predict an even more stable prototype GeS_2 (formation energy reduced by ~ 30 meV/atom compared to the MoS_2 phase). However, we do not expect out-of-plane long-range ferromagnetic order in either the CdI_2 or the GeS_2 crystal structures, since the spinwave gaps are negative in both cases. Interestingly, FeCl_2 in the CdI_2 crystal structure has positive single-ion anisotropy (A), which could indicate magnetic order. However, a negative anisotropic exchange coupling (B) yields an overall negative spinwave gap and the material thus serves as a good example of a case where the single-ion anisotropy is not a good indicator of magnetic order. To our knowledge there is no experimental reports of isolated 2D FeCl_x compounds. However, FeCl_3 in the BiI_3 crystal structure has been intercalated in bulk graphite exhibiting a ferromagnetic transition at temperature $T = 8.5$ K [34]. Recently it has also been employed as functional intercalation in few-layer graphene compounds to weaken restacking of graphene sheets [35] and bilayer graphene compounds [36] to promote magnetic order in graphene [37]. Nevertheless, according to our calculations, the FeCl_3

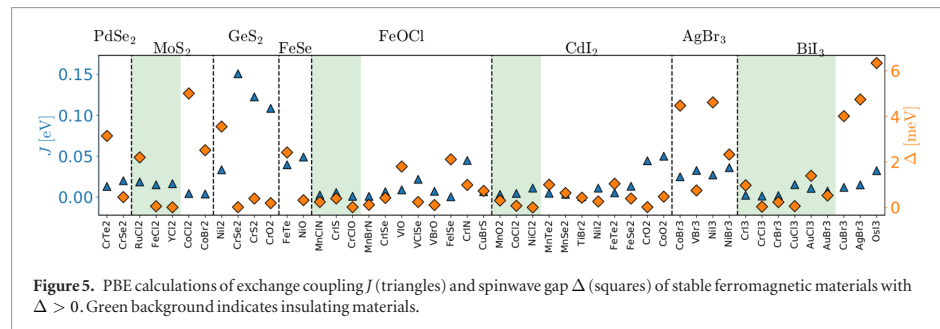


Figure 5. PBE calculations of exchange coupling J (triangles) and spinwave gap Δ (squares) of stable ferromagnetic materials with $\Delta > 0$. Green background indicates insulating materials.

Table 1. Prototypical crystal structure, geometry of the magnetic lattice and parameters used in equations (2)–(4) for materials investigated.

| Structure | Magnetic lattice | N_{FM} | N_{AFM} |
|---------------------|------------------|----------|-----------|
| MoS ₂ | Triangular | 2 | 4 |
| FeOCl | | | |
| CdI ₂ | | | |
| MoS ₂ Se | | | |
| WTe ₂ | | | |
| PdSe ₂ | Square | 0 | 4 |
| GeS ₂ | | | |
| FeSe | | | |
| AgBr ₃ | Honeycomb | 0 | 3 |
| BiI ₃ | | | |

crystal structure is less stable than the FeCl₂ ones and is not expected to exhibit ferromagnetic order as free standing layers due to a negative value of the spinwave gap. In bulk form FeCl₂ is known in the CdI₂ crystal structure with in-plane ferromagnetic order [38], but the long range order is stabilized by interlayer anti-ferromagnetic exchange coupling, which supports our assertion that exfoliated layers of this type will not exhibit magnetic order. Bulk FeCl₃ has also been reported to form different stacking polymorphs of the BiI₃ crystal structure, but the magnetic properties of these materials are not known [38].

3.2. MnO₂

Monolayers of MnO₂ in the CdI₂ crystal structure have been exfoliated in reference [39], but the magnetic properties have not yet been thoroughly investigated experimentally. Our calculations confirm a ferromagnetic ground state in agreement with previous calculations [40], where a critical temperature of 140 K was predicted. However, that result was obtained from energy mapping analysis using PBE + U DFT ($U = 3.9$ eV) and MC calculations based on the Ising model. From simulations of the Heisenberg model—explicitly including the finite anisotropy—we obtain a T_C of 63 K using Heisenberg parameters from a pure

Table 2. List of 2D magnetic insulating materials with positive exchange coupling J and positive spinwave gap Δ . Structure denotes the prototypical crystal structure and S is the spin carried by each magnetic atom. The critical temperature T_C is obtained from equation (5). The top part of the table contains dynamically and thermodynamically stable materials. The lower part of the table contains materials that are not expected to be stable in their pristine form but exhibit high critical temperatures.

| Formula | Structure | J (meV) | Δ (meV) | S [\hbar] | T_C (K) |
|-------------------|------------------|-----------|----------------|-----------------|-----------|
| FeCl ₂ | MoS ₂ | 15.14 | 0.053 | 2.0 | 202 |
| MnO ₂ | CdI ₂ | 3.35 | 0.305 | 1.5 | 63 |
| CoCl ₂ | CdI ₂ | 45.81 | 0.073 | 1.5 | 55 |
| YCl ₂ | MoS ₂ | 16.45 | 0.007 | 0.5 | 55 |
| CuCl ₃ | BiI ₃ | 15.34 | 0.057 | 1.0 | 33 |
| CrI ₃ | BiI ₃ | 2.31 | 0.971 | 1.5 | 31 |
| CrBr ₃ | BiI ₃ | 1.98 | 0.234 | 1.5 | 19 |
| NiCl ₂ | CdI ₂ | 11.08 | 0.001 | 1.0 | 17 |
| CrCl ₃ | BiI ₃ | 1.4 | 0.033 | 1.5 | 9 |
| RuCl ₂ | MoS ₂ | 18.65 | 2.196 | 2.0 | 598 |
| RuBr ₂ | MoS ₂ | 16.10 | 1.760 | 2.0 | 507 |

PBE calculations. The effect of Hubbard correction will be discussed in the next section.

3.3. YCl₂

A critical temperature of $T_C = 55$ K is found for YCl₂ in the MoS₂ prototype. There is neither experimental or theoretical reports on this material and it could pose an interesting new 2D magnetic compound. Our calculations indicate that it is highly stable in the ferromagnetic configuration with a magnetic moment of 1 μ_B per Y atom. However, since the material comprises a spin-1/2 system the classical MC calculations of the critical temperature may not be very accurate.

3.4. CrX₃

As reported in a previous study employing the same method [24] we predict CrI₃ in the BiI₃ structure to have $T_C = 31$ K, while the similar compounds and CrCl₃ and CrBr₃ have T_C of 9 K and 19 K respectively. We note that our calculated critical temperature for CrI₃ is somewhat lower than the experimental value of 45 K. This is mainly due to the fact that PBE tends

Table 3. Ferromagnetic materials in the TMDH crystal structure. The first two columns show nearest neighbour and next-nearest neighbour exchange coupling constants in meV. Columns three to six display anisotropy parameters calculated with respect to the two in-plane directions x and y in meV. In the second last column we state the crystallographic directions of magnetization listed from the hardest to the easiest axis. The last column shows the critical temperature in K obtained from MC calculations with these parameters.

| | J_1 | J_2 | A_x | A_y | B_x | B_y | Easy axis | T_C |
|--------|-------|-------|--------|--------|--------|--------|--------------------|-------|
| CrBrS | 6.41 | 4.01 | 0.051 | 0.027 | -0.004 | -0.0 | z, y, \mathbf{x} | 160 |
| CrIS | 5.71 | 4.85 | 0.084 | -0.223 | 0.025 | 0.033 | x, z, \mathbf{y} | 140 |
| CrBrSe | 7.10 | 5.97 | -0.018 | -0.042 | 0.022 | 0.028 | z, y, \mathbf{x} | 140 |
| CrClSe | 7.05 | 5.81 | -0.038 | -0.0 | 0.021 | 0.017 | z, x, \mathbf{y} | 130 |
| CrClS | 6.52 | 3.99 | 0.026 | -0.003 | -0.005 | 0.003 | z, y, \mathbf{x} | 130 |
| MnClN | 2.66 | 5.76 | 0.023 | 0.044 | 0.022 | 0.012 | x, y, \mathbf{z} | 75 |
| CrBrO | 0.42 | 0.11 | 0.012 | 0.039 | -0.0 | -0.003 | z, x, \mathbf{y} | 15 |
| CrClO | 1.08 | 0.74 | -0.010 | 0.034 | 0.004 | 0.001 | y, x, \mathbf{z} | 15 |

to underestimate the exchange coupling and can be improved by using a PBE + U scheme as discussed below. CrCl₃ has not previously been described in its 2D form, but it is known as ferromagnetic bulk compounds in the BiI₃ crystal structure with out-of-plane magnetization [38]. A recent experimental investigation employing ballistic Hall micromagnetometry on monolayer CrBr₃ reports a critical temperature of 27 K [41], slightly higher than our prediction of 19 K. The experimental Curie temperatures of bulk CrCl₃, CrBr₃, and CrI₃ are 27 K, 47 K, and 70 K respectively. Our calculated values show the same hierarchy, but are reduced compared to the bulk values due to the lack of interlayer exchange coupling.

3.5. CuCl₃

For CuCl₃ in the BiI₃ crystal structure we find a critical temperature of 33 K, which is similar to the calculated value of CrI₃. The material does, however, lie above the convex hull by 0.15 eV per atom, which could complicate experimental synthesis and characterization.

3.6. XCl₂

Bulk CoCl₂ and NiCl₂ are both known to display anti-ferromagnetic interlayer coupling and in-plane ferromagnetic order [38]. As seen in table 2, our calculations predict the materials to exhibit out-of-plane order. For NiCl₂, however, one should be a bit cautious due to the extremely small value of the spinwave gap Δ and more accurate calculations could lead to a ground state with in-plane magnetic order. Experimental measurements on bulk samples indicate anomalies in the heat capacity related to magnetic phase transitions at 24 K and 52 K. While the first result is in good agreement with our predicted properties, the second one is significantly higher and could be related to an additional phase transition in the 3D structure.

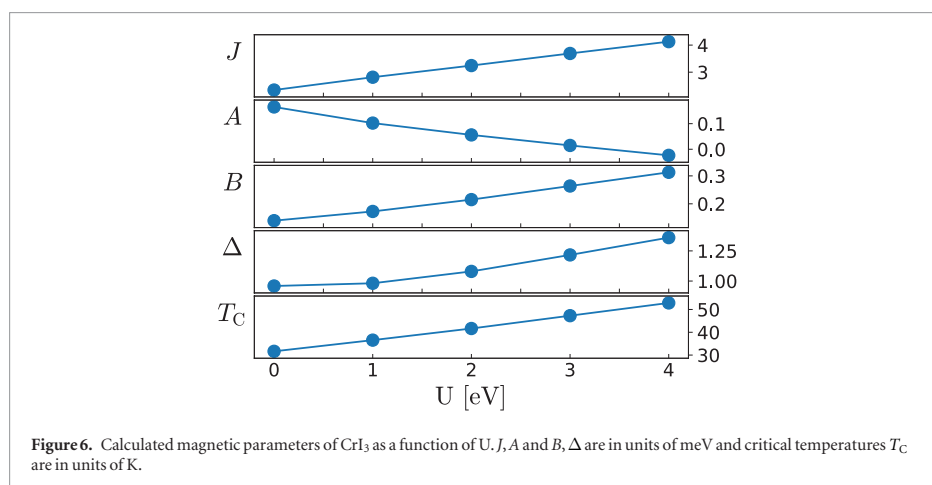
3.7. Metastable high- T_C compounds

The lower part of table 2 shows two materials that we do not predict to be stable, but may be of interest due to the large predicted critical temperatures. Here

we comment briefly on the case of RuCl₂ in the MoS₂ crystal structure, which we predict to be a dynamically stable insulator with a critical temperature of 598 K. It is, however, situated 0.5 eV above the convex hull, which will mostly likely pose an obstacle to experimental synthesis. Nevertheless, the calculations show that very high values of critical temperatures are indeed possible in 2D materials with realistic atomic-scale parameters. It should be mentioned that monolayers of RuCl₃ in the BiI₃ crystal structure have been exfoliated and characterized experimentally [42]. Moreover, in a recent study [43] the critical temperature of monolayer RuCl₃ was calculated using DFT and MC simulations based on the Heisenberg model and found $T_C = 14.21$ K [43]. However, a Hubbard term is required to open a gap and RuCl₃ in the BiI₃ crystal structure is metallic within PBE [44, 45], which is why we do not include it in table 2.

3.8. In-plane anisotropy

As mentioned above, materials with the TMDH crystal structure have been considered as effective triangular magnetic lattices with a single nearest-neighbour coupling. However, this model can only be used for a rough screening of materials. For example, CrBrS exhibits a strong in-plane anisotropy and the axis of magnetization are ordered (from the hardest axis to the easiest) as: x , y and z . In equation (1), in-plane anisotropy is not considered and we thus extend the model with the full set of anisotropy parameters A_x , A_y , B_x , and B_y , that measures the single-ion anisotropy and anisotropic exchange with respect to both x and y directions (relative to the z -direction). These parameters can be found by generalizing the energy mapping analysis equations (2) and (3) to include different in-plane directions. We then run MC calculations using the full set of parameters to find the critical temperatures, including nearest and next-nearest neighbours couplings J_1 and J_2 . We find several insulating materials in this crystal structure that shows ferromagnetic order. The results are shown in table 3. In particular, CrBrS and CrBrSe are predicted to have a critical temperature of 160 K and 140 K respectively, in good agreement with recent theoretical calculations



[46] and for CrI₃ we calculate a critical temperature of 140 K. We expect in-plane magnetization with similar critical temperature for CrClS(Se) as well, while for MnClN the easy axis is along the out-of-plane direction up to 75 K. Finally we obtain a Curie temperature of 15 K for CrBrO and CrClO, which has previously been predicted to have a Curie temperature of 160 K based on an Ising model approach [47]. Again, this comparison emphasizes that the magnetic anisotropy cannot simply be regarded as a mechanism that fixes the magnetization to the out-of-plane direction: approximating magnetic properties by the Ising model may yield a critical temperature that is wrong by an order of magnitude.

3.9. Hubbard U

Almost half of the materials present in C2DB contain at least one element with a partially filled d -shell. Local and semi-local xc-functionals such as PBE are known to overestimate delocalization of correlated electrons, due to the uncompensated Coulomb self-interaction of the electron. In the Hubbard model a term is introduced that acts as an effective electronic on-site repulsion and provides a penalty to delocalization. In order to determine the influence of the Hubbard correction we have recalculated exchange and anisotropy parameters for CrI₃ for a range of U values in the PBE + U scheme. The structure was fully relaxed for each value of U and the results are shown in figure 6. We observe that an increasing value of U leads to an overall increase of both Δ and J , which result in higher critical temperatures. The dependence of T_C on U is roughly linear with T_C increasing by 5 K per eV that U is increased.

In order to gain more insight into the general influence of U for the calculations of magnetic properties, we have recalculated the magnetic parameters and critical temperature for all magnetic materials in the

Table 4. Hubbard parameters employed in the PBE + U calculations.

| Element | Fe | Mn | Cr | Co | Ni | V | Cu |
|---------|-----|-----|-----|-----|-----|-----|-----|
| U (eV) | 4.0 | 3.8 | 3.5 | 3.3 | 6.4 | 3.1 | 4.0 |

C2DB containing $3d$ valence electrons. We used the optimal values determined in [48] and listed in table 4. For each material the structure was relaxed with the given value of U, but the stability analysis was based on bare PBE.

The inclusion of U can have a rather dramatic effect on the results. For example, the magnetic configuration of the ground state or the magnetic moment localized on the transition metal ion may change. The results for the stable materials are shown in figure 7, while the insulating systems are listed in table 5. Including a Hubbard term in the entire workflow (from the relaxation step onward) affects quantitatively and in some cases also qualitatively the ground-state. This means that the magnetic moment, the energy gap or the sign of Δ may change, making the comparison with table 2 meaningful only for a subset of materials. Compounds that are also present in table 2 are shown in bold face for comparison.

3.9.1. Effect of U on T_C

For MnO₂, the main effect of adding a Hubbard correction is to increase the exchange parameter J by a factor of two. Interestingly the anisotropy parameters A and B decrease and the spinwave gap Δ becomes less than half the value obtained with PBE. Nevertheless, the overall effect is an increase of the critical temperature from 63 K to 82 K. This number can be compared to the result in [40] where a critical temperature of 140 K was estimated from the Ising model.

For CrI₃ we predict a critical temperature of 50 K with PBE + U and similarly T_C increases from 19 K

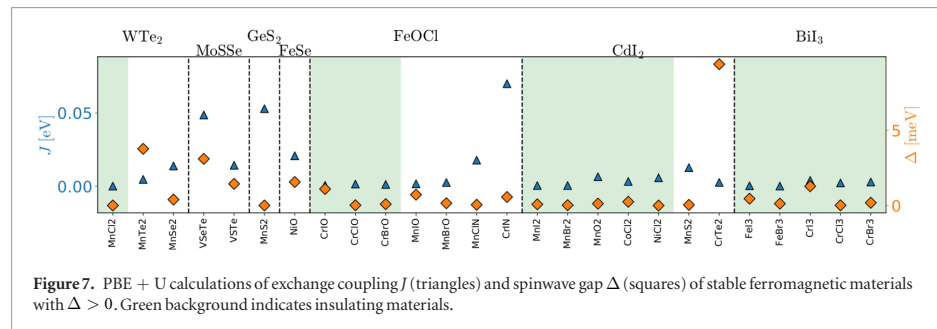


Figure 7. PBE + U calculations of exchange coupling J (triangles) and spin wave gap Δ (squares) of stable ferromagnetic materials with $\Delta > 0$. Green background indicates insulating materials.

to 24 K for CrBr_3 . These are significantly closer to the experimental value (45 K and 27 K respectively) than the values obtained with bare PBE. The critical temperatures of CoCl_2 and CrCl_3 are almost unaffected. These results indicate that it is non-trivial to predict how the inclusion of a Hubbard U influences the calculated critical temperatures in general.

For the compounds MnI_2 , MnBr_2 , and FeBr_3 , which all have large magnetic moment of $5\mu_B$ per magnetic atom we obtain rather low critical temperatures of 21, 16 and 2 K respectively. This is mainly due to small values of exchange coupling J for these materials. The inclusion of U in MnI_2 and MnBr_2 increases the electronic gap as well as the spinwave gap. But most importantly, it yields a ferromagnetic ground state, while the ground state is anti-ferromagnetic without the inclusion of U [49]. For MnI_2 The result appears to be in qualitative agreement with neutron scattering experiments on the bulk compounds, which reports a helical magnetic structure below a critical temperature of 3.4 K, with the moments being aligned in the individual planes [38, 50]. This could indicate that PBE + U provides a more accurate description than PBE, which does not predict magnetic order for MnI_2 . For MnBr_2 in the CdI_2 crystal structure, neutron scattering experiments on the bulk parent structure revealed an anti-ferromagnetic order below $T = 2.16$ K with magnetic moments lying in-plane [51]. However, this is not necessarily in contradiction with our calculations since the observed anti-ferromagnetic configuration is ‘double-striped’, a configuration that has not been considered in the present study. For FeBr_3 the Hubbard term makes the spin jump from $1/2$ to $5/2$ per Fe atom and opens a spinwave gap. A previous investigation of this material showed that it is predicted to be a quantum spin Hall insulator with PBE while PBE + U predicts a trivial insulator above a critical value of $U = 0.18$ eV [21].

3.9.2. Metastable high- T_C compounds

The lower part of table 5 lists materials, which are not predicted to be completely stable in their pristine form according to PBE calculations (we have not performed a full stability analysis with PBE + U). Bulk CoO has an anti-ferromagnetic rock-salt structure

Table 5. List of 2D non-metal materials with positive exchange coupling J and spin wave gap Δ , obtained from PBE + U calculations. Structure denotes the prototypical crystal structure and S is the spin carried by each magnetic atom. The structures in bold are present also in 2 for comparison. The top part contains stable materials, whereas the lower part contains materials with large critical temperatures that may be unstable in their pristine form.

| Formula | Structure | J (meV) | Δ (meV) | S [\hbar] | T_C (K) |
|-------------------------|------------------------|-----------|----------------|-----------------|-----------|
| CoCl₂ | CdI₂ | 3.21 | 0.249 | 1.5 | 57 |
| CrI₃ | BiI₃ | 3.95 | 1.280 | 1.5 | 50 |
| CrBr₃ | BiI₃ | 2.82 | 0.185 | 1.5 | 24 |
| MnI₂ | CdI₂ | 0.40 | 0.081 | 2.5 | 21 |
| MnBr₂ | CdI₂ | 0.41 | 0.024 | 2.5 | 16 |
| CrCl₃ | BiI₃ | 2.19 | 0.016 | 1.5 | 10 |
| NiCl₂ | CdI₂ | 5.69 | ~ 10–4 | 1.0 | 7 |
| FeBr₃ | BiI₃ | 0.04 | 0.124 | 2.5 | 2 |
| CoO | FeSe | 106.54 | 0.199 | 1.5 | 520 |
| FeS | FeSe | 28.99 | 0.591 | 2.0 | 413 |

with a critical temperature of 293 K [52]. According to PBE calculations the most stable 2D phase is a metallic CdI_2 crystal structure (parameters J and Δ are shown in figure 5). In the FeSe crystal structure, CoO has a low dynamic stability (0.5 eV/atoms above the convex hull) but we report it here due to the very high critical temperature of 520 K originating from the extraordinarily large exchange coupling predicted by PBE + U .

FeS in the FeSe crystal structure has a non-magnetic ground state with PBE, but is predicted to be highly stable and is situated on the convex hull. With PBE + U the ground state becomes ferromagnetic and we predict a high critical temperature of 413 K. According to previous calculations [53], however, the true ground state is a striped anti-ferromagnetic configuration, which is not taken into account in this work.

3.9.3. In-plane anisotropy

In table 6 we list Heisenberg parameters and critical temperatures for TMHC structures obtained from PBE + U calculations and MC calculations following the same procedure as in the previous section where no Hubbard correction was included. Comparing

Table 6. Parameters and results for TMHC structures obtained from PBE + U calculations. Symbols and units are the same as in table 3. Materials in bold are the ones listed in both tables.

| | J_1 | J_2 | A_x | A_y | B_x | B_y | Easy axis | T_C |
|-------|-------------|-------------|--------------|--------------|--------------|--------------------|-----------|-------|
| CrIS | 4.91 | 3.89 | 0.06 | − 0.483 | − 0.011 | − 0.01 | y, z, x | 135 |
| CrBrO | 1.12 | 0.78 | 0.043 | − 0.010 | 0.001 | 0.001 | x, z, y | 35 |
| CrIO | 0.49 | −1.46 | 0.586 | −0.123 | −0.008 | −0.003 | x, z, y | 25 |
| CrClO | 1.38 | 1.27 | 0.007 | 0.016 | 0.001 | − 10 ^{−4} | y, x, z | 20 |

the results with table 3, it is noted that MnClN and some of the Cr-based compounds, which exhibit a high critical temperature with pure PBE are not ferromagnetic insulators with PBE + U. On the other hand, a new material—CrIO—which did not show ferromagnetic order with bare PBE is predicted to exhibit ferromagnetic order at 25 K by PBE+U.

4. Conclusions

We have presented a high throughput computational screening for magnetic insulators based on the computational 2D materials database. In contrast to several previous studies of magnetism in 2D, we have emphasized the crucial role of magnetic anisotropy and used the spinwave gap as a basic descriptor that must necessarily be positive in order for magnetism to persist at finite temperatures. This criterion severely reduces the number of relevant candidates and we end up with 12 stable candidate materials for which the critical temperatures were calculated from classical MC simulations. Ten of the materials were predicted to have Curie temperatures exceeding that of CrI₃ employing bare PBE calculations. The classical MC simulations appear to comprise an accurate method for obtaining the critical temperatures for insulating materials with $S > 1/2$. However, the Heisenberg parameters that enter the simulations may be sensitive to the approximations used to calculate them. In the C2DB all calculations are performed with the PBE functional, which may have shortcomings for strongly correlated systems. We have thus tested how the results are modified if the parameters are evaluated with PBE+U instead and we find that the predictions do indeed change in a non-systematic way. For the hexagonal and honeycomb systems three materials that were predicted to be ferromagnetic (at finite temperature) are no longer predicted to show magnetic order when the PBE+U scheme is employed and three materials that were not magnetic with PBE become magnetic with PBE+U. For the six materials that are magnetic with both PBE and PBE+U the critical temperatures are slightly different in the two approximations. The biggest difference is seen for CrI₃ where inclusion of U increases the critical temperature from 31 K to 50 K, which is closer to the experimental value of 45 K.

In the present work we have mainly focused on insulators. This restriction is rooted in the simple fact that we do not have a reliable way to estimate Curie

temperatures of metallic 2D magnetic materials. Metallic ferromagnetism in 2D is, however, a highly interesting subject and we note that room temperature magnetism has recently been reported in the 2D metals VSe₂ [5] and MnSe₂ [4]. Moreover, figures 4 and 5 indicate that in the C2DB the largest values of both spinwave gaps and exchange couplings are found in metallic materials. Clearly, there is pressing need for theoretical developments of 2D itinerant magnetism that can be applied in conjunction with first principles simulations to provide accurate predictions of the magnetic properties of 2D metals.

Finally, we have restricted ourselves to ferromagnetic order and the exchange constants calculated in the present work will be included in the online version of the C2DB. Nevertheless, the C2DB contains 241 anti-ferromagnetic entries—50 of which are predicted to be stable. The prediction of a novel 2D anti-ferromagnetic compound would certainly comprise an important step forward in the study of 2D magnetism, but the theoretical treatment is complicated by the possibility of several ordered structures that may coexist at a given temperature—in particular for non-bipartite lattice such as the triangular one. We will leave the study of anti-ferromagnetism in 2D to future work.

Acknowledgments

T Olsen and D Torelli acknowledges supported from the Independent Research Fund Denmark, Grant No. 6108-00464A. K Thygesen acknowledges support from the European Research Council (ERC) under the European Union's Horizon 2020 research and innovation program (Grant No. 773122, LIMA).

ORCID iDs

Daniele Torelli  <https://orcid.org/0000-0002-4861-0268>

Kristian S Thygesen  <https://orcid.org/0000-0001-5197-214X>

Thomas Olsen  <https://orcid.org/0000-0001-6256-9284>

References

- [1] Mermin N D and Wagner H 1966 *Phys. Rev. Lett.* **17** 1133
- [2] Huang B et al 2017 *Nature* **546** 270
- [3] Gong C et al 2017 *Nature* **546** 265
- [4] O'Hara D J et al 2018 *Nano Lett.* **18** 3125

- [5] Bonilla M, Kolekar S, Ma Y, Diaz H C, Kalappattil V, Das R, Eggers T, Gutierrez H R, Phan M H and Batzill M 2018 *Nat. Nanotechnol.* **13** 289
- [6] Kosterlitz J M and Thouless D J 1973 *J. Phys. C: Solid State Phys.* **6** 1181
- [7] Holdsworth P C W and Bramwell S T 1994 *Phys. Rev. B* **49** 8811
- [8] Fei Z et al 2018 *Nat. Mater.* **17** 778
- [9] Gong C and Zhang X 2019 *Science* **363** eaav4450
- [10] Liu J, Shi M, Lu J and Anantram M P 2018 *Phys. Rev. B* **97** 8
- [11] Jiang S, Shan J and Mak K F 2018 *Nat. Mater.* **17** 406
- [12] Huang B et al 2018 *Nat. Nanotechnol.* **13** 544
- [13] Cardoso C, Soriano D, García-Martínez N A and Fernández-Rossier J 2018 *Phys. Rev. Lett.* **121** 67701
- [14] Taniguchi T et al 2017 *Sci. Adv.* **3** e1603113
- [15] Burch K, Mandrus D and Park J G 2018 *Nature* **563**
- [16] Wang Z, Gutiérrez-Lezama I, Ubrig N, Kroner M, Gibertini M, Taniguchi T, Watanabe K, Imamoglu A, Giannini E and Morpurgo A F 2018 *Nat. Commun.* **9** 2516
- [17] Björkman T, Gulans A, Krasheninnikov A V and Nieminen R M 2012 *Phys. Rev. Lett.* **108** 235502
- [18] Ashton M, Paul J, Sinnott S B and Hennig R G 2017 *Phys. Rev. Lett.* **118** 106101
- [19] Mounet N et al 2018 *Nat. Nanotechnol.* **13** 246
- [20] Haastrup S et al 2018 *2D Mater.* **5** 042002
- [21] Olsen T, Andersen E, Okugawa T, Torelli D, Deilmann T and Thygesen K S 2019 *Phys. Rev. Mater.* **3** 024005
- [22] Malarz K, Zborek M and Wrobel B 2005 *Task Q.* **9** 475
- [23] Kan M, Adhikari S and Sun Q 2014 *Phys. Chem. Chem. Phys.* **16** 4990
- [24] Torelli D and Olsen T 2018 *2D Mater.* **6** 015028
- [25] Enkovaara J et al 2010 *J. Phys.: Condens. Matter* **22** 253202
- [26] Hjorth Larsen A et al 2017 *J. Phys.: Condens. Matter* **29** 273002
- [27] Saal J E, Kirklín S, Aykol M, Meredig B and Wolverton C 2013 *JOM* **65** 1501
- [28] Kirklín S, Saal J E, Meredig B, Thompson A, Doak J W, Aykol M, Rühl S and Wolverton C 2015 *NPJ Comput. Mater.* **1** 15010
- [29] Olsen T 2016 *Phys. Rev. B* **94** 235106
- [30] Xu C, Feng J, Xiang H and Bellaiche L 2018 *NPJ Comput. Mater.* **4** 57
- [31] Olsen T 2017 *Phys. Rev. B* **96** 125143
- [32] Torun E, Sahin H, Singh S K and Peeters F M 2015 *Appl. Phys. Lett.* **106** 192404
- [33] Feng Y, Wu X, Han J and Gao G 2018 *J. Mater. Chem. C* **6** 4087
- [34] Dresselhaus M S and Dresselhaus G 2002 *Adv. Phys.* **51** 1
- [35] Qi X, Qu J, Zhang H B, Yang D, Yu Y, Chi C and Yu Z Z 2015 *J. Mater. Chem. A* **3** 15498
- [36] Kim N, Kim K S, Jung N, Brus L and Kim P 2011 *Nano Lett.* **11** 860
- [37] Bointon T H, Khrapach I, Yakimova R, Shytov A V, Craciun M F and Russo S 2014 *Nano Lett.* **14** 1751
- [38] McGuire M A 2017 *Crystals* **7** 121
- [39] Omomo Y, Sasaki T, Wang L and Watanabe M 2003 *J. Am. Chem. Soc.* **125** 3568
- [40] Kan M, Zhou J, Sun Q, Kawazoe Y and Jena P 2013 *J. Chem. Phys. Lett.* **4** 3382
- [41] Kim M et al 2019 Hall micromagnetometry of individual two-dimensional ferromagnets (arXiv: 1902.06988)
- [42] Weber D, Schoop L M, Duppl V, Lippmann J M, Nuss J and Lotsch B V 2016 *Nano Lett.* **16** 3578
- [43] Sarikurt S, Kadioglu Y, Ersan F, Vatansever E, Akturk O U, Yuksel Y, Akinci U and Akturk E 2018 *Phys. Chem. Chem. Phys.* **20** 997
- [44] Huang C, Zhou J, Wu H, Deng K, Jena P and Kan E 2017 *Phys. Rev. B* **95** 045113
- [45] Ersan F, Vatansever E, Sarikurt S, Yuksel Y, Kadioglu Y, Ozaydin H, Uzengi Akturk O, Akinci U and Ethem A 2018 *J. Magn. Magn. Mater.* **476** 111
- [46] Qi J, Wang H and Qian X 2018 Electrically tunable and high Curie temperature 2D ferromagnetism in Van der Waals layered crystals (arXiv:1811.02674)
- [47] Miao N, Xu B, Zhu L, Zhou J and Sun Z 2018 *J. Am. Chem. Soc.* **140** 2417
- [48] Wang L, Maxisch T and Ceder G 2006 *Phys. Rev. B* **73** 195107
- [49] Kulish V V and Huang W 2017 *J. Mater. Chem. C* **5** 8734
- [50] Cable J W, Wilkinson M K, Wollan E O and Koehler W C 1962 *Phys. Rev.* **125** 1860
- [51] Wollan E O, Koehler W C and Wilkinson M K 1958 *Phys. Rev.* **110** 638
- [52] Berkowitz A and Takano K 1999 *J. Magn. Magn. Mater.* **200** 552
- [53] Winiarski M, Zasada J and Samsel-Czekala M 2018 *Comput. Mater. Sci.* **142** 372

7.5 Paper V: First Principles Heisenberg Models of 2D magnetic materials: The Importance of Quantum Corrections to the Exchange Coupling

The publication, in a slightly earlier version, is submitted.

First Principles Heisenberg Models of 2D magnetic materials: The Importance of Quantum Corrections to the Exchange Coupling

Daniele Torelli¹ and Thomas Olsen¹

¹*Computational Atomic-scale Materials Design (CAMD), Department of Physics, Technical University of Denmark, DK-2800 Kgs. Lyngby, Denmark*

(Dated: December 31, 2019)

Magnetic materials are typically described in terms of the Heisenberg model, which provides an accurate account of thermodynamic properties when combined with first principles calculations. This approach is usually based on an energy mapping between density functional theory and a classical Heisenberg model. However, for two-dimensional systems the eigenenergies of the Heisenberg model may differ significantly from the classical approximation, which leads to modified expressions for exchange parameters. Here we demonstrate that density functional theory yields local magnetic moments that are in accordance with strongly correlated anti-ferromagnetic eigenstates of the Heisenberg Hamiltonian implying that density functional theory provides a description of these states that conforms with the quantum mechanical eigenstates of the model. We then provide expressions for exchange parameters based on a proper eigenstate mapping to the Heisenberg model and find that they are typically reduced by 10 % compared to a classical analysis. Finally, we calculate the corrections to critical temperature for magnetic ordering for a previously predicted set of two-dimensional insulators and find that the inclusion of quantum effects may reduce the predictions of critical temperatures by up to 5 %.

I. INTRODUCTION

The identification of ferromagnetism in a monolayer of CrI₃ in 2017¹ has initiated a vast interest in the field of two-dimensional (2D) magnetic materials.²⁻⁴ From a technological point of view, 2D materials comprise a highly versatile platform for the design of electronics devices with properties tailored to a specific applications. For example, bilayers of CrI₃ exhibit anti-ferromagnetic interlayer spin alignment, which may be switched to a ferromagnetic configuration by electrostatic gating. Thus bilayers of CrI₃ may act as efficient spin valves that can be controlled by a gate voltage and comprises and promising starting point for 2D spintronics applications.⁵⁻⁸ From a fundamental point of view the origin of magnetic order in 2D is distinctly different from its three-dimensional counterpart where magnetism is typically understood in terms of a spontaneously broken symmetry phase. In contrast, the Mermin-Wagner theorem⁹ states that continuous symmetries cannot be broken *spontaneously* in 2D at finite temperatures and magnetic order thus crucially relies on magnetic anisotropy, which introduces an *explicitly* broken spin rotational symmetry. Since the discovery of magnetic order in monolayers of CrI₃, several materials have joined the family of 2D magnetic compounds; most notably Fe₃GeTe₂,¹⁰ which is metallic (in contrast to CrI₃), FePS₃,¹¹ which exhibits anti-ferromagnetic order, and bilayers of CrGeTe₃,¹² which becomes non-magnetic in the monolayer limit as a consequence of (weak) in-plane magnetic anisotropy. These materials are all characterized by a magnetic structure distinct from that of CrI₃ and have significantly expanded the range of possibilities for studying 2D magnetism. Considering the rapid evolution of synthesis techniques for 2D materials^{13,14} it is expected that several new mag-

netic 2D materials will emerge in the near future. A wide range new magnetic 2D materials have already been predicted from first principles calculations^{15,16} and it remains to be seen whether any of these can be synthesized or exfoliated from bulk materials. However, such calculations only provide information about the magnetic ground state and additional modelling is required in order to predict whether or not magnetic order persist at finite temperatures^{17,18}. In particular, a general framework for obtaining critical temperatures for magnetic order in 2D comprises a major challenge.

The theory of 2D magnetism is still in its infancy and standard approaches that work reasonably well in 3D is bound to fail in 2D. For magnetic insulators the thermodynamic properties is expected to be described accurately by Heisenberg models.¹⁹ While such models are notoriously hard to solve, the thermodynamic properties at high temperatures are dominated by thermal fluctuations and quantum effects can be safely neglected such that a classical analysis suffices for obtaining critical temperatures¹⁸ and exponents. This approach can be applied to real materials if the model parameters are obtained by an energy mapping between total energies obtained from first principles calculations and the energies obtained from the model in certain spin configurations.²⁰⁻²⁵ Due to its simplicity this approach is always based on classical Heisenberg models, which works reasonably well for three-dimensional materials. However, in the case of 2D materials the anti-ferromagnetic configurations involved in the mapping are strongly correlated and are not necessarily well approximated by a classical configuration of the Heisenberg model.¹⁹ In this paper, we show that density functional theory (DFT) applied to 2D magnetic insulators predict renormalized local magnetic moments that are in agreement with correlated eigenstates of the Heisenberg Hamiltonian and thus

differ significantly from the classical prediction. This has two major implications: 1) It justifies the use of Heisenberg models for an accurate description of magnetic properties of insulators. 2) It shows that a proper energy mapping analysis should be based on the quantum states of the Heisenberg model. We will show that the latter point introduces a significant correction to the Heisenberg parameters compared with a classical analysis and this has crucial influence on the prediction thermodynamic properties such as the critical temperature for magnetic order.

II. THEORY

A. Spin of the anti-ferromagnetic state

We will consider the Heisenberg model with nearest neighbor interactions given by

$$H = -\frac{J}{2} \sum_{\langle ij \rangle} \mathbf{S}_i \cdot \mathbf{S}_j, \quad (1)$$

where the sum is over nearest neighbor (magnetic) atoms and J is the exchange constant. For a bipartite lattice there is a unique anti-ferromagnetic state where all sites are anti-aligned with neighboring sites. If $J < 0$ this comprises the classical ground state (the Neel state) and for simplicity we will assume the spins to be aligned along the z -direction in this state. However, this is not an eigenstate of the quantum model and standard spinwave analysis shows that there is a state with lower energy referred to as the non-interacting magnon (NIM) state,¹⁹ which we will regard as an approximate eigenstate of the Heisenberg Hamiltonian in the following. The NIM state has the same spin symmetry as the Neel state, but it is not an eigenstate of S_z^z . Instead the expectation value is given by

$$\langle S_z \rangle_{NIM} = S(1 - \alpha/S), \quad (2)$$

where the constant S is the largest eigenvalue of S_z and α is given by

$$\alpha = \frac{1}{2} \left[\left\langle \frac{1}{\sqrt{1 - |\gamma_{\mathbf{q}}|^2}} \right\rangle_{BZ} - 1 \right] \quad (3)$$

where

$$\gamma_{\mathbf{q}} = \frac{1}{N_{nn}} \sum_{\Delta} e^{-i\mathbf{q} \cdot \mathbf{R}_{\Delta}}. \quad (4)$$

Here $\langle \dots \rangle_{BZ}$ denotes a Brillouin zone average over \mathbf{q} and \mathbf{R}_{Δ} are the N_{nn} lattice vectors connecting nearest neighbor sites. The constant α is larger for low-dimensional models and thus becomes more important for 2D materials than for 3D materials. In the case of the honeycomb and square lattices the value of α can be evaluated numerically yielding 0.258 and 0.197 respectively.

Although the NIM state is obviously useful to describe properties of anti-ferromagnets ($J < 0$), the derivation does not require that J is negative. In particular, for a ferromagnetic Heisenberg model ($J > 0$) the NIM state can be regarded as the approximate eigenstate of highest energy. In exact DFT, it is expected such a state should be represented by a configuration where the spins share the symmetry of the Neel state. Since the associated spin densities are accurately described in DFT, the ratio m_{AFM}/m_{FM} should yield $(1 - \alpha/S)$ provided that the magnetic moments are strongly localized. However, it is far from obvious that standard approximations for the exchange-correlation functional will capture the intricate correlations in the anti-ferromagnetic state. In Sec. III we will provide evidence that a proper renormalization of the spin is captured in the Perdew-Burke-Ernzerhof (PBE)²⁶ approximation.

B. Evaluating exchange constants

For an N -site periodic bipartite lattice, the expectation value of the Hamiltonian (1) using the Neel state is $NJS^2N_{nn}/2$ where N_{nn} is the number of nearest neighbors. For an anti-ferromagnetic lattice ($J < 0$) this comprises the classical ground state and for a ferromagnetic lattice ($J > 0$) it is the classical state of highest energy. However, the NIM state has a lower (higher) energy for anti-ferromagnetic (ferromagnetic) models of the form (1). It is given by

$$E^{NIM} = \frac{N}{2} (N_{nn} S^2 J) \left[1 + \beta/S \right], \quad (5)$$

where

$$\beta = 1 - \left\langle \sqrt{1 - |\gamma_{\mathbf{q}}|^2} \right\rangle_{BZ}. \quad (6)$$

For the honeycomb and square lattices the value of β are given by 0.202 and 0.158 respectively.

Exchange coupling constants are routinely evaluated from DFT using ferromagnetic and anti-ferromagnetic spin configurations in the simulations.²⁰⁻²⁵ But it is usually assumed that such configurations can be mapped to the ferromagnetic state ($E^{FM} = -NJS^2N_{nn}/2$) as well as the Neel state ($E^{Neel} = NJS^2N_{nn}/2$), which always leads to an overestimation of J . In exact DFT, the total energy of a given spin configuration should be mapped to the eigenstate of the Heisenberg model of the same spin symmetry. In particular, anti-ferromagnetic configurations has to be mapped to the NIM state, which provides a much better description of the anti-ferromagnetic state than the Neel state. For bipartite lattices this yields the expression

$$J = \frac{\Delta E}{N_{nn} S^2 (1 + \beta/2S)}, \quad (7)$$

where $\Delta E = E^{NIM} - E^{FM}$ is the energy difference per magnetic atom obtained from DFT. Again, we remark

that the value of β is in general smaller in 3D systems due to the 3D BZ average and it is often a better approximation to neglect the correction when evaluating exchange constants in 3D. However, as we will see below the inclusion of correlation effects in the energy mapping analysis can lead to significant corrections to the predictions of exchange constants and critical temperatures in 2D.

C. Curie temperatures in 2D

The model (1) does not allow for magnetic order in 2D due to the Mermin-Wagner theorem⁹ and one needs to consider models with terms that explicitly break the spin-rotational symmetry. Such terms originate from spin-orbit coupling and here we will assume that the most important effect on the magnetic order comes from single-ion anisotropy and nearest neighbor anisotropic exchange. The Hamiltonian then takes the form

$$H = -\frac{J}{2} \sum_{\langle ij \rangle} \mathbf{S}_i \cdot \mathbf{S}_j - \frac{\lambda}{2} \sum_{\langle ij \rangle} S_i^z S_j^z - A \sum_i (S_i^z)^2, \quad (8)$$

where we have assumed isotropy in the xy -plane, which we take to comprise the atomic plane of the material. From hereon we assume that $J > 0$ and that the easy-axis is along the z -direction. A simple spin-wave analysis then shows that the magnetic excitation spectrum has a gap given by

$$\Delta = A(2S - 1) + \lambda S N_{nn}. \quad (9)$$

A finite gap in the spectrum implies a broken spin-rotational symmetry and the model is expected to exhibit magnetic order at finite temperatures. It should be noted that combinations of A and λ that lead to $\Delta < 0$ implies an instability, which originates from the fact that the z -axis is not an easy-axis and the spinwave analysis has not been carried out on the magnetic ground state. The anisotropy constants λ and A can be evaluated from DFT including spin-orbit coupling by considering energy differences between in-plane and out-of-plane spin configurations.¹⁶

The Curie temperature of the model (8) may be obtained by either classical Monte Carlo simulations¹⁸ or a renormalized spin-wave analysis.^{12,17,18} We have previously shown that renormalized spin-wave theory breaks down in the case of large single-ion anisotropy and in the present work we will evaluate Curie temperatures from classical Monte Carlo simulations. It may seem odd to rely on a classical analysis since we have argued that it is crucial to include quantum corrections when mapping DFT calculations to Heisenberg models. However, at temperatures in the vicinity of the critical temperature quantum fluctuations tend to be quenched by thermal fluctuations and a classical analysis becomes reliable even if they cannot be trusted at low temperatures. However, the spin-1/2 systems may comprise an important

exception to this, since the single-ion anisotropy term becomes proportional to the identity in that case. It follows that magnetic order cannot exist at finite temperatures in spin-1/2 systems unless $\lambda \neq 0$, which is in stark contrast to the predictions of classical Monte Carlo simulations where the value of S simply introduces a rescaling of the Heisenberg parameters. For $S \neq 1/2$, Monte Carlo simulations of the model (8) can be accurately fitted to a function of the form¹⁸

$$T_C = \frac{S^2 J T_C^{\text{Ising}}}{k_B} f\left(\frac{\Delta}{J(2S-1)}\right) \quad (10)$$

where

$$f(x) = \tanh^{1/4} \left[\frac{6}{N_{nn}} \log(1 + \gamma x) \right] \quad (11)$$

and $\gamma = 0.033$. T_C^{Ising} is the critical temperature of the corresponding Ising model (in units of JS^2/k_B), which are given by 1.52, 2.27, and 3.64 for honeycomb, square and hexagonal lattices respectively.

III. RESULTS

In order to assess the performance of semi-local functionals for the correlated anti-ferromagnetic configuration of real materials, we have calculated the absolute magnetization density

$$m_{Abs} = \int |m_{\uparrow}(\mathbf{r}) - m_{\downarrow}(\mathbf{r})| d\mathbf{r} \quad (12)$$

for a wide variety of 2D materials in both the ferromagnetic and anti-ferromagnetic state. We have included all

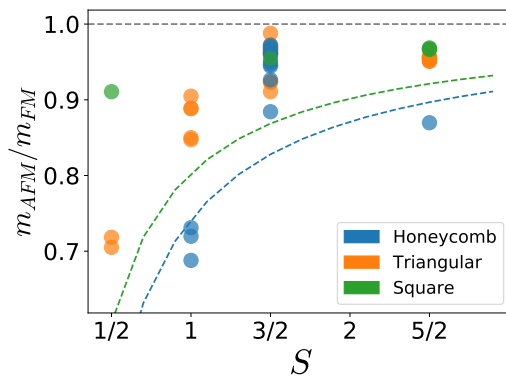


FIG. 1. Ratio of average magnetic moments in ferromagnetic configurations for 51 insulating magnetic materials in C2DB. The dashed lines show the results obtained from a spin-wave analysis of the Heisenberg model with square and honeycomb lattices.

insulating magnetic materials present in the Computational 2D Materials Database²⁷ (C2DB) where the magnetic atoms form either a honeycomb, square or triangular lattice. In this context, we define an insulator by a threshold of 0.2 eV for the band gap in both FM and AFM configurations to ensure that the basic electronic structure is not altered too much between the different spin configurations. The computational details can be found in Ref. 27, but here we just mention that all calculations were carried out with the electronic structure code GPAW^{28–30} using the PBE approximation²⁶ for the exchange-correlation energy. Since the triangular lattice is not bipartite the classical state of lowest/highest energy is not collinear, but comprises a 120° non-collinear structure.³¹ However, as the far majority of DFT calculations in the literature (including energy mapping studies) are based on collinear structures we choose to base the energy mapping analysis of triangular lattices on a "striped" anti-ferromagnetic configuration where each site has two aligned and four anti-aligned nearest neighbors.¹⁶ Since this state does not comprise an extremum in the classical energy landscape it is not possible to perform a spinwave analysis to obtain the quantum corrections to the spin, but due to the four anti-aligned nearest neighbors the correction is expected to be similar to the square lattice.

In Fig. 1 we display the ratio m_{AFM}/m_{FM} per magnetic atom along with the theoretical predictions given by Eq. (2). Although the calculations exhibit clear deviations from the Heisenberg prediction, there is a significant trend towards increasing quantum corrections with decreasing spin. It may be argued that a reduction of magnetic moments is expected in the anti-ferromagnetic state due to incomplete localization of the magnetic moments, which introduces cancellation of magnetization densities in the interstitial regions. However, such cancellation effects are expected to yield a ratio m_{AFM}/m_{FM} , which is *independent* of spin when averaged over a large class of materials. In contrast, Fig. 1 shows a clear tendency towards decreasing staggered magnetization with decreasing spin, which is in accordance with the correlated state predicted by the Heisenberg model.

The reduction of the ratio m_{AFM}/m_{FM} with decreasing spin provides some confidence that DFT is able to capture (at least partly) the intricate correlations of the anti-ferromagnetic state at the level of generalized gradient calculations. This implies that exchange parameters calculated from energy mapping to the Heisenberg model should be corrected according to Eq. (7). This in turn may have a strong influence on the calculation of critical temperatures from the expression (10). In Fig. III we show the quantum corrections to the exchange coupling parameters as well as the corrected critical temperatures relative to the classical estimates for all ferromagnetic insulators in the C2DB with $\Delta > 0$. In the case of exchange parameters the reduction only depends on the value of S , whereas the corrected critical temperatures also depend

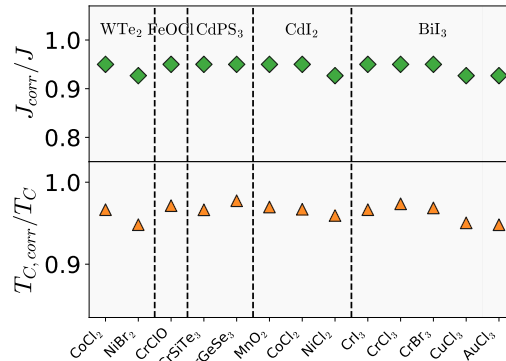


FIG. 2. Corrections to exchange parameters (top panel) and Curie temperatures (lower panel) obtained with PBE for all insulating ferromagnets with positive values of Δ present in the C2DB.

| Formula | Prototype | J_{corr} [meV] | Δ [meV] | S [$\hbar/2$] | $T_{C,corr}$ [K] |
|---------------------|-------------------|------------------|----------------|-------------------|------------------|
| AuCl ₃ | BiI ₃ | 9.99 | 1.39 | 1 | 58 |
| NiBr ₂ | WTe ₂ | 6.76 | 0.263 | 1 | 57 |
| CuCl ₃ | BiI ₃ | 14.14 | 0.058 | 1 | 35 |
| CrSiTe ₃ | CdPS ₃ | 3.4 | 0.304 | 3/2 | 35 |
| CoCl ₂ | WTe ₂ | 1.87 | 0.098 | 3/2 | 34 |
| CrI ₃ | BiI ₃ | 2.2 | 0.961 | 3/2 | 34 |
| CoCl ₂ | CdI ₂ | 1.89 | 0.058 | 3/2 | 30 |
| CrBr ₃ | BiI ₃ | 1.88 | 0.232 | 3/2 | 22 |
| MnO ₂ | CdI ₂ | 0.52 | 0.305 | 3/2 | 19 |
| CrClO | FeOCl | 1.0 | 0.069 | 3/2 | 16 |
| NiCl ₂ | CdI ₂ | 6.65 | 0.001 | 1 | 14 |
| CrCl ₃ | BiI ₃ | 1.33 | 0.033 | 3/2 | 12 |
| CrGeSe ₃ | CdPS ₃ | 0.91 | 0.018 | 3/2 | 9 |

TABLE I. List of 2D magnetic insulating materials with positive exchange coupling J and positive spinwave gap Δ for PBE calculations.

on the spinwave gap Δ . However, if $\Delta/J \ll 1$ the change in critical temperature becomes $\delta T_C/T_C = 3\delta J/4J$ and the change in critical temperature thus largely follows the exchange parameter. In general the reduction in critical temperatures is on the order of 5%. The absolute values of (non-corrected) critical temperatures have been published elsewhere and the predicted ferromagnetic materials have been discussed in detail with respect to stability and experimental results for bulk compounds.¹⁶ For completeness we report the list of materials again in Tab. I, but now including the quantum corrections to the critical temperature.

Although we have argued that PBE (partly) captures quantum nature of anti-ferromagnetic configurations, a

5

correct prediction of ground state energies for magnetic insulators pose a major challenge for DFT, since these materials typically involve strongly correlated electrons. This implies a large uncertainty in the prediction of exchange constants and critical temperatures. To quantify this we have repeated the calculations using PBE+U where we have adopted the values of the Hubbard corrections (U) used in Ref. 32. The corrections to J and T_C are summarized in Fig. 3 and Tab. II shows a detailed list of materials obtained with the Hubbard correction. The overall trend in the corrections shown in Fig. 3 is very similar to Fig. 2 However the list of ferromagnetic candidates in Tab. II is very different from Tab. I. Several of the materials in Tab. II is lacking from Tab. I and of the materials present in Tab. II were absent from Tab. I. Part of the reason is that we only include ferromagnetic insulators and the inclusion of the Hubbard correction may open a gap in a material that is predicted to be metallic without the Hubbard correction. In addition, the Hubbard correction may change the sign of the spin-wave gap when U is included in the calculations. In Tab. II we have highlighted all the materials present in both cases with bold face. We note that the value of $T_C = 50$ K for CrI_3 obtained with PBE+U is in close proximity to the experimental value of 45 K and seems to provide a much better prediction than bare PBE. This could, however, be a matter of luck and the value depends rather strongly on the choice of functional.³³ In particular, the results of an LDA+U calculation gives a reduction of J by 20 % and there is no *a priori* reason to believe that PBE should be better than LDA for the calculation of exchange constants. Nevertheless, the inclusion of Hubbard corrections typically provides a better description of the electronic structure in correlated materials and it is likely that Tab. II comprises a more reliable set of predictions than Tab. I.

IV. DISCUSSION

We have shown that DFT predicts a renormalization of localized magnetic moments in anti-ferromagnetic configurations of 2D insulators. The renormalization is in accordance with the predictions of the Heisenberg model and implies that energies of stationary states with anti-ferromagnetic spin alignment should be mapped to the corresponding correlated anti-ferromagnetic state of the Heisenberg model. This leads to a reduction in the predicted values of exchange parameters which in turn leads to a reduction of predicted Curie temperatures compared to an analysis based on classical Heisenberg models.

It is interesting to compare the present approach to the method of infinitesimal rotations of local spin variables derived by Liechtenstein et al.^{34,35} In that approach the magnetic force theorem is utilized to extract the exchange parameters from the ground state without any reference to different magnetic configurations. The methodology has the great advantage that all exchange parameters

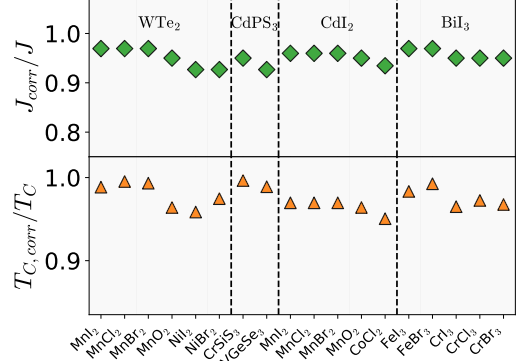


FIG. 3. Corrections to exchange parameters (top panel) and Curie temperatures (lower panel) obtained with PBE+U for all insulating ferromagnets with positive values of Δ present in the C2DB.

| Formula | Prototype | J_{corr} [meV] | Δ [meV] | S [$\hbar/2$] | $T_{C,\text{corr}}$ [K] |
|-----------------------------------|-----------------|-------------------------|----------------|-------------------|-------------------------|
| MnO_2 | WTe_2 | 6.18 | 0.123 | 3/2 | 83 |
| MnO_2 | CdI_2 | 6.11 | 0.125 | 3/2 | 82 |
| CoCl_2 | CdI_2 | 3.0 | 0.249 | 3/2 | 54 |
| CrI_3 | BiI_3 | 3.75 | 1.28 | 3/2 | 50 |
| CrBr_3 | BiI_3 | 2.68 | 0.185 | 3/2 | 27 |
| MnI_2 | CdI_2 | 0.38 | 0.081 | 5/2 | 20 |
| MnBr_2 | CdI_2 | 0.39 | 0.024 | 5/2 | 15 |
| NiI_2 | WTe_2 | 1.3 | 0.068 | 1 | 15 |
| CrCl_3 | BiI_3 | 2.07 | 0.016 | 3/2 | 14 |
| FeI_3 | BiI_3 | 0.21 | 0.456 | 5/2 | 14 |
| MnCl_2 | CdI_2 | 0.43 | 0.006 | 5/2 | 11 |
| MnI_2 | WTe_2 | 0.05 | 0.044 | 5/2 | 7 |
| NiBr_2 | WTe_2 | 1.07 | 0.001 | 1 | 7 |
| FeBr_3 | BiI_3 | 0.03 | 0.124 | 5/2 | 5 |
| MnBr_2 | WTe_2 | 0.03 | 0.006 | 5/2 | 5 |
| MnCl_2 | WTe_2 | 0.02 | 0.004 | 5/2 | 5 |
| VGeSe_3 | CdPS_3 | 0.13 | 0.051 | 1 | 4 |
| CrSiS_3 | CdPS_3 | 0.03 | 0.007 | 3/2 | 4 |

TABLE II. List of 2D magnetic insulating materials with positive exchange coupling J and positive spinwave gap Δ for PBE+U calculations.

can be extracted without relying on magnetic configurations that may or may not comprise stationary states in DFT. Moreover, it can be argued that the inclusion of different magnetic configurations (as in the present work) introduces changes in the electronic structure (and associated changes in the energy) that may not be related to magnetic interactions whereas the Liechtenstein approach does not suffer from this problem. However, the

method explicitly relies on the classical Heisenberg model and cannot include quantum effects at the level of magnetic interactions. In contrast, the stationary states of a given spin symmetry can naturally be regarded as eigenstates of the Heisenberg model and allows for a direct mapping to the quantum mechanical Heisenberg model. Nevertheless, for metallic systems, there is typically a significant change in the electronic structure between different magnetic configurations and the Liechtenstein approach seems to be the only viable approach in those cases.

For 2D ferromagnetic insulators the inclusion of quantum effects leads to corrections of the order of 5-10%. We emphasize, however, that the errors originating from inaccuracies in DFT are likely to be somewhat larger than this. Nevertheless, the assumption of any first principles framework for evaluating magnetic interactions must be that the calculations are reliable and in that case any energy mapping approach must be based on the quantum mechanical Heisenberg model. Moreover, the corrections are easily expressed in an analytical form and can be

included without any additional work. For more complicated lattices and exchange parameters beyond the nearest neighbor approximation the expression for the quantum corrections must be generalized, but this is straightforward to do for any given lattice. It should also be noted that this approach is not limited to 2D materials, but the corrections are in general larger compared to 3D materials.

The energy mapping scheme to obtain first principles Heisenberg models seems to provide and accurate and general framework for obtaining critical temperatures in ferromagnetic 2D insulators provided that DFT can provide the correct energies of different spin configurations. It is, however, not obvious that DFT can do that with present day functionals and there is a strong need for a systematic assessment of functionals for such calculations. Perhaps a more important point is the fact that no framework yet exist for evaluating critical temperatures in 2D metallic magnets. One possibility could be a generalization of the spin fluctuation theory developed by Moriya and Takahashi^{36,37} to 2D systems with magnetic anisotropy, but this is left to future work.

-
- ¹ B. Huang, G. Clark, E. Navarro-Moratalla, D. R. Klein, R. Cheng, K. L. Seyler, D. Zhong, E. Schmidgall, M. A. McGuire, D. H. Cobden, W. Yao, D. Xiao, P. Jarillo-Herrero, and X. Xu, *Nature* **546**, 270 (2017).
- ² C. Gong and X. Zhang, *Science* **363**, eaav4450 (2019).
- ³ M. Gibertini, M. Koperski, A. F. Morpurgo, and K. S. Novoselov, *Nat. Nanotechnol.* **14**, 408 (2019).
- ⁴ N. Sethulakshmi, A. Mishra, P. M. Ajayan, Y. Kawazoe, A. K. Roy, A. K. Singh, and C. S. Tiwary, *Mater. Today* **27**, 107 (2019).
- ⁵ T. Song, M. W.-Y. Tu, C. Carnahan, X. Cai, T. Taniguchi, K. Watanabe, M. A. McGuire, D. H. Cobden, D. Xiao, W. Yao, and X. Xu, *Nano Letters* **19**, 915 (2019).
- ⁶ E. Suárez Morell, A. León, R. H. Miwa, and P. Vargas, *2D Mater.* **6**, 025020 (2019).
- ⁷ S. Jiang, L. Li, Z. Wang, K. F. Mak, and J. Shan, *Nat. Nanotechnol.* **13**, 549 (2018), arXiv:1802.07355.
- ⁸ Z. Wang, T. Zhang, M. Ding, B. Dong, Y. Li, M. Chen, X. Li, J. Huang, H. Wang, X. Zhao, Y. Li, D. Li, C. Jia, L. Sun, H. Guo, Y. Ye, D. Sun, Y. Chen, T. Yang, J. Zhang, S. Ono, Z. Han, and Z. Zhang, *Nat. Nanotechnol.* **13**, 554 (2018).
- ⁹ N. D. Mermin and H. Wagner, *Phys. Rev. Lett.* **17**, 1133 (1966).
- ¹⁰ Z. Fei, B. Huang, P. Malinowski, W. Wang, T. Song, J. Sanchez, W. Yao, D. Xiao, X. Zhu, A. F. May, W. Wu, D. H. Cobden, J.-H. Chu, and X. Xu, *Nat. Mater.* **17**, 778 (2018).
- ¹¹ J.-U. Lee, S. Lee, J. H. Ryoo, S. Kang, T. Y. Kim, P. Kim, C.-H. Park, J.-G. Park, and H. Cheong, *Nano Lett.* **16**, 7433 (2016).
- ¹² C. Gong, L. Li, Z. Li, H. Ji, A. Stern, Y. Xia, T. Cao, W. Bao, C. Wang, Y. Wang, Z. Q. Qiu, R. J. Cava, S. G. Louie, J. Xia, and X. Zhang, *Nature* **546**, 265 (2017).
- ¹³ J. Zhou, J. Lin, X. Huang, Y. Zhou, Y. Chen, J. Xia, H. Wang, Y. Xie, H. Yu, J. Lei, D. Wu, F. Liu, Q. Fu, Q. Zeng, C. H. Hsu, C. Yang, L. Lu, T. Yu, Z. Shen, H. Lin, B. I. Yakobson, Q. Liu, K. Suenaga, G. Liu, and Z. Liu, *Nature* **556**, 355 (2018).
- ¹⁴ A. Shivayogimath, J. D. Thomsen, D. M. Mackenzie, M. Geisler, R. M. Stan, A. J. Holt, M. Bianchi, A. Crovetto, P. R. Whelan, A. Carvalho, A. H. Neto, P. Hofmann, N. Stenger, P. Bøggild, and T. J. Booth, *Nat. Commun.* **10**, 1 (2019), 1805.08002.
- ¹⁵ N. Mounet, M. Gibertini, P. Schwaller, D. Campi, A. Merkys, A. Marrazzo, T. Sohier, I. E. Castelli, A. Cepellotti, G. Pizzi, and N. Marzari, *Nature Nanotechnology* **13**, 246 (2018).
- ¹⁶ D. Torelli, K. S. Thygesen, and T. Olsen, *2D Mater.* **6**, 045018 (2019).
- ¹⁷ J. L. Lado and J. Fernández-Rossier, *2D Mater.* **4**, 035002 (2017).
- ¹⁸ D. Torelli and T. Olsen, *2D Mater.* **6**, 015028 (2018).
- ¹⁹ K. Yosida, *Theory of magnetism* (Springer Berlin, Heidelberg, 1996).
- ²⁰ H. Xiang, C. Lee, H.-J. Koo, X. Gong, and M.-H. Whangbo, *Dalton Trans.* **42**, 823 (2013).
- ²¹ A. Jacobsson, C. Etz, M. Ležaić, B. Sanyal, and S. Blügel, arXiv:1702.00599, 1 (2017).
- ²² D. Ködderitzsch, W. Hergert, W. M. Temmerman, Z. Szotek, A. Ernst, and H. Winter, *Physical Review B* **66** (2002), 10.1103/physrevb.66.064434.
- ²³ M. Pajda, J. Kudrnovský, I. Turek, V. Drchal, and P. Bruno, *Physical Review B* **64** (2001), 10.1103/physrevb.64.174402.
- ²⁴ T. Olsen, *Physical Review B* **96** (2017), 10.1103/physrevb.96.125143.
- ²⁵ S. K. Bose and J. Kudrnovský, *Physical Review B* **81** (2010), 10.1103/physrevb.81.054446.
- ²⁶ J. P. Perdew, K. Burke, and M. Ernzerhof, *Phys. Rev.*

- Lett. **77**, 3865 (1996).
- ²⁷ S. Haastrup, M. Strange, M. Pandey, T. Deilmann, P. S. Schmidt, N. F. Hinsche, M. N. Gjerding, D. Torelli, P. M. Larsen, A. C. Riis-Jensen, J. Gath, K. W. Jacobsen, J. Jørgen Mortensen, T. Olsen, and K. S. Thygesen, *2D Mater.* **5**, 042002 (2018).
- ²⁸ J. Enkovaara, C. Rostgaard, J. J. Mortensen, J. Chen, M. Dulak, L. Ferrighi, J. Gavnholt, C. Glinsvad, V. Haikola, H. a. Hansen, H. H. Kristoffersen, M. Kuisma, a. H. Larsen, L. Lehtovaara, M. Ljungberg, O. Lopez-Acevedo, P. G. Moses, J. Ojanen, T. Olsen, V. Petzold, N. a. Romero, J. Stausholm-Møller, M. Strange, G. a. Tritsarlis, M. Vanin, M. Walter, B. Hammer, H. Häkkinen, G. K. H. Madsen, R. M. Nieminen, J. K. Nørskov, M. Puska, T. T. Rantala, J. Schiøtz, K. S. Thygesen, and K. W. Jacobsen, *J. Phys. Condens. Matter* **22**, 253202 (2010).
- ²⁹ A. Hjorth Larsen, J. Jørgen Mortensen, J. Blomqvist, I. E. Castelli, R. Christensen, M. Dulak, J. Friis, M. N. Groves, B. Hammer, C. Hargus, E. D. Hermes, P. C. Jennings, P. Bjerre Jensen, J. Kermode, J. R. Kitchin, E. Leonhard Kolsbjerg, J. Kubal, K. Kaasbjerg, S. Lysgaard, J. Bergmann Maronsson, T. Maxson, T. Olsen, L. Pastewka, A. Peterson, C. Rostgaard, J. Schiøtz, O. Schütt, M. Strange, K. S. Thygesen, T. Vegge, L. Vilhelmsen, M. Walter, Z. Zeng, and K. W. Jacobsen, *J. Phys. Condens. Matter* **29**, 273002 (2017).
- ³⁰ T. Olsen, *Phys. Rev. B* **94**, 235106 (2016).
- ³¹ P. Maksimov, Z. Zhu, S. R. White, and A. Chernyshev, *Physical Review X* **9** (2019), 10.1103/physrevx.9.021017.
- ³² L. Wang, T. Maxisch, and G. Ceder, *Phys. Rev. B* **73**, 195107 (2006).
- ³³ T. Olsen, *MRS Communications*, 10.1557/mrc.2019.117 , 1 (2019).
- ³⁴ A. Liechtenstein, M. Katsnelson, V. Antropov, and V. Gubanov, *Journal of Magnetism and Magnetic Materials* **67**, 65 (1987).
- ³⁵ A. Liechtenstein, M. Katsnelson, and V. Gubanov, *Solid State Communications* **54**, 327 (1985).
- ³⁶ T. Moriya and Y. Takahashi, *Journal of the Physical Society of Japan* **45**, 397 (1978).
- ³⁷ T. Moriya, *Journal of Magnetism and Magnetic Materials* **100**, 261 (1991).

7.6 Paper VI: High throughput computational screening for two-dimensional magnetic materials based on experimental databases of three-dimensional compounds

The publication is in preparation.

High throughput computational screening for two-dimensional magnetic materials based on experimental databases of three-dimensional compounds

Daniele Torelli¹ and Thomas Olsen¹

¹*Computational Atomic-scale Materials Design (CAMD), Department of Physics, Technical University of Denmark, DK-2800 Kgs. Lyngby, Denmark*
(Dated: December 31, 2019)

We perform a computational screening for two-dimensional magnetic materials based on experimental bulk compounds present in the Inorganic Crystal Structure Database and Crystallographic Open Database. A recently proposed geometric descriptor is used to extract materials that are exfoliable into two-dimensional derivatives for which we obtain magnetic exchange and anisotropy parameters using density functional theory. For the ferromagnetic insulators we then calculate the Curie temperature from an approximate expression fitted to classical Monte Carlo simulations of anisotropic Heisenberg models and find XXX two-dimensional ferromagnets that have not been reported previously.

I. INTRODUCTION

The discovery of two-dimensional ferromagnets (2D) in 2017^{1,2} has initiated a vast interest in the field of magnetism in 2D. The origin of magnetic order in 2D is fundamentally different from the spontaneously broken continuous symmetry that is responsible for magnetism in three-dimensional materials. In particular, the Mermin-Wagner theorem states that a continuous symmetry cannot be broken at finite temperatures in 2D and magnetic anisotropy is therefore becomes a crucial ingredient for magnetic order in 2D. The first report on 2D ferromagnetism involved on a monolayer of CrI₃,¹ which has a strong easy-axis orthogonal to the plane and has a Curie temperature of 45 K. At the same time multiple layers of CrGeTe₃ was reported to exhibit ferromagnetic order down to the bilayer limit, but not in the case of monolayers due to the presence of an easy-plane, which comprises a continuous symmetry that cannot be broken spontaneously. Since then several materials have joined the family of 2D magnets. Most notably, CrBr₃,³ which have properties very similar to CrI₃ but with lower Curie temperatures of 34 K due to smaller magnetic anisotropy, Fe₃GeTe₂, which is metallic and has a Curie temperature of 130 K⁴, FePS₃,⁵ which is anti-ferromagnetic with an ordering temperature of 118 K, and VSe₂ where some evidence have been provided for ferromagnetic order at room temperature⁶ although the presence of magnetism is being debated⁷. In addition, several studies of magnetism in bilayers of various 2D materials have demonstrated that interlayer magnetic coupling can give rise to a plethora of new physical properties.⁸⁻¹⁶

Although the handful of known magnetic 2D materials exhibit a wide variety of interesting physics that are still being intensively explored, there is a dire need for discovering new materials with better stability at ambient conditions and higher critical temperatures for magnetic order. Such conditions are not only crucial for technological applications of 2D magnets, but could also serve as a boost the experimental progress in the field. In addition, the theoretical efforts in the field are largely limited

by the few materials that are available for comparison of measurements and calculations. An important step towards discovery of novel 2D materials were taken by Mounet et al.¹⁷ where Density Functional Theory (DFT) was applied to search for potentially exfoliable 2D materials in the Inorganic Crystal Structure Database (ICSD) and Crystallographic Open Database (COD). More 1000 potential 2D materials were identified and 56 of these were predicted to have a magnetically ordered ground state. Another approach towards 2D materials discovery were based on Computational 2D Materials Database (C2DB)¹⁸⁻²⁰ where more than 3700 2D materials have been computationally scrutinized based on lattice decoration of existing prototypes of 2D materials. Of these there are 152 ferromagnets and 50 anti-ferromagnets that are predicted to be stable by DFT. In addition to these high throughput screening studies there are several reports on particular 2D materials that are predicted to exhibit magnetic order in the ground state by DFT,²¹⁻²⁶ as well as a compilation of known van der Waals bonded magnetic materials that might serve as a good starting point for discovering new 2D magnets.²⁷

Due to the Mermin-Wagner theorem a magnetically ordered ground state does not necessarily imply magnetic order at finite temperatures and the 2D magnets discovered by high throughput screening studies mentioned above may not represent materials with observable magnetic properties. In three-dimensional bulk compounds the critical temperature for magnetic order is set by the magnetic exchange coupling between magnetic moments in the compound and a rough estimate of critical temperature can be obtained from mean field theory.²⁸ In 2D materials, however, this is no longer true since magnetic order cannot exist with magnetic anisotropy and mean field theory is always bound to fail. The critical temperature thus has to be evaluated from either classical Monte Carlo simulations or renormalized spin-wave theory of an anisotropic Heisenberg model derived from first principles^{2,29-31}. The former approach neglects quantum effects whereas the latter approximates interaction-mediated correlation effects at the mean field

level. Monte Carlo simulations are not well suited to high-throughput studies, but it has recently been shown that Monte Carlo simulations can be fitted to an analytical expression that is easily evaluated for a given material once the exchange and anisotropy parameters have been computed. This approach has been applied to the C2DB resulting in the discovery of 12 new 2D ferromagnetic insulators that are predicted to be stable.³² However, it is far from obvious that these materials can be synthesised in the lab even if DFT predicts them to be stable since they are not derived from experimentally known van der Waals bonded bulk compounds.

In the present work we have performed a full computational screening for magnetic 2D materials based on experimentally known van der Waals bonded materials present in the ICSD and COD. In contrast to previous high throughput screening of these databases we evaluate exchange and magnetic anisotropy constants for all materials with a magnetic ground state and use these to predict the Curie temperature from an expression fitted to Monte Carlo simulation of the anisotropic Heisenberg model. We find XXX Lattice decoration XXX

II. METHODOLOGY

The first step in the computational screening is to identify potentially exfoliable 2D structures from the bulk materials present in ICSD and COD. In Ref.¹⁷ this was accomplished by identifying layered chemically bonded sub-units and then calculate the exfoliation energy from DFT with van der Waals corrections. Here we instead use a recently proposed purely geometrical method that quantifies the amount of zero-dimensional (0D), one-dimensional (1D), two-dimensional and three-dimensional (3D) components present in a given material.³³ The method thus assigns a 0D, 1D, 2D, and 3D score to all materials and thus quantifies the 0D, 1D, 2D, and 3D character. The scores are defined such that they sum to unity and taking the 2D score > 0.5 thus provides a conservative measure of a material being (mostly) composed of 2D components that are likely to be exfoliable.

The magnetic properties of possible candidate 2D materials are then investigated using first principles Heisenberg models derived from DFT.^{2,29-31} In particular, if a 2D candidate material has a magnetic ground state we model the magnetic properties by the Hamiltonian

$$H = -\frac{J}{2} \sum_{\langle ij \rangle} \mathbf{S}_i \cdot \mathbf{S}_j - \frac{\lambda}{2} \sum_{\langle ij \rangle} S_i^z S_j^z - A \sum_i (S_i^z)^2, \quad (1)$$

where J is the nearest neighbor exchange coupling, λ is the nearest neighbor anisotropic exchange coupling, A is the single-ion anisotropy, and $\langle ij \rangle$ denotes sum over nearest neighbors. J may be positive(negative) signifying a ferromagnetic(anti-ferromagnetic) ground state and we have assumed that the z -direction is orthogonal

to the atomic plane and that there is in-plane magnetic isotropy. This model obviously does not exhaust the possible magnetic interactions in a material, but has previously been shown to describe the magnetic properties of CrI₃ accurately.^{29,30} Most importantly, it is not expected to provide a good description of itinerant magnets (metals) and for insulators the next and third nearest neighbors may be sizable. However, it provides a good starting point for computational screening studies.

The thermal properties can be investigated from either renormalized spin-wave calculations^{28-30,34,35} or classical Monte Carlo simulations.^{30,36} Due to the Mermin-Wagner theorem the magnetic anisotropy constants are crucial for having magnetic order at finite temperatures. The amount of anisotropy can be quantified by the ferromagnetic spin-wave gap

$$\Delta = A(2S - 1) + N_{nn}S\lambda \quad (2)$$

where S is the maximum eigenvalue of S_i^z and N_{nn} is the number of nearest neighbors. The gap is calculated by assuming out-of-plane magnetic order and in the present context a (unphysical) negative spin-wave gap signals that the ground state favors in-plane alignment of spins, which cannot persist at finite temperatures in the model (1). A positive spin-wave gap is thus required for magnetic order in the materials under consideration.

In Ref. 30 it was shown that the critical temperature for ferromagnetic order ($J > 0$) of the model (1) with $S > 1/2$ can be fitted to the function

$$T_C = \frac{S^2 J T_C^{\text{Ising}}}{k_B} f\left(\frac{\Delta}{J(2S - 1)}\right) \quad (3)$$

where

$$f(x) = \tanh^{1/4} \left[\frac{6}{N_{nn}} \log(1 + \gamma x) \right] \quad (4)$$

and $\gamma = 0.033$. T_C^{Ising} is the critical temperature of the corresponding Ising model (in units of JS^2/k_B). The expression (3) is readily evaluated for any 2D material with a ferromagnetic ground state once the Heisenberg parameters J , λ and A have been determined. This can be accomplished with four DFT calculations including spin-orbit coupling.^{31,32,37} All DFT calculations were performed with the electronic structure package GPAW^{38,39} including non-selfconsistent spinorbit coupling⁴⁰ and the Perdew-Burke-Ernzerhof⁴¹ (PBE) functional.

III. RESULTS

A. Computational screening of COD and ICSD

The ICSD and COD databases combined count more than 500.000 materials, but removing corrupted or incomplete entries and duplicates, reduces the number to 167767 bulk materials.³³ Of these, a subset of 4264 are

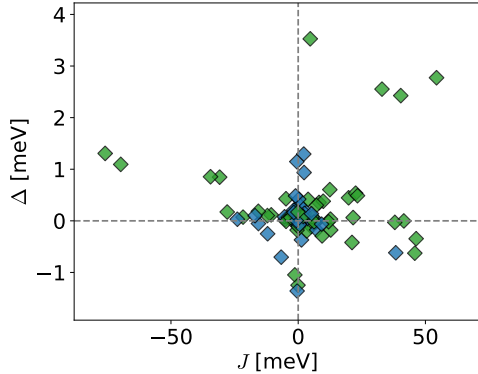


FIG. 1. Exchange coupling J and spinwave gap calculated for the magnetic 2D materials obtained from computational screening of ICSD and COD. Blue marks indicate insulators and green marks are metals.

predicted to have a 2D score higher than 0.5 and these materials are the starting point of the present study. We then perform a computational exfoliation using DFT by isolating the 2D component and performing a full relaxation of the resulting 2D material. We restrict ourselves to materials that has a 2D component with less than five different elements and less than a total of 20 atoms in the minimal unit cell. This reduces the number of candidate 2D materials to 651 compounds. We find 55 materials with a ferromagnetic ground state and 38 materials with an anti-ferromagnetic ground state. For all of these we calculate the exchange coupling J and the spinwave gap Δ according to the energy mapping approach.^{31,32,42} The results are shown in Fig. 1. The spinwave gap is on the order of 1 meV or less for all materials. The exchange couplings fall in the range of 0-10 meV for the insulators but can acquire somewhat larger values for the metals. However, the energy mapping analysis is somewhat ill-defined for metals, since the electronic structure may change significantly when comparing energy differences between ferromagnetic and anti-ferromagnetic configurations. In particular, for insulators the value of S is a well-defined integer that can be extracted from the ferromagnetic ground state without spin-orbit coupling. But for metals it is not clear what value to use in the model (1). In addition the model itself may not be suitable to describe the magnetic properties of metals.

For the ferromagnetic insulators we calculate the Curie temperature ($T_C > 10$) according to Eq. (3) and in Tab. I, we report these along with the values of J and Δ for materials that have $T_C > 10$ K. It is reassuring that the well-known Ising type 2D ferromagnets CrBr_3^3 and CrI_3^1 are reproduced by the screening. In addition, CrCl_3 , MnO_2 , CoCl_2 , and NiCl_2 have previously been predicted to be ferromagnetic 2D insulators from a com-

| Formula | J [meV] | Δ [meV] | S [\hbar] | T_C [K] |
|---------------------------|-----------|----------------|-----------------|-----------|
| CrHO_2 | 2.47 | 0.147 | 3/2 | 45 |
| NiRe_2O_8 | 2.18 | 1.294 | 1 | 38 |
| CrSiTe_3 | 3.60 | 0.307 | 1.5 | 37 |
| CrI_3 | 2.32 | 0.936 | 3/2 | 35 |
| CoCl_2 | 1.85 | 0.046 | 3/2 | 28 |
| CrBr_3 | 2.01 | 0.23 | 3/2 | 23 |
| MnO_2 | 0.54 | 0.305 | 3/2 | 19 |
| CrClO | 1.09 | 0.069 | 3/2 | 16 |
| CoCl_2O_8 | 0.26 | 0.419 | 3/2 | 13 |
| CrCl_3 | 1.38 | 0.032 | 3/2 | 13 |
| NiCl_2 | 7.15 | <0.001 | 2 | 11 |

TABLE I. List of 2D magnetic insulators with positive exchange coupling J and positive spinwave gap Δ that have a Curie temperature exceeding 10 K. The Curie temperature was calculated from Eq. (3).

putational screening study of the C2DB.^{18,32,42} Multilayered system CrSiTe_3 is reported to exhibit a large magnetic anisotropy in the direction perpendicular to the layers and a ferromagnetic phase transition has been observed at 33 K⁴³. Most importantly, however, the materials CrHO_2 , NiRe_2O_8 and CoCl_2O_8 are novel ferromagnetic insulators that have not been studied prior to the present work. They are predicted to exhibit ferromagnetic order below 45 K, 38 K, and 13 K respectively. We stress, however, that the results of a screening study like the present one should be taken as a preliminary prediction. The magnetic properties may be rather sensitive to the choice of functional^{31,32} and a detailed study of functional dependence or inclusion of Hubbard corrections is required in order to support the theoretical prediction of these 2D materials being ferromagnetic. In addition there may be challenges associated with the experimental exfoliation of these materials that are not taken into consideration here.

For metallic materials the prediction of thermodynamical properties is more challenging since it is not obvious that the Heisenberg Hamiltonian (1) comprises a good starting point for the analysis. Nevertheless, the exchange coupling J and spin-wave gap Δ still provides a rough measure of the magnetic interactions and magnetic anisotropy respectively. Alternatively, one could specify the energy difference per magnetic atom in ferromagnetic and anti-ferromagnetic configurations as well as the energy cost of rotating the magnetic moments from the out-of-plane direction to the atomic plane. However, for the sake of comparison we have chosen to report the values of J and Δ resulting from the energy mapping analysis although it comprises a rather naive approach for metals. In addition we evaluate the critical temperature that would characterize the model (3) using the calculated parameters. The results are shown in Tab. II. Again, we rediscover a few materials (FeTe and NiI_2) that were previously predicted to be ferromagnetic from computational screening of the C2DB. In addition, we find several materials with exchange couplings on the order of

| Formula | J [meV] | Δ [meV] | S [\hbar] | T_C [K] |
|----------------------------------|-----------|----------------|-----------------|-----------|
| FeTe | 40.31 | 2.426 | 1 | 252 |
| FeCl ₃ | 54.05 | 2.655 | 1/2 | 135 |
| Ca ₂ CoO ₃ | 4.73 | 3.527 | 3/2 | 107 |
| MgMnGe | 12.43 | 0.604 | 1 | 76 |
| RbTiS ₂ | 21.37 | 0.063 | 1/2 | 75 |
| NiI ₂ | 8.19 | 0.356 | 1 | 71 |
| CrGa ₂ S ₄ | 1.97 | 0.086 | 2 | 53 |

TABLE II. List of 2D magnetic metals with positive exchange coupling J and positive spinwave gap Δ that has an estimated Curie temperature exceeding 50 K. The Curie temperature was calculated from Eq. (3) except for materials with $S = 1/2$ where it was obtained from MC simulations

10-50 meV that far exceeds the values found for the insulators. We emphasize again that the comparison is not exactly fair since the values of J may change significantly due to large alterations in the electronic structure in the anti-ferromagnetic state, which do not only originate in magnetic interactions. Nevertheless, Tab. II provides a promising starting point for discovering new 2D itinerant ferromagnets, but there is a dire need for a better theoretical framework that can quantitatively deal with the thermodynamical properties of itinerant magnetism in 2D.

We finally note that known that certain known 2D ferromagnets like VSe₂⁶ and CrGeTe₃² are not present in Tabs. I-II due to in-plane magnetization, which results in a negative spinwave gap in the present study. For the case of CrGeTe₃ this is in accordance with the experimentally observed loss of magnetism in the monolayer limit whereas for VSe₂ the origin of magnetic order is still unresolved.⁷ In addition we do not find the itinerant 2D ferromagnet Fe₃GeTe₂,⁴ which is simply not present in a bulk parent form in either the COD or ICSD.

B. Combinatorial lattice decoration for new materials

Several theoretical approaches to materials discovery are based on the concept of combinatorial lattice decoration. That is, replacing different elements of a known material with similar elements in the periodic table while maintaining the stoichiometry and then calculate thermodynamic stability and various properties with DFT

or similar methods. For example, CrClO is predicted to be a stable ferromagnet (see Tab. I) and is likely that CrBrO or CrIO may also be stable - or perhaps MnClO. Such an approach is the basis of the C2DB where the majority of known 2D materials have been subjected to such combinatorial lattice decoration. Tabs. I and II contains several materials that do not belong to a known prototypical 2D material.

In order to extend the computational materials discovery based on the COD and ICSD we have performed a computational screening for novel 2D materials based

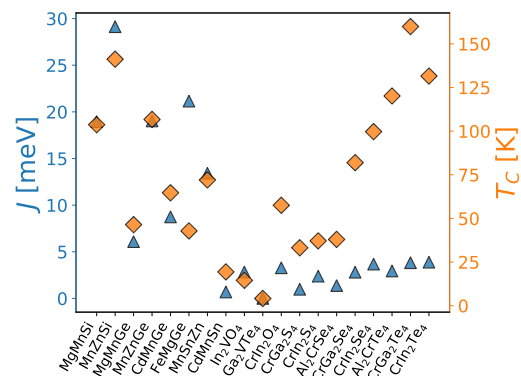


FIG. 2. Materials obtained by combinatorial lattice decoration of the MgMnGe and CrGa₂Se₄ prototypes.

on the prototypes defined by NiRe₂O₈, MgMnGe and CrGa₂Se₂. We perform the lattice decoration according to the rules defined in Ref. 18 and perform a full relaxation of 30, 27, and 24 materials conforming to these prototypes respectively. Of these 12, 14, and 20 materials yield a magnetic ground state. For the NiRe₂O₈ prototype only the defining material has $J > 0$ and $\Delta > 0$. From the remaining two prototypes we show the ferromagnetic materials with positive spin-wave gap in Fig. 2.

IV. DISCUSSION

¹ B. Huang, G. Clark, E. Navarro-Moratalla, D. R. Klein, R. Cheng, K. L. Seyler, D. Zhong, E. Schmidgall, M. A. McGuire, D. H. Cobden, W. Yao, D. Xiao, P. Jarillo-Herrero, and X. Xu, Nature **546**, 270 (2017).

² C. Gong, L. Li, Z. Li, H. Ji, A. Stern, Y. Xia, T. Cao, W. Bao, C. Wang, Y. Wang, Z. Q. Qiu, R. J. Cava, S. G. Louie, J. Xia, and X. Zhang, Nature **546**, 265 (2017).

³ Z. Zhang, J. Shang, C. Jiang, A. Rasmita, W. Gao, and

T. Yu, Nano Lett. **19**, 3138 (2019).

⁴ Z. Fei, B. Huang, P. Malinowski, W. Wang, T. Song, J. Sanchez, W. Yao, D. Xiao, X. Zhu, A. F. May, W. Wu, D. H. Cobden, J.-H. Chu, and X. Xu, Nat. Mater. **17**, 778 (2018).

⁵ J.-U. Lee, S. Lee, J. H. Ryoo, S. Kang, T. Y. Kim, P. Kim, C.-H. Park, J.-G. Park, and H. Cheong, Nano Lett. **16**, 7433 (2016).

- ⁶ M. Bonilla, S. Kolekar, Y. Ma, H. C. Diaz, V. Kalappattil, R. Das, T. Eggers, H. R. Gutierrez, M.-H. Phan, and M. Batzill, *Nat. Nanotechnol.* **13**, 289 (2018).
- ⁷ P. M. Coelho, K. Nguyen Cong, M. Bonilla, S. Kolekar, M.-H. Phan, J. Avila, M. C. Asensio, I. I. Oleynik, and M. Batzill, *J. Phys. Chem. C* **123**, 14089 (2019).
- ⁸ N. Sivadas, S. Okamoto, X. Xu, C. J. Fennie, and D. Xiao, *Nano Letters* **18**, 7658 (2018).
- ⁹ E. Suárez Morell, A. León, R. H. Miwa, and P. Vargas, *2D Mater.* **6**, 025020 (2019).
- ¹⁰ C. Cardoso, D. Soriano, N. García-Martínez, and J. Fernández-Rossier, *Physical Review Letters* **121**, 067701 (2018).
- ¹¹ S. Jiang, L. Li, Z. Wang, K. F. Mak, and J. Shan, *Nature Nanotechnology* **13**, 549 (2018).
- ¹² S. Jiang, L. Li, Z. Wang, K. F. Mak, and J. Shan, *Nat. Nanotechnol.* **13**, 549 (2018).
- ¹³ D. R. Klein, D. MacNeill, J. L. Lado, D. Soriano, E. Navarro-Moratalla, K. Watanabe, T. Taniguchi, S. Manni, P. Canfield, J. Fernández-Rossier, and P. Jarillo-Herrero, *Science* (80-.). **360**, 1218 (2018).
- ¹⁴ K. Kim, S. Y. Lim, J. Kim, J.-U. Lee, S. Lee, P. Kim, K. Park, S. Son, C.-H. Park, J.-G. Park, and H. Cheong, *2D Mater.* **6**, 041001 (2019).
- ¹⁵ H. H. Kim, B. Yang, S. Li, S. Jiang, C. Jin, Z. Tao, G. Nichols, F. Sfigakis, S. Zhong, C. Li, S. Tian, D. G. Cory, G.-X. Miao, J. Shan, K. F. Mak, H. Lei, K. Sun, L. Zhao, and A. W. Tsien, *Proc. Natl. Acad. Sci.* **116**, 11131 (2019).
- ¹⁶ K. Kim, S. Y. Lim, J.-U. Lee, S. Lee, T. Y. Kim, K. Park, G. S. Jeon, C.-H. Park, J.-G. Park, and H. Cheong, *Nature Communications* **10**, 345 (2019).
- ¹⁷ N. Mounet, M. Gibertini, P. Schwaller, D. Campi, A. Merkys, A. Marrazzo, T. Sohier, I. E. Castelli, A. Cepellotti, G. Pizzi, and N. Marzari, *Nature Nanotechnology* **13**, 246 (2018).
- ¹⁸ S. Hastrup, M. Strange, M. Pandey, T. Deilmann, P. S. Schmidt, N. F. Hinsche, M. N. Gjerding, D. Torelli, P. M. Larsen, A. C. Riis-Jensen, J. Gath, K. W. Jacobsen, J. Jørgen Mortensen, T. Olsen, and K. S. Thygesen, *2D Mater.* **5**, 042002 (2018).
- ¹⁹ T. Olsen, E. Andersen, T. Okugawa, D. Torelli, T. Deilmann, and K. S. Thygesen, *Phys. Rev. Mater.* **3**, 024005 (2019).
- ²⁰ A. C. Riis-Jensen, T. Deilmann, T. Olsen, and K. S. Thygesen, *ACS Nano* **13**, 13354 (2019).
- ²¹ N. Miao, B. Xu, L. Zhu, J. Zhou, and Z. Sun, *Journal of the American Chemical Society* **140**, 2417 (2018).
- ²² R. I. Gonzalez, J. Mella, P. Díaz, S. Allende, E. E. Vogel, C. Cardenas, and F. Munoz, *2D Materials* **6**, 045002 (2019).
- ²³ N. Sethulakshmi, A. Mishra, P. M. Ajayan, Y. Kawazoe, A. K. Roy, A. K. Singh, and C. S. Tiwary, *Mater. Today* **27**, 107 (2019).
- ²⁴ T. Kong, K. Stolze, E. I. Timmons, J. Tao, D. Ni, S. Guo, Z. Yang, R. Prozorov, and R. J. Cava, *Advanced Materials* **31**, 1808074 (2019).
- ²⁵ M. Kan, J. Zhou, Q. Sun, Y. Kawazoe, and P. Jena, *The Journal of Physical Chemistry Letters* **4**, 3382 (2013).
- ²⁶ S. Sarikurt, Y. Kadioglu, F. Ersan, E. Vatansever, O. Ü. Aktürk, Y. Yüksel, Ü. Akıncı, and E. Aktürk, *Phys. Chem. Chem. Phys.* **20**, 997 (2018).
- ²⁷ M. McGuire, *Crystals* **7**, 121 (2017).
- ²⁸ K. Yosida, *Theory of magnetism* (Springer Berlin, Heidelberg, 1996).
- ²⁹ J. L. Lado and J. Fernández-Rossier, *2D Mater.* **4**, 035002 (2017).
- ³⁰ D. Torelli and T. Olsen, *2D Mater.* **6**, 015028 (2018).
- ³¹ T. Olsen, *MRS Communications*, 10.1557/mrc.2019.117 , 1 (2019).
- ³² D. Torelli, K. S. Thygesen, and T. Olsen, *2D Mater.* **6**, 045018 (2019).
- ³³ P. M. Larsen, M. Pandey, M. Strange, and K. W. Jacobsen, *Physical Review Materials* **3** (2019), 10.1103/physrevmaterials.3.034003.
- ³⁴ S. V. Tyablikov, *Methods Quantum Theory Magn.* (Springer US, Boston, MA, 1967).
- ³⁵ C. Gong and X. Zhang, *Science* **363**, eaav4450 (2019).
- ³⁶ X. Lu, R. Fei, and L. Yang, *Physical Review B* **100**, 205409 (2019).
- ³⁷ T. Olsen, *Physical Review B* **96**, 125143 (2017).
- ³⁸ A. Hjorth Larsen, J. Jørgen Mortensen, J. Blomqvist, I. E. Castelli, R. Christensen, M. Dulak, J. Friis, M. N. Groves, B. Hammer, C. Hargus, E. D. Hermes, P. C. Jennings, P. Bjerre Jensen, J. Kermode, J. R. Kitchin, E. Leonhard Kolsbjerg, J. Kubal, K. Kaasbjerg, S. Lysgaard, J. Bergmann Maronsson, T. Maxson, T. Olsen, L. Pastewka, A. Peterson, C. Rostgaard, J. Schiøtz, O. Schütt, M. Strange, K. S. Thygesen, T. Vegge, L. Vilhelmsen, M. Walter, Z. Zeng, and K. W. Jacobsen, *J. Phys. Condens. Matter* **29**, 273002 (2017).
- ³⁹ J. Enkovaara, C. Rostgaard, J. J. Mortensen, J. Chen, M. Dulak, L. Ferrighi, J. Gavnholt, C. Glinsvad, V. Haikola, H. a. Hansen, H. H. Kristoffersen, M. Kuisma, a. H. Larsen, L. Lehtovaara, M. Ljungberg, O. Lopez-Acevedo, P. G. Moses, J. Ojanen, T. Olsen, V. Petzold, N. a. Romero, J. Stausholm-Møller, M. Strange, G. a. Tritsarlis, M. Vanin, M. Walter, B. Hammer, H. Häkkinen, G. K. H. Madsen, R. M. Nieminen, J. K. Nørskov, M. Puska, T. T. Rantala, J. Schiøtz, K. S. Thygesen, and K. W. Jacobsen, *J. Phys. Condens. Matter* **22**, 253202 (2010).
- ⁴⁰ T. Olsen, *Phys. Rev. B* **94**, 235106 (2016).
- ⁴¹ J. P. Perdew, K. Burke, and M. Ernzerhof, *Phys. Rev. Lett.* **77**, 3865 (1996).
- ⁴² D. Torelli and T. Olsen, *arxiv.org/abs/1912.05230* , 1 (2019).
- ⁴³ L. D. Casto, A. J. Clune, M. O. Yokosuk, J. L. Musfeldt, T. J. Williams, H. L. Zhuang, M.-W. Lin, K. Xiao, R. G. Hennig, B. C. Sales, J.-Q. Yan, and D. Mandrus, *APL Materials* **3**, 041515 (2015).

Bibliography

- [1] K. S. Novoselov et al. “Electric Field Effect in Atomically Thin Carbon Films”. In: *Science* 306.5696 (2004), pp. 666–669. ISSN: 0036-8075. DOI: 10.1126/science.1102896. eprint: <https://science.sciencemag.org/content/306/5696/666.full.pdf>. URL: <https://science.sciencemag.org/content/306/5696/666>.
- [2] L.D. Landau. *Zur Theorie der Phasenumwandlungen II*. Vol. 11. Physikalische Zeitschrift der Sowjetunion. 1937, pp. 26–35.
- [3] Changgu Lee et al. “Measurement of the Elastic Properties and Intrinsic Strength of Monolayer Graphene”. In: *Science* 321.5887 (2008), pp. 385–388. ISSN: 0036-8075. DOI: 10.1126/science.1157996. eprint: <https://science.sciencemag.org/content/321/5887/385.full.pdf>. URL: <https://science.sciencemag.org/content/321/5887/385>.
- [4] Feng Wang et al. “Gate-Variable Optical Transitions in Graphene”. In: *Science* 320.5873 (2008), pp. 206–209. ISSN: 0036-8075. DOI: 10.1126/science.1152793. eprint: <https://science.sciencemag.org/content/320/5873/206.full.pdf>. URL: <https://science.sciencemag.org/content/320/5873/206>.
- [5] Oleg V. Yazyev and Lothar Helm. “Defect-induced magnetism in graphene”. In: *Phys. Rev. B* 75 (12 Mar. 2007), p. 125408. DOI: 10.1103/PhysRevB.75.125408. URL: <https://link.aps.org/doi/10.1103/PhysRevB.75.125408>.
- [6] M. M. Ugeda et al. “Missing Atom as a Source of Carbon Magnetism”. In: *Phys. Rev. Lett.* 104 (9 Mar. 2010), p. 096804. DOI: 10.1103/PhysRevLett.104.096804. URL: <https://link.aps.org/doi/10.1103/PhysRevLett.104.096804>.
- [7] Héctor González-Herrero et al. “Atomic-scale control of graphene magnetism by using hydrogen atoms”. In: *Science* 352.6284 (2016), pp. 437–441. ISSN: 0036-8075. DOI: 10.1126/science.aad8038. eprint: <https://science.sciencemag.org/content/352/6284/437.full.pdf>. URL: <https://science.sciencemag.org/content/352/6284/437>.
- [8] Rahul Raveendran-Nair et al. “Dual origin of defect magnetism in graphene and its reversible switching by molecular doping”. In: *Nature communications* 4 (June 2013), p. 2010. DOI: 10.1038/ncomms3010.
- [9] Bruno Uchoa et al. “Localized Magnetic States in Graphene”. In: *Physical review letters* 101 (Aug. 2008), p. 026805. DOI: 10.1103/PhysRevLett.101.026805.
- [10] Oleg V. Yazyev and M. I. Katsnelson. “Magnetic Correlations at Graphene Edges: Basis for Novel Spintronics Devices”. In: *Phys. Rev. Lett.* 100 (4 Jan. 2008), p. 047209. DOI: 10.1103/PhysRevLett.100.047209. URL: <https://link.aps.org/doi/10.1103/PhysRevLett.100.047209>.
- [11] Zhiyong Wang et al. “Proximity-Induced Ferromagnetism in Graphene Revealed by the Anomalous Hall Effect”. In: *Phys. Rev. Lett.* 114 (1 Jan. 2015), p. 016603. DOI: 10.1103/PhysRevLett.114.016603. URL: <https://link.aps.org/doi/10.1103/PhysRevLett.114.016603>.
- [12] Peng Wei et al. “Strong interfacial exchange field in the graphene/EuS heterostructure.” In: *Nature materials* 15 7 (2015), pp. 711–6.
- [13] Hongxin Yang et al. “Anatomy of Dzyaloshinskii-Moriya Interaction at Co/Pt Interfaces”. In: *Phys. Rev. Lett.* 115 (26 Dec. 2015), p. 267210. DOI: 10.1103/PhysRevLett.115.267210. URL: <https://link.aps.org/doi/10.1103/PhysRevLett.115.267210>.

- [14] Denis Maryenko et al. “Observation of anomalous Hall effect in a non-magnetic two-dimensional electron system”. In: *Nature communications*. 2017.
- [15] Cheng Gong and Xiang Zhang. “Two-dimensional magnetic crystals and emergent heterostructure devices”. In: *Science* 363.6428 (2019). ISSN: 0036-8075. DOI: 10.1126/science.aav4450. eprint: <https://science.sciencemag.org/content/363/6428/eaav4450.full.pdf>. URL: <https://science.sciencemag.org/content/363/6428/eaav4450>.
- [16] N. D. Mermin and H. Wagner. “Absence of Ferromagnetism or Antiferromagnetism in One- or Two-Dimensional Isotropic Heisenberg Models”. In: *Phys. Rev. Lett.* 17 (22 Nov. 1966), pp. 1133–1136. DOI: 10.1103/PhysRevLett.17.1133. URL: <https://link.aps.org/doi/10.1103/PhysRevLett.17.1133>.
- [17] Bevin Huang et al. “Layer-dependent Ferromagnetism in a van der Waals Crystal down to the Monolayer Limit”. In: *Nature* 546 (Mar. 2017). DOI: 10.1038/nature22391.
- [18] Cheng Gong et al. “Discovery of intrinsic ferromagnetism in two-dimensional van der Waals crystals”. In: *Nature* 546 (Apr. 2017). DOI: 10.1038/nature22060.
- [19] Dante J. O’Hara et al. “Room Temperature Intrinsic Ferromagnetism in Epitaxial Manganese Selenide Films in the Monolayer Limit”. In: *Nano Letters* 18.5 (2018). PMID: 29608316, pp. 3125–3131. DOI: 10.1021/acs.nanolett.8b00683. eprint: <https://doi.org/10.1021/acs.nanolett.8b00683>. URL: <https://doi.org/10.1021/acs.nanolett.8b00683>.
- [20] Manuel Bonilla et al. “Strong Room Temperature Ferromagnetism in VSe₂ Monolayers on van der Waals substrates”. In: *Nature Nanotechnology* (Jan. 2018). DOI: 10.1038/s41565-.
- [21] Wei Yu et al. “Chemically Exfoliated VSe₂ Monolayers with Room-Temperature Ferromagnetism”. In: *Advanced Materials* 31.40 (2019), p. 1903779. DOI: 10.1002/adma.201903779. eprint: <https://onlinelibrary.wiley.com/doi/pdf/10.1002/adma.201903779>. URL: <https://onlinelibrary.wiley.com/doi/abs/10.1002/adma.201903779>.
- [22] A.K. Geim and Irina Grigorieva. “Van der Waals heterostructures”. In: *Nature* 499 (July 2013), pp. 419–25. DOI: 10.1038/nature12385.
- [23] Aaron L. Sharpe et al. “Emergent ferromagnetism near three-quarters filling in twisted bilayer graphene”. In: *Science* 365.6453 (2019), pp. 605–608. ISSN: 0036-8075. DOI: 10.1126/science.aaw3780. eprint: <https://science.sciencemag.org/content/365/6453/605.full.pdf>. URL: <https://science.sciencemag.org/content/365/6453/605>.
- [24] Yuan Cao et al. “Unconventional superconductivity in magic-angle graphene superlattices”. In: *Nature* 556.7699 (Mar. 2018), pp. 43–50. DOI: 10.1038/nature26160. URL: <https://doi.org/10.1038/nature26160>.
- [25] Baoxing Zhai et al. “Two-dimensional ferromagnetic materials and related van der Waals heterostructures: a first-principle study”. In: *Journal of Semiconductors* 40.8 (Aug. 2019), p. 081509. DOI: 10.1088/1674-4926/40/8/081509. URL: <https://doi.org/10.1088/1674-4926/40/8/081509>.
- [26] J. C. Slonczewski. “Conductance and exchange coupling of two ferromagnets separated by a tunneling barrier”. In: *Phys. Rev. B* 39 (10 Apr. 1989), pp. 6995–7002. DOI: 10.1103/PhysRevB.39.6995. URL: <https://link.aps.org/doi/10.1103/PhysRevB.39.6995>.
- [27] D.C. Ralph and M.D. Stiles. “Spin transfer torques”. In: *Journal of Magnetism and Magnetic Materials* 320.7 (2008), pp. 1190–1216. ISSN: 0304-8853. DOI: <https://doi.org/10.1016/j.jmmm.2007.12.019>. URL: <http://www.sciencedirect.com/science/article/pii/S0304885307010116>.
- [28] J. S. Moodera et al. “Large Magnetoresistance at Room Temperature in Ferromagnetic Thin Film Tunnel Junctions”. In: *Phys. Rev. Lett.* 74 (16 Apr. 1995), pp. 3273–3276. DOI: 10.1103/PhysRevLett.74.3273. URL: <https://link.aps.org/doi/10.1103/PhysRevLett.74.3273>.
- [29] A V Khvalkovskiy et al. “Basic principles of STT-MRAM cell operation in memory arrays”. In: *Journal of Physics D: Applied Physics* 46.7 (Feb. 2013), p. 074001. DOI: 10.1088/0022-3727/46/7/074001. URL: <https://doi.org/10.1088/0022-3727/46/7/074001>.

- [30] A. Jahan et al. “Material screening and choosing methods – A review”. In: *Materials & Design* 31.2 (2010), pp. 696–705. ISSN: 0261-3069. DOI: <https://doi.org/10.1016/j.matdes.2009.08.013>. URL: <http://www.sciencedirect.com/science/article/pii/S0261306909004361>.
- [31] Francis Crick. *What Mad Pursuit: A Personal View of Scientific Discovery*. 1990.
- [32] Keith Butler et al. “Machine learning for molecular and materials science”. In: *Nature* 559 (July 2018). DOI: 10.1038/s41586-018-0337-2.
- [33] Tim Mueller, Aaron Kusne, and Rampi Ramprasad. “Machine Learning in Materials Science: Recent Progress and Emerging Applications”. In: May 2016, pp. 186–273. ISBN: 9781119103936. DOI: 10.1002/9781119148739.ch4.
- [34] Daniele Torelli and Thomas Olsen. “Calculating critical temperatures for ferromagnetic order in two-dimensional materials”. English. In: *2D materials* 6.1 (2019). ISSN: 2053-1583. DOI: 10.1088/2053-1583/aaf06d.
- [35] Sten Haastrup et al. “The Computational 2D Materials Database: high-throughput modeling and discovery of atomically thin crystals”. English. In: *2D materials* 5.4 (2018). Original content from this work may be used under the terms of the Creative Commons Attribution 3.0 licence. Any further distribution of this work must maintain attribution to the author(s) and the title of the work, journal citation and DOI. ISSN: 2053-1583. DOI: 10.1088/2053-1583/aacfc1.
- [36] Thomas Olsen et al. “Discovering two-dimensional topological insulators from high-throughput computations”. English. In: *Physical Review Materials* 3.2 (2019). ISSN: 2475-9953. DOI: 10.1103/PhysRevMaterials.3.024005.
- [37] Daniele Torelli, Kristian Sommer Thygesen, and Thomas Olsen. “High throughput computational screening for 2D ferromagnetic materials: the critical role of anisotropy and local correlations”. English. In: *2D materials* 6.4 (2019). ISSN: 2053-1583. DOI: 10.1088/2053-1583/ab2c43.
- [38] Kei Yosida. *The theory of Magnetism*. Vol. 122. Springer Series in Solid-State Sciences. Springer, 1996.
- [39] J. M. D. Coey. *Magnetism and Magnetic Materials*. Cambridge University Press, 2010. DOI: 10.1017/CB09780511845000.
- [40] Carsten Timm. *Lecture notes in Theory of Magnetism*. International Max Planck Research School for Dynamical Processes in Atoms, Molecules and Solids, Feb. 2015.
- [41] Thomas Schrefl et al. “Domain structures and switching mechanisms in patterned magnetic elements”. In: *Journal of Magnetism and Magnetic Materials* 175.1 (1997). Proceedings of the First Toyota Workshop on Magnetism and Magnetic Materials for High Density Information Storage, pp. 193–204. ISSN: 0304-8853. DOI: [https://doi.org/10.1016/S0304-8853\(97\)00156-X](https://doi.org/10.1016/S0304-8853(97)00156-X). URL: <http://www.sciencedirect.com/science/article/pii/S030488539700156X>.
- [42] Alexander Dobin and Hans Juergen Richter. “Domain Wall Assisted Magnetic Recording”. In: *Applied Physics Letters* 89 (May 2006). DOI: 10.1063/1.2335590.
- [43] Claas Abert. “Micromagnetics and spintronics: models and numerical methods”. In: *The European Physical Journal B* 92 (2018), pp. 1–45.
- [44] M. H. Seaberg et al. “Nanosecond X-Ray Photon Correlation Spectroscopy on Magnetic Skyrmions”. In: *Phys. Rev. Lett.* 119 (6 Aug. 2017), p. 067403. DOI: 10.1103/PhysRevLett.119.067403. URL: <https://link.aps.org/doi/10.1103/PhysRevLett.119.067403>.
- [45] S. Muhlbauer et al. “Skyrmion Lattice in a Chiral Magnet”. In: *Science* 323.5916 (2009), pp. 915–919. ISSN: 0036-8075. DOI: 10.1126/science.1166767. eprint: <https://science.sciencemag.org/content/323/5916/915.full.pdf>. URL: <https://science.sciencemag.org/content/323/5916/915>.
- [46] Lars Bergqvist and Anders Bergman. “Realistic finite temperature simulations of magnetic systems using quantum statistics”. In: *Physical Review Materials* 2 (Aug. 2017). DOI: 10.1103/PhysRevMaterials.2.013802.

- [47] Richard Evans et al. “Atomistic spin model simulations of magnetic nanomaterials”. In: *Journal of physics. Condensed matter : an Institute of Physics journal* 26 (Mar. 2014), p. 103202. DOI: 10.1088/0953-8984/26/10/103202.
- [48] Werner Heisenberg. “Mehrkörperproblem und Resonanz in der Quantenmechanik”. In: *Zeitschrift für Physik* 38 (), pp. 411–426.
- [49] P. A. M. Dirac. “On the Theory of Quantum Mechanics”. In: *Proceedings of the Royal Society of London. Series A, Containing Papers of a Mathematical and Physical Character* 112.762 (1926), pp. 661–677. ISSN: 09501207. URL: <http://www.jstor.org/stable/94692>.
- [50] Andreas Frisk et al. “Magnetic X-ray spectroscopy of two-dimensional CrI₃ layers”. In: *Materials Letters* 232 (2018), pp. 5–7. ISSN: 0167-577X. DOI: <https://doi.org/10.1016/j.matlet.2018.08.005>. URL: <http://www.sciencedirect.com/science/article/pii/S0167577X18311893>.
- [51] P. A. M. Dirac. “The Quantum Theory of the Electron”. In: *Proceedings of the Royal Society of London Series A* 117.778 (Feb. 1928), pp. 610–624. DOI: 10.1098/rspa.1928.0023.
- [52] David. Griffiths. *Introduction To Quantum Mechanics*. Pearson Prentice Hall, 2004.
- [53] J. J. Mortensen, L. B. Hansen, and K. W. Jacobsen. “Real-space grid implementation of the projector augmented wave method”. English. In: *Phys. Rev. B* 71.3 (Jan. 2005), p. 035109. ISSN: 1098-0121. DOI: 10.1103/PhysRevB.71.035109.
- [54] J Enkovaara et al. “Electronic structure calculations with GPAW: a real-space implementation of the projector augmented-wave method”. In: *Journal of Physics: Condensed Matter* 22.25 (June 2010), p. 253202. DOI: 10.1088/0953-8984/22/25/253202. URL: <https://doi.org/10.1088/0953-8984/22/25/253202>.
- [55] P. E. Blochl. “Projector augmented-wave method”. In: *Phys. Rev. B* 50 (24 Dec. 1994), pp. 17953–17979. DOI: 10.1103/PhysRevB.50.17953. URL: <https://link.aps.org/doi/10.1103/PhysRevB.50.17953>.
- [56] Ask Hjorth Larsen et al. “The atomic simulation environment—a Python library for working with atoms”. In: *Journal of Physics: Condensed Matter* 29.27 (June 2017), p. 273002. DOI: 10.1088/1361-648x/aa680e. URL: <https://doi.org/10.1088/1361-648x/aa680e>.
- [57] V. Fock. “Näherungsmethode zur Lösung des quantenmechanischen Mehrkörperproblems”. In: *Z. Physik* 61 (Jan. 1930), pp. 126–148.
- [58] J. C. Slater. “The Self Consistent Field and the Structure of Atoms”. In: *Phys. Rev.* 32 (3 Oct. 1928), pp. 339–348. DOI: 10.1103/PhysRev.32.339. URL: <https://link.aps.org/doi/10.1103/PhysRev.32.339>.
- [59] L. H. Thomas. “The calculation of atomic fields”. In: *Mathematical Proceedings of the Cambridge Philosophical Society* 23.5 (1927), pp. 542–548. DOI: 10.1017/S0305004100011683.
- [60] Enrico Fermi. “Statistical method to determine some properties of atoms”. In: *Rendiconti Lincei. Scienze Fisiche e Naturali* 22 (Dec. 2011), pp. 283–314.
- [61] W. Kohn P. Hohenberg. “Inhomogeneous electron gas”. In: *Phys. Rev.* 136 (1964), B864–B871.
- [62] W. Kohn and L. J. Sham. “Self-Consistent Equations Including Exchange and Correlation Effects”. In: *Phys. Rev.* 140 (4A Nov. 1965), A1133–A1138. DOI: 10.1103/PhysRev.140.A1133. URL: <https://link.aps.org/doi/10.1103/PhysRev.140.A1133>.
- [63] Axel D. Becke. “Perspective: Fifty years of density-functional theory in chemical physics”. In: *The Journal of Chemical Physics* 140.18 (2014), 18A301. DOI: 10.1063/1.4869598. eprint: <https://doi.org/10.1063/1.4869598>. URL: <https://doi.org/10.1063/1.4869598>.
- [64] Erich Runge and E. K. U. Gross. “Density-Functional Theory for Time-Dependent Systems”. In: *Phys. Rev. Lett.* 52 (12 Mar. 1984), pp. 997–1000. DOI: 10.1103/PhysRevLett.52.997. URL: <https://link.aps.org/doi/10.1103/PhysRevLett.52.997>.
- [65] Narbe Mardirossian and Martin Head-Gordon. “Thirty years of density functional theory in computational chemistry: an overview and extensive assessment of 200 density functionals”. In: *Molecular Physics* 115.19 (2017), pp. 2315–2372. DOI: 10.1080/00268976.2017.1333644.

- [66] Kieron Burke. “Perspective on density functional theory”. In: *The Journal of Chemical Physics* 136.15 (2012), p. 150901. DOI: 10.1063/1.4704546.
- [67] Ivan Yakovkin and Peter Dowben. “The problem of the band gap in LDA calculations”. In: *Surface Review and Letters (SRL)* 14 (June 2007), pp. 481–487. DOI: 10.1142/S0218625X07009499.
- [68] John P. Perdew, Kieron Burke, and Matthias Ernzerhof. “Generalized Gradient Approximation Made Simple”. In: *Phys. Rev. Lett.* 77 (18 Oct. 1996), pp. 3865–3868. DOI: 10.1103/PhysRevLett.77.3865. URL: <https://link.aps.org/doi/10.1103/PhysRevLett.77.3865>.
- [69] Thomas Olsen. “Designing in-plane heterostructures of quantum spin Hall insulators from first principles: $1T' - \text{MoS}_2$ with adsorbates”. In: *Phys. Rev. B* 94 (23 Dec. 2016), p. 235106. DOI: 10.1103/PhysRevB.94.235106. URL: <https://link.aps.org/doi/10.1103/PhysRevB.94.235106>.
- [70] S. L. Dudarev et al. “Electron-energy-loss spectra and the structural stability of nickel oxide: An LSDA+U study”. In: *Phys. Rev. B* 57 (3 Jan. 1998), pp. 1505–1509. DOI: 10.1103/PhysRevB.57.1505. URL: <https://link.aps.org/doi/10.1103/PhysRevB.57.1505>.
- [71] F. Aryasetiawan et al. “Calculations of Hubbard U from first-principles”. In: *Physical Review B* 74 (Mar. 2006). DOI: 10.1103/PhysRevB.74.125106.
- [72] Matteo Cococcioni and Stefano de Gironcoli. “Linear response approach to the calculation of the effective interaction parameters in the LDA + U method”. In: *Phys. Rev. B* 71 (3 Jan. 2005), p. 035105. DOI: 10.1103/PhysRevB.71.035105. URL: <https://link.aps.org/doi/10.1103/PhysRevB.71.035105>.
- [73] Sarah Tolba et al. “The DFT+U: Approaches, Accuracy, and Applications”. In: May 2018. ISBN: 978-1-78923-132-8. DOI: 10.5772/intechopen.72020.
- [74] H. Xiang et al. “Magnetic properties and energy-mapping analysis”. In: *Dalton transactions (Cambridge, England : 2003)* 42 (Nov. 2012). DOI: 10.1039/c2dt31662e.
- [75] Alexander Tsirlin. “Spin-chain magnetism and uniform Dzyloshinsky-Moriya anisotropy in BaV_3O_8 ”. In: *Physical Review B* 89 (Aug. 2013). DOI: 10.1103/PhysRevB.89.014405.
- [76] Danis Badrtdinov et al. “Magnetism of coupled spin tetrahedra in ilinskite-type $\text{KCu}_5\text{O}_2(\text{SeO}_3)_2\text{Cl}_3$ ”. In: *Scientific Reports* 8 (Dec. 2018). DOI: 10.1038/s41598-018-20350-z.
- [77] Robert Strawderman. “Monte Carlo Methods in Statistical Physics by M. E. J. Newman; G. T. Barkema”. In: *Journal of the American Statistical Association* 96 (Jan. 2001). DOI: 10.2307/2670314.
- [78] Wolfhard Janke. “Monte Carlo Methods in Classical Statistical Physics”. In: *Computational Many-Particle Physics*. Ed. by H. Fehske, R. Schneider, and A. Weiße. Berlin, Heidelberg: Springer Berlin Heidelberg, 2008, pp. 79–140. ISBN: 978-3-540-74686-7. DOI: 10.1007/978-3-540-74686-7_4. URL: https://doi.org/10.1007/978-3-540-74686-7_4.
- [79] G. van Rossum. *Python tutorial, Technical Report CS-R9526*. Centrum voor Wiskunde en Informatica (CWI), May 1995.
- [80] Nicholas Metropolis et al. “Equation of State Calculations by Fast Computing Machines”. In: *The Journal of Chemical Physics* 21.6 (1953), pp. 1087–1092. DOI: 10.1063/1.1699114.
- [81] Ulli Wolff. “Collective Monte Carlo Updating for Spin Systems”. In: *Phys. Rev. Lett.* 62 (4 Jan. 1989), pp. 361–364. DOI: 10.1103/PhysRevLett.62.361. URL: <https://link.aps.org/doi/10.1103/PhysRevLett.62.361>.
- [82] Yu Liu et al. “Thickness-dependent magnetic order in CrI_3 single crystals”. In: *Scientific Reports* 9 (Aug. 2019). DOI: 10.1038/s41598-019-50000-x.
- [83] J L Lado and J Fernández-Rossier. “On the origin of magnetic anisotropy in two dimensional CrI_3 ”. In: *2D Materials* 4.3 (June 2017), p. 035002. DOI: 10.1088/2053-1583/aa75ed. URL: <https://doi.org/10.1088/2053-1583/aa75ed>.

- [84] Alessandro Codello. “Exact Curie temperature for the Ising model on Archimedean and Laves lattices”. In: *Journal of Physics A: Mathematical and Theoretical* 43.38 (Aug. 2010), p. 385002. DOI: 10.1088/1751-8113/43/38/385002. URL: <https://doi.org/10.1088/1751-8113/43/38/385002>.
- [85] Changsong Xu et al. “Interplay between Kitaev interaction and single ion anisotropy in ferromagnetic CrI₃ and CrGeTe₃ monolayers”. In: *npj Computational Materials* 4 (Dec. 2018). DOI: 10.1038/s41524-018-0115-6.
- [86] Lucas Webster and Jia-An Yan. “Strain-tunable magnetic anisotropy in monolayer CrCl₃, CrBr₃, and CrI₃”. In: *Phys. Rev. B* 98 (14 Oct. 2018), p. 144411. DOI: 10.1103/PhysRevB.98.144411. URL: <https://link.aps.org/doi/10.1103/PhysRevB.98.144411>.
- [87] Tista Mukherjee et al. “Strain induced electronic and magnetic properties of 2D magnet CrI₃ : a DFT approach”. In: *Journal of Physics: Condensed Matter* 31 (May 2019). DOI: 10.1088/1361-648X/ab1fcf.
- [88] D. Soriano, C. Cardoso, and J. Fernández-Rossier. “Interplay between interlayer exchange and stacking in CrI₃ bilayers”. In: *Solid State Communications* 299 (2019), p. 113662. ISSN: 0038-1098. DOI: <https://doi.org/10.1016/j.ssc.2019.113662>. URL: <http://www.sciencedirect.com/science/article/pii/S0038109819303680>.
- [89] Sten Haastrup. “Computational discovery and characterization of novel 2D materials”. PhD thesis. DTU Physics, Department of Physics, 2018.
- [90] *Computational 2D Materials Database (C2DB)*. <https://cmr.fysik.dtu.dk/c2db/c2db.html>.
- [91] *MyQueue*. <https://myqueue.readthedocs.io/en/latest/>.
- [92] Yi-Hsien Lee et al. “Synthesis of Large-Area MoS₂ Atomic Layers with Chemical Vapor Deposition”. In: *Advanced Materials* 24.17 (2012), pp. 2320–2325. DOI: 10.1002/adma.201104798. eprint: <https://onlinelibrary.wiley.com/doi/pdf/10.1002/adma.201104798>. URL: <https://onlinelibrary.wiley.com/doi/abs/10.1002/adma.201104798>.
- [93] He Bai et al. “A controllable synthesis of uniform MoS₂ monolayers on annealed molybdenum foils”. In: *Materials Letters* 204 (2017), pp. 35–38. ISSN: 0167-577X. DOI: <https://doi.org/10.1016/j.matlet.2017.05.097>. URL: <http://www.sciencedirect.com/science/article/pii/S0167577X17308339>.
- [94] Manish Chhowalla et al. “The Chemistry of Two-Dimensional Layered Transition Metal Dichalcogenide Nanosheets”. In: *Nature chemistry* 5 (Apr. 2013), pp. 263–75. DOI: 10.1038/nchem.1589.
- [95] Andrea Splendiani et al. “Emerging Photoluminescence in Monolayer MoS₂”. In: *Nano Letters* 10.4 (2010). PMID: 20229981, pp. 1271–1275. DOI: 10.1021/nl903868w. eprint: <https://doi.org/10.1021/nl903868w>. URL: <https://doi.org/10.1021/nl903868w>.
- [96] Sajid Husain et al. “Spin pumping in the Heusler alloy Co₂FeAl/MoS₂ heterostructure: Ferromagnetic resonance experiment and theory”. In: *Phys. Rev. B* 98 (18 Nov. 2018), p. 180404. DOI: 10.1103/PhysRevB.98.180404. URL: <https://link.aps.org/doi/10.1103/PhysRevB.98.180404>.
- [97] Jiawen You, Md Hossain, and Zhengtang Luo. “Synthesis of 2D transition metal dichalcogenides by chemical vapor deposition with controlled layer number and morphology”. In: *Nano Convergence* 5 (Dec. 2018). DOI: 10.1186/s40580-018-0158-x.
- [98] D.G. Pettifor. “A chemical scale for crystal-structure maps”. In: *Solid State Communications* 51.1 (1984), pp. 31–34. ISSN: 0038-1098. DOI: [https://doi.org/10.1016/0038-1098\(84\)90765-8](https://doi.org/10.1016/0038-1098(84)90765-8). URL: <http://www.sciencedirect.com/science/article/pii/0038109884907658>.
- [99] Henning Glawe et al. “The optimal one dimensional periodic table: a modified Pettifor chemical scale from data mining”. In: *New Journal of Physics* 18.9 (Sept. 2016), p. 093011. DOI: 10.1088/1367-2630/18/9/093011. URL: <https://doi.org/10.1088/1367-2630/18/9/093011>.

- [100] Vadym Kulish and Wei Huang. “Single-layer metal halides MX₂ (X = Cl, Br, I): Stability and tunable magnetism from first principles and Monte Carlo simulations”. In: *J. Mater. Chem. C* 5 (July 2017). DOI: 10.1039/C7TC02664A.
- [101] Xiao-Liang Qi and Shou-Cheng Zhang. “Topological insulators and superconductors”. In: *Rev. Mod. Phys.* 83 (4 Oct. 2011), pp. 1057–1110. DOI: 10.1103/RevModPhys.83.1057. URL: <https://link.aps.org/doi/10.1103/RevModPhys.83.1057>.
- [102] M. Z. Hasan and C. L. Kane. “Colloquium: Topological insulators”. In: *Rev. Mod. Phys.* 82 (4 Nov. 2010), pp. 3045–3067. DOI: 10.1103/RevModPhys.82.3045. URL: <https://link.aps.org/doi/10.1103/RevModPhys.82.3045>.
- [103] B. Andrei Bernevig, Taylor L. Hughes, and Shou-Cheng Zhang. “Quantum Spin Hall Effect and Topological Phase Transition in HgTe Quantum Wells”. In: *Science* 314.5806 (2006), pp. 1757–1761. ISSN: 0036-8075. DOI: 10.1126/science.1133734. eprint: <https://science.sciencemag.org/content/314/5806/1757.full.pdf>. URL: <https://science.sciencemag.org/content/314/5806/1757>.
- [104] Haijun Zhang et al. “Topological insulators in Bi₂Se₃, Bi₂Te₃ and Sb₂Te₃ with a single Dirac cone on the surface”. In: *Nature Physics* 5 (May 2009), pp. 438–442. DOI: 10.1038/nphys1270.
- [105] Motohiko Ezawa. “Spin valleytronics in silicene: Quantum spin Hall–quantum anomalous Hall insulators and single-valley semimetals”. In: *Phys. Rev. B* 87 (15 Apr. 2013), p. 155415. DOI: 10.1103/PhysRevB.87.155415. URL: <https://link.aps.org/doi/10.1103/PhysRevB.87.155415>.
- [106] Xiaofeng Qian et al. “Quantum spin Hall effect in two-dimensional transition metal dichalcogenides”. In: *Science* 346.6215 (2014), pp. 1344–1347. ISSN: 0036-8075. DOI: 10.1126/science.1256815. eprint: <https://science.sciencemag.org/content/346/6215/1344.full.pdf>. URL: <https://science.sciencemag.org/content/346/6215/1344>.
- [107] Qin Liu et al. “Magnetic Impurities on the Surface of a Topological Insulator”. In: *Phys. Rev. Lett.* 102 (15 May 2009), p. 156603. DOI: 10.1103/PhysRevLett.102.156603. URL: <https://link.aps.org/doi/10.1103/PhysRevLett.102.156603>.
- [108] Wang-Kong Tse et al. “Quantum anomalous Hall effect in single-layer and bilayer graphene”. In: *Phys. Rev. B* 83 (15 Apr. 2011), p. 155447. DOI: 10.1103/PhysRevB.83.155447. URL: <https://link.aps.org/doi/10.1103/PhysRevB.83.155447>.
- [109] Xian-Lei Sheng and Branislav K. Nikolić. “Monolayer of the 5d transition metal trichloride OsCl₃: A playground for two-dimensional magnetism, room-temperature quantum anomalous Hall effect, and topological phase transitions”. In: *Phys. Rev. B* 95 (20 May 2017), p. 201402. DOI: 10.1103/PhysRevB.95.201402. URL: <https://link.aps.org/doi/10.1103/PhysRevB.95.201402>.
- [110] Peng Chen, Jinyu Zou, and Bang-Gui Liu. “Intrinsic ferromagnetism and quantum anomalous Hall effect in CoBr₂ monolayer”. In: *Phys. Chem. Chem. Phys.* 19 (Mar. 2017). DOI: 10.1039/C7CP02158E.
- [111] Junwei Liu, Xiaofeng Qian, and Liang Fu. “Crystal Field Effect Induced Topological Crystalline Insulators In Monolayer IV–VI Semiconductors”. In: *Nano Letters* 15.4 (2015). PMID: 25741907, pp. 2657–2661. DOI: 10.1021/acs.nanolett.5b00308. eprint: <https://doi.org/10.1021/acs.nanolett.5b00308>. URL: <https://doi.org/10.1021/acs.nanolett.5b00308>.
- [112] Chengwang Niu et al. “Two-Dimensional Topological Crystalline Insulator and Topological Phase Transition in TlSe and TlS Monolayers”. In: *Nano Letters* 15.9 (2015). PMID: 26241305, pp. 6071–6075. DOI: 10.1021/acs.nanolett.5b02299. eprint: <https://doi.org/10.1021/acs.nanolett.5b02299>. URL: <https://doi.org/10.1021/acs.nanolett.5b02299>.
- [113] *Release notes*. <https://wiki.fysik.dtu.dk/gpaw/releasenotes.html>.
- [114] Michael A. McGuire. “Crystal and Magnetic Structures in Layered, Transition Metal Dihalides and Trihalides”. In: *Crystals* 7.5 (2017). ISSN: 2073-4352. DOI: 10.3390/cryst7050121. URL: <https://www.mdpi.com/2073-4352/7/5/121>.

- [115] J M Kosterlitz and D J Thouless. “Ordering, metastability and phase transitions in two-dimensional systems”. In: *Journal of Physics C: Solid State Physics* 6.7 (Apr. 1973), pp. 1181–1203. DOI: 10.1088/0022-3719/6/7/010. URL: <https://doi.org/10.1088%2F0022-3719%2F6%2F7%2F010>.
- [116] S. T. Bramwell and P. C. W. Holdsworth. “Magnetization: A characteristic of the Kosterlitz-Thouless-Berezinskii transition”. In: *Phys. Rev. B* 49 (13 Apr. 1994), pp. 8811–8814. DOI: 10.1103/PhysRevB.49.8811. URL: <https://link.aps.org/doi/10.1103/PhysRevB.49.8811>.
- [117] *OQMD: The Open Quantum Materials Database*. <http://oqmd.org/documentation/vaspl>.
- [118] Scott Kirklin et al. “The Open Quantum Materials Database (OQMD): Assessing the accuracy of DFT formation energies”. In: *npj Computational Materials* 1 (Dec. 2015), p. 15010. DOI: 10.1038/npjcompumats.2015.10.
- [119] Matthew Yankowitz et al. “van der Waals heterostructures combining graphene and hexagonal boron nitride”. In: *Nature Reviews Physics* 1 (Jan. 2019), p. 1. DOI: 10.1038/s42254-018-0016-0.
- [120] Evgeny Alexeev et al. “Resonantly hybridized excitons in moiré superlattices in van der Waals heterostructures”. In: *Nature* 567 (Mar. 2019), pp. 81–86. DOI: 10.1038/s41586-019-0986-9.
- [121] Peter Mahler Larsen et al. “Definition of a scoring parameter to identify low-dimensional materials components”. In: *Phys. Rev. Materials* 3 (3 Mar. 2019), p. 034003. DOI: 10.1103/PhysRevMaterials.3.034003. URL: <https://link.aps.org/doi/10.1103/PhysRevMaterials.3.034003>.
- [122] G. Bergerhoff et al. “The inorganic crystal structure data base”. In: *Journal of Chemical Information and Computer Sciences* 23.2 (1983), pp. 66–69. DOI: 10.1021/ci00038a003. eprint: <https://pubs.acs.org/doi/pdf/10.1021/ci00038a003>. URL: <https://pubs.acs.org/doi/abs/10.1021/ci00038a003>.
- [123] Saulius Gražulis et al. “Crystallography Open Database (COD): An open-access collection of crystal structures and platform for world-wide collaboration”. English (US). In: *Nucleic Acids Research* 40.D1 (Jan. 2012). ISSN: 0305-1048. DOI: 10.1093/nar/gkr900.
- [124] *Definition of a scoring parameter to identify low-dimensional materials components*. <https://cmr.fysik.dtu.dk/lowdim/lowdim.html>.
- [125] V Carteaux et al. “Crystallographic, magnetic and electronic structures of a new layered ferromagnetic compound Cr₂Ge₂Te₆”. In: *Journal of Physics: Condensed Matter* 7.1 (Jan. 1995), pp. 69–87. DOI: 10.1088/0953-8984/7/1/008. URL: <https://doi.org/10.10882F0953-89842F72F12F008>.
- [126] Huiwen Ji et al. “A ferromagnetic insulating substrate for the epitaxial growth of topological insulators”. In: *Journal of Applied Physics* 114.11 (2013), p. 114907. DOI: 10.1063/1.4822092.
- [127] Anubhav Jain et al. “The Materials Project: A materials genome approach to accelerating materials innovation”. In: *APL Materials* 1.1 (2013), p. 011002. ISSN: 2166532X. DOI: 10.1063/1.4812323. URL: <http://link.aip.org/link/AMPADS/v1/i1/p011002/s1%5C&Agg=doi>.
- [128] S. Arapan, Pablo Nieves, and S. Cuesta-López. “A high-throughput exploration of magnetic materials by using structure predicting methods”. In: *Journal of Applied Physics* 123 (Feb. 2018), p. 083904. DOI: 10.1063/1.5004979.
- [129] Nicolas Mounet et al. “Two-dimensional materials from high-throughput computational exfoliation of experimentally known compounds”. In: *Nature nanotechnology* 13.3 (Mar. 2018), pp. 246–252. ISSN: 1748-3387. DOI: 10.1038/s41565-017-0035-5. URL: <https://doi.org/10.1038/s41565-017-0035-5>.
- [130] Yu Zhu et al. “Systematic search for two-dimensional ferromagnetic materials”. In: *Phys. Rev. Materials* 2 (8 Aug. 2018), p. 081001. DOI: 10.1103/PhysRevMaterials.2.081001. URL: <https://link.aps.org/doi/10.1103/PhysRevMaterials.2.081001>.

- [131] Zhou Jiang et al. “Screening and Design of Novel 2D Ferromagnetic Materials with High Curie Temperature above Room Temperature”. In: *ACS Applied Materials & Interfaces* 10.45 (2018), pp. 39032–39039. DOI: 10.1021/acsami.8b14037. eprint: <https://doi.org/10.1021/acsami.8b14037>. URL: <https://doi.org/10.1021/acsami.8b14037>.

